Catalase-Peroxidase: A Structure that Facilitates Electron Transfer, Protein-based Cofactor Formation, and Antibiotic Activation

by

Callie Marie Barton

A dissertation submitted to the Graduate Faculty of
Auburn University
in partial fulfillment of the
requirements for the
Degree of Doctor of Philosophy

Auburn, Alabama
December 10th, 2022

Keywords: catalase-peroxidase (KatG), peroxidase, peroxidase electron donors (PxEDs), proximal tryptophan, MYW adduct, S315T

Approved by
Douglas C. Goodwin, Chair, Professor and Dept. Chair, Chemistry and Biochemistry
Holly Ellis, Professor, Biochemistry and Molecular Biology, East Carolina University
Steven Mansoorabadi, J. Milton Harris Associate Professor, Chemistry and Biochemistry
Angela Calderon, Associate Professor Drug Discovery and Development, Harrison College of Pharmacy

Abstract

Catalase-peroxidase (KatG) is a heme-dependent enzyme that uses a single active for the degradation of H_2O_2 by two distinct mechanisms. One is a catalase mechanism where two equivalents of H_2O_2 are disproportionated with each catalytic cycle, one being reduced to two H_2O and the other being oxidized to O_2. The second is a peroxidase mechanism where H_2O_2 is reduced to two H_2O and an exogenous electron donor or peroxidatic electron donor (PxED) is oxidized. There is a broad range of possible PxEDs and which of these are utilized depends on the peroxidase in question as well as the electron donors, that are available in the physiological surroundings of the enzyme. Interestingly, KatG is widely (though not universally) distributed among prokaryotes, including some archaeal species; it is also found in fungi. Interestingly, KatG is very commonly found among *pathogenic* bacteria and fungi. These include some of the most notorious threats to human health and food security. They include but are not limited to, *Mycobacterium tuberculosis, Escherichia coli O157:H7, Yersinia pestis, Acinetobacter baumanii, Aeromonas hydrophila, Magnaporthe grisea* and *M. oryzae*, etc. The enzyme appears to impart an advantage to these organisms in light of the near universal reliance by higher eukaryotes on H_2O_2 as a defense against pathogen invasion. In the case of *M. tuberculosis* KatG, it is responsible for the activation of the antitubercular prodrug isoniazid and it is essential for the drug's antibiotic activity. Accordingly, mutations to the *katG* gene and the corresponding changes to the KatG enzyme structure are at the heart of 70% of isoniazid resistance.

The overall structure of the enzyme as well as specific arrangements of the KatG active site are similar to those of a heme-dependent peroxidase from the peroxidase-

catalase enzyme superfamily (formerly known as the plant peroxidase superfamily). Interestingly, it is the only enzyme in the entire superfamily with robust catalase activity—the rest of the superfamily's members are monofunctional peroxidases. KatG's unique catalase activity operates by a mechanism which is distinct from all other heme-based catalases, and this mechanism depends on a protein-based cofactor found nowhere else in nature, a Met-Tyr-Trp (MYW) covalent adduct which is post-translationally and autocatalytically generated the active site of KatG. Redox cycling of this MYW cofactor between its fully covalent and free-radical states is integral for robust catalase activity from an otherwise catalase-inactive, heme-peroxidase active site. Interestingly and counterintuitively, KatG's catalase and peroxidase activities are synergistic with one another. The peroxidase activity serves to prevent the inactivation of KatG's catalase activity. This function appears to depend on a protein structure, which is uniquely rich in oxidizable amino acids, especially Trp and Tyr. It has been proposed that these residues serve as electron-hole transfer conduits to move misdirected oxidizing equivalents to the enzyme's surface. Here, PxEDs can reduce and resolve these potentially destructive protein oxidation events without interfering in KatG's catalase function. Notably, it has also been put forward that the mechanism for antibiotic activation depends on properly directed intraprotein radical transfer reactions.

KatG has a structure that is particularly well suited for through-protein electron transfer. For example, the enzyme's N-terminal domain (which contains the active site and heme cofactor) has four times the expected contribution of Trp residues to its amino acid composition. Structurally, the oxidizable amino acids in the KatG N-terminal domain appear to divide into four sectors or networks, each of which has a Trp residue

which is closest point of the network to active site and the heme cofactor. One network is dominated by the MYW cofactor (headed by Trp 107); its primary function is to support catalase activity. Three other networks are each headed by a strictly conserved Trp, including KatG's so-called proximal tryptophan (W321), as well as W412 and W91. The purpose of the research described in this dissertation is to evaluate the role of these networks of oxidizable amino acids in KatG function within two contexts: 1) KatG prior to the autocatalytic establishment of the MYW cofactor, and 2) the fully functional MYW-bearing KatG enzyme. To the former, does the highly oxidizable framework of the KatG structure facilitate or interfere with formation of the MYW cofactor? To the latter, what is the relative contribution of each sector of KatG's oxidizable scaffold to the preservation of KatG's catalase activity?

In order to evaluate the autocatalytic formation of the MYW cofactor, we first had to establish an expression and purification protocol that would result in protein without the fully formed MYW cofactor. To form the MYW cofactor, heme and peroxide are needed. Knowing this, we expressed KatG without heme and developed a reconstitution procedure that allowed for the proper insertion of the heme into the active site without forming the MYW cofactor. We called with protein, reconstituted KatG (*r*KatG). We also expressed and purified the protein in the presence of heme for the purpose of having a protein with the fully formed MYW cofactor. We called this protein mature KatG (*m*KatG). First, it was important to ensure the heme was in the correct pocket with the correct spin states in *r*KatG, which was confirmed with UV-Visible spectra and EPR. Second, it was essential to confirm the MYW cofactor had not formed in rKatG and had

formed in *m*KatG, which was done through peptide mapping of tryptic digested protein with LC-MS/MS.

Once the protocol was established and the presence or absence of the MYW cofactor had been confirmed, the protocol was used in KatG variants where oxidizable residues had been replaced with non-oxidizable phenylalanine. This allowed for the evaluation of the role of the network of oxidizable amino acids on the facilitation or interference of the autocatalytic formation of the MYW cofactor. It also allowed for the evaluation of the role of the network of oxidizable amino acids on the preservation of the active site through electron transfer. First, the investigation of the formation of the MYW adduct began with the observations of heme transition states in reactions with limited-turnover H_2O_2 concentrations compared to reactions with H_2O_2 concentrations supportive of steady-state catalytic turnover. This was followed up with electron paramagnetic resonance (EPR) to track the protein radical formation of the MYW cofactor. Second, the heme intermediates generated by these KatG variants heme were evaluated when reacted with other peroxides, like peracetic acid (PAA), which would allow the enzyme to form initial heme intermediates without allowing the enzyme to perform catalase turnover. Other heme intermediates were observed with reactions with PxEDs like ABTS and ascorbic acid to investigate through-protein electron transfer. Another technique used to investigate the effects of the network of oxidizable amino acids was the extent of O_2 production. In this, how much O_2 each KatG variant produced at different pH's, in the presence and absence of PxED, served to connect changes in each variant's oxidizable amino-acid network to any diminished ability to sustain with O_2 production. This experiment was also used for determining if each KatG variant was still active or inactive

at the end of the initial reaction with H_2O_2 indicating the networks ability to prevent inactivation of the enzyme. To this extent we also performed inactivation assays at varying pH's to even more directly evaluate each KatG variants' ability to prevent inactivation.

In this work we also investigated how electron transfer throughout the enzyme can effect antibiotic inactivation. More specifically, how the prodrug isoniazid's (INH) most resistant strains that are caused by the S315T mutation to the *katG* gene effect electron transfer within KatG enzyme. We began this investigation by producing the S315T KatG variant in both the *r*KatG and *m*KatG forms. We used stopped-flow spectroscopy to observe the change in heme intermediates when reacted with varying concentrations of H_2O_2 and other peroxides to investigate this. We also used the extent of O_2 production and evaluations of inactivation as different pH's in the presence and absence of ABTS. Finally, we used EPR to evaluate protein-radicals throughout the reactions with both forms of the enzyme.

Knowing how this network of oxidizable amino acids interferes with, or contributes to, the formation of the MYW adduct can elucidate not only mechanistically how the formation occurs but also more specific roles for each of the amino acids investigated. Knowing the pathway of electron transfer throughout the enzyme can help to elucidate how KatG performs its catalase and peroxidase function more efficiently and how KatG prevents itself from becoming inactivated. These studies also revealed how often one of these pathways is used in relation to the other pathways and how that may be a function of distance from the active site, further elucidating how electron transfer can occur within the active site. All of this knowledge, and more specifically the investigation

of the S315T mutant can all contribute to the study on antibiotic resistance. Knowing mechanistically how this mutant functions can help to develop future drugs to combat these specific INH resistance strains. This will provide for many future studies in drug development.

Future mechanistic studies should be pursued which more extensively characterize transient protein-based radicals through RFQ-EPR. This would include isotopic and other modes of labeling of KatG and its variants, including but not limited to deuterated Tyr, deuterated Trp, Fe^{57}, selenomethionine, etc. High-frequency EPR investigations in combination with the capture of transient intermediates and labeled KatG and labeled KatG variants is anticipated to yield much greater definition of MYW adduct formation events, off-catalase electron transfer events, in addition to those events central to the enzyme's catalase activity. Future LC and LC-MS/MS studies should be engaged to further characterize the peroxide stoichiometry for MYW, YW, and YW quinoid formation against the backdrop of WT KatG in contrast to variants, which limit alternative pathways for through-protein radical transfer. Other studies to confirm the electronic structure of heme intermediates involved in the MYW adduct formation and the kinetics of each step in the mechanism will also need to be completed. All of these things can be accomplished with a combination of optical stopped-flow, RFQ-EPR, and RFQ-Mössbauer spectroscopies along with LC-MS and LC-MS/MS analyses.

This work was supported by a grant from the National Science Foundation (MCB 1616059)

Acknowledgements

I am not able to fully able to express how grateful I am to the many people who have encouraged, prepared, and challenged me to arrive where I am today. I could not possibly thank each of you individually in this short space. However, I have written a short thank you below.

To Dr. Doug Goodwin, my graduate research advisor and mentor, my sincere gratitude for investing your time and energy into me as a scientist. I am grateful for your patience and understanding in mentorship, you are an incredible leader that I have learned so much from. This research and dissertation would not have been possible without your encouragement and assistance. Thank you for contributing to my career and professional life, I have enjoyed my time in your lab immensely.

I also want to thank my academic committee members, Dr. Holly Ellis, Dr. Steve Mansoorabadi, Dr. Angela Calderon, and Dr. Kristine Griffett, my university reader, for their assistance and commitment to help me throughout graduate school. I would also like to thank Dr. Eduardus Duin for his assistance in EPR. To past and current members of the Goodwin group, Dr. Hui Xu, Dr. Jessica R. Krewall, Dr. Jahangir Alam, Tarfi Aziz, Rejaul Islam, Chidozie Ugochukwu, Savannah Petris, Aishah Lee, and Madeleine Forbes – thank you for your help and companionship. A thank you to Dr. Kyle Willian, my teaching mentor, I have learned so much from you as a teacher. I will miss your labs and the excitement that came with the science in your labs. I only hope to make science as exciting for others as you have for me.

My greatest appreciations for to my husband, Matt Barton, and my dog Millie for journeying with me through graduate school. Thank you for the late night rides to the

school to swop cultures, for always encouraging me not to give up on those really hard days, and for always listening to my practice talks and editing the many papers. A wholehearted thank you to my friends and family as well, I would not be here without your encouragement. Special thank you to my mom, Carol Jackson, and dad, Paul Jackson, for your encouragement and getting me to a point where I could complete such an accomplishment.

Finally, and most of all, thank you to my Lord and Savior Jesus Christ, he who has saved me and given me a purpose. It is only by his guidance and strength that I am able to accomplish the work presented in this document.

Table of Contents

List of Figures

List of Tables

Chapter 1 Literature Review

Oxygen structure and reactivity

Aerobic organisms utilize O_2 for metabolic benefit to generate energy. The versatility of O_2 to participate in redox transformations is essential to the success of a concept critical to aerobic life. Simultaneously, it is at the center of numerous pathological failures for aerobic organisms. The former is exemplified in the process of converting energy from carbon sources into ATP production by the process of oxidative phosphorylation.[1-4] One example of the latter is the unregulated production of reactive oxygen species (ROS) through poorly controlled interactions between O_2 and transition metals.

When molecular oxygen is found in the triplet ground-state ($^3O_2$) it is relatively unreactive toward other biological molecules in their singlet ground states. In ground-state O_2 there are two unpaired electrons of parallel spin which are distributed one each across two 2p π^* orbitals (Figure 1.1 A). A very high activation energy, just less than 100 kJ/mol, is necessary to convert O_2 to one of two singlet states. For one, the two electrons are paired in a single 2p π^* orbital, and for the second, the spin of one electron is flipped such that single electrons of antiparallel spin occupy the pair of 2p π^* orbitals. In its singlet states, O_2 becomes highly reactive with a wide range of biological molecules because the contribution of spin restriction to the reaction barrier is absent.[1-5] Participation of singlet O_2 in reactions in biological systems is a relatively rare event. Much more commonly, the spin barrier to triplet O_2 reaction is relaxed by redox active transition metals that facilitate electron transfer from singlet biological molecules to O_2 to generate superoxide ($O_2^{\bullet-}$), hydrogen peroxide (H_2O_2), hydroxyl ($OH^{\bullet}$) radicals, and/or

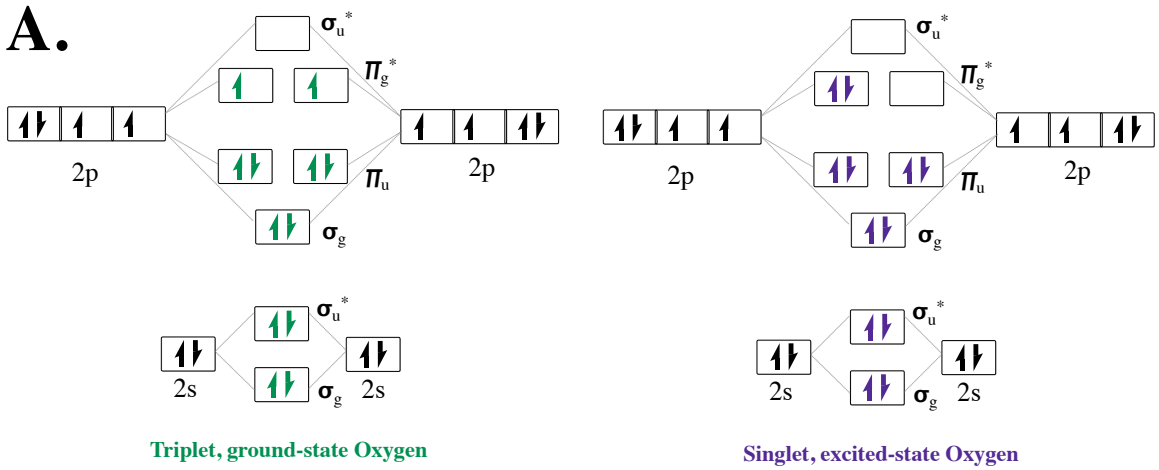

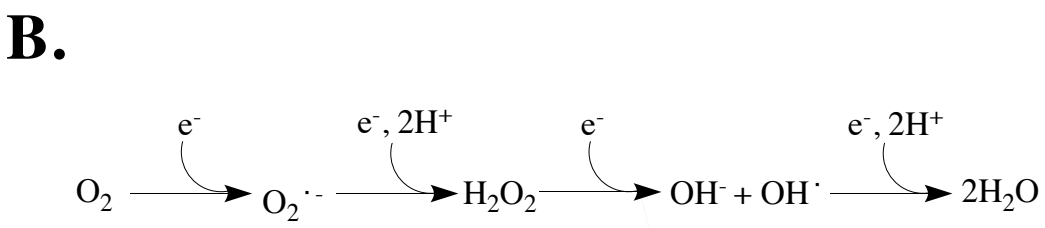

Figure 1.1. Molecular orbital diagram and electron reduction of O_2 (A) Molecular orbital diagram of triplet and single state oxygen. (B) The four-electron reduction of molecular O_2 to water.

H_2O (Figure 1.1B). This is accommodated by the ability of redox-active transition metals to occupy multiple oxidation and spin states. Transition metals are also used in the activation of O_2, through charge transfer from the metal surface to the stable dioxygen molecule. This results in the dioxygen molecule being more reactive to the reactions, such as CO, and lowers the barrier for O-O dissociation.[5]

The use of transition metals can be attributed to life with O_2 as well, as without them the spin restrictions in the presence of O_2 would result in uncontrolled consequences. Because of this there are systems in place designed to control the interaction between transition metals and O_2, such as transition metal transportation and storage as well as oxygen transportation and storage. These systems can result in partially reduced oxygen species ($O_2^{\bullet-}$, H_2O_2, and $OH^{\bullet}$) as well as other related derivatives (peroxyl and alkoxyl radicals) and are called reactive oxygen species (ROS) because of their ability to react rapidly and achieve full reduction to water (Figure 1.1B).[1]

ROS: Defending against H_2O_2

Reactive oxygen species (ROS) are a class molecules and ions, containing oxygen, many of which arise from the partial reduction of ozone (O_3) and dioxygen (O_2).[1-3] Some examples of ROS are radicals like superoxide ($O_2^{\bullet-}$), hydroxyl ($OH^{\bullet}$), peroxyl ($ROO^{\bullet}$), alkyoxyl ($RO^{\bullet}$), as well as nonradicals like hydrogen peroxide (H_2O_2), singlet oxygen ($^1O_2$), and ozone (O_3). ROS are generated through several sources or mechanisms in nature.

Within a biological context, ROS are most commonly formed as a result of premature and incomplete reduction of oxygen during cellular respiration. Molecular oxygen is used as a terminal electron acceptor in oxidative phosphorylation, which can

produce several opportunities for O_2 reduction prior to a terminal oxidase. The initial production of such reactions is almost always $O_2^{\bullet-}$. ROS have received a lot of attention for the negative consequences they bring to cellular systems, their accumulation can cause damaging consequences for every class of biological molecules.[4, 6-10] Because of this, higher eukaryotes rely on ROS as a defense mechanism for antimicrobial defense. They have drawn a lot of attention because of their ability to damage biomolecules. For example, ROS can cause direct damage to proteins, lipids, and nucleic acids, all of which would lead to cell death. When protein oxidation or nitrosylation occurs a variety of enzymatic processes and growth factors are impaired, resulting in marked cellular dysfunction.[11] When lipids are affected, cell death through cellular phospholipids, a major component of the cell membrane, occurs by activation of sphingomyelinase and the release of ceramide, which activates apoptosis.[12] Nucleic acid oxidation has been connected to physiologic and premature aging as well as DNA strand breaks, ultimately leading to necrosis and/or maladaptive apoptosis.[13]

Hydrogen peroxide (H_2O_2) is a ROS that on its own is not particularly damaging to cells, as it is not especially reactive. However, it is used to generate more damaging, highly oxidizing ROS such as hydroxyl radical ($OH^{\bullet}$) and HOCl. The hydroxyl radical ($OH^{\bullet}$) can oxidize just about any biological molecule because of its high reduction potential (E°’ = 2.32 V) and diffusion-controlled rates. The site of adventitious binding of the metal ions (i.e. Fe, Cu, and other transition metals) determines the site of $OH^{\bullet}$-based biological damage that catalyzes the $OH^{\bullet}$-generated reaction sequence. Similarly, phagocytic leukocytes can produce H_2O_2 that is used by myeloperoxidase to generate HOCl. HOCl is a highly bactericidal agent that at high concentrations reacts

indiscriminately with a broad range of biological molecules. Even at very low concentrations and in early stages of phagolysosome action, HOCl dramatically curtails cell growth and division. Indeed, HOCl has been noted to be over 15 times more effective than H_2O_2 at inhibiting *E. coli* growth and cell division.[14] Therefore, the need to preemptively detoxify H_2O_2 and prevent HOCL formation is made even more evident in pathogens facing host defense. Due to the catalytic activity of superoxide dismutase (SOD), superoxide ($O_2^{\bullet-}$) is rapidly converted into H_2O_2, and O_2. Due to the pK_a of $O_2^{\bullet-}$ (4.8), SOD is particularly effective in neutral pH environments where it overcomes the anionic repulsion of two equivalents of $O_2^{\bullet-}$ substrate. In more acidic environments, the uncatalyzed disproportionation of $O_2^{\bullet-}$ and $HO_2^{\bullet}$ is quite rapid on its own. In either case, the H_2O_2 produced from this reaction results in a one-electron reduction to generate hydroxyl radicals. The low-pH generation and disproportionation of $O_2^{\bullet-}$ is important in its own right in light of the context where it occurs. Phagocytic leukocytes, once activated, begin rapid and extensive O_2 reduction to $O_2^{\bullet-}$. Concomitant with this phenomenon the pH is diminished to ~5.0, ensuring the rapid accumulation of H_2O_2. Hydrogen peroxide generated in this environment becomes the substrate for peroxidase-catalyzed (pseudo)halide oxidation to corresponding (pseudo)hypohalite ions. In neutrophils, the dominant peroxidase in this environment is myeloperoxides, which is able to oxidize halides up to and including Cl^-. Accordingly, myeloperoxidase is able to catalyze H_2O_2-dependent HOCl production. HOCl is central to the microbicidal activities of neutrophils.

Of course, SOD is essential for effective cellular defense against the damaging consequences of ROS generation; it catalyzes the breakdown of superoxide radicals to O_2

and H_2O_2. However, while SOD is necessary for an effective cellular response to threats posed by ROS, it is far from sufficient. The result of SOD activity leaves H_2O_2, which can be converted to far more lethal products. Effective systems for the rapid and safe disposal of H_2O_2 are also essential for cellular survival.

H_2O_2-degrading antioxidant proteins

There are two reactions employed in biological systems for disposal and detoxification of H_2O_2: *catalase and peroxidase.* The catalase mechanism decomposes H_2O_2 to form water and oxygen ($2\ H_2O_2 \rightarrow 2\ H_2O + O_2$). In contrast, the peroxidase mechanism uses the reduction of a variety of electron donors to break down H_2O_2 ($H_2O_2 + 2\ RH \rightarrow 2\ H_2O + 2\ R^{\bullet}$). The vast majority of H_2O_2-degrading enzymes fit into either one or the other category; that is, they are either monofunctional catalases or they are monofunctional peroxidases. However, there is an enzyme whose activity does not fit neatly into either of those categories. It is known as a catalase-peroxidase, and it has the unique ability to efficiently perform *both* of these reactions. Catalases, peroxidases, and/or catalase-peroxidase play an important role in the safe disposal of these ROS from organisms across all kingdoms of life. Across all of these H_2O_2 decomposition catalysts, there is a division into those that use a heme cofactor, and those that do not. The latter group includes mechanisms based on active thiols or selenocysteine (e.g., AhpC or glutathione peroxidase, respectively). In this review, heme-dependent enzymes will be the focus.

Catalases

The sole function of catalases is to decompose H_2O_2. They do this by disproportionating H_2O_2 into H_2O and O_2. Catalase activity has been observed with three

metal-based cofactors. A small group found in select eubacteria and archaea relies on a dinuclear manganese cluster.[15, 16] Most recently, a di-iron catalase reminiscent of hemerythrin was identified in *M. tuberculosis*; it is the first of its kind. [17, 18] By far, the most abundant type of monofunctional catalases utilize heme.[19]

Catalase clades/ structural types. Although there are bifunctional heme-dependent catalases, they are related to plant peroxidases and will be addressed below. Most heme-dependent catalases are a monofunctional. More specifically heme-dependent catalases are widely distributed in nature; these are typically homo-tetramers where each subunit bears a heme prosthetic group.[16] In most monofunctional catalases, heme *b* is used. The heme-based monofunctional catalases can be separated into three clades: 1, 2, and 3. Clade 1 contains the so-called small subunit catalases from plants, a smaller subunit from Fimicutes group A, and a small subset of proteobacteria minor group (*Sinorhizobium* clade).[20, 21] Clade 2 contains large subunit catalases from fungi and a few different subsets of proteobacteria; for example, *Polaromonas* and *Burkholderia*.[21, 22] Clade 2 also contains other small subgroups; Actinobacterial with Archeal representatives, Firmicutes, Bacteriodetes group, and Mycetozoen.[21] Finally, clade 3 contains a small subunit catalase from proteobacteria, fungi, animals, and plants.[23, 24] Clade 3 is the subfamily with the largest number of members. In fact, many bacteria possessing catalase gene paralogues of the first two clades also have a representative in the third clade. Clade 3 enzymes exclusively utilize heme *b*, but they are unique in their use of and NADPH as a second redox-active cofactor. Interestingly, the NADPH is bound about 20Å from the heme. The proposed role of this NADPH is to serve as an electron source by directly converting the intermediates back to the resting state,

preventing inactivation of the enzyme.[21] Similarly, this discussion will focus on protein oxidation and strategies that KatG uses to prevent inactivation.

Catalase active site structure and mechanism. As mentioned above, regardless of clade, monofunctional catalases all coordinate the iron of their heme cofactor using a tyrosine phenoxide anion. By convention, this is referred to as the heme's proximal ligand where the side of the heme coordinated to the protein-based ligand is considered its proximal side (Px). An adjacent arginine residue serves to stabilize the ligand in its anionic tyrosinate form. The anionic character of this tyrosine produces a very negative, -500 mV, Fe^{III}/Fe^{II} reduction potential for the heme. Indeed, it has been observed that some catalases cannot be reduced by sodium diothionite. This property produces several consequences. First, catalases are invariably isolated with the heme in its ferric state. Second, the low potential and the anionic character of the ligand serve to stabilize higher iron oxidation states such as Fe^{IV}=O.[25, 26] Heme coordination by anionic ligands is a common theme among heme enzymes which utilize ferryl states for catalytic function (e.g cytochromes P450 [14] and peroxidases, and [imidazolate]).

For these monofunctional catalases, the distal side of the heme contains an invariant histidine, asparagine, and serine (Figure 1.2A). The histidine serves to bind H_2O_2 through a hydrogen-bond network and is proposed to serve as a general base to abstract protons from the H_2O_2 during compound I formation[25, 26] The asparagine residue is thought to stabilize the negative charge on the distal O as the O-O bond is polarized and heterolytically cleaved. Lastly the serine residue participates in a hydrogen bond thought to increase its nucleophilicity, therefore stabilizing the heme pocket for facile H_2O_2 oxidation.[25, 26] In order to reduce compound I, the distal histidine has been

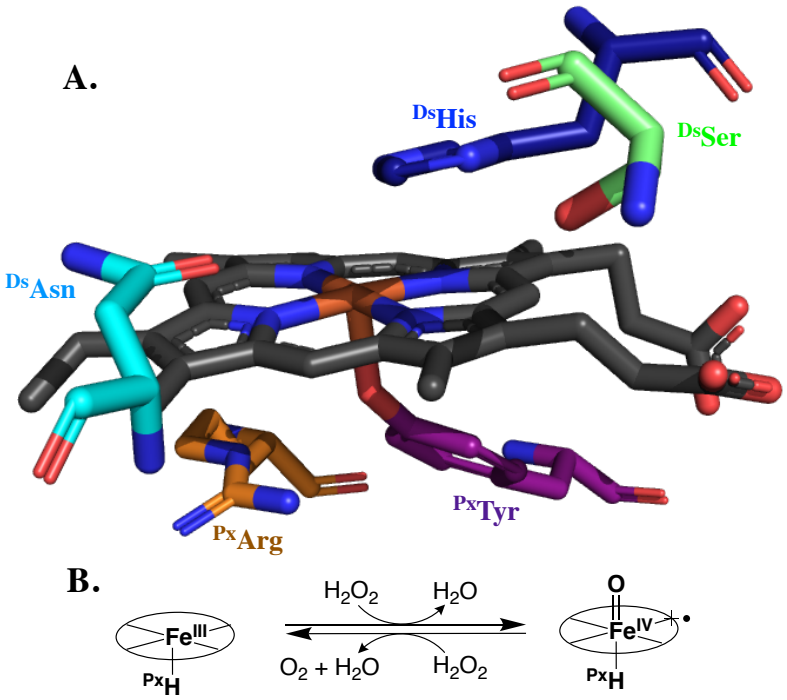

Figure 1.2. Active site of a heme-dependent monofunctional catalase. The active site contains four strictly conserved residues in distal cavity a histidine (^{Ds}His) (navy), a serine (^{Ds}Ser) (lime), and an asparagine (^{Ds}Asn) (teal), and in the proximal cavity, a tyrosine (^{Px}Tyr) (purple), and an arginine (^{Px}Arg) (orange) (A). The catalytic mechanism of a monofunctional catalase cycles between ferric and ferryl-oxo[porphyrin]$^{\bullet+}$ oxidation states (B). Structure of Catalase HPII from *E*. coli. Image constructed using PyMol, using coordinates from the PDB accession entry 1IPH.[95]

proposed to oxidize H_2O_2 for the release of O_2 and H_2O as an acid-base catalyst would do.[27] These four residues of all monofunctional catalases are needed to perform catalase activity (Figure 1.2B). These ferryl (Fe^{IV}=O) heme states are also known to react with different peroxides and electron donors. These catalases are very limited in the kind of reactions that form Fe^{IV}=O states. Another important feature of monofunctional catalases that can help resolve these reactions is that the heme Is found in the center of the protein, about 20Å away from the surface.[25] They have a very narrow access channel to the active site heme that only allows for small molecules such as H_2O_2 and ethanol to enter. This access channel is not large enough for molecules such as peroxidatic electron donors, one of the many reasons these catalases generally show poor peroxidase activity.

Peroxidases

Similar to catalases, peroxidases also function to eliminate H_2O_2. However, in terms of structure, mechanistic details, and physiological function, there is substantially greater diversity represented among peroxidase-active enzymes as compared to the catalases. There are four known superfamilies of heme containing peroxidases; peroxidase-catalase (Px-Ct), peroxidase cyclooxygenase (Px-Cx), peroxidase-chlorite dismutase, and peroxidase-peroxygenase.[28] Heme-containing peroxidases were previously known as the plant/fungal peroxidase while peroxidase-catalase (Px-Ct) was previously known as non-animal peroxidases. Peroxidase cyclooxygenase (Px-Cx) was previously known as the animal peroxidases or mammalian peroxidases. In both Px-Cx and Px-Ct His-based ligation of the heme is common, but modulation of the ligand by H-bonding is distinct for these two superfamilies.

Of the four superfamilies exhibiting heme-dependent peroxidase-like activity, the peroxidase-catalase superfamily is the most relevant to the research presented in this dissertation. Peroxidase-catalase (Px-Ct) representatives are found in plants, fungi and bacteria.[29-31] Enzymes from this group were the first to be characterized in terms of structure, mechanism, and function. Cytochrome *c* peroxidase (C*c*P) and horseradish peroxidase (HRP) are perhaps the two best known representatives of the Px-Ct superfamily. The canonical Px-Ct enzyme fold is composed of 10 α-helices (A-J) and little or no β-sheets. In fact, the helical structure surrounding the active site heme is distinct and includes three of the ten α-helices: B, E, and F. The heme used by all Px-Ct members is heme *b*. Similarly, there are five invariant residues which occupy the canonical Px-Ct active site (Figure 1.3A). A proximal-cavity histidine (^{Px}His) coordinates the heme. A substantial anionic character is imparted to the ^{Px}His by a strong H-bond to an aspartate (^{Px}Asp). The distal cavity has a histidine (^{Ds}His), which acts as a general base for an initial proton abstraction from H_2O_2 during the first reaction of the catalytic cycle to form the Fe^{IV}=O[porphyrin]$^{\bullet+}$ intermediate. The electronic properties of the ^{Ds}His are modulated by an H-bond to an invariant ^{Ds}Asn. Finally, an arginine (^{Ds}Arg) (Fig. 1.3A) helps to polarize the O-O bond of H_2O_2 for heterolytic cleavage during the first reaction of the catalytic cycle (Figure 1.3A-B).

Like the monofunctional catalases, the peroxidase catalytic cycle can be divided into two main components. In the first, the enzyme is oxidized from its ferric form to a state known as compound I (Fe^{IV}=O[porphyrin]$^{\bullet+}$) concomitant with the reduction of H_2O_2 to H_2O. It is thought that the ^{Ds}His and ^{Ds}Arg assist in this first step where H_2O_2 is oriented and bound to the ferric enzyme. This then allows for the heterolytic O-O bond

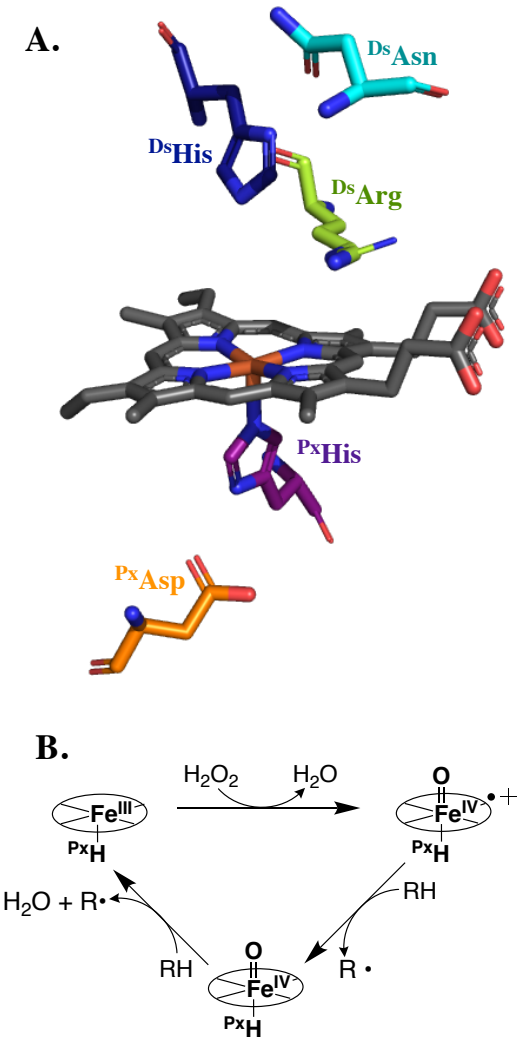

Figure 1.3. Typical active site of enzymes from peroxidase-catalase superfamily. The active site structure is characterized by five strictly conserved residues and a heme *b* prosthetic group. (A) a typical peroxidase catalytic cycle is also shown. (B) Structure was generated from coordinates deposited under PDB accession domain 1H5A (horseradish peroxidase in *Armoracia* rusticana).[78] Residues which occupy the cavity proximal to the heme are Px (e.g. ^{Px}Asp), Residues which occupy the cavity distal to the heme are Ds (e.g. ^{Ds}Asn),

cleavage. The standard completion of a peroxidase cycle where two sequential one-electron reductions of the enzyme are accomplished with an aromatic single-electron donor (e.g., phenol, guaiacol, ABTS, o-dianisidine, etc.) is shown in Figure 1.3B. The physiological function of a given peroxidase relates to what is oxidized in the second part of its catalytic cycle. The mechanism by which they accomplish this oxidation is distinctly different from monofunctional catalases and can be accomplished in two ways. The first, mentioned above, occurs with two sequential one-electron steps; the second involves a single two-electron reduction step. The oxidation of halides and pseudohalides (X-) to the corresponding hypohalite anions (OX-) is the most common example of this second type of peroxidase cycle. The peroxidatic electron donors (PxEDs) that can be used in the former sequential one-electron reduction mechanism vary vastly across different heme peroxidases. They can be small inorganic complexes like Mn-oxalate, large irregular structures like lignin, phenolic compounds such as ferulic acid, and even small proteins like cytochrome *c*. Large organic compounds like o-dianisidine and ABTS are commonly used because of the colorimetric properties of their oxidized products. Compounds like these can change color based on the peroxidatic turnover over of the enzyme and they are known to be easily stabilized to their respective oxidized radical form. This form is often where we find the intense visible absorption spectra.

Catalase-peroxidases

Catalase-peroxidases (KatGs) are enzymes capable of both disproportioning H_2O_2 and using H_2O_2 to oxidize PxEDs. These bifunctional enzymes are fascinating because their catalase activity (k_{cat} ~3,000 s^{-1}) is two to three orders of magnitude higher than typical heme peroxidases (k_{cat} ~10 s^{-1}).[32] The catalase activities of KatG's are more

closely comparable to typical monofunctional heme catalases even though, beyond the heme cofactor, KatGs bear no structural resemblance to monofunctional catalases. In order for KatGs to perform catalase activity they need a heme *b* cofactor and a protein derived cofactor known as the MYW adduct. The M**Y**W adduct is built around a strictly conserved tyrosine found in a KatG-unique structure called large loop 1 (LL1).[33] Interestingly, KatG is the only member of the peroxidase-catalase superfamily, which has the LL1 structure. The tryptophan in the MY**W** adduct is just above and roughly coplanar with the heme group (Figure 1.4). Substitutions of any of these three amino acid residues by site-directed mutagenesis abolishes the catalase activity but retains the peroxidase activity. Substitutions to the tyrosine or tryptophan results in no cross-link formation, where exchange of methionine to cysteine allows the covalent bond formation between the tyrosine and the tryptophan but produces a catalase negative variant.[34]

In spite of the novel MYW adduct of KatG, the identity and arrangement of amino acids surrounding the KatG heme *b* cofactor are well conserved across the entire peroxidase-catalase superfamily. The proximal side of the heme has a highly conserved triad consisting of Asp-His-Trp, and the distal side of the heme has a Trp-His-Arg highly conserved. Indeed, leaving the Trp residues aside, the remaining four residues in these two pockets are strictly conserved across the entire superfamily. In all of these enzymes, the proximal histidine is coordinated to the heme as the fifth ligand, and it forms a strong H-bond with the Asp. The proximal Trp which is found in all class I enzymes of the superfamily (KatG, C*c*P, ascorbate peroxidase, etc.) is also H-bonded to this Asp through its indole NH (Figure 1.4). The H-bond network of the proximal side has been shown to increase the anionic character of the proximal His ligand, serving to stabilize high valent

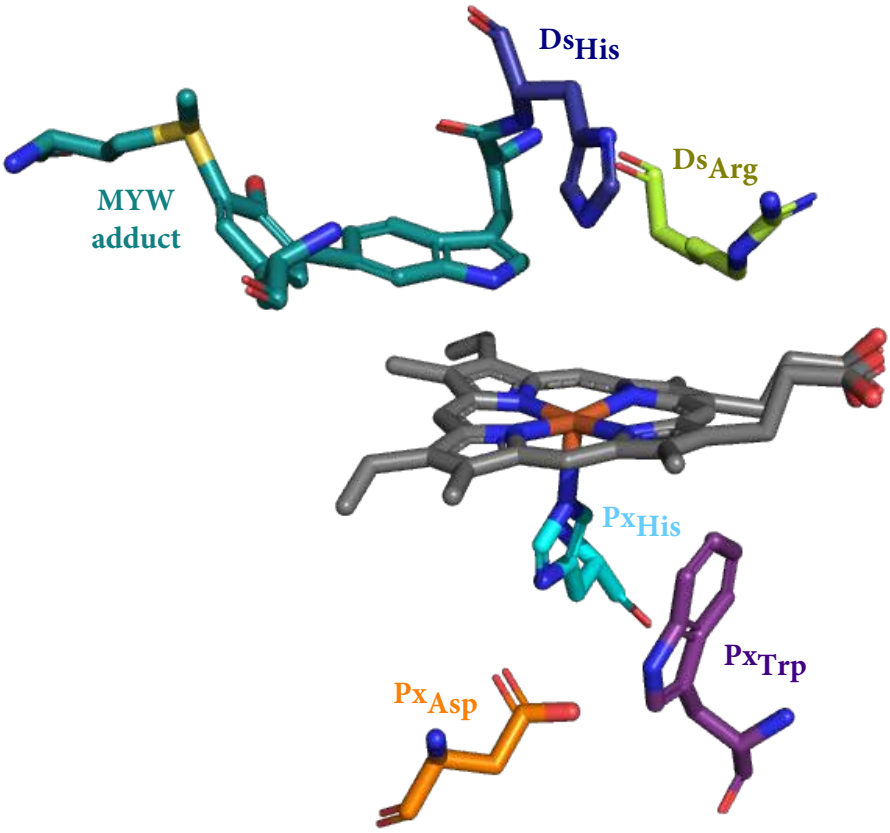

Figure 1.4. Key residues found in the active site of KatG. The Px superscript is used to indicate residues which occupy the cavity proximal to the heme (e.g., ^{Px}Trp), Ds identifies residues which occupy the cavity distal to the heme (e.g. ^{Ds}Arg). Structure was taken from PDB accession domain 2CCA.[94]

(e.g., Fe^{IV}=O) heme states.[35] In KatG it has also been proposed to contribute to protein stability.[36] It also serves to stabilize protein-based radical intermediates centered on the proximal Trp as cation rather than neutral radical species. The distal histidine serves as a general base to facilitate the deprotonating of H_2O_2 and assist in the formation of compound I intermediate.[37-39] Similarly, the distal arginine helps to stabilize compound I by electrostatic interaction of the positively charged side chain and the negatively charged distal oxygen of the bound H_2O_2 during heterolytic O-O cleavage.[37] The roles seen here in the active site of KatG are identical to those observed in other heme peroxidase.[29-31] In spite of all of these similarities, the active site structure of KatG is entirely unique, and it is what allows the enzyme to support robust catalase turnover within the structure of a peroxidase. In this work we will focus on *Mycobacterium tuberculosis* KatG and its catalase activity, peroxidase activity, MYW cofactor biosynthesis, and its ability to facilitate intramolecular electron transfer throughout the enzyme.

Mechanistic formation of the MYW adduct

KatG's robust catalase activity is imparted by a unique post-translational modification between three residues near the active-site heme. These residues include an active site Trp (W107), a Tyr (Y229) on a KatG-conserved loop structure, and a near-by Met (M255) that undergo a covalent linkage after reacting with peroxides in the presence of heme (*M. tuberculosis* numbering). This protein-derived cofactor is known as the novel Met-Tyr-Trp cross-link (MYW cofactor) (Figure 1.4) and has been confirmed by x-ray crystallography[40, 41] and mass spectrophotometric analyses[34, 42, 43] to be conserved across KatGs from all species, and vital to the catalase activity of KatG. In KatG's

catalase cycle, a ferryl-oxo porphyrin cation radical intermediate (Fe^{IV}=O[por]$^{\bullet+}$) is formed by an initial reaction of ferric KatG with H_2O_2. The MYW cofactor is then needed to reduce the porphyrin to generate the Fe^{IV}=O[MYW]$^{\bullet+}$ state. The rate of this intramolecular electron transfer is very rapid, so much so that the features of Fe^{IV}=[por]$^{\bullet+}$ state have not been observed by either UV-vis or EPR-based rapid reaction techniques with any wild-type KatG.

The mechanistic details of the MYW adduct formation remain undetermined, despite its essential contribution to the catalase activity of KatG. A mechanism for MYW formation has been proposed by others and is represented in Figure 1.5.[34, 43] It has been proposed that the MYW formation involves two reactions with a peroxide (e.g. hydrogen peroxide or peracetic acid) involving several transient, protein-based radicals and two stable, covalent intermediates. These two intermediates are the YW adduct and the quinoid form of the YW adduct.[34, 43, 44] However, there are experimental discrepancies which have remained unaccounted for. For example, there is a reproducible discrepancy between the number of oxidizing equivalents proposed to be needed and the quantity that actually results in MYW adduct formation. Specifically, the formation of the MYW adduct is ~33% efficient and the use of peracetic acid (PAA) as a two-electron oxidant requires the use of 6 molar equivalents.[34, 43] Despite numerous studies on the formation of KatG's MYW adduct, the heme and protein-based radical intermediates have yet to be experimentally determined.

Knowing the discrepancy between how many peroxide equivalents are needed and the high number of oxidizable amino acids in KatG's active site, it could be inferred that those amino acids are in some way involved in the formation of the MYW adduct.

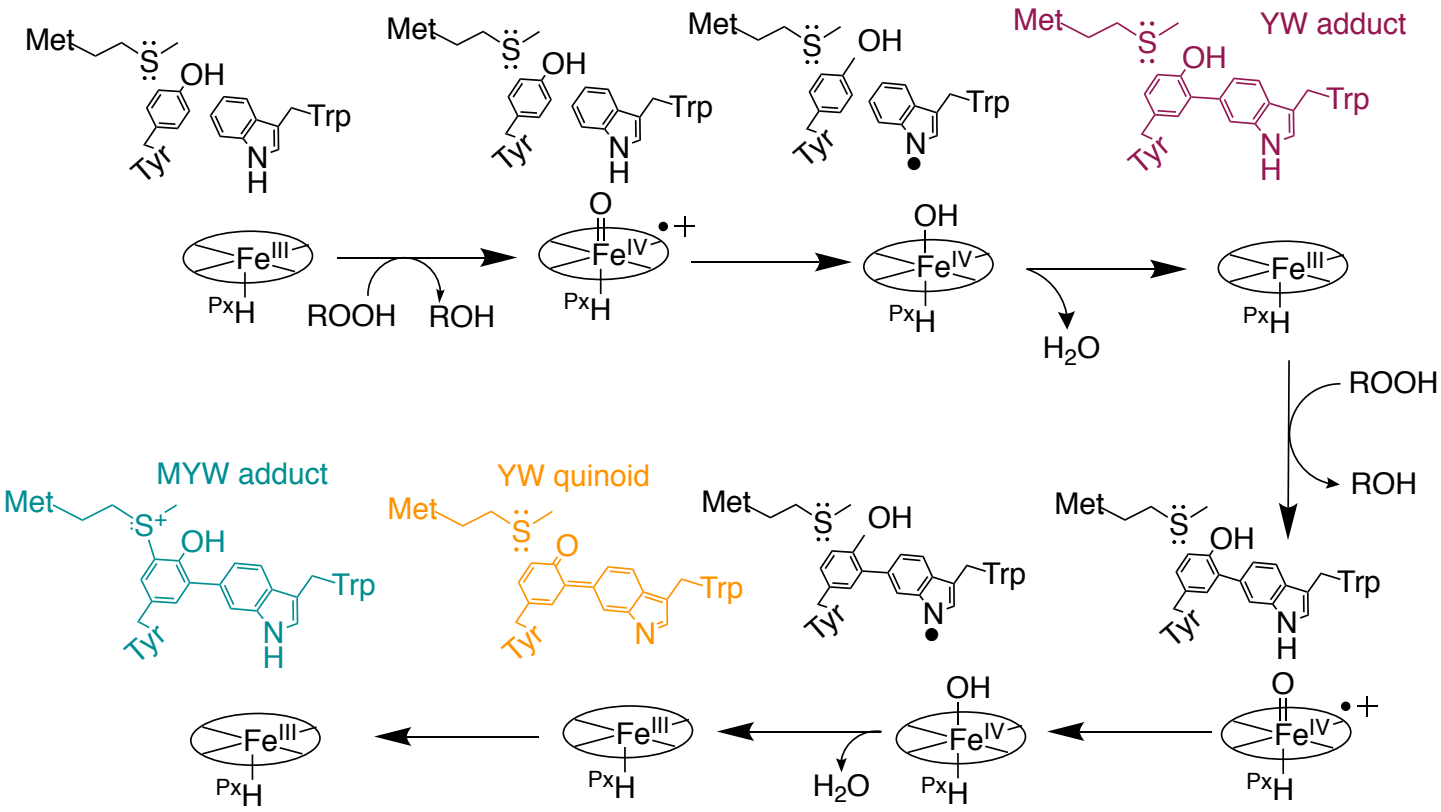

Figure 1.5. Proposed mechanism for the autocatalytic formation of the MYW cofactor. The covalent linkage of Met255, Tyr229, and Trp107 has been proposed to progress by two peroxidase-dependent steps catalyzed by high-valent heme species. The reaction following each addition of peroxide is represented as a different line above. Three stable protein-base intermediates are predicted to have distinct optical features: the YW adduct (magenta), the quinoid rearrangement of the YW adduct (orange), and the full MYW adduct (teal).[34]

Particularly the proximal tryptophan (W321), could be used to facilitate the regeneration of the (Fe^{IV}=O[por]$^{\bullet+}$) intermediate which is used as an active species to generate intermediates to form the MYW adduct (Figure 1.6.). If the proximal tryptophan can be used in this way, it is also possible to that other oxidizable amino acids near the active site (W412, Y413, and W91) could also be involved in the formation of the MYW adduct, either as facilitators or detractors.

Production of WT KatG lacking its MYW cofactor

In order to study the formation of the MYW cofactor, we needed a form of protein that retained all three participants in the MYW adduct but had yet to establish the covalent bonds between the side chains. It would also be necessary to generate the MYW adduct upon the experimental addition of peroxides. It has been established that the formation of the MYW cofactor needs two things: heme and peroxide. Therefore, we expressed *Mt*KatG in the BL-21 (DE3) pLysS cell line without supplementing culture media with heme. This is in contrast to utilization of the C41 (DE3) pHPEX3 cell line with heme-supplemented media. Expression was also carried out at a lower temperature (20° *vs*. 37°) and for an extended period of time (16 hours *vs*. 4 hours). Following Ni-NTA-based isolation of His-tagged KatG and a simple buffer exchange step, apo KatG (*a*KatG) was the dominant form (i.e., >95%) of protein generated. Accordingly, our *a*KatG product showed spectra with almost no absorption due to heme near 405 nm (i.e., Soret band) and a strong protein peak around 280 nm (Figure 1.7). For wild-type apo KatG (*a*WT KatG) minimal catalase activity was detected, and this was attributed to the very small percentage of KatG, less than 5%, that received endogenously generated heme cells during expression. This solved the first of the two problems; however, it was also

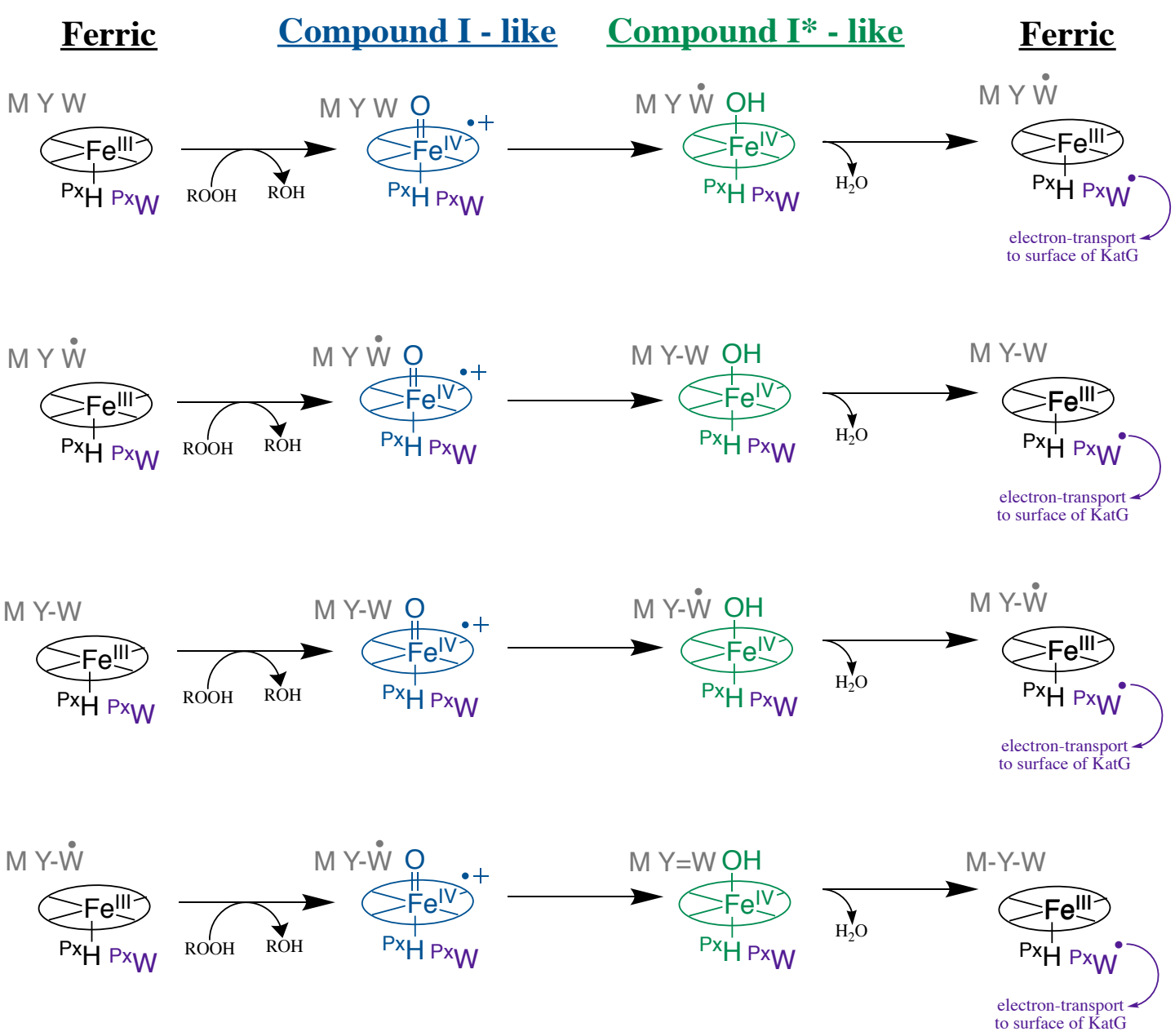

Figure 1.6. Proposed Mechanism for formation of the MYW adduct, including the proximal tryptophan. In this proposal, four equivalents of peroxide is needed, each line represents another addition of peroxide and the resulting intermediates. The proximal tryptophan (^{Px}W) shown here in purple is proposed to facilitate the regeneration of compound I. The radical interactions of the MYW are shown here in grey.

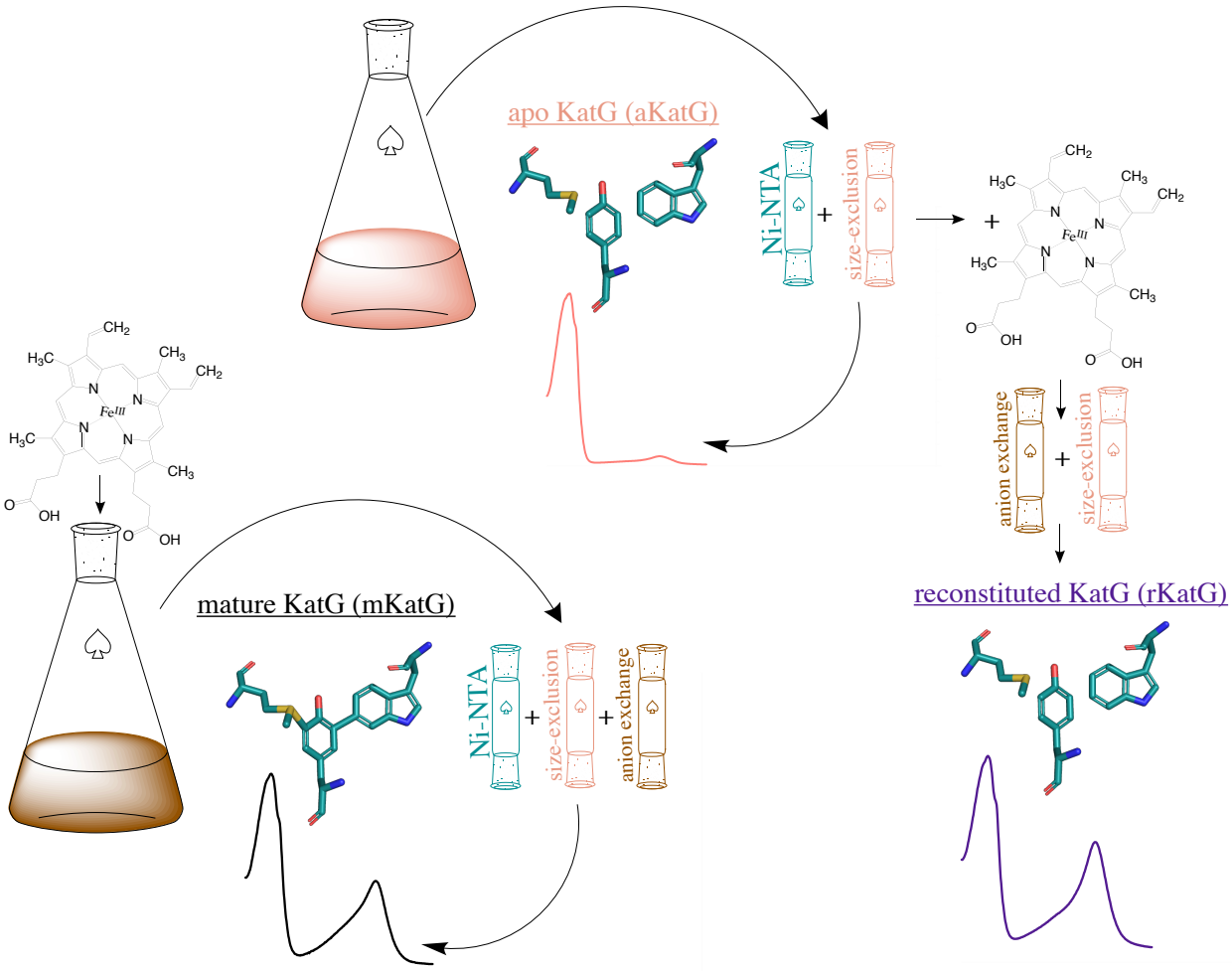

Figure 1.7. Schematic representation of KatG preparation. KatG expressed in the absence of heme (apo or aKatG) lacks both heme and the MYW cofactor (pink). Reconstituted or rKatG, prepared by reconstituting aKatG with heme after purification, still lacks the MYW cofactor, but its heme cofactor is in place as evidenced by protein-bound heme spectra (purple). KatG expressed in the presence of heme (mature or mKatG) results in heme incorporation during expression and subsequent formation of the MYW cofactor, presumably due to the presence of endogenous peroxides generated by host cells (black).

necessary to reconstitute this protein so that the MYW adduct could be generated by the precise and controlled addition of peroxides *in vitro*.

This latter issue was resolved with a reconstitution procedure that began with frozen *a*KatG, allowed to thaw, and diluted to appropriate concentrations and mixed with specifically calculated heme solution so that the total volume of heme was half that of the protein solution. This was allowed to incubate for 30 minutes before adding equal parts buffer to heme solution volume. The protein was allowed to incubate in the presence of heme, and was then and concentrated. Anion-exchange chromatography was used to enrich for the reconstituted form (i.e., *r*WT KatG) in preference to remaining *a*WT KatG. Finally, a desalting/buffer-exchange column step was included to remove any remaining unbound heme and elute *r*WT KatG in its 5 mM phosphate storage buffer before the product was assessed for activity. The wild-type version of this protein was expressed as *r*WT KatG and resulted in a 10-fold increase in the heme Soret band (i.e., λ_{max} ~405 nm) relative to that observed for our *a*WT KatG product. *r*WT KatG had catalase activity comparable to that of KatG expressed to include heme and the MYW cofactor upon purification (*m*KatG) (Figure 1.7). These two observations ensured that heme incorporation was successful for *r*WT KatG. There were small spectral differences observed in the heme Soret peak between *r*WT KatG and *m*WT KatG that were attributed to a difference in heme coordination. Spectra recorded for *r*WT KatG indicated a high-spin (HS) 6-coordinate heme as evident from by the narrower Soret band around 406 nm and a lesser contribution from a shoulder to the Soret band observed below 400 nm, which is typical of 5-coordinate heme. The EPR spectra of *r*WT KatG also supported an

enriched 6-coordinate HS heme as it indicated a greater contribution from an axial state relative to a rhombic state than was observed for *m*WT KatG.

Once these alternative KatG purification products were established, it was important to determine if the MYW cofactor was in *m*KatG and lacking in *a*KatG and *r*KatG. We accomplished this using LC-MS/MS. First, comparisons of LC elution profiles (monitored at 310-330 nm) of trypsin-cleaved *m*KatG, *a*KatG, and *r*KatG showed that heme was present in *m*KatG and *r*KatG but virtually absent from *a*KatG. However, both aKatG and rKatG showed much lower signal due to the MYW cofactor than that observed for *m*KatG. Ions with *m/z* values consistent with the MYW cofactor ions were detected by positive-ion-mode MS to elude at 32 min, confirming the assignment of this feature in the LC elution profile as the crosslinked peptides arising from the MYW cofactor.[34, 42, 43] These predicted values suggested the increase in absorbance observed around 300-340 nm when KatG proteins are reacted with peroxides may indicate the MYW adduct formation. Other members of the lab performed these observations of WT KatG. However, I mention them here for comparison in future chapters to KatG variants.

Protein-based Radicals in KatG

KatG falls into the class I or family I of the peroxidase-catalase superfamily. Historically, these have been known as the plant peroxidases, or more accurately, non-animal peroxidases. The canonical members of this superfamily include cytochrome c peroxidase (C*c*P) (class I), lignin peroxidase (LiP) (class II), and horseradish peroxidase (HRP) (class III). By contrast, the so-called animal peroxidases include lactoperoxidase,

myeloperoxidase, cyclooxygenase, etc, and are now referred to as the peroxidase-cyclooxygenase superfamily.

Interestingly, KatG is the only truly catalase-active member of the peroxidase-catalase superfamily. Indeed, it uses a single active site to break down H_2O_2 by catalase and peroxidase mechanisms. It is noteworthy that although KatG has virtually no structural identity with typical monofunctional catalases, both enzymes do have a very narrow and restrictive access channel leading to the heme. Typical PxEDs are not able to access the heme of either KatGs or monofuctional catalases. Nevertheless, KatG does have significant peroxidase activity where typical catalases do not. What KatG does have is a highly oxidizable structure which connects the active site to the enzyme's solvent accessible surface. Accordginly, we consider KatG to use protein-based radicals for its unique catalytic abilities, not only its catalase activity (i.e., $MYW^{\cdot+}$ discussed above), but also its peroxidase activity. While the active site of KatG is virtually superimposable with cytochrome *c* peroxidase, KatG's N-terminal has significantly more oxidizable amino acid residues. More specifically, the active-site containing domain of KatG has 18 Trp, 12 Tyr, and 13 Met. To demonstrate the large amount of oxidizable amino acids, Figure 1.8 displays the oxidizable amino acids found on the surface of the enzyme. The presence of this large number of oxidizable amino acid residues is what makes KatG's protein-based radical mechanism possible. In this protein-based radical mechanism, an oxidizing radical (or electron hole) begins at the active site upon reaction between the heme and peroxide. Through the redox cycling of oxidizable amino-acid residues (i.e., Tyr and Trp), this electron hole migrates to the solvent-exposed surface where it can be scavenged by exogenous PxEDs. The H-bonding network within the active site is also thought to

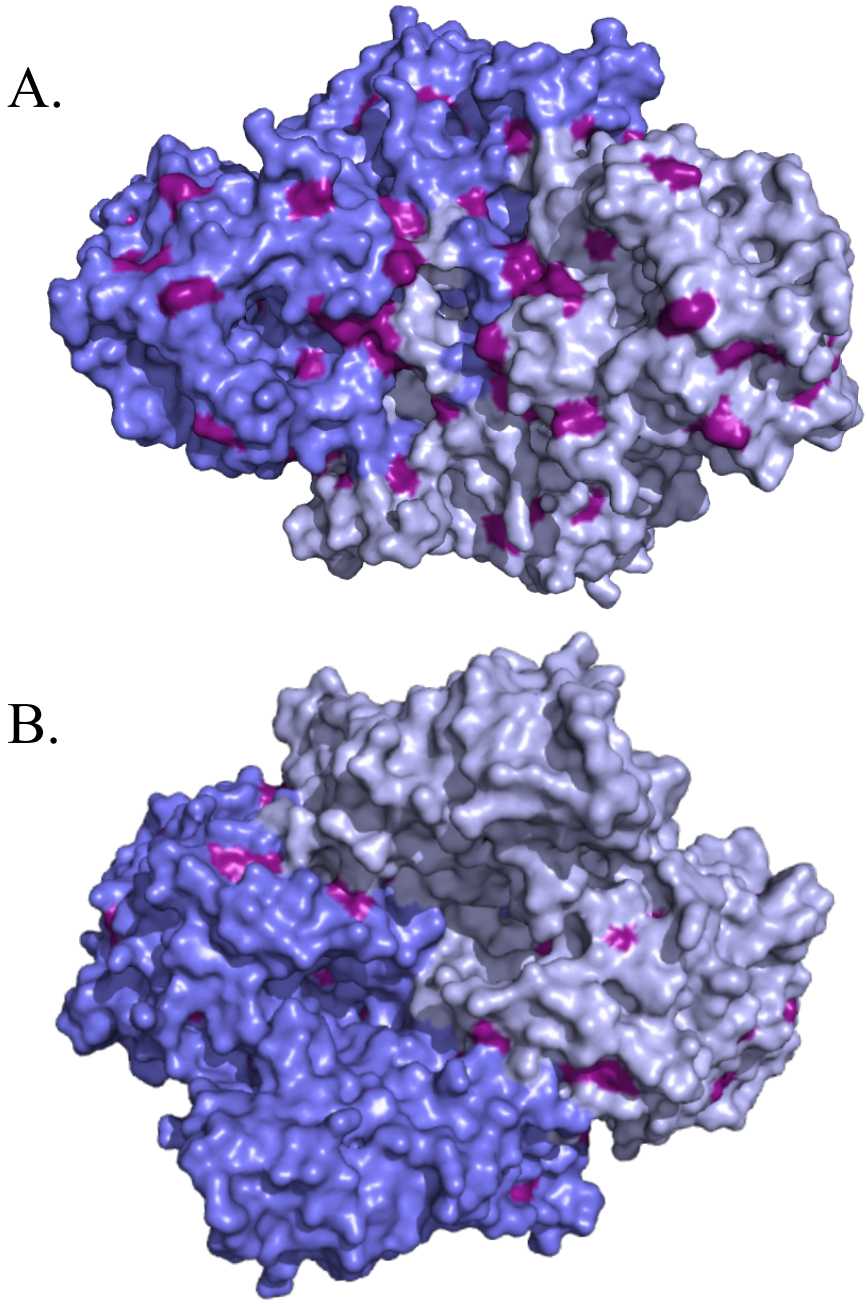

Figure 1.8 Oxidizable amino acids found on the surface of KatG. One of KatG's subunits is shown in purple, and the second is shown in grey. All Tyr, Trp, and Met residues with solvent-exposed components are shown in magenta. The side of KatG bearing the active-site access channel for each subunit is shown (A), as is the surface obtained from rotating the structure 180° around the vertical *z* axis (B). This image was constructed using PyMol, from coordinates deposited under the PDB accession entry 2CCA.[94]

play an important role in KatG intramolecular electron transfer processes.[45, 46] KatG uses two distinct protein-based radicals to catalyze two distinct mechanistic activities; the MYW narrow doublet radical (catalase) and a radical centered on the proximal tryptophan (peroxidase).

The MYW cofactor protein-based radical

Studies have shown that a unique narrow doublet (MYW) radical cofactor is essential for catalase activity of KatG.[40, 47] This radical is the only radical observed by RFQ-EPR when KatG is reacted with steady-state concentrations of H_2O_2 during active *catalatic* turnover, and is known to have tyrosyl-like character.[48] This radical persists throughout until the conclusion of the H_2O_2 consumption. Mutations to any of these three residues results in lack of catalase activity, as well as lack of the ability to produce the narrow doublet radical.[48] The radical is known to form in the presence of heme and peroxide. A proposed formation by heme catalyzed free-radical chemistry as well as an additional proposed mechanism is further discussed in Chapter 2.

The proximal tryptophan protein-based radical

A protein-based radical assigned to the proximal Trp has been observed when KatG is reacted with PAA.[49] It has been hypothesized to form an exchange-coupled interaction with a nearby ferromagnetic center, presumably the heme because of its very close proximity. Interestingly, a tryptophanyl radical with identical characteristics is observed when KatG is reacted with steady-state concentrations of its natural substrate, H_2O_2; however, this species is only observed as catalase activity diminishes and the reaction approaches H_2O_2 depletion. Conditions which prevent inactivation completely prevent the accumulation of this protein-based radical.[44] These data suggest that the

proximal tryptophan is the first residue to be oxidized in a mechanism which deviates from active catalase turnover. This radical is then thought to migrate to the solvent accessible surface of KatG via groups/chains of redox active amino acid side chains (i.e., Trp and Tyr). It is thought that peroxidase electron donors like isoniazid act to reduce these remote protein-based radicals, as the narrow access channel of KatG would not allow for direct access to the heme. This idea is further investigated in Chapter 3, including other possible oxidizable amino acid resides and pathways for electron transfer.

Intramolecular Electron Transfer

As mentioned previously, transition metals are known to help with the activation of O_2. In KatG, the transition metal is iron which is found in the heme *b* cofactor. This, of course, is buried deep inside the enzyme. In order for these transition metals to meet some of their targets, such as larger molecules that cannot access the active-site channel, intramolecular electron transfer is vital. Most of these electron transfer reactions involve a series of redox cycling, which produce a net movement of electrons from the protein surface to the active site. It is also helpful to view this phenomenon as the transfer of electron holes in the opposite direction; that is transferring from the active site to the enzyme surface where they can be scavenged by PxEDs in solution. In order for these reactions to occur, one must first have oxidizable amino acids close enough together to react with one another on a reasonable time scale, forming some type of rapid electron-transfer pathway. In KatG's case, there is a preponderance of oxidizable amino acids that seem to form a pathway from the active-site heme to the surface of the enzyme. Other enzymes like cytochrome c peroxidase (CcP), and MauG also utilize intramolecular electron transfer for similar functions.

Cytochrome c peroxidase

From previous discussion we can see that KatG's active site is most like those of the plant peroxidase-like superfamily. In fact, KatG's active site is virtually superimposable with other members of this family. For example, cytochrome c peroxidase (CcP) and KatG have at least six residues that are identical in their active sites (Figure 1.9). While CcP is a monofunctional peroxidase it is also unique in that it uses a large protein-based substrate (ferrocytochrome c) as a PxED. This substrate is too large for direct access to CcP heme and requires through-protein radical transfer that includes CcP's proximal tryptophan (W91). In KatG, the most PxEDs are too large to access the heme by way of the very narrow active site channel. This is also solved by through - protein radical transfer using KatG's the proximal tryptophan (W321). In both enzymes when a suitable PxED is not present, the protein will become irreversibly inactivated.

In C*c*P, during reactions with H_2O_2 a well-establish compound (Fe^{IV}=O[Trp-191]$^{\bullet+}$) is known to form. Indicating C*c*P proximal tryptophan is used as a site to initial radical transfer.[49, 50] Similarly, KatG has been shown to use its proximal tryptophan, W321 for off-pathway electron transfer as well. This is evident by the radical (Fe^{IV}=O[Trp-321]$^{\bullet+}$) observed when KatG is reacted with PAA.[44] KatG also has residues like W412, Y413, and W91 that begin these electron transport pathways that are not evident in C*c*P. Instead, C*c*P has a phenylalanine and glutamate or is missing an amino acid completely in these residues location (Figure1.9) C*c*P is also rich in oxidizable residues with 9.2% of its amino acids being oxidizable. Interestingly enough only 11 of these residues are shared with KatG, this includes four residues where Trp has been replaced with Tyr and vise versa (Figure 1.10). Among these conserved residues in

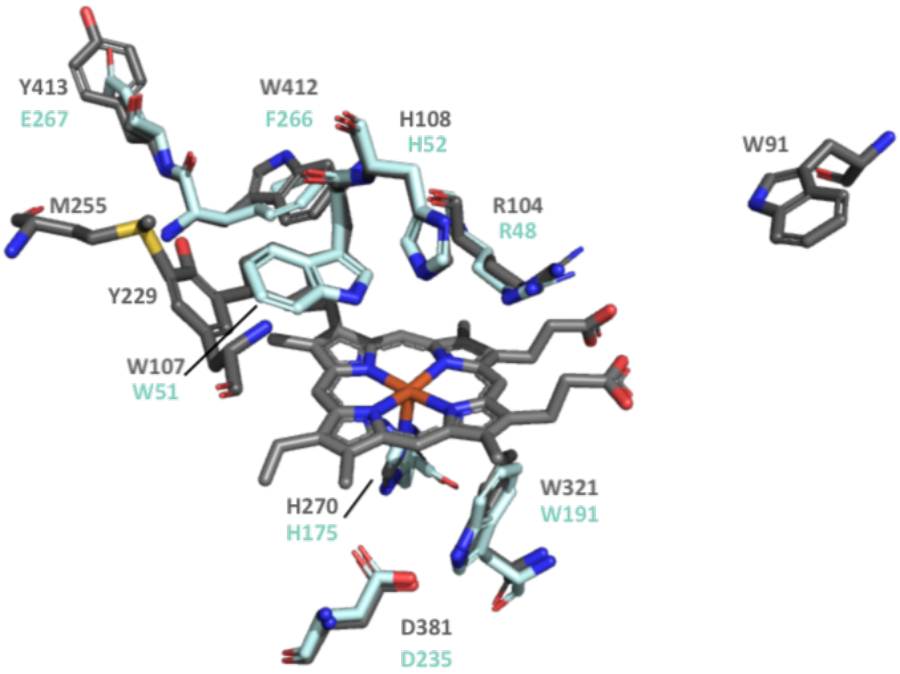

Figure 1.9. Superimposed KatG and CcP active site. KatG is shown with carbons in grey and CcP is shown with carbons in light cyan. Only the heme is from KatG is shown (the heme from C*c*p is indistinguishable). Residue numbering in grey corresponds to residues from *M. tuberculosis* KatG (*Mt*KatG) and numbering in light cyan corresponds to C*c*P residues. This image was generated using Pymol, using coordinates from PDB accession entries 2CCA[94] and 2CYP[96] for *Mt*KatG and yeast C*c*P, respectively.

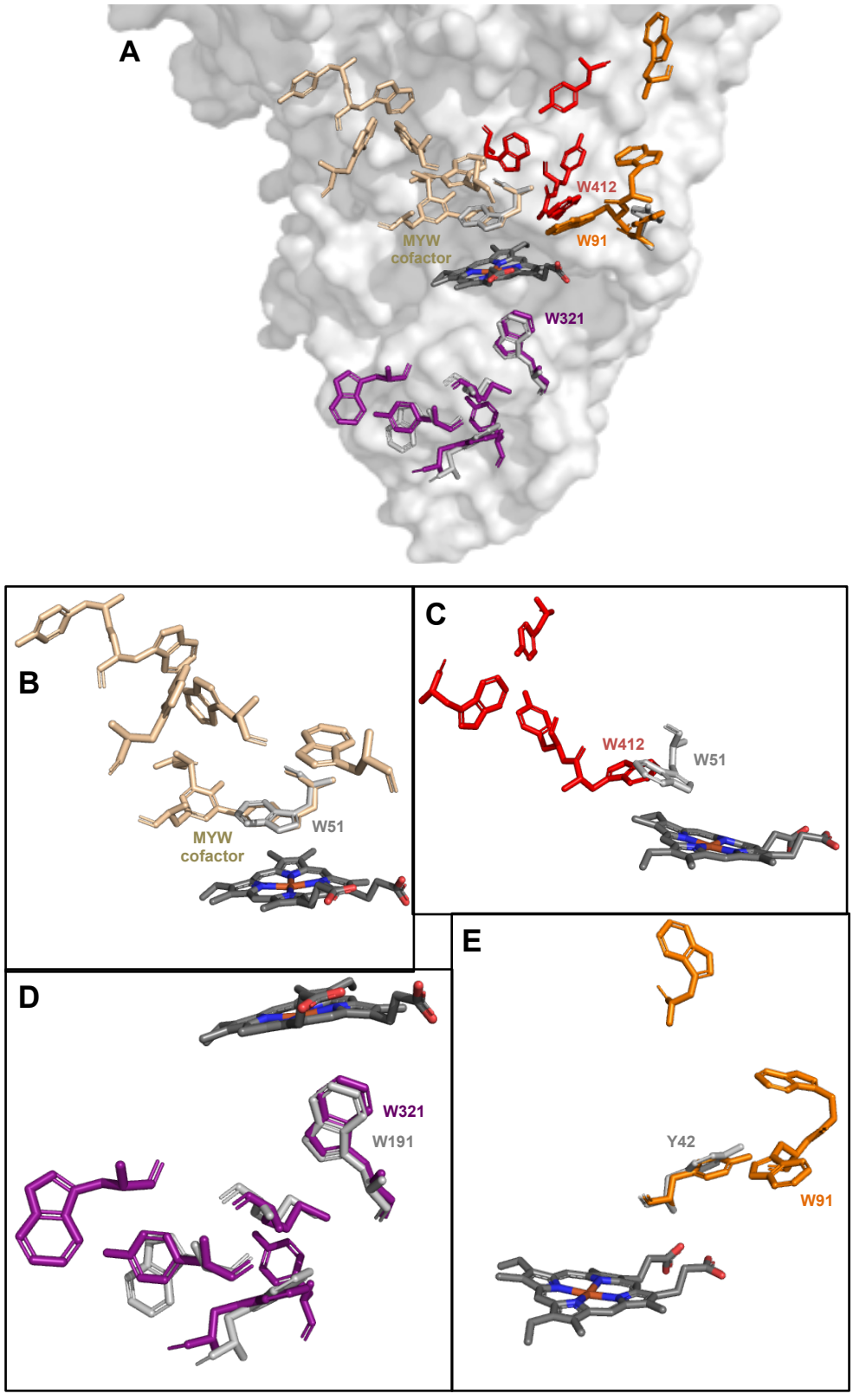

Figure 1.10 Oxidizable amino acids in KatG and CcP. Overview of all pathways found in both KatG (residues shown in various colors), and CcP (residues shown in grey) (A) The heme shown is that from KatG; the heme from C*c*P is superimposable on the KatG heme. The pathways of KatG oxidizable amino acids that begind with W107 of the MYW cofactor, (copper) and W51 of C*c*P (grey) are shown (B) as is the pathways corresponding to KatG W412 (red) along with C*c*P W51 (grey) (C) The KatG pathways marked by the proximal Trp (W321) (magenta) is overlayed with the analogous C*c*P path marked by W91 (grey) (D) The KatG W91 pathway is shown (orange) overlayed with CcP Y42 (grey) (E) This image was constructed using PyMol, with coordinates deposited under the PDB accession entry 2CCA[94] and 2CYP.[96]

C*c*P one electron-hole hopping pathway is clear, this pathway begins with the proximal tryptophan W191 (Figure 1.10 D). However, KatG has at least four possible electron-hole hopping pathways (Figure 1.10). The most obvious of these and the one that is very likely to be utilized is the pathway that begins with the proximal tryptophan (W321) and goes through Met377-Tyr353 and or Trp 341 before reaching the surface of the enzyme.

While there is substantial evidence that proximal tryptophan is a hot-spot for KatG protein-based radical formation pathway,[44] other residues close to the active site have also show evidence of oxidation.[51] For example, using site-specific Trp substitution, isotopic labeling of Trp and or Tyr residues and multi-frequency EPR analysis, a radical assigned to a Trp 14.5 Å away from the heme iron and linked via a H-bonded network is shown to be the sole Trp radical site for KatG. This residue is known as W91 in *Mt*KatG, W94 in *Bp*KatG, and W106 in *Sy*KatG. The same residue that begins one of the pathways indicated in Figure 1.10 E. In this work, all of the pathways found in KatG are investigated for through-protein electron transfer.

MauG

There are also other enzymes that use electron transfer and oxidizable amino acids when molecular O_2 is not the target. For example, MauG is a diheme protein that catalyzes the posttranslational modification of another protein, methylamine dehydrogenase (MADH) to generate the protein derive cofactor tryptophan tryptophyquinone (TTQ).[52-63] This reaction is a six-electron oxidation that requires the crosslinking of two Trp residues, oxygenation of a Trp residue and oxidation of the final quinol TTQ.[54, 55, 59] This catalysis does not involve direct contact between the protein substrate and either of the hemes in MauG.[56, 57] Instead, much like C*c*P and KatG,

MauG uses a hole hopping mechanism of electron transfer in which Trp residues are reversibly oxidized (Figure 1.11).[59,61]

S315T: Radical Electron Transfer

The pro-drug isonicotinyl hydrazide (INH) requires activation by KatG once it has been taken up by M. tuberculosis.[64, 65] It has been proposed that INH activation results in the conversion of INH to the corresponding isonicotinoyl radical (IN$^{\bullet}$) by KatG.[66] The IN$^{\bullet}$ then reacts with NAD^+ creating an isonicotinoyl-NAD (IN-NAD) adduct (Figure 1.12). IN-NAD then binds and inhibits the enoyl acyl-carrier protein reductase (InhA). This inhibition prevents the formation of mycolic acid biosynthesis, a process fundamental to the structural integrity of the mycobacterial cell wall.[67, 68] However, neither the mechanism by which KatG initiates INH activation nor the steps leading up to the formation of the IN-NAD adduct are well understood. It is known that KatG catalyzes the reduction of O_2 to superoxide using electron donors such as NADH and INH.[69, 70] While the route for electron transfer to the heme, from NADH, is not known, it is known that the pathway leading through Trp 139, *Bp* KatG numbering, or Trp 412, *MtB* KatG numbering, is used for the transfer from INH.[71] Although the role of superoxide in formation in normal metabolism is not evident, the process of INH activation in *Mtb* KatG has adapted superoxide to the formation of IN-NAD. While superoxide formation and the peroxidatic process are quite different, they both utilize electron transport pathways to bring electrons to the heme cavity from the surface-bound electron donor.

Multi-drug resistant (MDR) TB strains occur due to resistance to the two most frequently administered antitubercular drugs, rifampicin and INH. It has been estimated

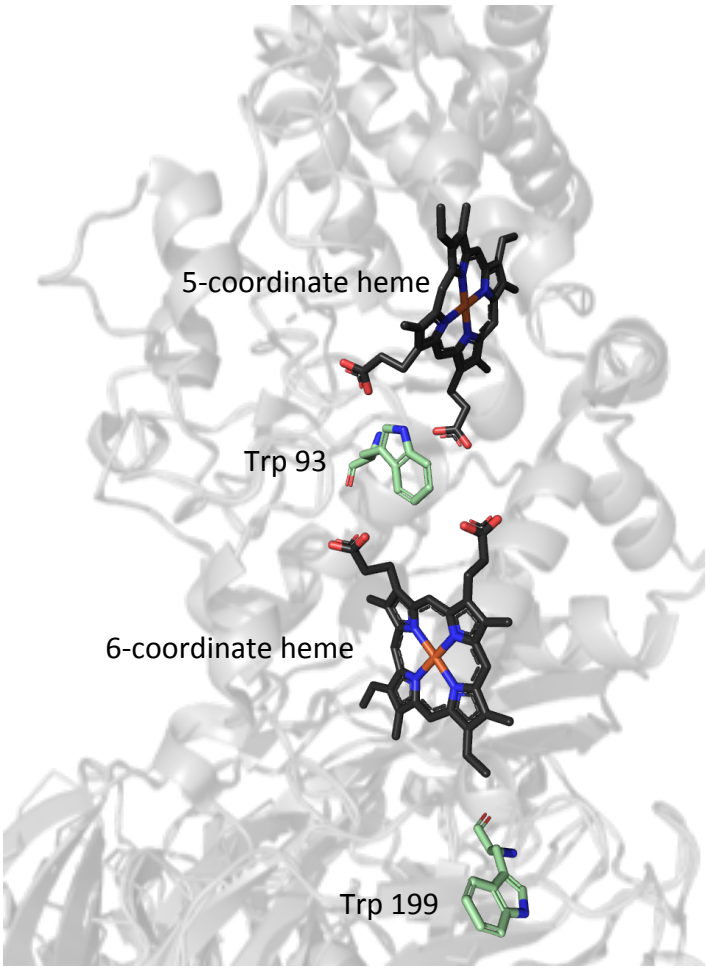

Figure 1.11. Proposed hole-hopping pathway through MauG active site. Heme shown in dark grey, Trp shown in mint. PDB accession number 4Y5R[52]

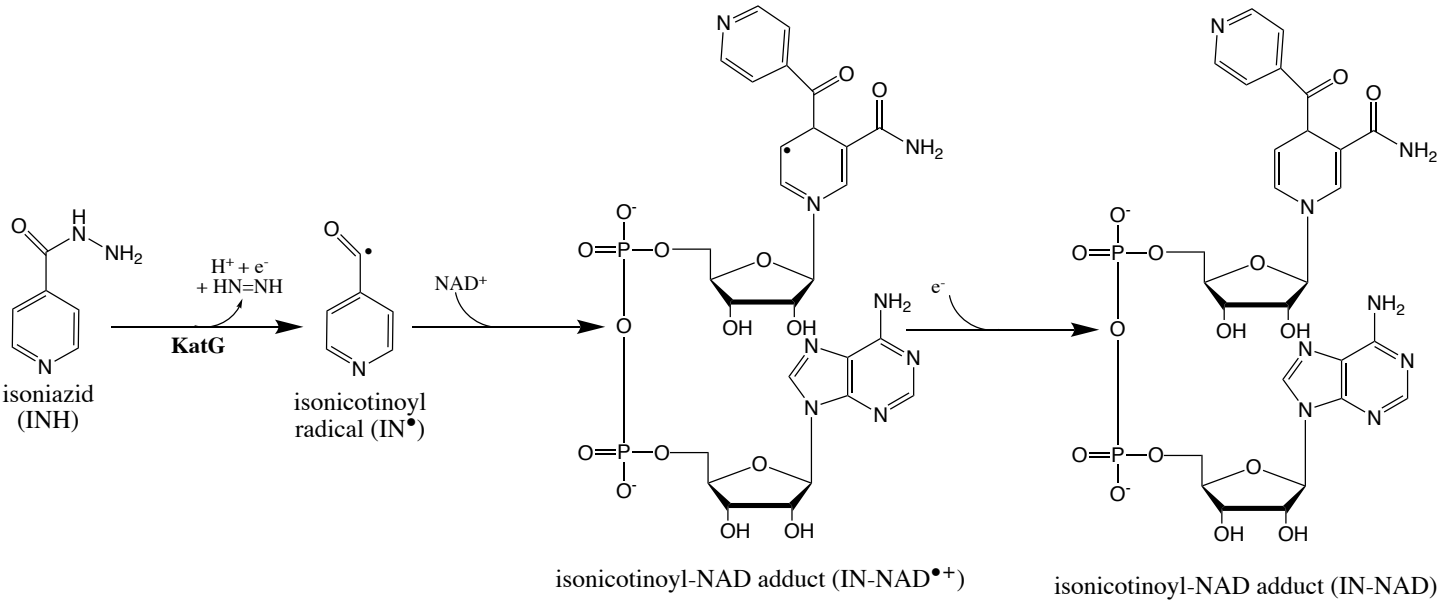

Figure 1.12. Formation of IN-NAD adduct from INH and NAD^+. Shown is a schematic representation of the activation of INH by KatG to an acyl radical intermediate followed by the subsequent addition NAD^+ to form IN-NAD.

from multiple studies that mutations to the *katG* gene account for the large majority of isoniazid resistant TB (~70%). The most frequently observed modification to the KatG enzyme which accounts for KatG-based isoniazid resistance (~70%) produces the S315T KatG variant. Serine 315 is situated at the entrance to the active-site access channel. Cumulatively, then, it is found that the S315T KatG substitution is present among nearly 50% of MDR TB patients, for example, in South Sumatra.[72] This supports the claim that the largest single cause of INH drug resistance in MDR TB patients is mutation, which results in the production of S315T KatG by *M. tuberculosis*. Understanding how S315T substitution in KatG affects catalase activity, peroxidase activity, enzyme inactivation, observed heme intermediates, protein radicals formed, and the formation of the MYW adduct can inform how the addition of a single methyl group to KatG prevents activation of INH and lead to a better understanding of INH activation and IN-NAD formation.

Chapter 2: Production of KatG Variants to Evaluate the Impact of an Oxidizable Scaffold on Protein-based Cofactor Formation

Introduction

Catalase-peroxidase (KatG) is a bifunctional, heme-dependent enzyme that possesses both catalase and peroxidase activities. KatG is also striking in the large number of oxidizable amino acids in its structure. In the active-site containing N-terminal domain of *M. tuberculosis* KatG there are 18 tryptophans, 12 tyrosines, and 13 methionines. One of the most studied of these oxidizable residues is the proximal tryptophan (W321 by *M. tuberculosis* numbering) (Figure 2.1), which is proposed to be an underlying defense mechanism for transferring misdirected and potentially destructive oxidizing equivalents away from the active site.[44, 51, 73] Unlike KatG's MYW cofactor, neither W321 nor any of its oxidized forms (e.g., $W321^{\cdot+}$) is an intermediate of catalase activity. Rather it appears to be an electron-transfer conduit, which contributes to a peroxidase-like mechanism to restore inactive intermediates back to catalase turnover, preventing inactive intermediates from accumulating.

Other than W321 and W107 (the Trp contributor to the MYW cofactor), there are several other oxidizable amino acids found close to the active site, including W412, Y413, and W91 (Figure 2.1). Because autocatalytic biosynthesis of the MYW cofactor involves oxidation of residues near the heme center, it is reasonable to propose that any of these amino acids might impact the formation of the MYW adduct by serving as alternative protein-based electron sources for heme reduction during the MYW cofactor formation process. The W321F, W412F, Y413F, and W91F KatG variants were used to

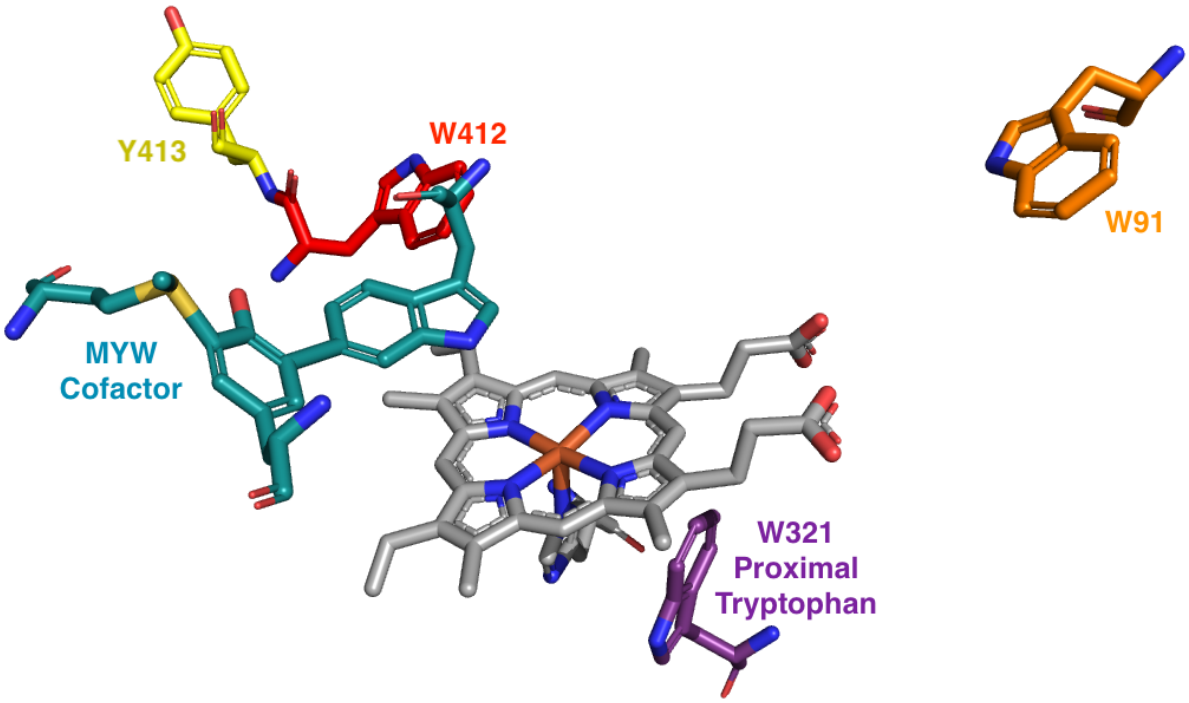

Figure 2.1. Active site of *M. tuberculosis* KatG depicting the Methionine-Tyrosine-Tryptophan (MYW) cross-link and the Proximal Tryptophan (W321), as well as other oxidizable amino acids found close to the active site (Y413, W412, W91). MYW cofactor shown in blue, Proximal Tryptophan (W321) shown in purple, Y413F shown in yellow, W412 shown in red, and W91 shown in orange. This image was constructed using PyMol, from coordinates deposited under the PDB accession entry 2CCA.[94]

investigate the role of each oxidizable residue, and by extension the network of oxidizable amino acids connected with each, in the formation of the MYW cofactor.

In order to study how these amino acids were involved in the formation of the MYW adduct, we produced variants where the oxidizable residue (Tyr or Trp) was replaced with a non-oxidizable phenylalanine. Accordingly, these variants are referred to as W321F KatG, W412F KatG, W91F KatG, and Y413F KatG respectively. Having created KatG variants with each of these substitutions, it was also necessary to produce versions of each one of them where the covalent link between the Met 255, Tyr 229, and Trp 107 of the MYW adduct had yet to be established. Typically, KatG is prepared using an *E. coli* strain (C41 [DE3] pHPEX3) specially designed for expression of heme-dependent enzymes grown in heme-supplemented media. After purification, KatG produced in this system not only contains heme, but also the fully formed MYW adduct. We refer to this protein as mature KatG (*m*KatG). Clearly, *m*KatG is a form that is not suitable for monitoring the formation of the MYW cofactor. To be able to monitor the formation of the MYW adduct, it is first necessary to express and isolate KatG which lacks heme. That is, it is in its apo- form (*a*KatG). Here, *E. coli* (BL-21[DE3] pLysS) unable to take up heme from culture media is used to express KatG in media with no heme supplementation. If heme is not present in the active site, the MYW adduct cannot form, even if endogenously generated peroxides are present during expression. Abundant *a*KatG was generated in this system, *a*KatG so produced was then reconstituted with heme to generate *r*KatG. The strategy here was to be able to generate the MYW adduct of rKatG at will upon the addition of peroxide (Figure 1.9). KatG is a relatively large protein (homodimer or homotetramers ~80 kDa/subunits). It shows very limited ability to

refold properly upon full denaturation/unfolding. Also, the active-site channel is small and would need some level of unfolding or denaturation for the heme to be inserted properly for KatG reconstitution. Given these difficulties, other expression protocols for generating KatG in its apo form and then reconstituting with heme have not been successful in producing protein with high enough yields for any kind of mechanistic investigation.

It is known that in order to form the MYW adduct, heme must be present in the active site, and second, peroxide must also be present or supplied as an oxidant.[34] Here, we describe the highly efficient expression of W91F, W321F, W412F, Y413F, and S315T KatG with each in their *a*KatG and *m*KatG forms. The *a*KatG form of each variant was successfully reconstituted with heme to form the *r*KatG form of each variant in high yield. We will compare *r*KatG to *m*KatG, where heme has been incorporated during expression, resulting in formation of the MYW cofactor in purified enzyme. The strong heme absorption features limit the probability for experimental identification of the spectral features of the MYW adduct intermediates. These methods are confirmed with LC-MS/MS and agree with previously published work. Furthermore, we present these methods in five different variants; W321F KatG, W412F Kat, W91F KatG, Y413F KatG, and S315T KatG. Lastly, we present electron paramagnetic resonance (EPR) data to demonstrate the spin states observed for *m*KatG and *r*KatG, further supporting the reconstitution procedure.

Materials and Methods:

Materials

T4 DNA ligase, P*fu* polymerase, and *Escherichia coli* (XL-1 Blue and BL-21 Gold [DE3] pLysS) were obtained from Agilent (La Jolla, CA). All oligonucleotide primers were purchased from Invitrogen (Carlsbad, CA). All restriction enzymes and high-fidelity Phusion PCR master mix with GC buffer were acquired from New England Biolabs (Beverly, MA). Ampicillin and isopropyl β-D-thioglactopyranoside (IPTG) were purchased form Gold Biotechnology (St. Louis, MO). H_2O_2 (30%), peracetic acid (PAA), hemin, imidazole, calcium chloride hydrate, phenylmethylsufonyl fluoride (PMSF) were purchased from Sigma Aldrich (St. Louis, MO). Miller LB, benzonase nuclease and diammonium 2,2'-azino-bis(3-ethyl-benzothiazoline-6-sulfonate) (ABTS) were obtained from VWR Life Science. Chloramphenicol, mono- and dibasic sodium phosphate, sodium chloride, sodium acetate trihydrate, Tris-HCl, KCl, $MgSO_4$, MgCl, and tetracycline hydrochloride were all purchased from Fisher Scientific (Pittsburg, PA). Imidazole and nickel sulfate hexahydrate were purchased from Alfa Aesar (Haverhill, MA). Ni-NTA resin was purchased from G-Biosciences (St. Louis, MO). Centrifuge filters (30 kDa-cutoff) were purchased from Pall Laboratories (Port Washington, NY). Macro-Prep High Q anion exchange resin and Econo-Pac (10DG) buffer exchange/desalting columns were obtained from Bio-Rad (Hercules, CA). Mass spectrometry-grade TPCK-treated trypsin was purchased from Promega (Madison WI). All buffers and media were prepared using water purified through a Barnstead Genpure pro UV-UF water system (18.2 MΩ/cm resistivity).

Site Directed Mutagenesis

Site-directed mutagenesis to generate plasmid constructs for the expression of W321F, W412F, W91F, and Y413F KatG variants was performed by the so-called "Round-the-Horn" method.[74] The template for mutagenesis was pMRLB11, a pET23b+-derived plasmid bearing the *M. tuberculosis katG* gene. The protein generated using this expression construct is *Mt*KatG bearing a six-histidine tag on its C-terminal end to aid in Ni-based purification. The pMRLB11 plasmid was obtained under the TB Vaccine Testing and Research Materials Contract at Colorado State University.

The forward primer for the W321F substitution (5'-GAGGTGGTA**TTT**ACGAACACCCCGACGAAATGGCAC-3') was designed to include a site for codon replacement (bold) as well as a mutation designed to introduce a diagnostic restriction site *BsaA I* (underlined). The reverse primer for W321F mutagenesis (5'-GATGCCGCTGGTGATCGCGTCCTTACCG-3') required no nucleotide substitutions. The forward primer design for W412F substitution (5'-AGGCC**TTT**TACAAGCTGATCCACCGAGACA-3') was designed to include a site for codon replacement (bold) as well as a mutation design to introduce a diagnostic restriction site for *Stu*I (underlined). The reverse primer for W412F (5'-TGGCGAACTC GTCGGCGAATTCCT-3') required no substitution. The forward primer design for W91F substitution (5'-CTA CGGTCACTACGGGCCCCTGTTTATCC-3') was designed to include a site for a mutation design to introduce a diagnostic restriction site *Apa I* and *BamH I* (underlined). The reverse primer for W91F (5'-TCTGCGGG**AAA**CCAC GGCTGCGAG-3') included a site for codon replacement (bold) as well as a mutation designed to introduce a diagnostic restriction site for Apa I (underlined). The forward

primer design for Y413F substitution (5'-GTTCAAGCTGATCCACCGAGACATGG-3') included a site for a mutation design to introduce a diagnostic restriction site *Stu I* (underlined). The reverse primer for Y413F (5'-C**AAG**CCTTGGCGAACTCGTCGC-3') included a site for codon replacement (bold). All sets of primers were modified to include a 5-phosphoryl group, allowing for blunt-end ligation during PCR. All PCR reactions were carried out using Phusion High-Fidelity polymerase in GC buffer-containing Master-Mix and 3% DMSO. All PCR products were initially treated with *Dpn I* to degrade the starting template and then ligated using T4 DNA Ligase.

Transformation

Ligation products were used to transform *E. coli* XL-1 Blue cells by a standard heat-shock protocol. Transformants were selected using ampicillin-containing media. Success of the transformation was confirmed by use of specific restriction enzyme digestion according to substitutions. Candidates that passed the screening were sent for full DNA sequence analysis (Laragen Sequencing, Culver City, CA). Once sequence confirmed that the intended substitution and codon change had been accomplished along with the absence of any unintended substitutions or frame-shifts, the plasmids were then used to transform *E.coli* (C41 [DE3] pHPEX3 and BL21 [DE3] pLysS) according to a standard heat-shock protocol. These transformants were then selected based on their ampicillin, tetracycline, and/or chloramphenicol resistance.

Expression, Purification, and Reconstitution

*m*KatG

E.coli (C41 [DE3] pHPEX3) transformed with pMRLB11 plasmid mutated to generate the intended KatG variant was used to produce the mature KatG (*m*KatG) form

of each variant. Expression was carried out in Luria Bertani, Miller broth supplemented with ampicillin (100 μg/mL) and tetracycline (200 μg/mL) at 37° C with constant agitation (200 rpm). When an appropriate cell density was achieved (i.e., OD_{600} of 0.30-0.45), target protein expression was induced by the addition of IPTG (final concentration = 1 mM) and the culture was supplemented with hemin (final concentration = 8 μM). Following induction, cultures were incubated at 37° C for 4 hours with constant agitation (200 rpm). At four hours post-induction, cells were harvested by centrifugation (1,957 g) for 20 mins at 4-8° C with a Sorvall RC5B refrigerated centrifuge. KatG expression was verified by TCA precipitation and SDS-PAGE gel analysis. Harvested cells were frozen at -20°C prepared for purification.

To prepare the cells for KatG purification, they were first resuspended in 50 mM phosphate, pH 7, 200 mM NaCl (5 mL/L expression volume. Phenylmethylsulfonyl fluoride (PMSF) (50 mM stock solution in 95% EtOH) was then added to the resuspended cells at 200 μL/L expression-volume. This mixture was homogenized using a Dounce glass tissue grinder. Homogenized cells were lysed by sonication (8 cycles: 42 s on, 42 s off; 3.5 duty and constant output) using a Branson 250 Sonifier (Danbury, CT). Benzonase nuclease was added to the cell lysate at 2 μL/L expression-volume, and the mixture was allowed to incubate at 4° C for 4 hours with constant gentle agitation. Following incubation, the cell lysate was centrifuged at 12,298 g at 4° C for 1 hour to separate soluble protein from cellular debris and other insoluble constituents. Slow deceleration was utilized to minimize disturbance of the pellet. The supernatant was then added to pre-washed Ni-NTA resin and allowed to incubate at 4° C for 12 hours with constant agitation. The supernatant/Ni-NTA resin mixturewas then poured into a column

and the resin was allowed to settle. The Ni-NTA column was then washed, in order, with the following solutions: 50 mM Tris, pH 8; 50 mM phosphate, 200 mM NaCl, pH 7; and 50 mM phosphate, 200 mM NaCl, pH 7, supplemented with 20, 50, 100, 200, and 500 mM imidazole. Most of the KatG variants eluted with 100 mM imidazole as visualized by and SDS-PAGE. The fractions containing KatG were combined and concentrated using centrifugal filters (30 kDa MW cutoff). The concentrated protein was added to Econo-Pac 10 DG desalting columns for buffer exchange, eluting in 50 mM sodium phosphate, pH 7. After buffer exchange, a visible asborption spectrum of the protein purification product to evaluate protein quantity, protein quality, and heme occupancy. Protein was further concentrated in preparation for anion exchange chromatography using Macro-Prep High Q resin and a linear elution gradient ranging from 50 mM sodium phosphate, pH 7, to 50 mM sodium phosphate, pH 7, 500 mM NaCl. Following analyses by SDS-PAGE and UV-visible absorption spectroscopy, the purest and most heme-enriched fractions of KatG were combined and concentrated. Finally, exchange into enzyme storage buffer (5 mM sodium phosphate, pH 7) was performed using centrifugal filtration, diluting with new buffer, and repeating 3-5 times to ensure optimal buffer exchange. The spectral features of the protein were assessed by taking a spectrum of the resulting purified product. The catalase activity of the purified enzyme was also evaluated. The purified protein was then aliquoted and stored at -80° C.

*r*KatG

E.coli (BL-21 Gold [DE3] pLysS) transformed with pMRLB11 plasmid mutated to generate the intended KatG variant was used to produce KatG in its apo form (i.e., *a*KatG). Expression was carried out in Luria Bertani, Miller broth supplemented with

chloramphenicol (100 μg/mL) and tetracycline (200 μg/mL) at 37° C with constant agitation (200 rpm). When an appropriate cell density was achieved (i.e., OD_{600} of 0.30-0.45), target protein expression was induced by the addition of IPTG (final concentration = 1 mM) and the temperature was reduced to 20° C. The cells were grown for 12 hours with constant agitation (200 rpm) prior to harvesting by centrifugation at 1,957 g for 20 mins at 4-8° C. KatG expression was verified by TCA precipitation of aliquots of cells drawn from expression culture hourly between the time of induction and cell harvesting, resuspending pellets in SDS-PAGE loading buffer, and separating by SDS-PAGE. Harvested cells were frozen at -20°C until purification.

The purification of *a*KatG was carried out as described above for *m*KatG up until anion exchange chromatography. Prior to anion exchange chromatography, *a*KatG would be frozen at -80° C for at least 12 hours, after which the protein was reconstituted according to a procedure established by Tarfi Aziz from the Goodwin Laboratory. Briefly, frozen *a*KatG was allowed to thaw slowly on ice and diluted to 50 μM in 5 mM phosphate, pH 7. A hemin stock solution (~1.5 mM) was freshly prepared in 10 mM NaOH. This hemin solution was then diluted with H_2O to produce a 0.875-molar ratio hemin solution with a final volume of heme solution that is one half the volume of the total volume of protein. A 100 mM KP_i buffer, pH 6.2, was also made that is half the volume of the total volume of protein. This would be the same volume as 0.875-fold molar ratio hemin solution. These three solutions are then gently mixed together and left on ice for 4-6 hours at 4° C with intermittent gentle agitation. This mixture was then concentrated using 30 kDa-cutoff centrifuge filters to obtain a final volume of 3 mL. This procedure resulted in a final concentration of ~ 850 μM for a 6 L expression. Econo-Pac

10G desalting column (BioRad) were then used to accomplish the removal of unbound heme and elute the reconstituted enzyme in 5 mM phosphate, pH 7.0. This served to remove adventitiously bound hemin and allow the protein with properly bound heme to migrate through the column first.

Following elution of protein from the desalting column, it is subject to further purification by anion exchange, according to the same protocol described above for *m*KatG. Anion exchange and selection of eluted fractions selects for heme-bound KatG in preference to enzyme lacking heme. Finally, the *r*KatG product is concentrated using 30 kDa cutoff centrifuge filters, subject to buffer exchange with the centrifuge filters. The *r*KatG prepared by this protocol is then evaluated by UV-visible absorption (250-700 nm) to determine how successful to reconstitution was. This was done by comparing the heme Soret peak at 406 nm of *r*KatG and *a*KatG, where there should be about a 10-fold increase in absorbance. A pyridine hemochromagen assay is used to determine the concentration. The protein is then aliquoted out and stored in 5 mM phosphate buffer, pH 7 at -80° C.

Optical Spectra

After purification, all three types of protein; apo KatG (*a*KatG), reconstituted KatG (*r*KatG), and mature KatG (*m*KatG) were analyzed using the Shimadzu UV-visible Spectrophotometer. This was performed in a 1 mL cuvette with 100 mM phosphate buffer, pH 7.0 at 25° C.

Enzyme Assays

After purification, mature and reconstituted KatG's were evaluated by assessing their catalase and peroxidase activities using spectrophotometric methods (Shimadzu

UV1601-PC). Catalase activity was determined by monitoring the decrease in absorbance at 240 nm (ε = 39.4 $M^{-1}cm^{-1}$) over 60 s upon reaction of 20 nM enzyme with varying concentrations of H_2O_2 (0.05 - 50 mM). All of these assays were carried out at ambient temperature using 100 mM phosphate, pH 7.0. For peroxidase activity, we monitored the oxidation of ABTS to $ABTS^{\bullet+}$ at 417 nm (ε = 34,700 $M^{-1}cm^{-1}$) for 60 s. All reactions contained 20 nm enzyme and 0.1 mM ABTS. H_2O_2 concentrations were varied from 0.05 to 50 mM. All assays were conducted at ambient temperature using 50 mM acetate, pH 5.0. The maximum catalytic output and catalytic efficiency were reported as k_{cat} and k_{on} (i.e., k_{cat}/K_M), respectively. If a standard rectangular hyperbolic increase in rate as a function of substrate concentration was observed, the data were fit using a standard Michaelis-Menten equation (equation **1**) formulated to return k_{on} instead of K_M. Initial rates (μM H_2O_2 consumed or μM $ABTS^{\bullet+}$ generated) obtained from experimental data were divided by total enzyme concentration ($[E]_T$) so that k_{cat} could be assessed from direct inspection of the rectangular hyperbolic data. These kinetic parameters (k_{on} and k_{cat}) were obtained from nonlinear least-squares fitting of Michaelis-Menten plots using GraphPad Prism software.

$$\frac{V_0}{[E]_T} = \frac{k_{cat}[H_2O_2]}{k_{cat}/k_{on} + [H_2O_2]} \quad [1]$$

Tryptic Digest and Liquid Chromatography Mass Spectrometry

For ESI-LC-MS analyses, all KatG variants were digested using Promega sequencing-grade modified trypsin (Promega [#V5111]) at a 200:1 KatG to protease ratio in a total reaction volume of 250 μL. All digests were perfomed for 3 hours at 37° C in 50 mM ammonium bicarbonate, pH 8.0. All digests were quenched with 20 μL glacial acetic acid and stored (not more than 24 hours) at 4° C prior to analysis. When pretreated

with peroxide, KatG variants were reacted with peroxide (1 – 10 molar equivalents of PAA, 5 equivalents of H_2O_2, or 50 equivalents of H_2O_2) for 1 hour before adding trypsin. Analyses were performed at the Auburn University Mass spectrometry Center housed in the Department of Chemistry and Biochemistry on an ultra-performance LC system (ACQUITY. Waters Corp., USA) coupled with a quadrupole time-of-flight mass spectrometer (Q-TOF Premier, Waters, Beverly, MA) with electrospray ionization (ESI) in positive ion mode using MassLynx software (V4.1). Samples (10 μL) were injected onto a C18 column (Waters UPLC BEH C18 2.1x50 mm, 1.7 μM) and peptides were separated using the gradient described belowat a 300 μL/min. flow rate. Mobile phase solution A (water with 0.1% formic acid) and solution B (95% acetonitrile, 5% water, 0.1% formic acid) were started at 3% B and held for 2 minutes followed by a linear ramp to 50% B over the next 58 minutes. There was then a linear ramp to 100% B by 62 minutes, which was held for an additional 5 minutes followed by a return to 3% B over the next 3 minutes with 10 minutes of re-equilibration to the starting condition.

The mass spectrometer was set as follows. The capillary voltage was set at 3.1kV, the sample cone voltage was 30 V, and the extraction cone was 4.3 V. The source and desolvation temperatures were maintained at 125 and 300° C, respectively, with the desolvation gas flow at 600 L/hr. The MS scan (100 to 4,000 *m/z*) was 1.0 s with a 0.02 s inter-scan delay using the centroid data format. Tandem MS scans were 0.5 to 1.0 s long with a 0.02 second inter-scan delay with a collision energy ramp from 20 V to 40 V. The lock mass was used to correct instrument accuracy with a 2 ng/μL solution of leucine enkephalin (Bachem [4000332]).

Manual Quench and Electron Paramagnetic Resonance

Purified KatG proteins were concentrated to 150 μM for evaluation of the FeIII (i.e., resting state) by EPR. A final volume of 300 μL of each enzyme sample was placed in an EPR tube (Wilmad Glass, Vineland, NJ). The EPR tube was then slowly lowered into N_2 (*l*) (77 K) until all of the protein was frozen. The samples were then stored at 77 K in N_2 (*l*) until they could be evaluated by EPR.

All EPR spectra were collected on a Bruker EMX X-band spectrometer operating in perpendicular mode. The parameters were as follows: 4.5 K (He (*l*) temperature, 9.392 GHz frequency, 1.00×10^4 receiver gain, 100 kHz modulation frequency, 1.0 G modulation amplitude, 0.630 mW microwave power, 327.680 ms conversion, 327.680 ms time constant, 335.544 s sweep time, and resolution of 1024 points. For comparison of spectra across various time points, 0.630 mW power was used even if the EPR signal was slightly saturated; temperature- and power-saturation studies were additionally performed to identify powers sufficiently low to avoid power saturating EPR signals.

Results and Discussion

Reconstitution and Spectroscopic Evaluation of KatG Variants

The incorporation of heme into purified *a*KatG variants was shown to be successful by direct comparison of the heme Soret peak at 406 nm of *r*KatG variants and *m*KatG variants (Figure 2.2). An increase in the optical purity ratio (Abs_{405}/Abs_{281}) of ~10 fold was observed for *r*KatG variants relative to *a*KatG variants as a result of the reconstitution process. Along with that, our reconstitution procedure resulted in proteins (*r*KatGs) capable of robust catalase and peroxidase activities which were very similar to the corresponding *m*KatG variants (Table 2.1). This ensured that the heme was

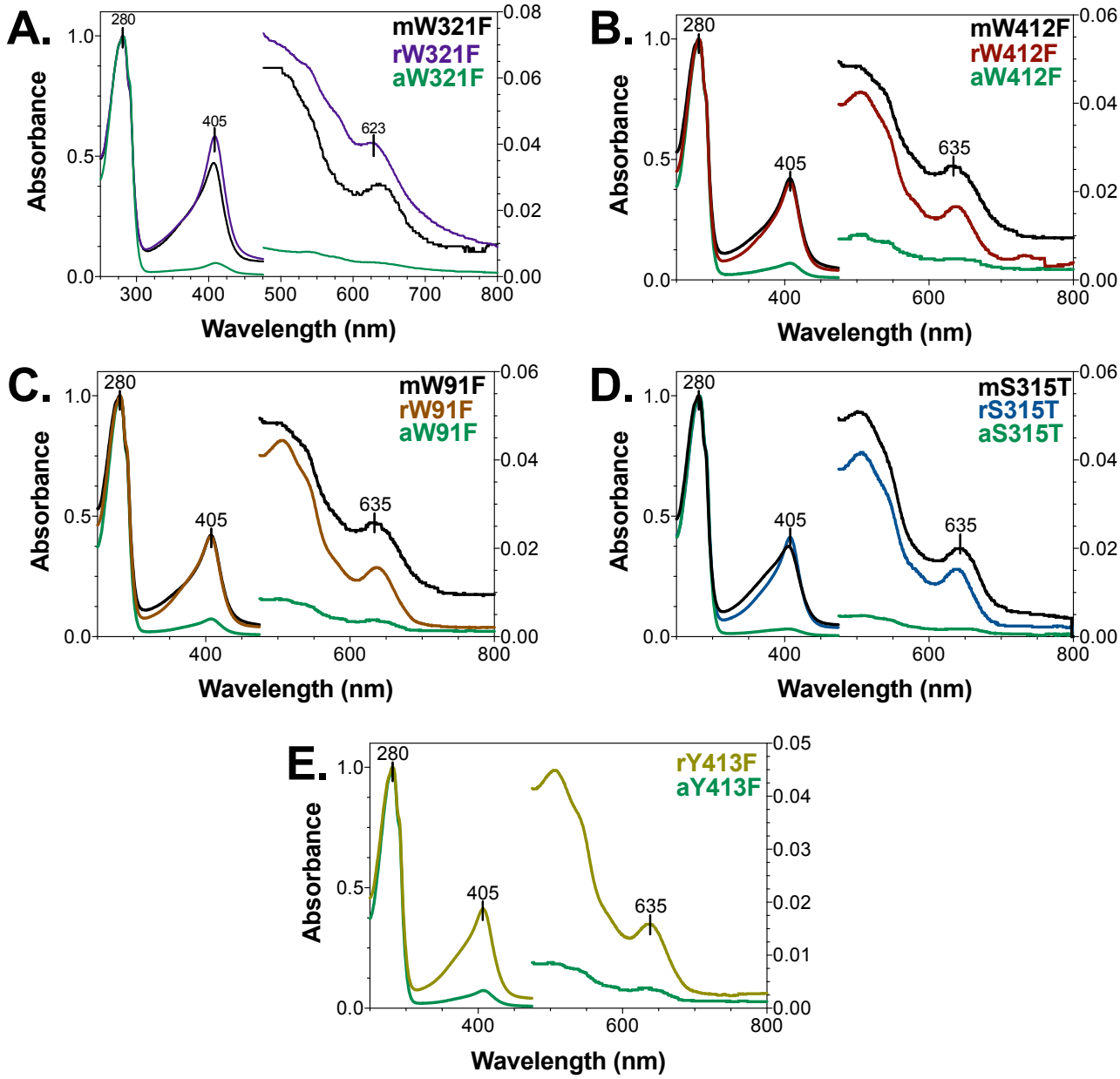

Figure 2.2. Comparison of KatG expression and purification across variants. UV-visible absorption spectra of reconstituted W321F KatG (*r*W321F) shown in purple (A), reconstituted W412F KatG (*r*W412F) shown in red (B), reconstituted W91F KatG (*r*W91F) shown in orange (C), reconstituted S315T KatG (*r*S315T) shown in blue (D), reconstituted Y413F KatG (*r*Y413F) shown in yellow (E), mature KatG shown in black, and apo KatG shown in green. All spectra were recorded at 25° C using 100 mM phosphate buffer, pH 7.0.

Table 2.1: Standard catalase activity parameters for WT KatG and variants

Activity	KatG	Kinetic Parameters	
		k_{cat} (s^{-1})	k_{cat}/K_m ($M^{-1}s^{-1}$)
Catalase (pH 7.0)[a]	*r*WT	4630 ± 19	(1.1 ± 0.10) × 10^6
	*m*WT	4780 ± 36	(1.0 ± 0.20) × 10^6
	*r*W91F	2500 ± 200	(9.2 ± 1.5) × 10^5
	*m*W91F	2700 ± 200	(7.4 ± 1.0) × 10^5
	*r*W321F	2160 ± 40	(1.5 ± 0.1) × 10^6
	*m*W321F	3500 ± 110	(1.8 ± 0.1) × 10^6
	*r*W412F	3330 ± 120	(2.3 ± 0.3) × 10^6
	*m*W412F	3660 ± 110	(1.5 ± 0.1) × 10^6
	*r*Y413F	3800 ± 200	(5.3 ± 0.5) × 10^6
	r*S315T*	3350 ± 120	(1.5 ± 0.2) × 10^6
	mS315T	2800 ± 180	(4.2 ± 0.2) × 10^5
Catalase (pH 5.0)[c]	*r*WT	64.1 ± 0.02	(4.1 ± 0.3) × 10^3
	*m*WT	466 ± 0.03	(3.79 ± 0.03) × 10^4
	*r*W91F	313 ± 55	(2.5 ± 1.6) × 10^5
	*m*W91F	371 ± 55	(1.4 ± 0.6) × 10^5
	*r*W321F	346 ± 15	(5.3 ± 0.5) × 10^5
	*m*W321F	1420 ± 120	(2.0 ± 0.4) × 10^5
	*r*W412F	1690 ± 180	(4.1 ± 0.4) × 10^4
	*m*W412F	1050 ±110	(6.8 ± 0.9) × 10^4
	*r*Y413F	760 ± 100	(7.0 ± 1.7) × 10^4
	rS315T	600 ± 40	(8.1 ± 1.3) × 10^4
	mS315T	1010 ± 40	(1.2 ± 0.4) × 10^5
Peroxidase (H_2O_2)[d]	*r*WT	2.44 ± 0.1	(3.2 ± 0.4) × 10^4
	*m*WT	1.66 ± 0.1	(2.5 ± 0.2) × 10^4
	*r*W91F	25 ± 4	(2.3 ± 0.8) × 10^4
	*m*W91F	10 ± 0.5	(3.4 ± 0.6) × 10^4
	*r*W321F	4.5 ± 0.1	(5.1 ± 0.7) × 10^4
	*m*W321F	2.0 ± 0.3	(3.9 ± 0.3) × 10^4
	*r*W412F	4.7 ± 0.2	(3.7 ± 0.7) × 10^4
	*m*W412F	6.4 ± 0.2	(3.8 ± 0.7) × 10^4
	*r*Y413F	3.5 ± 0.5	(3.8 ± 0.2) × 10^4
	rS315T	6.2 ± 0.2	(4.8 ± 0.5) × 10^4
	mS315T	5.0 ± 0.4	(4.2 ± 0.4) × 10^4

[a]Activity by H_2O_2 consumption (240 nm) 23 °C in 100 mM phosphate, pH 7.0.
[b]Activity was determined by O_2 production at 23 °C in 100 mM phosphate, pH 7.0.
[c]Activity was determined by O_2 production at 23 °C in 50 mM acetate, pH 5.0.
[d]Peroxidase parameters determined using 0.1 mM ABTS in 50 mM acetate, pH 5.0.

incorporated successfully. Though the purified *r*KatG variants show substantial heme incorporation and appropriate catalase activity, there are small spectral differences in some of the KatG variants. This difference is most evident in the heme Soret peak between the ferric forms of the *r*KatG and *m*KatG variants, and indicates a difference in heme coordination (Figure 2.2). This difference was most evident in W412F KatG, W91F KatG, and S315T KatG. The purified *r*KatG variants showed features more consistent with a high-spin (HS) 6-coordinate heme as evidenced by a narrower Soret band with a λ_{max} near 406 nm combined with a lesser contribution from a hypsochromic (i.e., blue-shifted) shoulder on the Soret peak, which is typical of 5-coordinate HS heme. This was supported in subsequently obtained EPR spectra. These data indicated a greater contribution from axial *g*-tensor anisotropy relative to rhombic *g*-tensor aniostropy (Figure 2.9, Figure 2.11).

Mass spectrometric detection of the MYW cofactor

In order to evaluate the kinetics and steps of the formation of the MYW adduct, one must first confirm that the *r*KatG variants are indeed lacking the MYW adduct. One must also confirm that the *m*KatG variants have formed the MYW adduct in order to make this direct comparison. The LC elution profiles (310 - 330 nm) of trypsin-cleaved *m*W321F KatG, *r*W321F KatG, and *r*W321F KatG treated with H_2O_2 are consistent with this hypothesis (Figure 2.3). Not only did these elution profiles confirm nearly identical levels of heme incorporation for *r*W321F KatG compared to *m*W321F KatG, but they also indicated that *r*W321F KatG produced much lower signals corresponding to the MYW adduct/peptide (~32 min elution) than was observed for *m*W321F. These data also indicated that with the treatment of *r*W321F KatG with H_2O_2 resulted in an increase in

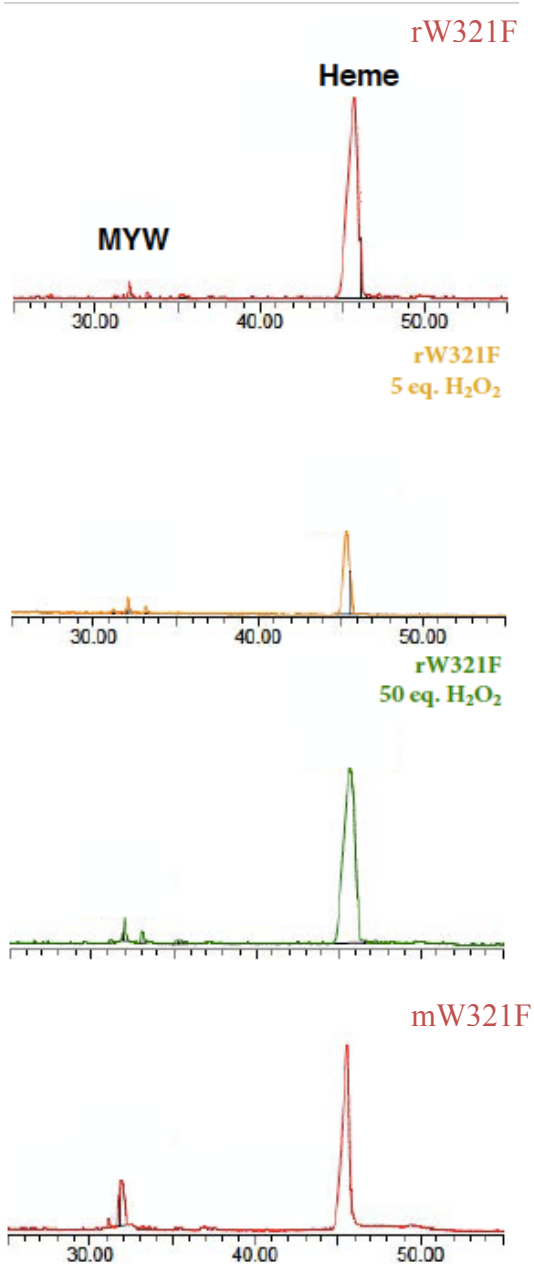

Figure 2.3. L.C. Chromatogram of W321F KatG and heme cofactors at 330 nm. W321F KatG was tryptic digested and absorbance at 330 nm was monitored during separation by LC-MS. Though the MYW adduct was present in *r*W321F (top red) *r*W321F treated with 5 eq. of H_2O_2 (yellow), *r*W321F treated with 50 eq. of H_2O_2 (green), and *m*W321F (bottom red) the absorbance for the PTM is greatest for *m*W312F. Additionally the absorbance for the MYW adduct (32 min) and heme (45 min) were able to be detected at 330 nm and found to be consistent with previously collected UV-Vis data.

formation of the MYW adduct to a level similar to *m*W321F KatG. We observed very similar results with the W412F KatG variant (Figure 2.4). This variant indicated the same amount of MYW adduct formation in the *a*W412F KatG as the *r*W412F KatG, indicating no new MYW adduct formation took place during the reconstitution procedure. Only that present due to the very small portion of our *a*KatG preparations, which already contained heme from expression (i.e., ~5%) was present after reconstitution. Likewise, similar results were obtained from *r*W91F KatG (Figure 2.5). However, it is important to note that we were unable to produce a high enough concentration of *m*W91F KatG for comparison in this case.

Detected MS ions corresponding to peptides eluting at 32 min agree with the assignment of this peak as the MYW adduct and its associated tryptic peptides.[7-9] Figure 2.6 and Table 2.2 list the specific MS ions detected and their corresponding peptide structure. The full MYW adduct, including the tryptic peptides of each MYW adduct member was detected in a number of charged states (5+, 6+, 7+, and 8+) with a parent ion of 6,881 *m/z*. All of these charged states were detected in W321F KatG, W412F KatG, and W91F KatG no matter the type of protein (i.e., *a*KatG, *r*KatG, or *m*KatG). Consistent with previous reports, products resulting from the fragmentation of the MYW adduct between the γ-carbon and the sulfur atom of the Met 255 residue were also detected (Table 2.2, Figure 2.7, Figure 2.8). [7] This in-source fragmentation resulted in the detection of a 4,867 peptide product, which is known to be the YW adduct with an addition thiomethyl group *ortho* to the phenolic OH if Tyr 229 (including the tryptic peptides of both the Tyr and Trp adduct members). Additionally, the second product of this fragmentation (2014 Da) corresponding the M255-bearing tryptic peptide without the

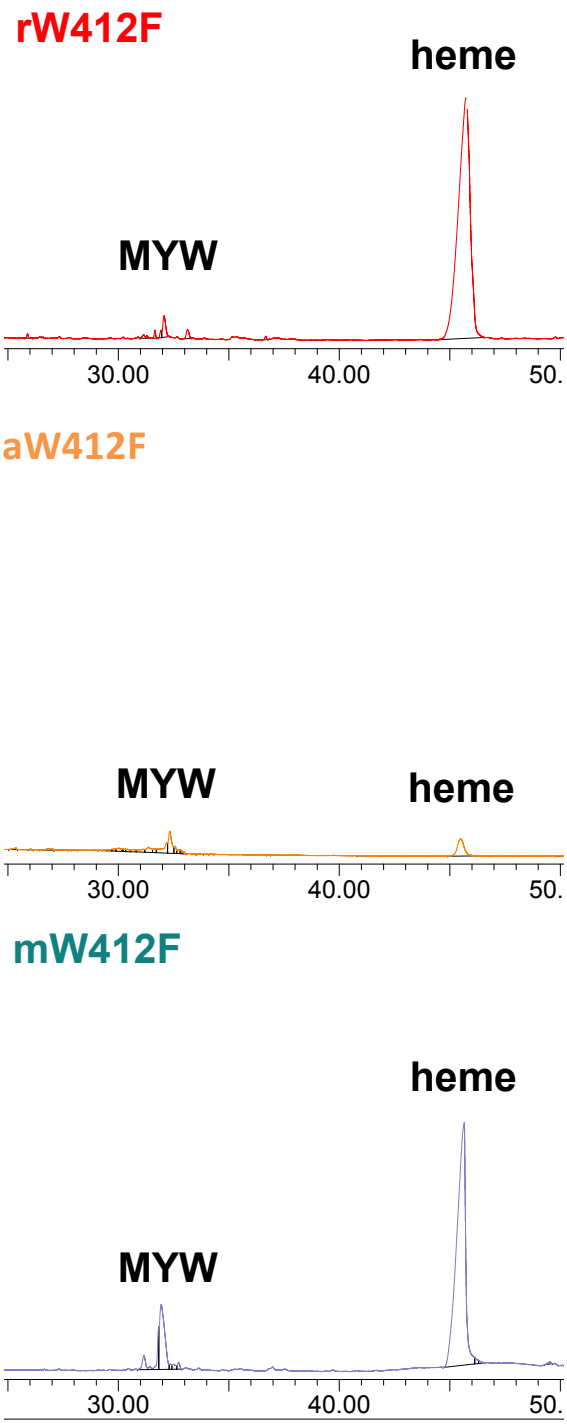

Figure 2.4. L.C. Chromatogram of W412F KatG and heme cofactors at 330 nm. W412F KatG was tryptic digested and absorbance from the MYW adduct was monitored during separation by LC-Ms. Though the MYW adduct was present in *r*W412F (red), *a*W412F (yellow), and *m*W412F (blue) it was the most abundant for *m*W412F. Additionally the absorbance for the MYW adduct (32 min) and heme (45 min) were able to be detected at 330 nm and found to be consistent with the previously collected UV-Vis data.

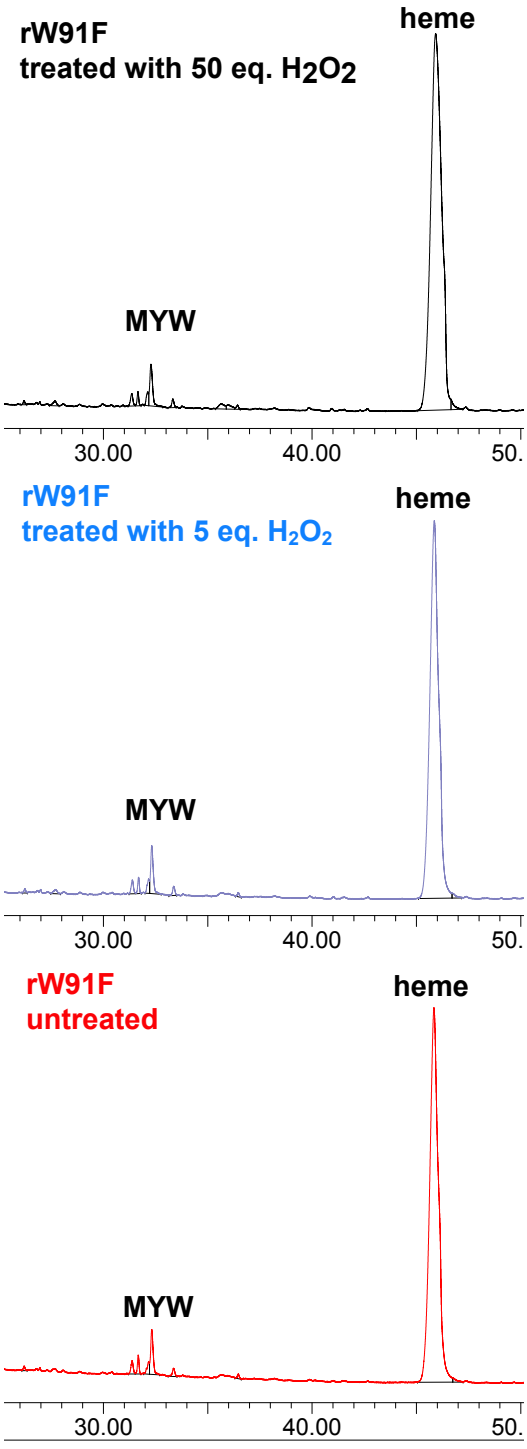

Figure 2.5. L.C. Chromatogram of W91F KatG and heme cofactors at 330 nm. *r*W91F KatG was treated with varying equivalents of H_2O_2, tryptic digested and absorbance at 330 nm was monitored during separation by LC-MS. Though the MYW adduct was present in the untreated *r*W91F (red), *r*W91F treated with 5 equivalents of H_2O_2 (blue), *r*W91F treated with 50 equivalents of H_2O_2 (black) the absorbance for the PTM increased with increasing treatment of H_2O_2. Additionally, the absorbance for the MYW adduct (32 min) and heme (45 min) were able to be detected at 330 nm and found to be consistent with previously collected UV-Vis data.

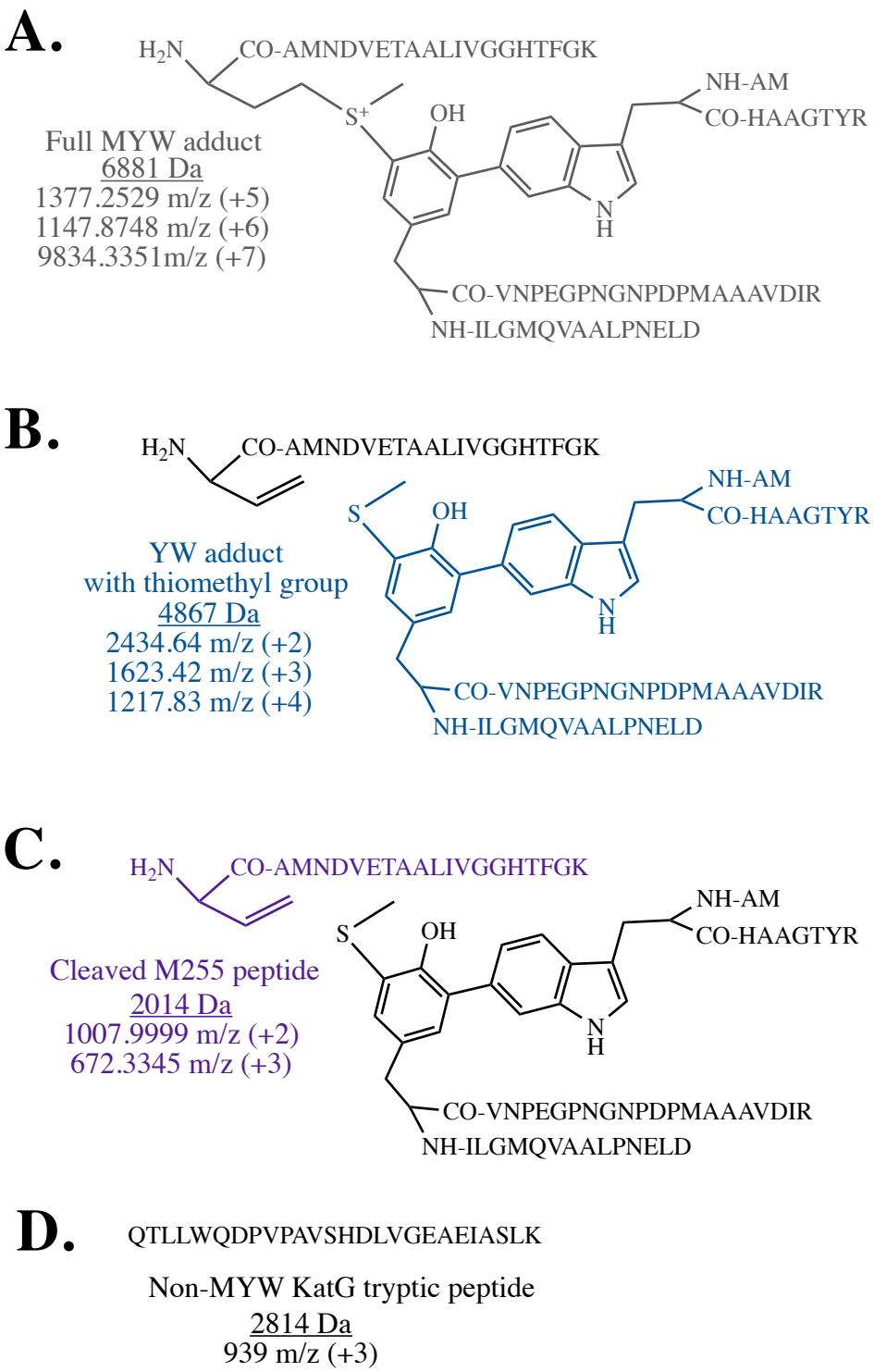

Figure 2.6. Tryptic peptides detected by LC-MS and LC-MS/MS. The structures, peptide fragments, and the weight of the parent ion and m/z values for the ions detected.

Table 2.2. Tryptic peptides detected by mass spectrometry

Identity of Detected Ion	Ion Detected	Parent Ion
Full MYW adduct	1377.2529 (+5) 1147.8748 (+6) 984.3351 (+7)	6881 Da
YW adduct with thiomethyl group	2434.64 (+2) 1623.42 (+3) 1217.83 (+4)	4867 Da
Cleaved M255 peptide	1007.9999 (+2) 672.3345 (+3)	2014 Da

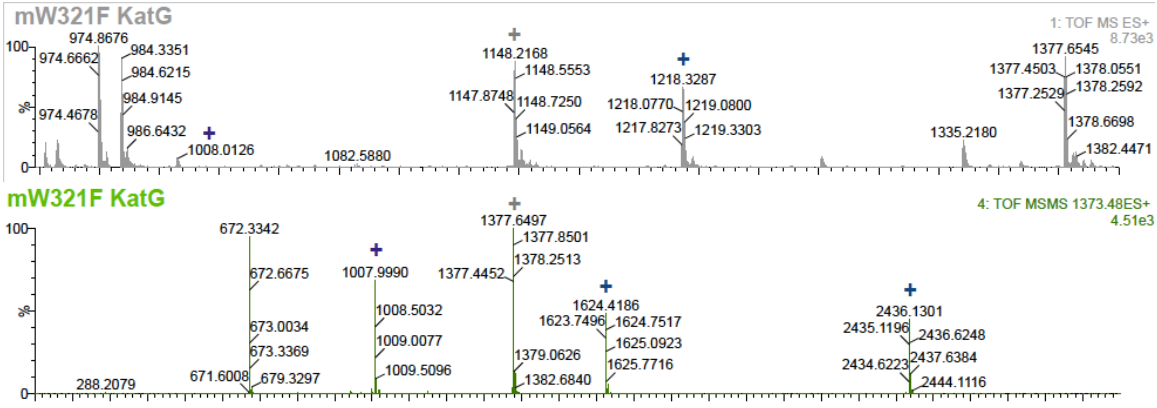

Figure 2.7. Confirmation of MYW adduct in mW321F KatG by LC-MS and tandem MS. Presence of the formed, covalently linked MYW cofactor in W321F mKatG was detected by LC-MS (A). Tandem MS of the 1377.6 m/z ion, which further confirms the formation of the MYW cofactor by identification of the M255 tryptic peptide without the thiomethyl group of M255 at 1007.99 m/z (B).

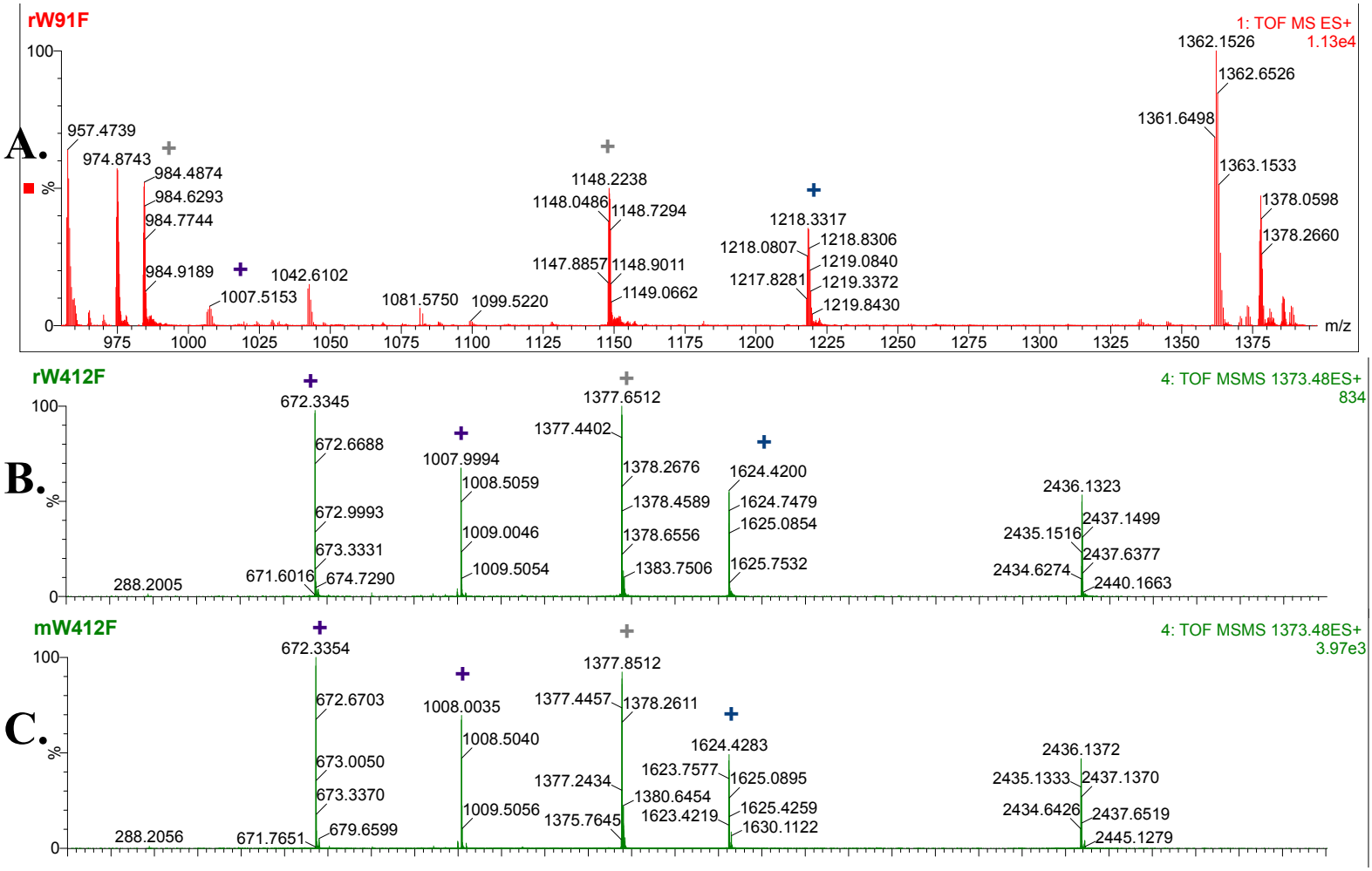

Figure 2.8. Conformation of MYW adduct in *m*W321F KatG by LC-MS and tandem MS. Presence of the formed, covalently linked MYW cofactor in rW91F KatG was detected by LC-MS (A). Tandem MS of the 1377.6 m/z ion, which further confirms the formation of the MYW cofactor by identification of the M255 tryptic peptide without the thiomethyl group of M255 at 1008 m/z (B). Tandem MS of the 1377.6 m/z ion, which also confirms the formation of the MYW adduct (C).

thiomethyl group. In particular, tandem MS analysis of 1,147.8748 (6+) *m/z* ion provides evidence for this event via the ions 1007.999 (2+) *m/z* and 672.33 (3+) *m/z* ion which correspond to a product with a mass of 2014.00 Da. Similarly, 1,217.83 (4+) *m/z*, 1623.42 (3+) *m/z*, and 2434.64 (2+) *m/z* ions were all observed and are accounted for by in-source fragmentation of the full MYW adduct, yielding (H_3C-S-)YW. This is in agreement with previous observations of *M. tuberculosis* KatG and KatGs from other organisms. [7-9]

The MYW adduct-related ions were present in all forms of the protein, including *a*KatG variants, *r*KatG variants, *r*KatG variants treated with peroxide, and *m*KatG variants. Even though this was the case, the ions were present in much greater intensity in the *m*KatG variants and the *r*KatG variants treated with peroxide (Figure 2.7, Figure 2.8). This was consistently observed no matter the variant of KatG, and the same was also observed in WT KatG. There is also a non-MYW adduct tryptic peptide, with an observed 939 (3+) *m/z*, co-eluted with the MYW adduct peptide during the chromatographic separation. This ion is seen across all samples, irrespective of KatG variant. The identity of this non-MYW adduct tryptic peptide was confirmed by comparison with a previous peptide mapping and the analysis of KatG peptides (data not shown). This peptide served as an internal standard for comparing the relative abundance of MYW adduct derived ions in the varying proteins, both in terms of variant and preparation protocol (Figure 2.7, Figure 2.8). When this 939 (3+) m/z ion was used as an internal standard it was evident that *m*KatG variants contained a greater concentration of formed MYW adduct than either a*K*atG variants or *r*KatG variants (so long as the latter had not been treated with peroxide). It was not unexpected that the *r*KatG variants would

have some population of MYW adduct formation. Despite being expressed and purified in the absence of exogenous heme, a small amount of purified *a*KatG had received endogenous heme from the *E. coli* cells during expression (Figure 2.4). The intensity of the MYW-ions in the *a*KatG variants and the *r*KatG variants samples were substantially lower in population than the *m*KatG variants. As mentioned elsewhere, treatment of *r*KatG variants with H_2O_2 resulted in a substantial increase in MYW-associated products (Figure 2.7,Figure 2.8). Accordingly, it is not expected that lower MYW product signal intensities would be due to difficulties in ionization across the different protein preparations because H_2O_2 increased the intensity of the ions in *r*KatG enzyme preparations across all variants tested.

EPR spectra of ferric (resting) forms of KatG variants

We used EPR to confirm the heme states in *m*KatG variants and *r*KatG variants. For *m*W321F and *r*W321F KatG, both were dominated by high-spin ferric species typical of the WT KatG resting state (Figure 2.9), indicating that the reconstitution had properly incorporated the heme into the active site. Interestingly, the *m*W321F KatG preparation showed a mixture of coordination states with some contribution from axial and rhombic *g*-tensor anisotropy. The former is connected to hexacoordinate heme, and the retention of the high-spin state ($g_x = g_y = \sim 6.0$; $g_z \sim 1.99$) indicated that the sixth ligand is a weak-field ligand, likely a H_2O molecule. Even in the *m*W321F KatG protein, the latter makes a relatively small contribution to the sum of species present, but shoulders observed on either side of the $g = 6.0$ axial signal correspond to a rhombic distortion field ($g_x > 6.0$; $g_y < 6.0$, and $g_z \sim 1.97$). This is indicative of a pentacoordinate high-spin state, where H_2O is presumably absent from the ligand sphere.

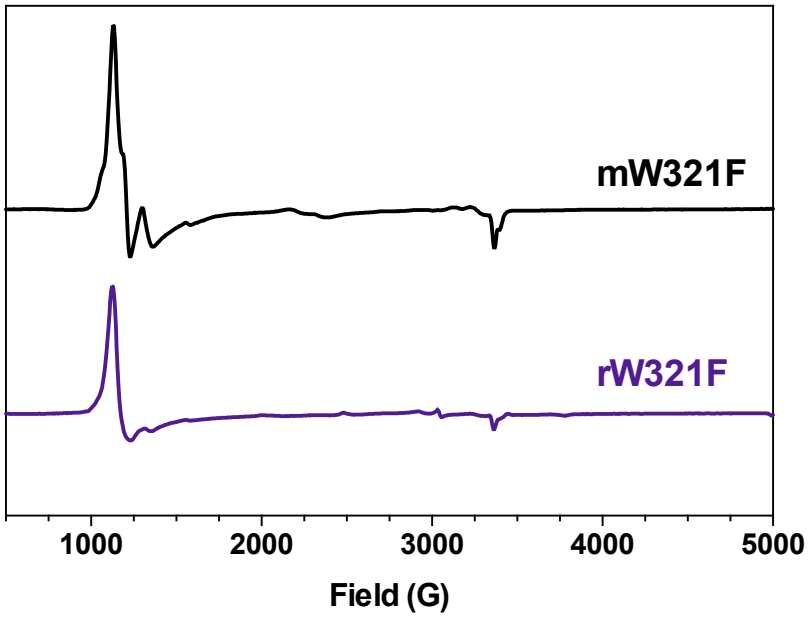

Figure 2.9. Electron Paramagnetic Resonance of Ferric W321F KatG. *m*W321F KatG (black) and *r*W321F KatG (purple) at 150 μM in 50 mM acetate, pH 5. These samples were frozen with liquid nitrogen and collected at 4.5° K using 9.8 Hz frequency.

Another difference observed for *m*W321F KatG and *r*W321F KatG was the intensity, this was consistently observed when *r*W321F KatG was compared to other variants such as *r*W412F KatG, *r*W91F KatG, and *r*Y413F KatG (Figure 2.10). The trend of a high-spin resting state is consistent across these variants, indicating that the neither mutations nor the reconstitution procedure had an effect on the heme state of the isolated enzymes. The *r*W91F, *r*W412F, and *r*Y413F KatG enzymes all showed EPR spectra highly similar to the wild-type enzyme. In all of these variants a similar distribution of signal intensities for axial versus rhombic *g*-tensor anisotropy was observe. Specifically, the axial (presumably hexacordinate HS) state dominated over a much less populated rhombic (presumably pentacoordinate HS) state.

However, there was a substantial contrast observed with the S315T KatG variant (Figure 2.11). There was a larger difference in *m*S315T KatG and *r*S315T KatG in terms of the contribution of the axial versus rhombic *g*-tensor anisotropy. Interestingly, the *r*S315T KatG protein showed a very similar distribution of these states as observed for all the other *r*KatG perparations of KatG variants investigated as part of this research (i.e., *r*W91F, *r*W321F, *r*W412F, and *r*Y413F KatG). However, with *m*S315T KatG a substantial *increase* in rhombic signal was detected. Indeed, it appeared that it exceeded the contribution of the axial signal (see g_z contributions at 1.99 and 1.97). This would suggest that the pentacoordinate HS state dominates over the hexacoordinate HS state with S315T KatG. This has been observed previously with *Mtb* KatG,[75] but the striking observation here is that this novel bias in the S315T KatG variant appears only to be observed if the enzyme has established its MYW adduct. A connection between the S315 residue, which resides at the entrance to the KatG active-site access channel and the

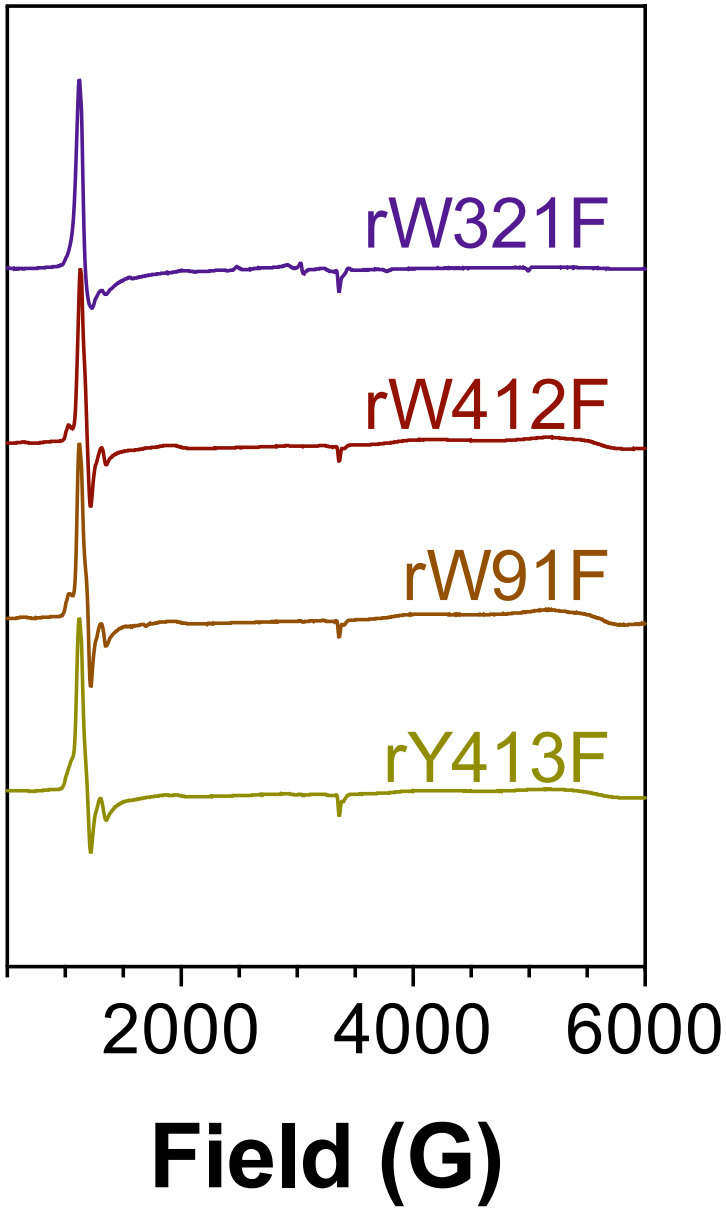

Figure 2.10. Electron Paramagnetic Resonance of Ferric reconstituted KatG variants. *r*W321F KatG (purple), *r*W412F KatG (red), *r*W91F KatG (orange), and *r*Y413F KatG (yellow) at 150 μM in 50 mM acetate, pH 5. These samples were frozen with liquid nitrogen and collected at 4.5° K using 9.8 Hz frequency.

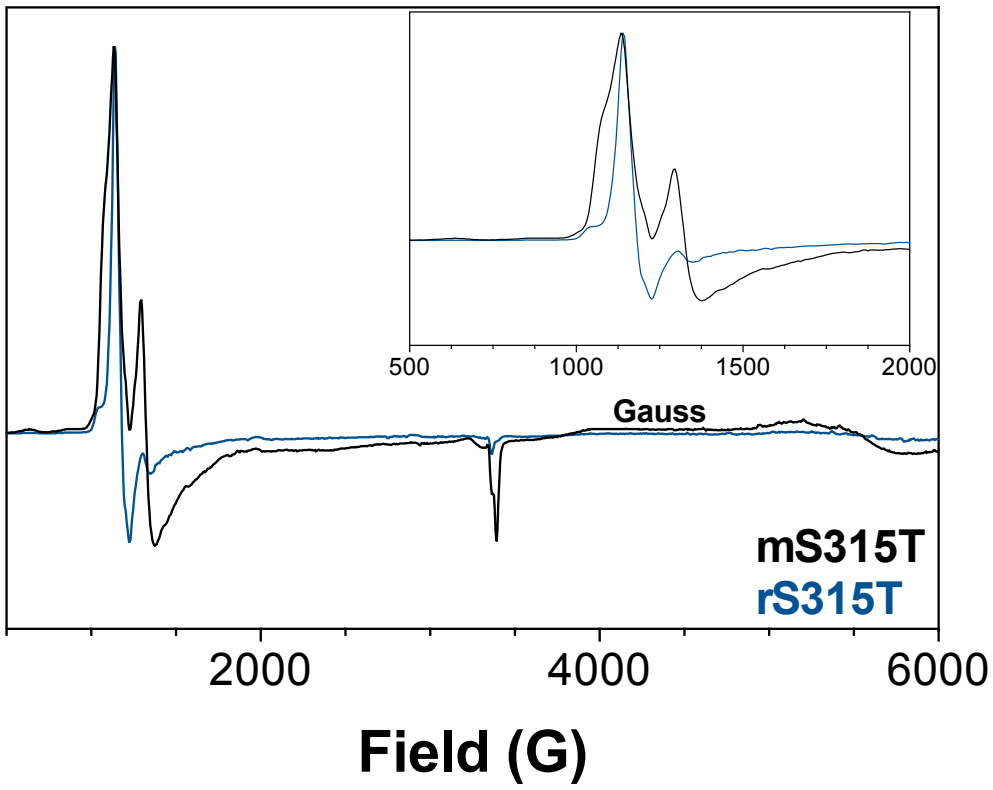

Figure 2.11. Electron Paramagnetic Resonance of Ferric reconstituted KatG variants. *m*S315T (black) and *r*S315T (blue) at 150 μM in 50 mM acetate, pH 5. The inset shows a closer view of the field around 1,000 to 15,000 GHz. These samples were frozen with liquid nitrogen and collected at 4.5° K using 9.8 Hz frequency.

MYW adduct in terms of active-site water occupancy is interesting as it relates to INH activation.

Conclusions

With a new protocol developed in our lab for producing KatG protein with heme cofactor, lacking the protein-derived cofactor, we present preliminary data on the character and reactivity of the W321F KatG, W412F KatG, W91F KatG, Y413F KatG, and S315T KatG variants. In comparison of spectra, one can observe that the reconstitution procedure eliminates interference from adventitiously bound heme; the heme is in the correct orientation in the active site, and the electronic state of the heme is nearly identical to that of WT KatG. This indicates that the variants themselves have not disrupted the heme environment. One can also conclude that the reconstitution procedure produced little to no effect on the catalase activity or the peroxidase activity of the enzyme. We used LC-MS/MS analysis to confirm the presence of the fully formed MYW adduct in *m*KatG variants, as well as a much-diminished intensity and contribution from the MYW adduct in the *a*KatG variants and the *r*KatG variants. With EPR we confirmed that the spin-state of the heme is exclusively high-spin across all variants and all preparation protocols. Previous studies have shown that low-spin heme states in KatG are almost always the result of substantial active-site rearrangements that eliminate catalase and peroxidase activities of the enzyme.[76-78] Across all *r*KatG preparations of variants investigated the hexacoordinate HS state appeared to dominate over any pentacoordinate HS states. This held in all cases where mKatG preparations were evaluated. The *m*S315T variant was the lone exception, where it appeared that establishment of the MYW adduct

along with the serine to threonine substitution at the mouth of the KatG active-site access channel produced a protein dominated instead by a pentacoordinate HS heme state.

In the following chapters we will describe the use of stopped-flow spectroscopy to analyze the intermediates observed for each variant and its effect on the formations of the MYW adduct. We will also explore the rates of formation of the MYW adduct intermediates, based on the effects of the missing oxidizable amino acid. Finally, we will determine the reaction differences with different peroxides, and their effects on the MYW adduct formation. Taken together, the results presented in this chapter have set a stage for a more in-depth study of the impact of critical oxidizable amino acids in the KatG structure on MYW adduct formation as well as the impact of these residues on the ability of mature (i.e., MYW-bearing) KatG to sustain its catalase activity prior to inactivation.

Chapter 3: Effect of active-site oxidizable residues on MYW cofactor formation and through-protein electron transfer

Introduction

Catalase-peroxidases (KatG) use a peroxidase scaffold to support robust catalase activity, an ability no other member of its superfamily possesses.[79, 80] Catalase and peroxidase activities both involve the reduction of an equivalent of H_2O_2 to H_2O with each turn of the catalytic cycle. What defines catalase activity is the H_2O_2 oxidation to O_2 that is necessary to return the enzyme to its starting state. In contrast, peroxidases require the oxidation of an exogenous electron donor to return to the starting state. In some peroxidases, exogenous or peroxidatic electron donor (PxED) oxidation is a relatively simple electron transfer to a high-valent heme intermediate at the porphyrin edge. The canonical horseradish peroxidase (HRP) provides a good example of this phenomenon.[36] For other peroxidases, the *net* result is the same, but far more complex through-protein radical transfer mechanism is required. This may be necessitated by an exceedingly narrow peroxidase active-site access channel and/or a very large (e.g., protein-based) PxED, either of which precludes ready access to a heme edge for facile electron transfer.[36]

Through-protein electron transfer is not unique to a subset of peroxidases; it has been observed with increasing frequency across a wide range of redox enzymes. In general, electrons can tunnel through the protein matrix in microseconds with a moderate release of free energy over distances in the 15 to 20 Å range.[81] In order to span greater distances or move electrons faster, multiple charge transfers (or hops) are required. When one of the reactants is a strong oxidant, it is convenient to consider the movement of a

positively charged "hole" in a direction opposite of the electron.[81] Such hole-hopping can occur *via* temporary oxidation of a series of tryptophan (Trp) and/or tyrosine (Tyr) residues is a critical aspect of the function of a wide variety of oxidoreductases. For example, the enzyme MauG uses a diheme active site in coordination with two Trp residues to oxidize a quinol tryptophylquinone (TTQ) cofactor of methylamine dehydrogenase (MADH). [52-63]

For KatG in particular, high-potential, high-valent heme intermediates generated upon reaction with peroxides must often be reduced *via* through-protein electron transfer from a PxED at the enzyme's surface due to extremely narrow channel to the enzyme's active site. The abundance of Met, Tyr, and Trp residues within the KatG N-terminal domain is remarkable. For example, the enzyme from *M. tuberculosis* contains 24 tryptophans, 21 tyrosines, and 18 methionines. Interestingly, the vast majority of these (19 Trp, 16 Tyr, and 14 Met) are concentrated in the N-terminal domain. This is made all the more remarkable by the fact that both domains of KatG's structure are peroxidases from gene duplication and fusion.[42] The N-terminal domain retains its heme, a functioning active site, and the overwhelming majority of oxidizable residues. The C-terminal domain has none of these things, suggesting that the oxidizable protein scaffold is an important part of function.

A protein family member closely related to KatG, cytochrome *c* peroxidase (C*c*P), may provide some insight as to the role of such a highly oxidizable protein scaffold. C*c*P has been shown to protect its redox-active cofactor and active site from oxidative damage by allowing the protein periphery to sacrificially sustain oxidative modification by utilizing electron transfer pathways throughout the enzyme.[82] In C*c*P's

case, the primary structure of the enzyme aids not only in its catalytic function, but also in the process of bringing relief from oxidative stress.

It is possible that the high percentage of oxidizable amino acids found in KatG's active site have a similar function in protecting the enzyme from oxidative stress, as well as improving catalase activity. It certainly provides the necessary scaffold for such intraprotein electron-transfer (or hole-hopping) phenomenon. Indeed, about 11% of this active-site bearing domain is comprised of Met, Tyr, or Trp residues; this is nearly double that of the average protein.[44, 51] Remarkably, this same domain contains about four times the Trp residues of a typical protein.[44, 51] Accordingly, in KatG, there are multiple pathways of these oxidizable amino acids that begin close to the active site and work their way to the surface of the enzyme (Figure 3.1). It has been proposed that these pathways/networks/chains may serve a protective role in the enzyme by deactivating high-potential reactive intermediates formed in uncoupled catalytic turnover. Such a highly oxidizable protein framework serves to transfer oxidizing equivalents away from critical active site structures and to the surface for scavenging by peroxidatic electron donors (PxEDs) such as ABTS.[44, 51, 73] This creates a seamless integration of KatG's catalase and peroxidase activities where observable peroxidase-based oxidation events actually mark the preservation and extension of KatG catalase activity.[44, 51]

Examination of the KatG structure reveals that there are four principal groupings of these oxidizable amino acid residues. This is deduced by supposing that the ultimate source of electron-hole generation in the enzyme would be the active-site heme center where ferryl-oxo and other highly oxidized reaction intermediates are generated. As such, there would be a nearest protein-based point from which electrons could be delivered to

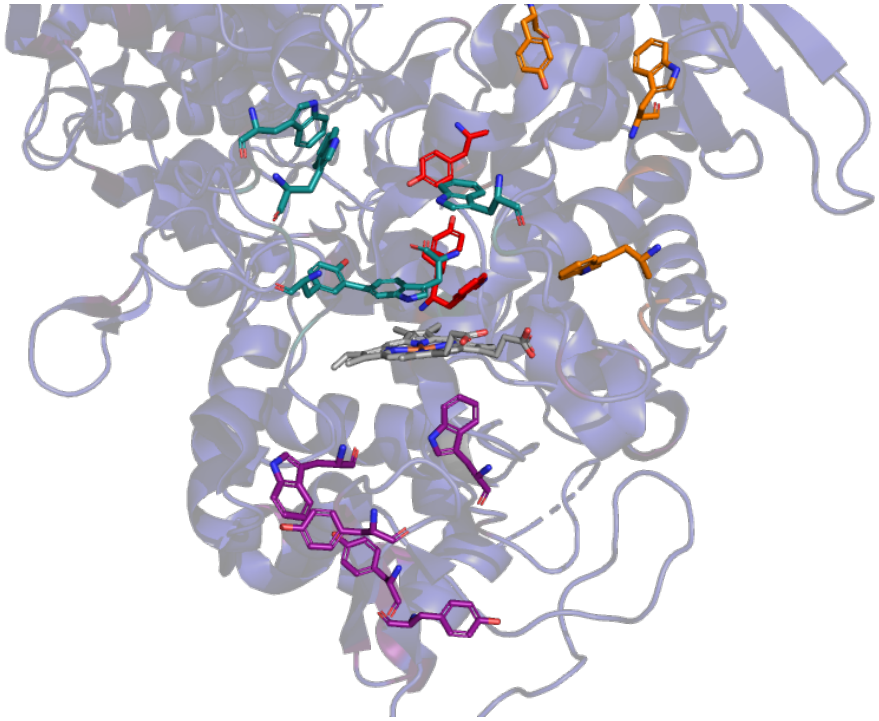

Figure 3.1 Oxidizable amino acid pathways in KatG's active site. The heme center of KatG is shown here in grey. The proximal tryptophan and its following oxidizable amino acids are shown in purple. The MYW adducts Tyr and Trp as well as their pathway amino acids are shown in deep teal. W91 and its pathway amino acids are shown in orange. W412 and Y413 pathway are shown in red. This image was constructed using PyMol, from coordinates deposited under the PDB accession entry 2CCA.[94]

reduce such intermediates. A chain to facilitate electron-hole hopping to the enzyme surface would have to be traced by a series/group of Trp/Tyr residues in close enough proximity to each other (e.g., < 10 Å) to facilitate very rapid electron transfer events.

The four heme-adjacent residues representing the four networks/groupings of oxidizable residues are W107 (the Trp component of the MYW cofactor), W321 (the proximal tryptophan), W91, and W412. For three of four of these residues, there is evidence that these residues participate as points of protein oxidation. Tryptophan 107 is part of an oxidatively generated protein-based covalent adduct.[51] Tryptophan 321, the so-called proximal Trp) is known to be oxidized to a radical under multiple reaction conditions not only in KatG,[49, 51] but also the equivalent residue in KatG's closest superfamily relative, cytochrome *c* peroxidase.[42] Tryptophan 91 has also been shown as a point of protein-based radical formation in KatG from *M. tuberculosis* and *B. pseudomallei*.[42] Although tryptophan 412 has not yet been directly observed to be oxidized to its corresponding radical, it is only ~11 Å from the heme iron, and residues within its network/group have been shown to be oxidized following KatG reaction with the peroxide peracetic acid.[83]

We surmised that there are two distinct realms of KatG catalysis and function where a preponderance of oxidizable amino acids (especially Trp and Tyr) could have a substantial impact. The first, discussed above, is during its active disposal of H_2O_2 through its catalase activity. Our group has observed that off-catalase electron-hole transfer events can be passed by the KatG protein to its surface where a suitable PxED can be oxidized as a mechanism to preserve catalase activity and account for the

enzyme's peroxidase activity. The extent to which the four networks identified above contribute to such a mechanism has not been investigated.

The second realm of KatG catalysis that may be impacted by the enzyme's highly oxidizable scaffold is in its post-translational transition to a mature catalase-active enzyme. Specifically, in the reactions forming the MYW protein-based cofactor. This adduct has been proposed to form by way of a radical mechanism supported by the KatG heme and an exogenous peroxide.[34, 43] This mechanism requires the specific oxidation of covalent adduct contributors (i.e., W107 and/or Y229). The presence of other oxidizable residues within the active site and their link to extended networks for electron-hole transfer may facilitate or even detract from MYW formation. To the former, one could envision a scenario where only a Fe^{IV}=O[porphyrin]$^{\bullet+}$ state was competent for oxidative steps leading to MYW formation. Given that these are single-electron oxidation steps, a remaining Fe^{IV}=O state would need to be reduced to the Fe^{III} enzyme. The networks of oxidizable amino acids in KatG could serve that process. For example (Figure 3.2), the proximal tryptophan (W321) could be used to return the enzyme back to a ferric state, enabling the subsequent reaction of Fe^{III} KatG with peroxide to form the next equivalent of the Fe^{IV}=O[porphyrin]$^{\bullet+}$ state However, there are numerous other hole-hopping pathways that may be utilized, including those headed by W412 and W91F. Electron-hole hopping through these pathways may not be ordered or systematic, therefore these pathways could also be facilitating turnover of biosynthesis of the MYW cofactor as shown in Figure 3.2. To the latter (i.e., oxidizable networks distracting from MYW formation), it is possible oxidizable residues other than the MYW precursors (e.g. W321, W91, and/or W412) may be oxidized in lieu of Trp 107 and/or Tyr 229 and/or partial

adducts (e.g., YW). Either of these scenarios could account for the fact that substantially greater equivalents of peroxide (3×) are required for MYW generation than the bare minimum anticipated based on the 4e- oxidation necessary to convert unassociated M255, Y229, and W107 to the mature MYW cofactor. [34, 43] Regardless, the impact of networks of oxidizable residues on the ability of KatG to autocatalytically establish its MYW cofactor have not been investigated.

The model for through-protein electron-hole hopping implies a path for electron-hole transfer from a highly oxidized heme center through a network of oxidizable amino acids to the enzyme's surface. Accordingly, the most strategic point for disrupting electron hole migration through a network of oxidizable residues would be to render the closest point to the heme center non-oxidizable. In order to accomplish this, we have used site-directed mutagenesis to replace oxidizable tryptophan residues with nonoxidizable phenylalanine for the heme-adjacent representatives of three of KatG's putative through-protein electron transfer networks of redox-active amino acids. That is, we have produced W91F, W321F, and W412F KatG variants. A fourth variant, Y413F KatG, was generated as an additional probe of the W412 network—it is the next oxidizable group in the chain. We used this set of KatG variants to investigate the participation and role of redox-active amino acid networks in 1) KatG's autocatalytic formation of its MYW adduct, and 2) their contribution to sustaining KatG's catalase activity. It should be noted that though the Goodwin lab has produced a W107F KatG variant, it is not of value for this project as it is required for MYW adduct formation and KatG catalase activity, both of which are parameters under investigation in this study.

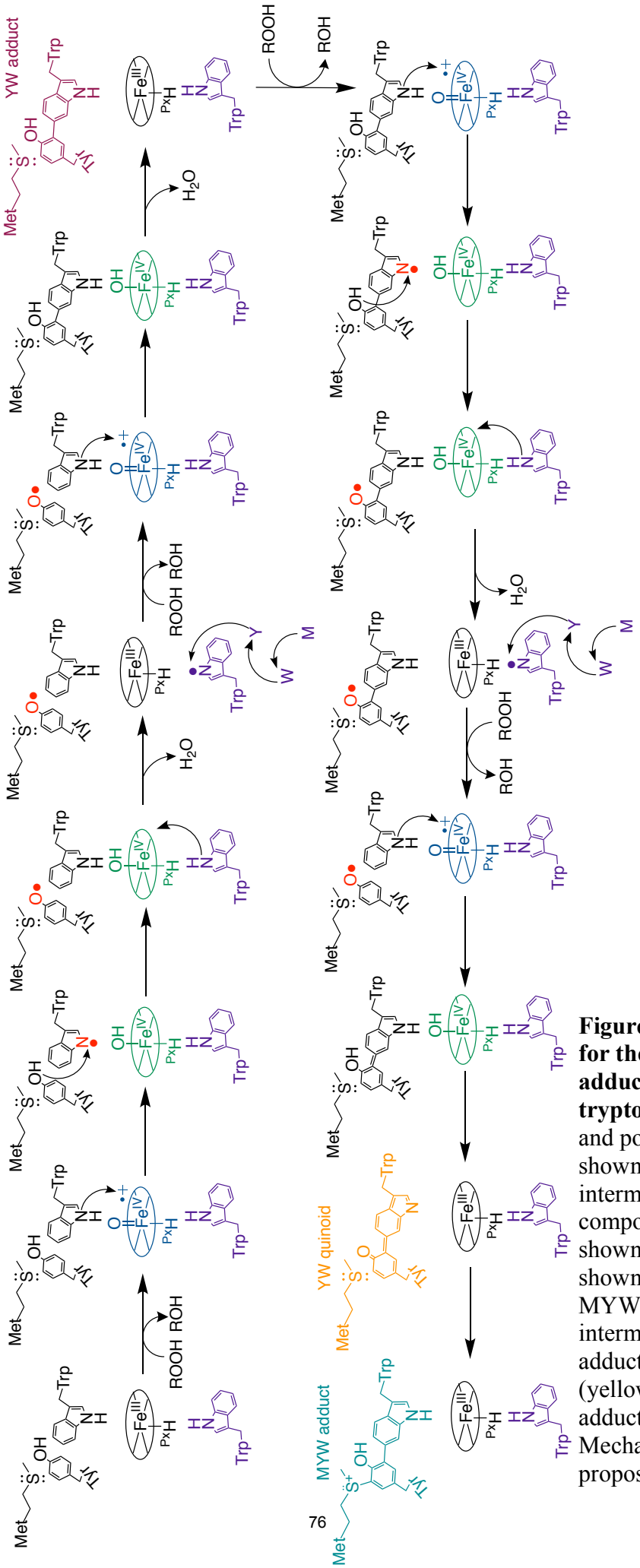

Figure 3.2. Possible mechanism for the formation of the MYW adduct including the proximal tryptophan. Proximal tryptophan and possible oxidizable pathway shown in purple, compound I like intermediates shown in blue, compound II like intermediates shown in green, and radicals shown in red on Tyr and Trp of MYW adduct. Observable intermediates such as the YW adduct (pink), YW quinoid (yellow), and the final MYW adduct (teal) are also shown. Mechanism adapted from that proposed by Ghiladi, et al.[34]

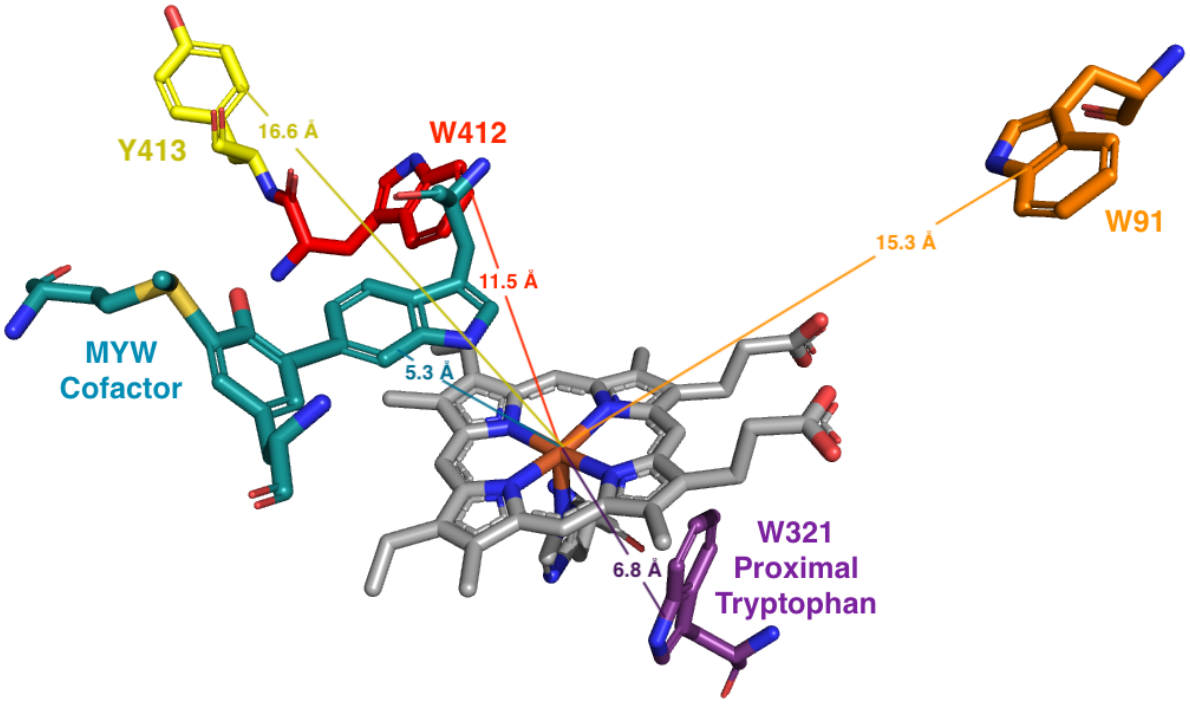

Figure 3.3 Active-site oxidizable amino acids and there distance from the active site. W321F shown in purple, W91 shown in orange, MYW cofactor shown in teal, W412 shown in red, and Y413 shown in yellow. This image was constructed using PyMol, from coordinates deposited under the PDB accession entry 2CCA.[94]

Materials and Methods

Stopped-Flow Spectroscopy to investigate MYW cofactor

The steady-state heme intermediates and other spectral changes of KatG variants were monitored by a PC-upgraded SX18.MV rapid reaction analyzer from Applied Photophysics (Surrey, UK). In all experiments, 3 μM enzyme was utilized. The reactivity of *r*KatG variants were compared to their *m*KatG counterparts when reacted against a range of H_2O_2 concentrations (e.g., 1 to 667 molar equivalents). Additionally, *r*KatG variants were pre-treated with low molar equivalents of PAA (1-20 equivalents), incubated for 10 minutes, and then reacted with H_2O_2 to observe changes in heme intermediate transitions that may take place as compared to *m*KatG or *r*KatG reacted with H_2O_2 alone. Pre-treatments were carried out in 50 mM phosphate, pH 7.0, even if the reaction with H_2O_2 was carried out in 50 mM acetate, pH 5.0. This was to ensure the stability of the protein during exposure to PAA. The oxidation of ABTS was also monitored by stopped-flow over a range of H_2O_2 concentrations and 0.1 mM ABTS. Kinetic data were fit globally using the Pro Kineticist software package (Applied Photophysics, Surrey, UK). Observed apparent rate constants were determined using proposed reaction scheme: A → B, B → C, and C → D.

Rapid Freeze-Quench and Electron Paramagnetic Resonance

Purified KatG protein was concentrated to 300 μM for RFQ-EPR sample preparation, for a final concentration of 150 μM in a final volume around 300 μL in an EPR tube (Wilmad Glass, Vineland, NJ). Steady-state supporting and limited-turnover concentrations of H_2O_2 (667 and 5 molar equivalents, respectively) were prepared fresh in ddH_2O. Samples were prepared using a KinTek RFQ-3 Quench-Flow Instrument

(KinTek Corporation, Snow Shoe, PA). The enzyme-substrate mixture ejected from the KinTek Quench-Flow instrument was caught in a funnel with a quartz EPR tube attached, filled with liquid ethane, and surrounded with liquid nitrogen-isopentane mixture at ~120 K. Samples were then packed using metal packing rods in a KinTek temperature-controlled packing apparatus regulated by liquid nitrogen-isopentane mixture ~120 K. Residual ethane was quickly slung out from the EPR tubes, and samples were then stored at 77 K in liquid nitrogen until read on the EPR spectrometer.

EPR spectra were collected on a Bruker EMX X-band spectrometer operating in perpendicular mode. The parameters used, unless otherwise specified are as follows: 4.5 K temperature, 9.392 GHz microwave frequency, 1.00×10^4 receiver gain, 100 kHz modulation frequency, 1.0 G modulation amplitude, 0.630 mW microwave power, 327.680 ms conversion, 327.680 ms time constant, 335.544 s sweep time, and resolution of 1024 points. For comparison of spectra across various time points, a microwave power of 0.630 mW was used even if the EPR signal was slightly saturated; power-saturation studies were additionally performed to differential power saturation characteristics for various species/time points.

Stopped-flow Spectroscopy to investigate electron transfer

The steady-state heme intermediates and other spectral changes of KatG variants were monitored by a PC-upgraded SX18.MV rapid reaction analyzer from Applied Photophysics (Surrey, UK). In all experiments, 3 μM enzyme was utilized as a final (i.e., post-mixing) concentration. All reactions shown were carried out using 50 mM acetate, pH 5.0, at 4 °C. Reactions were carried out using both *r*KatG and *m*KatG reacted with H_2O_2, PAA, ABTS, ascorbic acid, or some combination of these reactants.

Inactivation Assay

Inactivation of the enzyme was measured on a 1601-PC UV-visible spectrophotometer (Shimadzu Instruments, Kyoto, Japan) by measuring the remaining catalase activity after treatment with H_2O_2. In order to determine the remaining catalase activity of the KatG variants, we first treated the protein with an array of concentrations of H_2O_2. The KatG protein under investigation was first diluted to 200 nM with 5 mM phosphate, pH 7, followed by reaction with H_2O_2 (0, 0.5, 1.0, and 5.0 mM). The reaction was allowed to incubate for 15 minutes with gentle agitation followed by 45 minutes on the bench, all at ambient temperature. Each treatment of H_2O_2 was then evaluated for catalase activity at 240 nm (H_2O_2 ε_{240} = 39.4 $M^{-1}cm^{-1}$) to monitor the remaining catalase activity. All remaining-activity assays contained 10 mM H_2O_2 and were carried out in 100 mM phosphate, pH 7, at ambient temperature. An average activity was calculated for each concentration of H_2O_2 from 15 replicates (three replicates of each incubation reaction with each reaction being repeated five times). replicate test at each of those incubations). These activities were then normalized to the activity of enzyme without any pre-reaction with H_2O_2.

Extent of Oxygen Production

The extent of O_2 production was evaluated using a Clark-type O_2-sensitive electrode (Hansatech, Pentney, Norfolk, UK). All reactions were carried out at ambient temperature following electrode calibration. All reactions contained 5 nM enzyme that was reacted with 0.5 mM H_2O_2. Two pH conditions were explored: 50 mM acetate, pH 5.0, and 100 mM phosphate, pH 7.0. The PxED ABTS, when present, was included at a concentation of 0.1 mM.

Tryptic Digest and HPLC

A 250 μL sample of 50 μM enzyme in 50 mM ammonium bicarbonate, pH 7.0 was incubated with a range of concentrations of PAA (0 to 10 equivalents) for 1 hr at 25° C. The samples were then digested with sequencing-grade trypsin and analyzed by HPLC. Peptides were eluted with a linear gradient from 20-60% of Buffer B (5% formic acid, 10% H_2O, and 90% Acetonitrile) over 4 hours was employed to elute the peptide fragment containing the MYW cross-link or cross-linked peptide fragments (CLPF). Buffer A consisted of 5 % formic acid and 95% H_2O. Single wavelength detection at 330 nm was utilized. The extent of CLPF formation was determined via peak integration. This experiment was repeated in triplicate, and data reported as an average ± S.D. **Results and Discussion**

Results and Discussion

Heme states observed upon reaction of Phe-substitution KatG variants with H_2O_2

W321F KatG. Across all Phe-substitution KatG variants, there were substantial contrasts between the intermediates observed upon reaction of H_2O_2 with *r*KatG preparations of enzyme versus those detected with *m*KatG preparations. Reaction of *r*W321F KatG with 5 molar equivalents H_2O_2 (i.e., 15 μM) (Figure 3.4) produced a substantial and rapid (< 50 ms) decrease in Soret band (λ_{max} 407 nm) absorption intensity along with decreases in intensity in charge transfer bands (λ_{max} ~505 nm and ~640 nm) (Figure 3.4A). Together with an increase in absorption between 550 and 600 nm, a broad and rather featureless absorption profile was observed from 475 – 700 nm. This is consistent with the formation of a Fe^{IV}=O[porphyrin]$^{\cdot}$ intermediate also known as compound I and is commonly observed in heme peroxidases, especially those of the peroxidase-catalase superfamily. Horseradish peroxidase (HRP) and ascorbate peroxidase

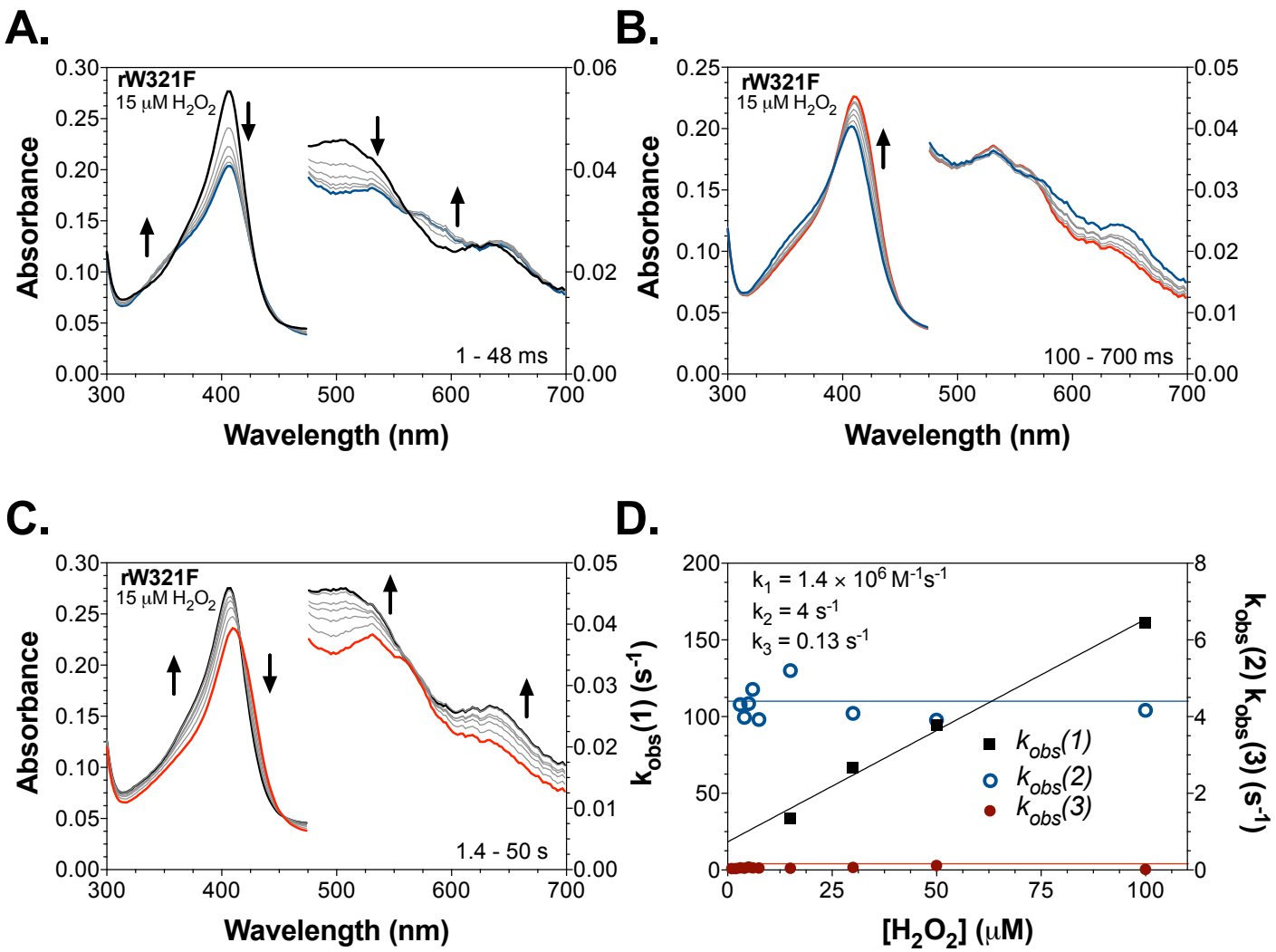

Figure 3.4. Heme states observed for *r*W321F KatG upon reaction with a limited-turnover H_2O_2 concentration. Reaction of *r*W321F KatG with 15 μM H_2O_2 (i.e., 5 molar equivalents) produces conversion from the Fe^{III} (i.e., resting) state to a compound I-like (i.e., Fe^{IV}=O[porphyrin]$^{\bullet+}$) state over the first 48 ms of reaction time (A), followed by conversion to a compound II-like (Fe^{IV}=O) intermediate (B), then a return to the ferric state (C). Rate constants for observed intermediates in *r*W321F KatG (D). Arrows indicate the direction of absorption change over the time range of each panel. All reactions have been carried out using 3 μM KatG in 50 mM acetate, pH 5.0 at 4° C.

(APx) are two well-known examples.[29, 30] A subsequent transition was observed over the next 600 ms where the Soret band red shifted to 411 nm and absorption bands at ~530 nm and ~560 nm emerged (Figure 3.4B). These spectral features are consistent with the formation of the Fe^{IV}=O intermediate known as compound II (Figure 3.4B). Finally, the intermediate with compound II-like features slowly (over 50 s) gave way to the reemerging Fe^{III} state characterized by intense Soret band absorption at 407 nm as well as prominent charge-transfer bands at 505 and 640 nm (Figure 3.4C).

The dependence of each of these transitions on H_2O_2 concentration was evaluated (Figure 3.4D). The k_{obs} for the rapid conversion of Fe^{III} *r*W321F KatG to the compound I-like species was linearly dependent on H_2O_2 concentration. A second-order rate constant (k_1) was estimated from the slope as 1.4×10^6 $M^{-1}s^{-1}$. The subsequent formation of the compound II-like species was independent of H_2O_2 concentration, returning a first order rate constant of 4 s^{-1}. The slow return of the Fe^{III} enzyme was also H_2O_2 independent with a first-order rate constant of 0.13 s^{-1}.

Within the context of KatG catalysis, particularly in light of the robust catalase activity of the enzyme, these results are remarkable. In short, with catalase-active KatG it has been impossible to observe the compound I (i.e., Fe^{IV}=O[porphyrin]$^{\cdot+}$) or compound II-like (i.e., Fe^{IV}=O) states upon reaction with H_2O_2. With relatively low H_2O_2 concentrations (e.g., those utilized in Figure 3.4), the rate-determining step for catalatic turnover is Fe^{III} enzyme oxidation, so only the Fe^{III} form has been observed under these kinds of reaction conditions. When much higher concentrations of H_2O_2 are utilized (i.e., multiple hundreds of molar equivalents), a Fe^{III}-$O_2^{\cdot-}$-like state is observed and appears to be the form of enzyme that dominates during steady-state *catalatic* consumption of H_2O_2.

This heme state is distinct from the canonical Fe^{IV}=O[porphyrin]$^{\cdot+}$ and Fe^{IV}=O states observed in Figure 3.4. Interestingly, until now these intermediates have only been observable with KatG under one of two circumstances: 1) with variants that abrogate the enzyme's catalase activity (e.g., Y229F[37, 84] KatG, W107F[37, 38, 85] KatG, KatG$^{\Delta LL1}$, etc.,)[51, 84] or 2) when using a peroxide (e.g., peracetic acid [PAA]) that only supports oxidation of the Fe^{III} enzyme, but not the reduction of high valent heme states back to the Fe^{III} form.[44, 79, 86] Clearly *r*W321F KatG is catalase active (see Table 2.1) and these intermediates were detected upon reaction with H_2O_2

When the concentration of H_2O_2 reacted with *r*W321F KatG was increased to enable steady-state catalase turnover, the first heme state observed was the Fe^{IV}=O[porphyrin]$^{\cdot+}$ or compound I-like intermediate (1.2 – 50 ms) followed by a Fe^{IV}=O or compound II-like intermediate (~ 0.7 s) (Figure 3.5A). The spectra for these two species were nearly identical to those captured upon reaction with low H_2O_2 concentration (see Figure 3.4). However, instead of a return of the Fe^{III} state from compound II-like, a transition to a Fe^{III}-$O_2^{\cdot-}$ or compound III-like species was first observed as indicated by absorption bands at 418 nm (Soret), 542 nm (Q_{01}) and 578 nm (Q_{02}) (Figure 3.5). This transition occurred over a period of about 8 s. After the accumulation and persistence of the compound III-like state, the Fe^{III} form of *r*W321F KatG emerged slowly over the next minute of reaction time.

Here as well, this is a progression of heme states that has not been previously observed with KatG. Invariably, in previous investigations of catalase-active KatG (wild-type or variants), the Fe^{III}-$O_2^{\cdot-}$ or compound III-like state is the first observed species in stopped-flow experiments with these concentrations of H_2O_2. It is the state which

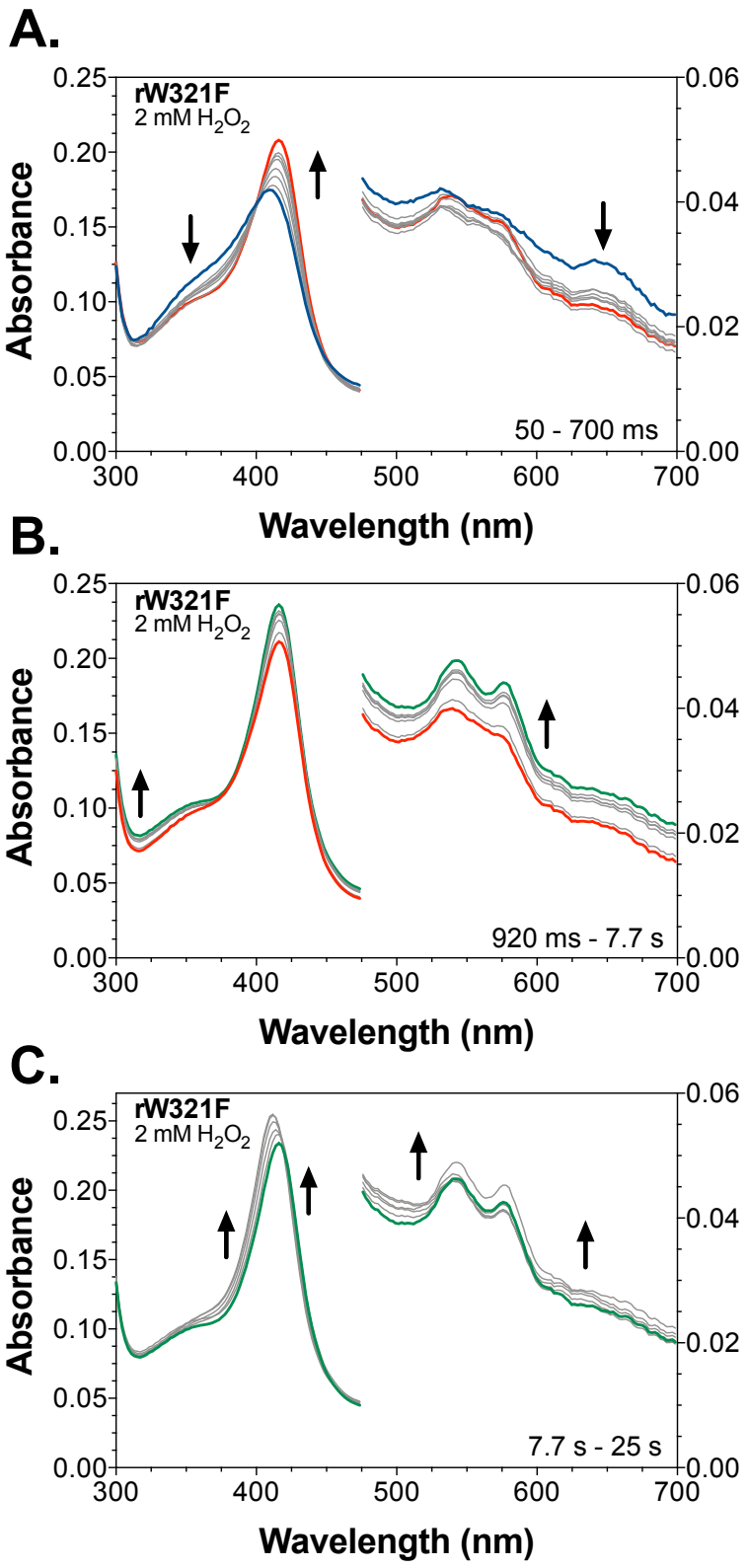

Figure 3.5. *r*W321F KatG heme states observed upon reaction with an H_2O_2 concentration supportive of steady-state catalase turnover. Reaction with 667 molar equivalents H_2O_2 (i.e, 2 mM) produced a compound I-like intermediate first which transitioned to a compound II-like state (A) which then converted to a compound III-like intermediate (B) before returning to the ferric state (C). All reactions were carried out at 4° C in 50 mM acetate, pH 5.0, using 3 μM KatG. Arrows indicate the direction of absorption changes.

dominates during steady-state catalase-based disposal of H_2O_2 by KatG. Indeed, this can be easily observed with *m*W321F KatG where a compound III-like state is detected 1.2 ms after mixing with 2 mM H_2O_2 (Figure 3.6A); this is the earliest possible time that species can be reliably detected in stopped-flow experiments. Upon H_2O_2 depletion the slow recovery of the Fe^{III} enzyme is observed (Figure 3.6B).[44, 79, 85, 87] The only other circumstance where the compound III-like state has been observed with KatG is with catalase-inactive variants (e.g., Y229F[37, 84] KatG, W107F[37, 38, 85] KatG, $KatG^{\Delta LL1}$, etc.) [51, 84] and it is an intermediate on the path to H_2O_2-dependent irreversible inactivation of the enzyme. In this way, catalase-inactive KatG becomes very much like its monofunctional peroxidase counterparts (e.g., HRP, CcP, etc.). Reaction of these enzymes with H_2O_2 in the absence of a PxED as a reducing substrate results in a rapid progression from Fe^{III} enzyme to compound I to compound II to compound III, where the last intermediate in that series is inactive.[19]

The results shown here with *r*W321F KatG demonstrates features of both reaction sequences. The progression of a compound I-like species to a compound II-like state to species like compound III observed for *r*W321F KatG is the typical path to inactivation for catalase-inactive peroxidases; however, following the accumulation of the compound III-like state, *r*W321F KatG depletes H_2O_2 as an active catalase enzyme would, enabling the eventual return of the Fe^{III} (i.e., resting) state. This series of intermediates is consistent with the *in situ* production of a catalase-active KatG (i.e., the steps concluding with the appearance of the compound III-like state) followed by the catalase-dependent depletion of the remaining H_2O_2 and return of the ferric enzyme. In this scenario, the steps leading up to the compound III-like state would coincide with the heme- and

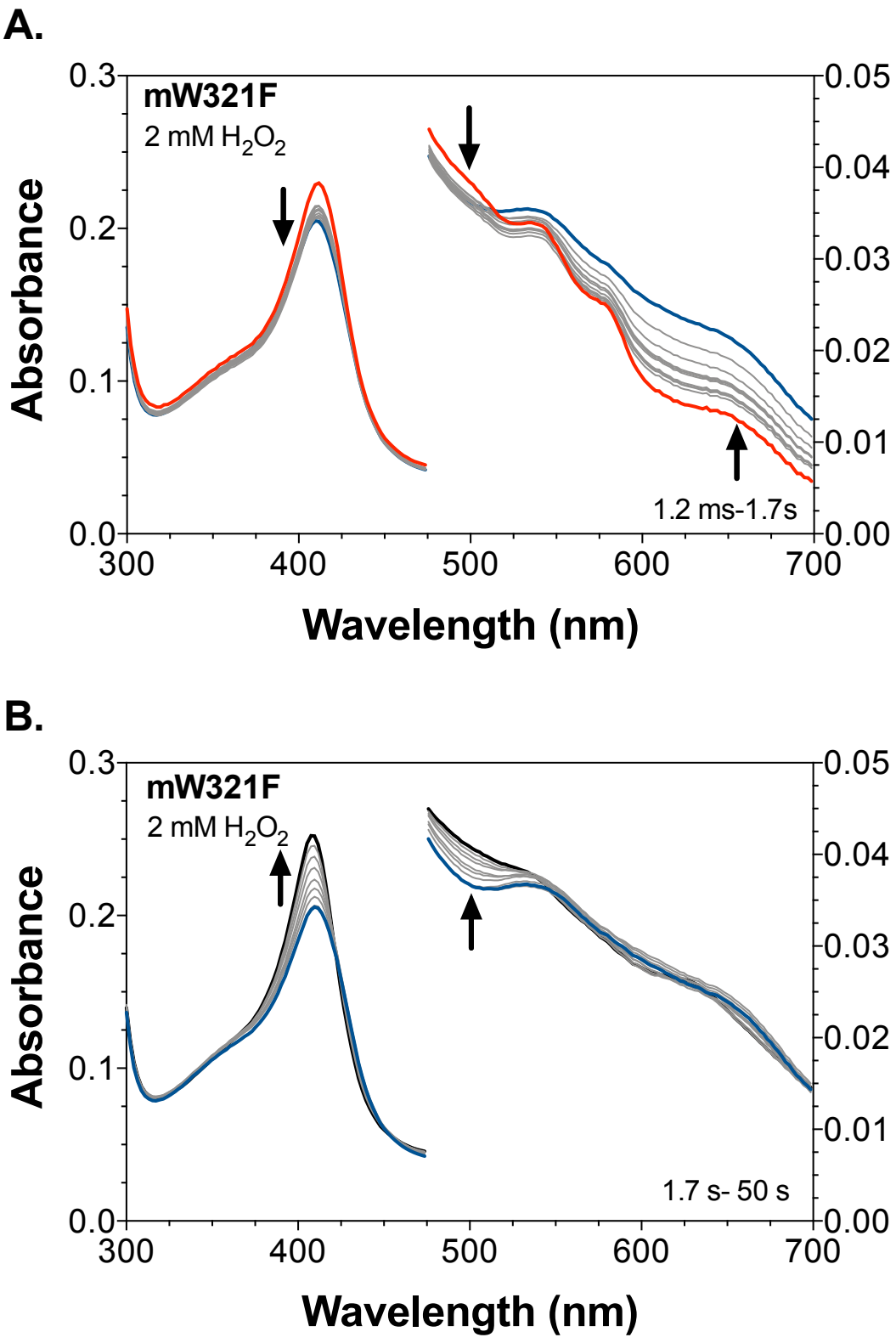

Figure 3.6. Optical spectra from reaction of *m*W321F KatG a steady-state supporting concentration of H_2O_2. Upon reaction with 2 mM H_2O_2 (667 molar equivalents), *m*W321F KatG advances from a compound II-like to a compound I-like intermediate (A) followed by the a return of the ferric state (B). All reactions were carried out at 4° C in 50 mM acetate, pH 5.0, using 3 μM KatG. Arrows indicate the direction of absorption changes.

peroxide-dependent establishment of KatG's unique MYW covalent adduct and protein-based cofactor.

To test this hypothesis, the effect of pretreatment of *r*W321F KatG with peracetic acid (PAA) on the progression of heme states in optical stopped-flow experiments was evaluated. Pre-establishing the MYW cofactor with PAA would be expected to produce a form of *r*W321F KatG that behaves like the mature enzyme, *m*W321F KatG, upon reaction with H_2O_2. As described above, reaction of untreated *r*W321F KatG with 5 molar equivalents H_2O_2 produces a rapid formation of the compound I-like (Fe^{IV}[porphyrin]$^{\cdot+}$) state as is evident from the substantial decrease in Soret band intensity at 407 nm (Figure 3.7A). Pretreatment of *r*W321F KatG with one, then two, then five molar equivalents of PAA progressively eliminated the accumulation of the compound I-like species (Figure 3.7A) consistent with a change in rate-determining step that would accompany the appearance of catalase activity. Similarly, pretreatment of *r*W321F KatG with five molar equivalents PAA produced an enzyme with a steady-state kinetic profile identical to that observed for *m*W321F KatG (Figure 3.6). Specifically, the first intermediate observed upon reaction with H_2O_2 was the compound III-like state which dominated during the steady-state disposal of H_2O_2. At the time of substrate (i.e., H_2O_2 depletion), a compound I-like state is observed (Figure 3.7B), after which the slow reemergence of the Fe^{III} enzyme occurs.

W412F KatG. Aside from W107, the tryptophan contributor to KatG's MYW protein-based cofactor, W412 is the next closest to the active site heme after the proximal tryptophan (W321) (see Figure 3.3). For comparison to the W321F variant, we evaluated the reactions of *r*W412F and *m*W412F KatG with H_2O_2 under limited-turnover (i.e., 1 –

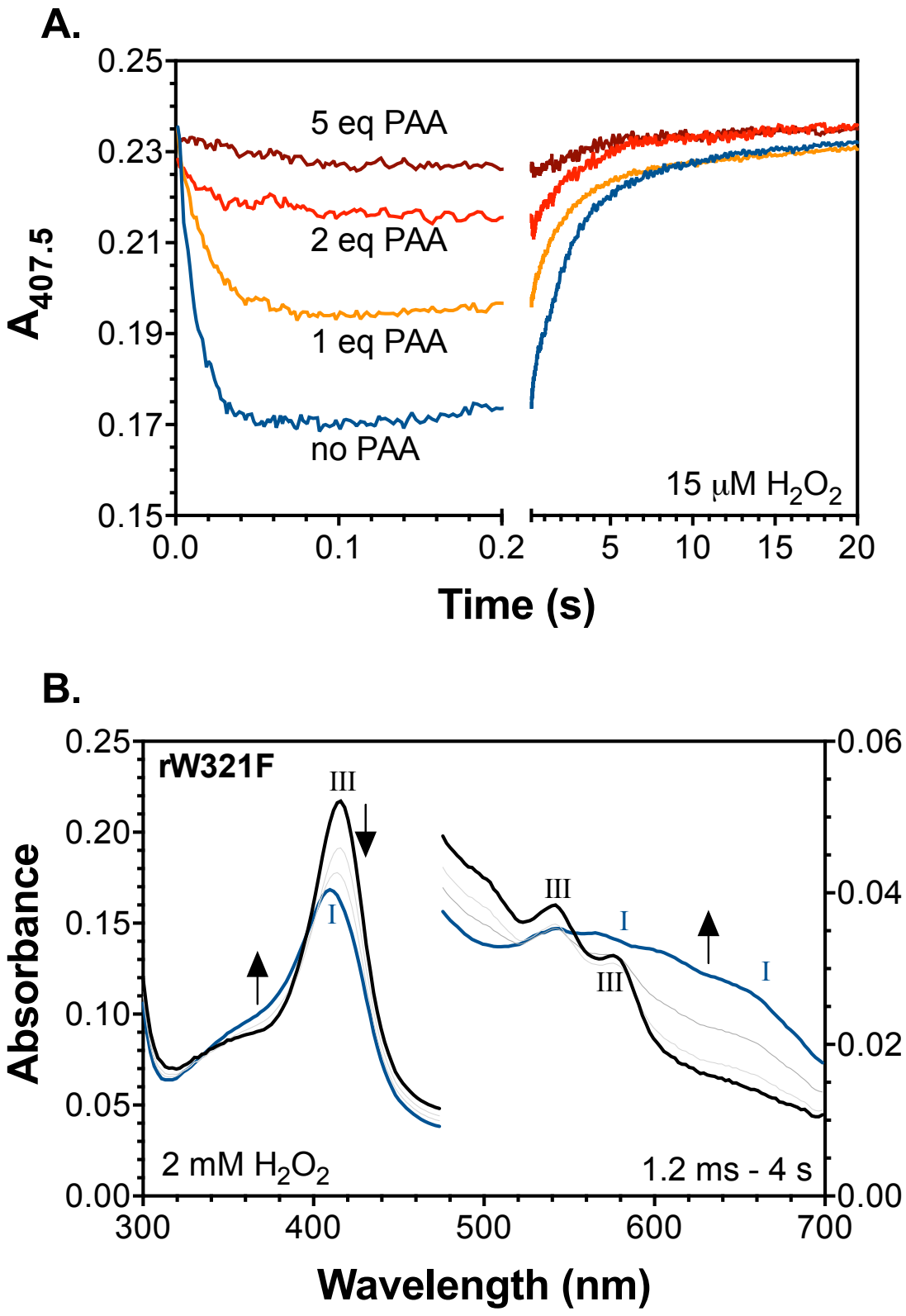

Figure 3.7. Effect of *r*W321F KatG pre-incubation with PAA on heme states observed during subsequent reactions with H_2O_2. Following pre-reaction of *r*W321F KatG with the concentrations of PAA indicated, the enzyme was reacted with 5 molar equivalents H_2O_2 and each reaction was monitored at 407 nm (A). Similarly, *r*W321F KatG was pre-treated with 5 molar equivalents PAA followed by a steady-state-supporting concentration of H_2O_2 (2 mM) (B). All reactions were carried out at 4° C in 50 mM acetate, pH 5.0, using 3 μM KatG. Arrows indicate the direction of absorption changes.

10 molar equivalents) and steady-state (i.e., > 300 molar equivalents) conditions. Upon reaction with limited-turnover concentrations of H_2O_2 (e.g., 5 molar eq.), *r*W412F rapidly converted from its Fe^{III} state (λ_{max} 407, 505, and 640 nm) to a clear compound II-like (Fe^{IV}=O) intermediate (λ_{max} 418, 530, and 560 nm) within 84 ms (Figure 3.8A). This was followed by the slow conversion of *r*W412F KatG back to its Fe^{III} state (Figure 3.8B). Interestingly, this return to the Fe^{III} state was accompanied by an increase in absorption near 310 nm consistent with the features of the MYW adduct and/or its covalent precursors (e.g., YW and YW quinoid).[34] It is also noteworthy that no compound I-like heme state was detected prior to the formation of the compound II-like intermediate. This is in stark contrast to the behavior of *r*W321F KatG. The effect of H_2O_2 concentration on the rate of each of the two observed reactions of *r*W412F KatG was evaluated (Figure 3.8C). The k_{obs} initial formation of the compound II-like state was linearly dependent on H_2O_2 concentration, returning a second-order rate constant of 2.9×10^6 $M^{-1}s^{-1}$. This was highly similar to the rate constant for the formation of the compound I-like species observed for *r*W321F KatG (see Figure 3.4D). The second reaction observed under limited-turnover conditions was independent of H_2O_2 concentration, returning a first-order rate constant of about 0.22 s^{-1}. Both the spectral features observed during this second reaction as well as its apparent rate constant indicated that it was same re-emergence of the Fe^{III} enzyme from the compound II-like state as was observed for *r*W321F KatG. Thus, for *r*W412F KatG the formation of compound I and its conversion to compound II-like state are not observed, again, in contrast to *r*W321F KatG. This indicates one of two possibilities: 1) Formation of compound I does not occur at all with *r*W412F KatG (i.e., there is a direct conversion of the Fe^{III} enzyme to a Fe^{IV}=O state), or

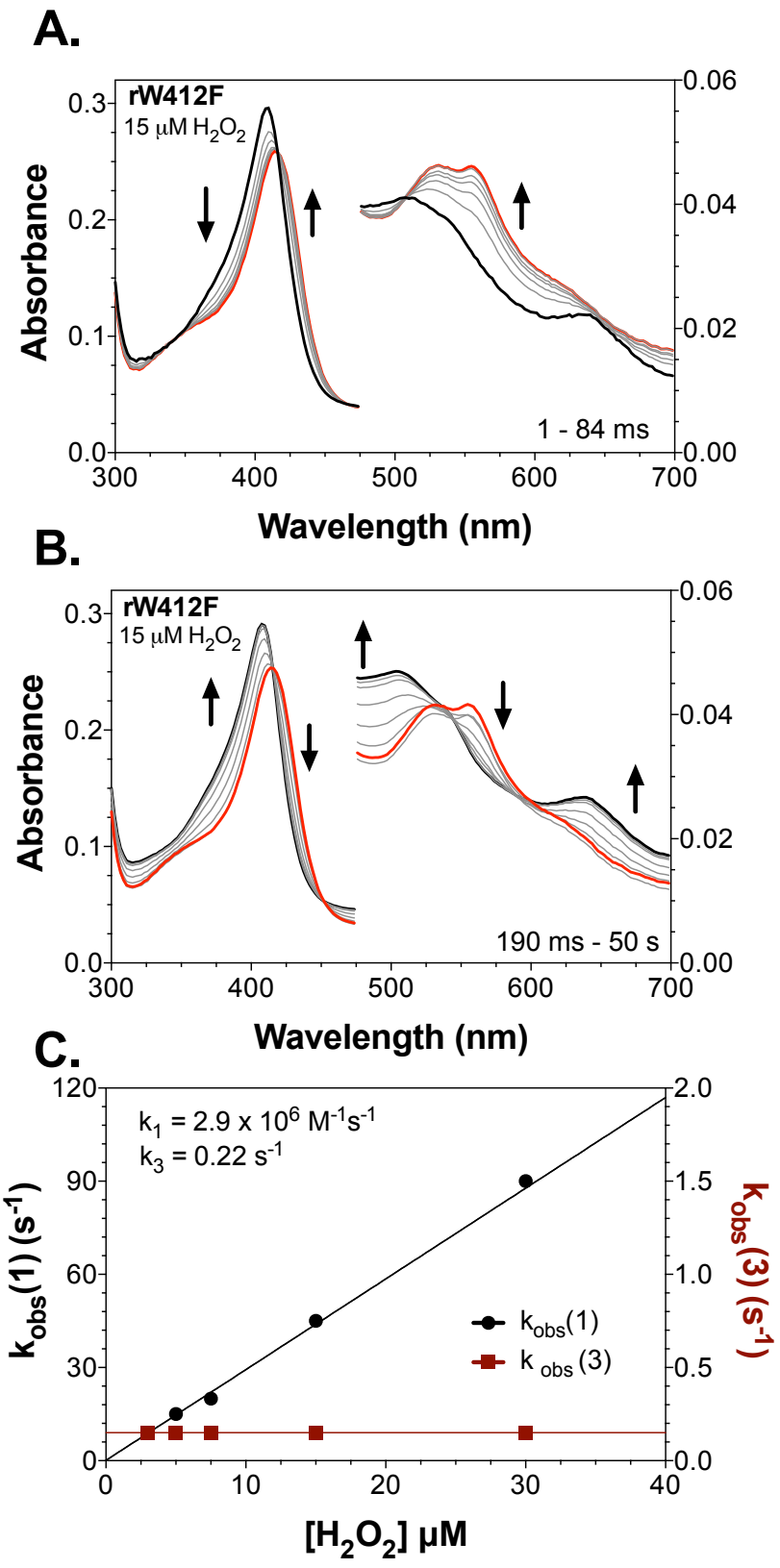

Figure 3.8. Optical spectra and estimated rate constants for *r*W412F KatG reaction with limited-turnover concentrations of H_2O_2. Mixing of 15 μM H_2O_2 (5 eq.) with *r*W412F KatG by stopped-flow produces the conversion of ferric enzyme to a compound II-like state within 84 ms (A). This is followed by the return to the ferric state over the next 50 s (B). The effect of H_2O_2 concentration on reaction rates enabled estimation of a rate constant for each transition (C). All reactions were carried out at 4° C in 50 mM acetate, pH 5.0, using 3 μM KatG. Arrows indicate the direction of absorption changes.

2) the reduction of the compound I-like intermediate is so rapid relative to its formation, that it does not accumulate to any appreciable level. Although there is some precedent for each of these possibilities in heme protein reactivity, the peroxidase active site on which KatG is based leans much more heavily to the latter.[88] The former is most often observed with homolytic scission of the peroxide O-O bond, which is not often observed with peroxidases.[88, 89] The latter is observed with heterolytic scission of the O-O bond followed by very rapid intramolecular electron transfer to reduce the $[porphyrin]^{\cdot+}$ at the expense of a nearby oxidizable aromatic amino acid. The classic example of this is the formation of the so-called compound ES in cytochrome *c* peroxidase (CcP), a $Fe^{IV}=O[^{Px}Trp]^{\cdot+}$ state.[49, 50] Our observation that a compound I-like state accumulates in a KatG variant missing its proximal tryptophan (i.e., W321F KatG) aligns well with the latter explanation. The slow rate constants we observe for W321F, and W412F are not for compound III-like state formation, but rather, what is happening in those slow reactions when the concentrations of H_2O_2 are really low is the return of the ferric enzyme.

As with *r*W321F KatG, we also reacted *r*W412F KatG with concentrations of H_2O_2 able to sustain steady-state catalase turnover (e.g., 667 molar equivalents) should the enzyme be capable of doing so. The first heme state observed under these conditions (1.2 ms after mixing) was a compound II-like form (i.e., $Fe^{IV}=O$) with absorption maxima at 420, 535, and 560 nm. Over a period of about 10 s, the initial compound II state converted to a compound III-like (i.e., $Fe^{III}\text{-}O_2^{\cdot-}$) state ($\lambda_{max}$ 418, 540, 578 nm) (Figure 3.9A). Concomitant with these changes, an increase in absorbance near 310 nm was also detected. Here again, this is consistent with the features of the MYW adduct and/or its covalent precursors (e.g., YW and YW quinoid).[34] This would suggest that the

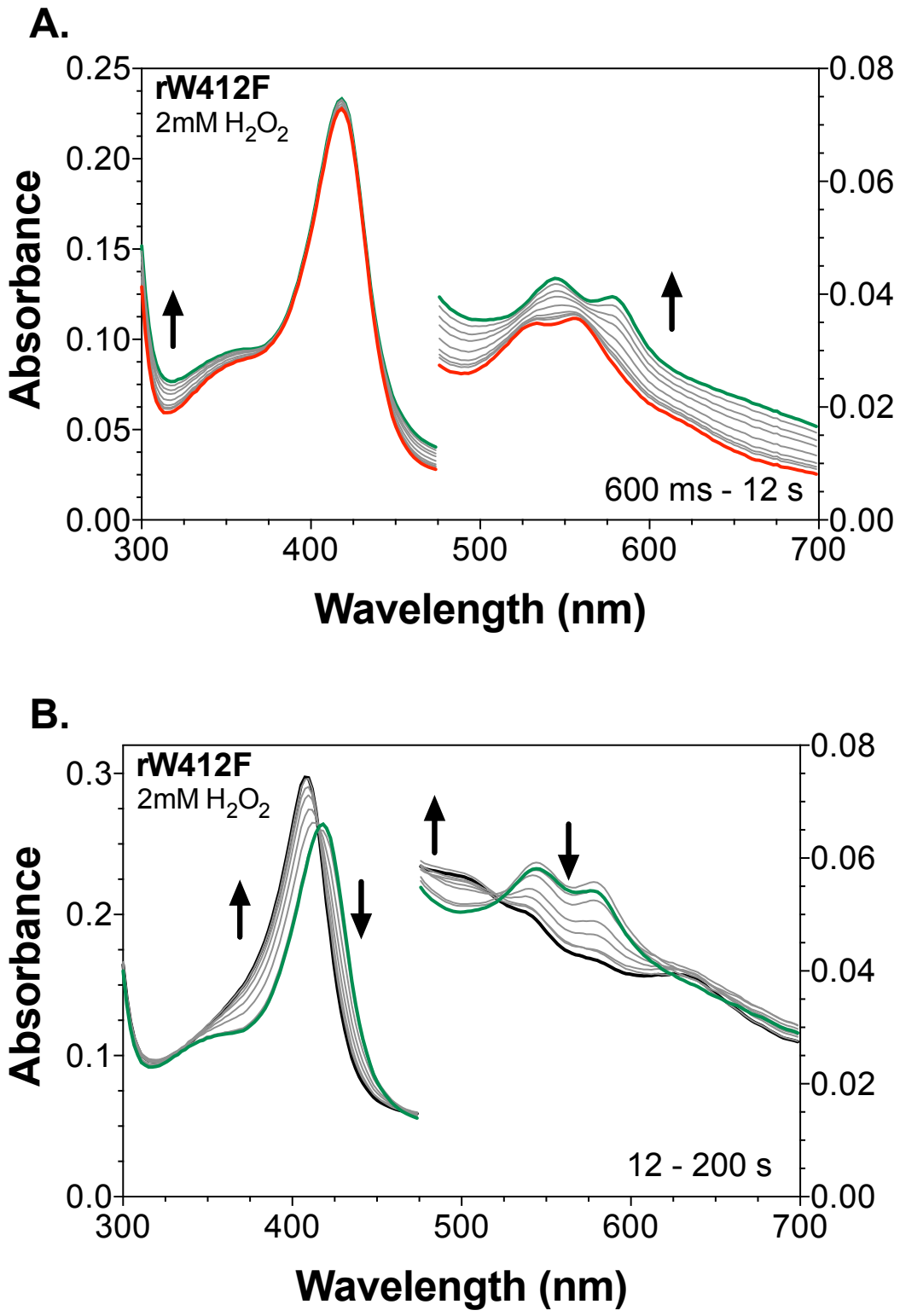

Figure 3.9. *r*W412F KatG heme states observed upon reaction with an H_2O_2 concentration supportive of steady-state catalase turnover. Reaction with 667 molar equivalents H_2O_2 (i.e, 2 mM) produced a compound II-like intermediate first which transitioned to a compound III-like state (A) before returning to the ferric state (B). All reactions were carried out at 4° C in 50 mM acetate, pH 5.0, using 3 µM KatG. Arrows indicate the direction of absorption changes.

emergence of the steady-state intermediate which dominates during KatG-based catalase turnover (i.e., Fe^{III}-$O_2^{\cdot-}$) coincides with putative formation of the MYW cofactor. As observed for *r*W321F KatG, following the appearance and steady-state persistence of the Fe^{III}-$O_2^{\cdot-}$ state, the Fe^{III} form of the enzyme slowly reemerged following the depletion of H_2O_2 (Figure 3.9B).

In contrast to its reconstituted form, reaction of *m*W412F KatG with limited-turnover concentrations of H_2O_2 showed little if any shift from the starting Fe^{III} state (Figure 3.10A), suggesting that the enzyme's robust catalase activity depleted this low concentration of H_2O_2 within the stopped-flow dead time. Reaction of *m*W412F KatG with enough H_2O_2 to support steady-state turnover showed a compound III-like state at the earliest possible time of detection (1.2 ms) with no preceding compound II-like intermediate. Upon H_2O_2 depletion, the Fe^{III} form of the enzyme reemerged (Figure 3.10B).

Evaluations of reaction time courses at 401 nm (tracking the Fe^{III} enzyme) and 315 (tracking putative MYW adduct formation) were instructive. Across the board, reconstituted (*r*) forms of KatG showed a delay in the return of the Fe^{III} state that the mature (*m*) forms do not. The W412F KatG variant is one example (Figure 3.11A). From the standpoint of kinetic competence, events corresponding to MYW cofactor formation would have to fit entirely within the delay unique to the reconstituted form of the enzyme. This is exactly what is observed when *r*W412F KatG's reaction with H_2O_2 is monitored at 315 nm. The early increase in absorption at that wavelength was completed well before absorption at 401 nm increases corresponding to the depletion of H_2O_2 and the return of the enzyme's Fe^{III} state (Figure 3.11B). It is also notable that once 315 nm

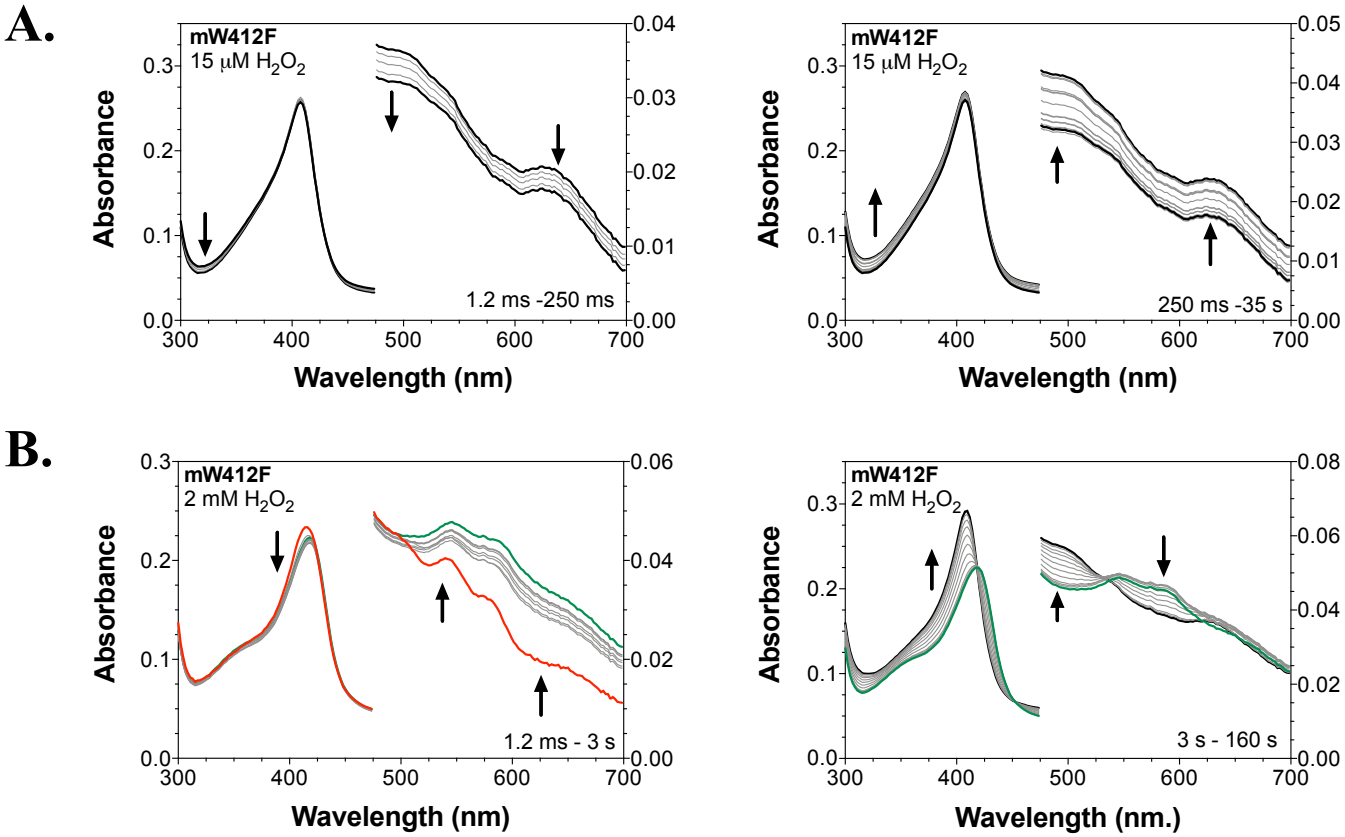

Figure 3.10. Stopped-Flow spectroscopy of *m*W412F KatG reacted with low and high H_2O_2. 15 μM H_2O_2 *m*W412F KatG does not have enough H_2O_2 to turn over past the ferric enzyme, or the H_2O_2 is consumed in the dead time of the instrument (A). 2 mM H_2O_2 *m*W412F KatG advances from Compound II-to Compound III-like, then a return to the ferric state (B). All reactions have been carried out using 3 μM KatG in 50 mM acetate, pH 5.0 at 4° C.

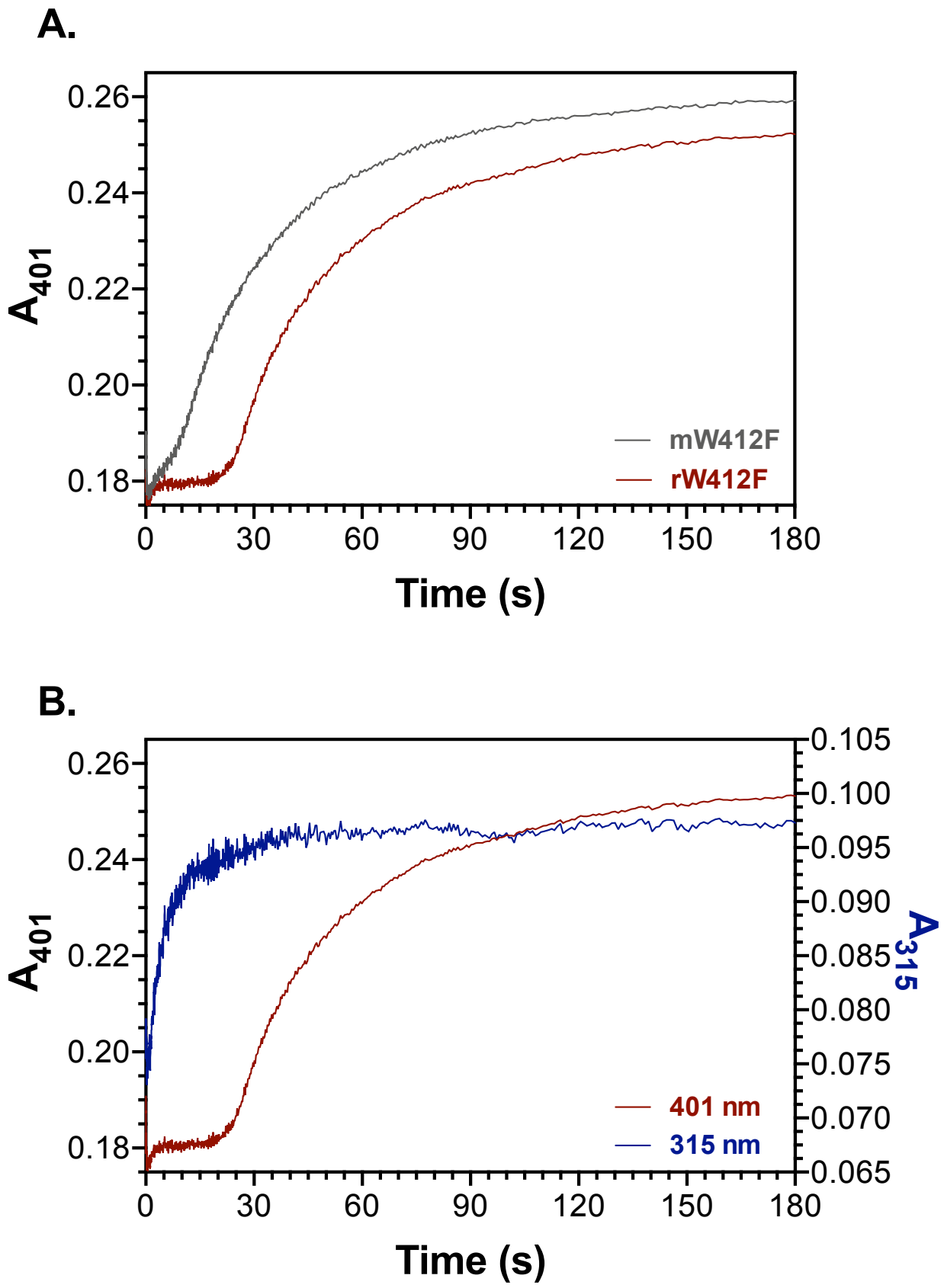

Figure 3.11 Stopped-Flow spectroscopy of *r*W412F KatG absorbance changes. 2 mM H_2O_2 *r*W412F and *m*W412F KatG return to the ferric enzyme (A). Change in absorbance at 401 nm and 315nm (B). All reactions have been carried out using 3 µM KatG in 50 mM acetate, pH 5.0 at 4° C.

absorption increases early in the reaction, it never decreases again, even as the Fe^{III} state returns. This is consistent with the irreversible nature of MYW cofactor formation.

Under this reaction system, following mixing with H_2O_2 two events would need to occur before the enzyme's resting (i.e., Fe^{III}) state would return: 1) The MYW adduct which supports catalase activity must form, and then, 2) the newly created catalase activity must consume the balance of H_2O_2 remaining in the reaction. Thus, increasing the concentration of H_2O_2 would be expected to extend the latter contribution but not the former. This is exactly what we observed. Reaction of *r*W412F KatG with increasing concentrations of H_2O_2 increases the time necessary for catalase-based consumption of the substrate, and therefore, the subsequent return of the resting enzyme (Figure 3.12A). In contrast, the establishment of the MYW adduct monitored at 315 nm is unchanged (Figure 3.12B).

W91F KatG. As with W321 and W412, W91 appears to be part of a network of oxidizable aromatic amino acids within the KatG N-terminal domain, which includes W90, Y98, and W149, within this group W91 is closest to the heme center. It is more distant from the heme iron (15.3 Å) than the active site representatives of the two other networks, W321 (6.8 Å) and W412 (11.5 Å). Nevertheless, there is evidence from studies on other KatG enzymes that the analogous residue, W106 in *Synechocystis* P6803 KatG[46, 51] and W95 in *Burkholderia pseudomallei* KatG[51, 86], is a point of protein oxidation. In the case of this tryptophan, its participation through-protein electron transfer may be facilitated by an H_2O-based H-bonded network that connects the W91 indole NH to the propionate chains of the heme cofactor.

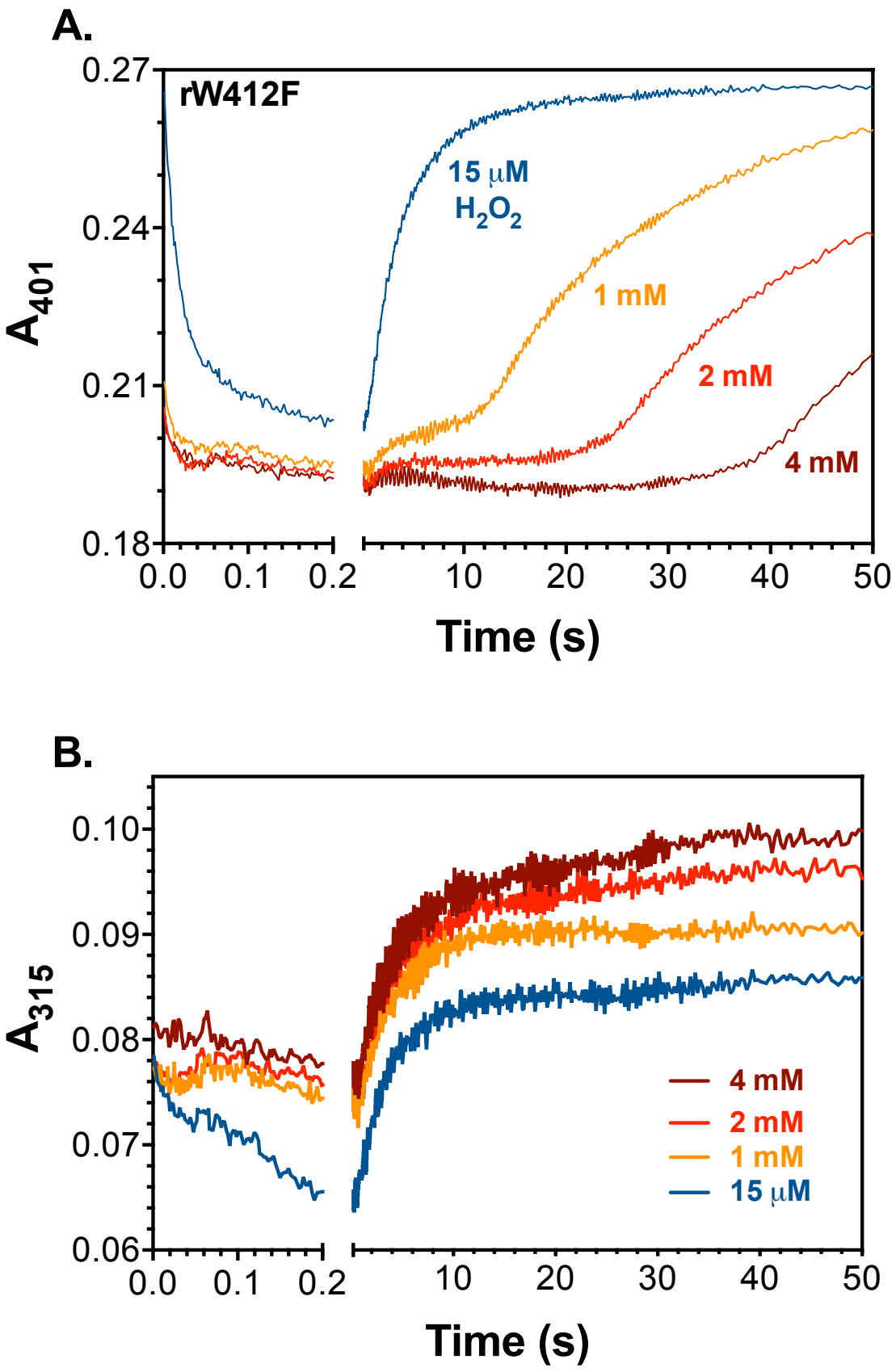

Figure 3.12 Stopped-Flow spectroscopy of *r*W412F KatG reacted with varying H_2O_2. Change in absorbance at 401 nm (A) change in absorbance at 315 (B). All reactions have been carried out using 3 μM KatG in 50 mM acetate, pH 5.0 at 4° C.

Reaction of *r*W91F KatG with limited-turnover concentrations of H_2O_2 (e.g., 5 molar equivalents) produced nearly identical results as observed for *r*W412F KatG (Figure 3.13). Specifically, there was a rapid (i.e., < 200 ms) and apparent direct conversion of the Fe^{III} enzyme to a compound II-like (Fe^{IV}=O) intermediate (Figure 3.13A). This was followed by a slow (i.e., > 60 s) reversion of the compound II-like state back to the Fe^{III} enzyme (Figure 3.13B). The rate of the first reaction was directly proportional to H_2O_2 concentration, and the second reaction was H_2O_2 concentration independent (Figure 3.13C). The second-order rate constant (k_1) estimated for the first reaction was 2.8×10^6 M^{-1} s^{-1}, and first-order rate constant (k_3) estimated for the second reaction was 0.17 s^{-1}. In both cases, these rate constants were highly similar to those observed for the analogous reactions of W412F KatG (see Figure 3.8C).

When concentrations of H_2O_2 able to support steady-state catalase activity were applied, the first *r*W91F heme state observed was a Fe^{IV}=O (i.e., compound II-like) intermediate. Over several seconds, this Fe^{IV}=O state converted to a compound III-like or Fe^{III}-$O_2^{\cdot -}$ form (Figure 3.14A) that typifies KatG performing catalase-based H_2O_2 degradation under steady-state conditions. Once *r*W91F KatG was able to deplete H_2O_2, the Fe^{III} (i.e., resting) state of the enzyme slowly returned (Figure 3.14B). Consistent with the other reconstituted variant preparations, the conversion of *r*W91F Fe^{IV}=O to the steady-state Fe^{III}-$O_2^{\cdot -}$ form coincided with an irreversible increase in absorbance around 315 nm (Figure 3.14A) as would be expected for the formation of the MYW adduct and/or one of its covalent precursors.

As observed with rW412F, the duration of *r*W91F KatG steady-state catalatic consumption of H_2O_2 (as monitored by the Fe^{III} state at 401 nm) (Figure 3.15A and B)

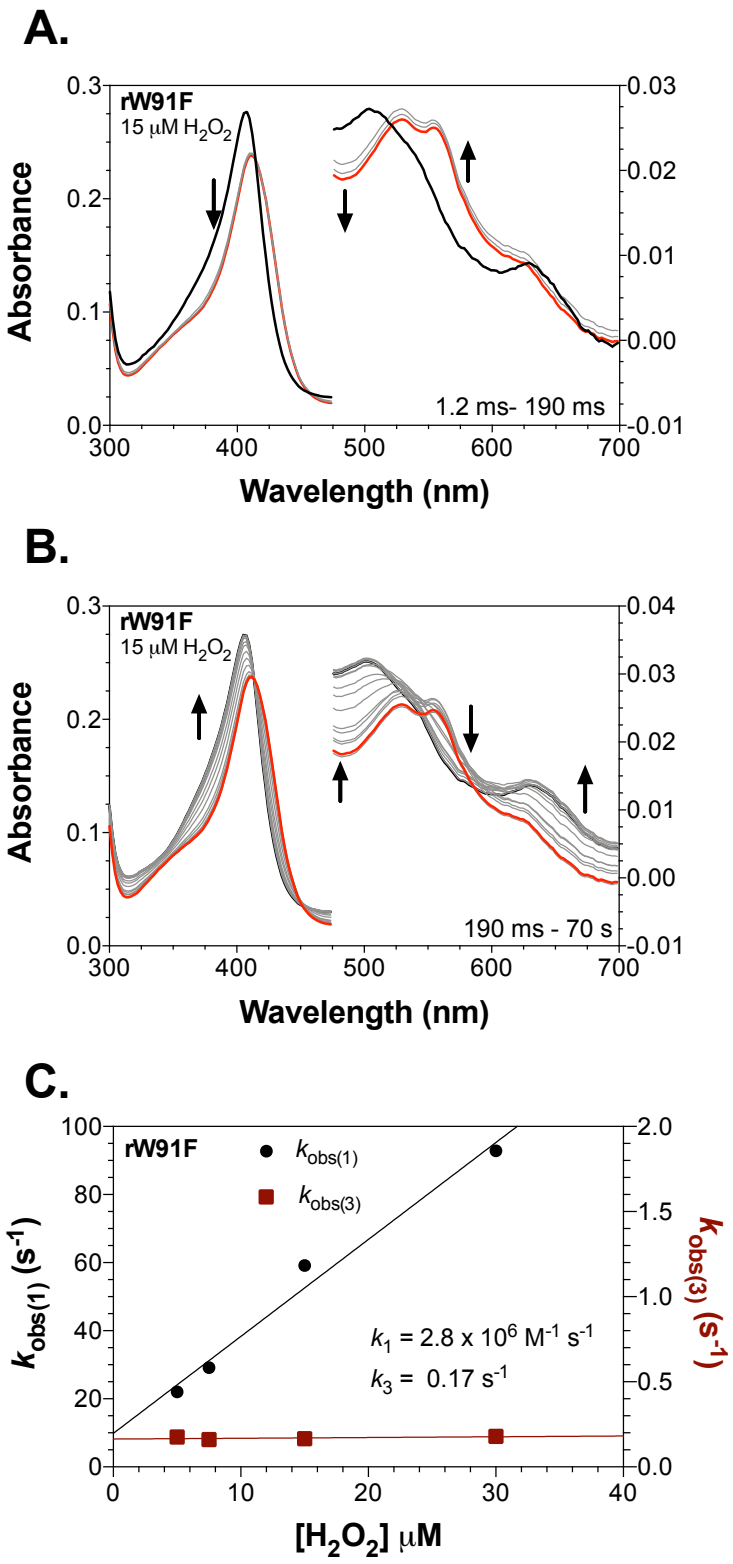

Figure 3.13. Optical spectra and estimated rate constants for *r*W91F KatG reaction with limited-turnover concentrations of H_2O_2. Mixing of 15 μM H_2O_2 (5 eq.) with *r*W91F KatG by stopped-flow produces the conversion of ferric enzyme to a compound II-like state within 190 ms (A). This is followed by the return to the ferric state over the next 70 s (B). The effect of H_2O_2 concentration on reaction rates enabled estimation of a rate constant for each transition (C). All reactions were carried out at 4° C in 50 mM acetate, pH 5.0, using 3 μM KatG. Arrows indicate the direction of absorption changes.

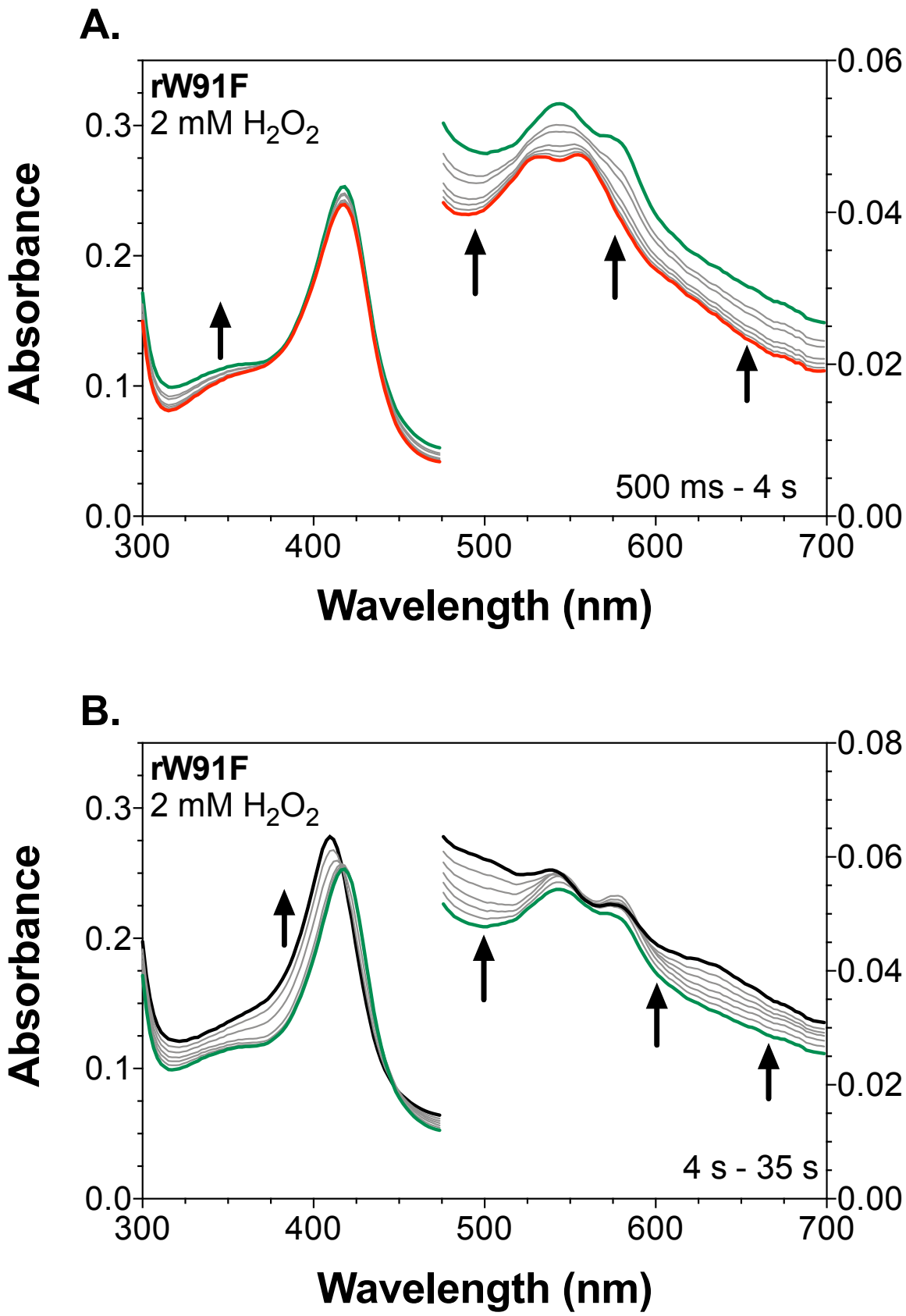

Figure 3.14. *r*W91F KatG heme states observed upon reaction with an H_2O_2 concentration supportive of steady-state catalase turnover. Reaction with 667 molar equivalents H_2O_2 (i.e, 2 mM) produced a compound II-like intermediate first which transitioned to a compound III-like state (A) before returning to the ferric state (B). All reactions were carried out at 4° C in 50 mM acetate, pH 5.0, using 3 μM KatG. Arrows indicate the direction of absorption changes.

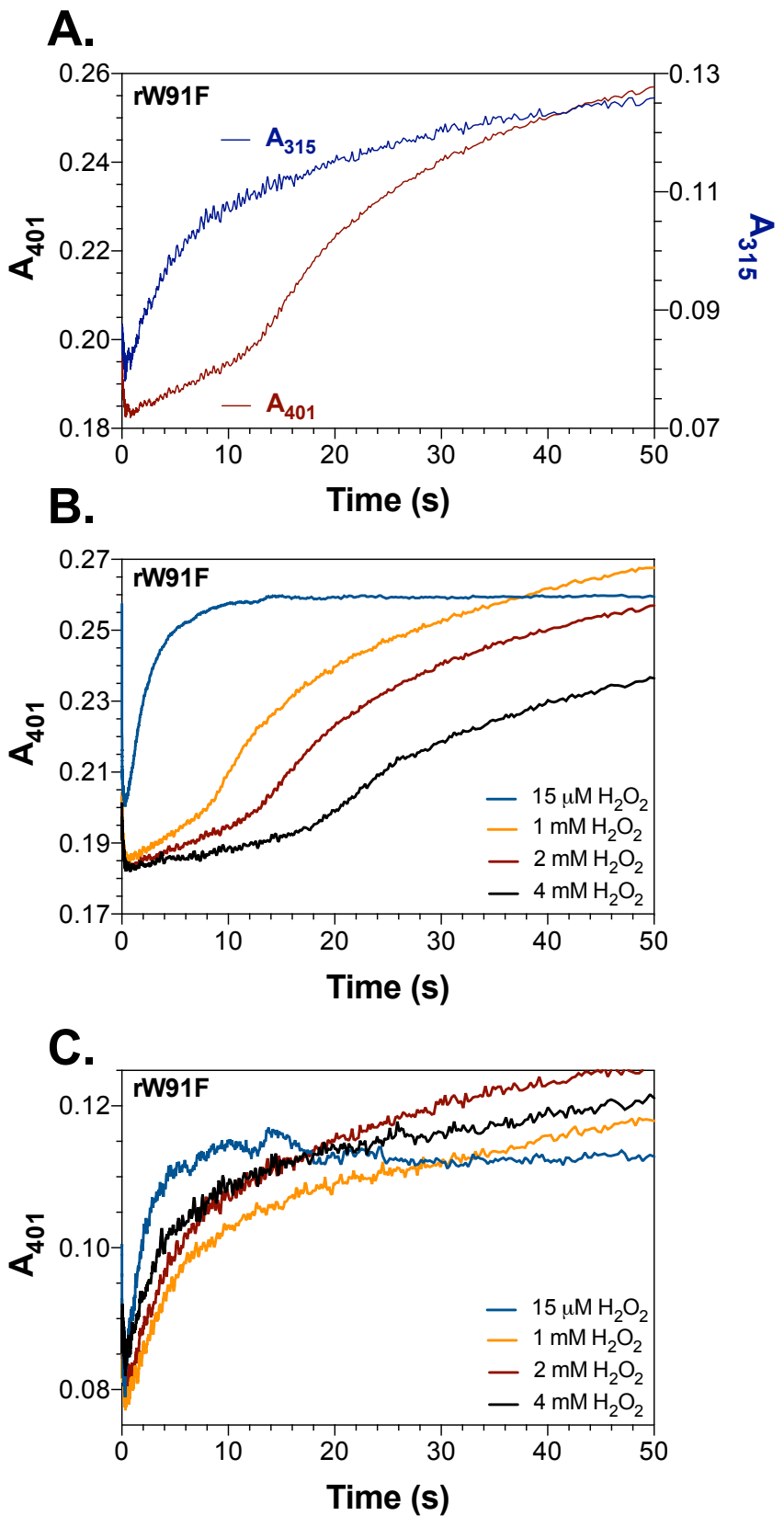

Figure 3.15 Stopped-Flow spectroscopy of *r*W91F KatG reacted with varying H_2O_2. Change in absorbance at 401 nm and 315 nm (A) change in absorbance at 401 (B) change in absorbance at 315 nm. All reactions have been carried out using 3 μM KatG in 50 mM acetate, pH 5.0 at 4° C.

and the establishment of the MYW covalent cofactor (as monitored at 315 nm) (Figure 3.15A and C) were distinct. The latter always concluded prior to the former, and the latter was largely independent of H_2O_2 concentration whereas the former increased with increasing H_2O_2 concentration. As we observed for the other variants, reaction of *m*W91F KatG with limited-turnover concentrations of H_2O_2 produced no discernable changes in optical spectra (Figure 3.16A). The Fe^{III} state remained the dominant heme state. Reaction of the *m*W91F variant with a concentration of H_2O_2 able to support steady-state catalytic turnover generated a Fe^{III}-$O_2^{\cdot-}$-like state as has been detected with the other variants. However, broad increases in absorption across the spectrum were indicative of protein aggregation. These were some of the first indications that KatG lacking an oxidizable Trp at this position was compromised in its capacity to sustain catalatic H_2O_2 decomposition.

Y413F KatG. Of all the Phe-substitution variants generated and evaluated for this work, the Y413F enzyme uniquely targets a second-sphere oxidizable residue. The W412F variant removes the oxidizable aromatic amino acid closest to the active site heme in this network. Though Y413 immediately follows W412 in sequence, the side chains of the two residues are oriented in roughly opposite directions with the indole side chain of W412 pointed toward the heme buried in the interior active site and the phenolic side chain of Y413 making contact with the solvent-accessible surface.

Reaction of *r*Y413F KatG with 5 molar equivalents H_2O_2 (i.e., limited-turnover conditions) produced nearly identical spectra as observed for *r*W412F and rW91F KatG (Figure 3.17). Upon reaction with 7.5 μM H_2O_2, the Fe^{III} enzyme was converted in less than 40 ms to an intermediate resembling a canonical Fe^{IV}=O heme state (Figure 3.17A).

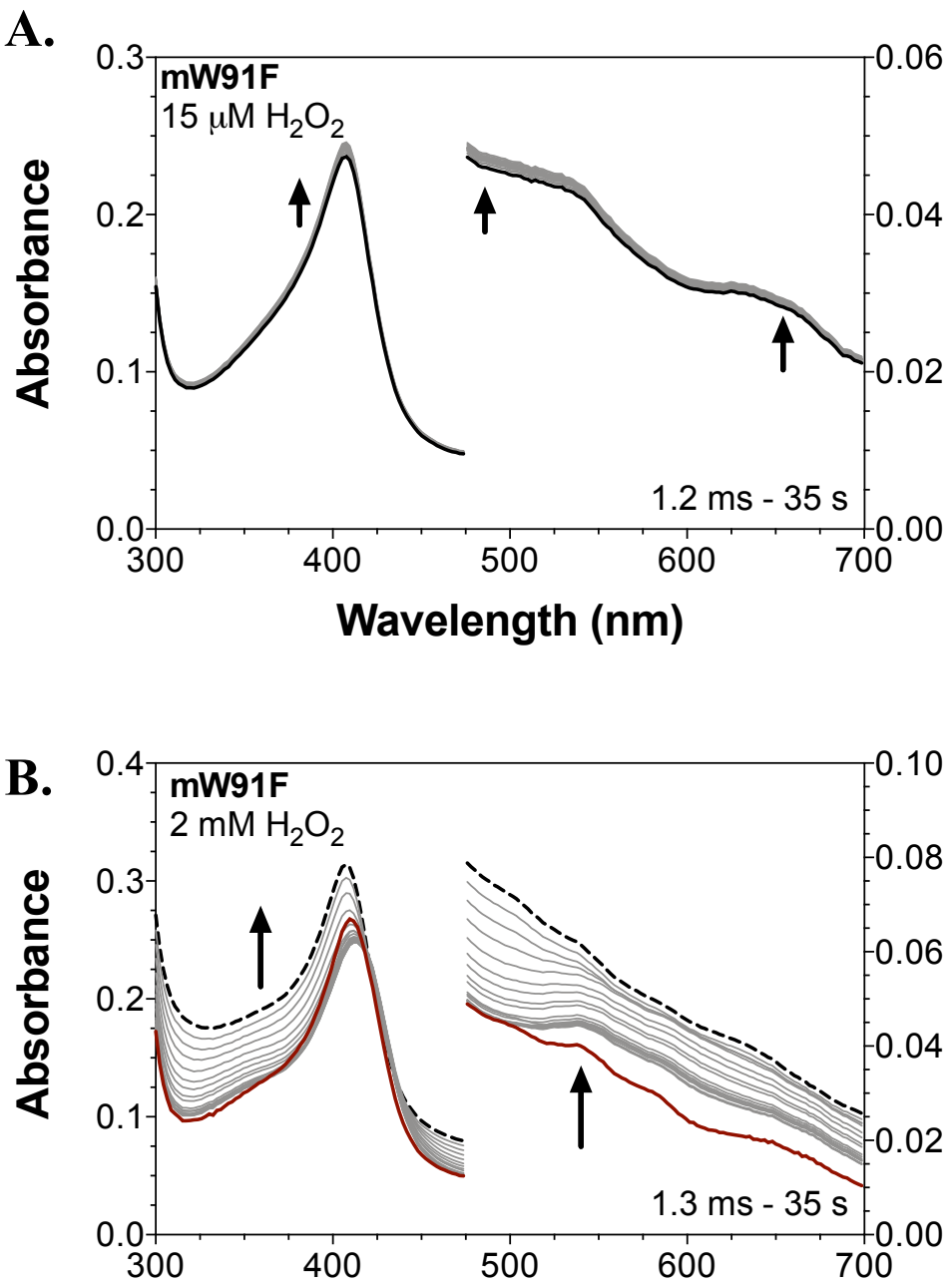

Figure 3.16. Stopped-Flow spectroscopy of *m*W91F KatG reacted with low and high H_2O_2. 15 μM H_2O_2 *m*W491F KatG does not have enough H_2O_2 to turn over past the ferric enzyme, or the H_2O_2 is consumed in the dead time of the instrument (A). 2 mM H_2O_2 *m*W91F KatG advances from Compound II-to a return to the ferric state with light scatter (B). All reactions have been carried out using 3 μM KatG in 50 mM acetate, pH 5.0 at 4° C.

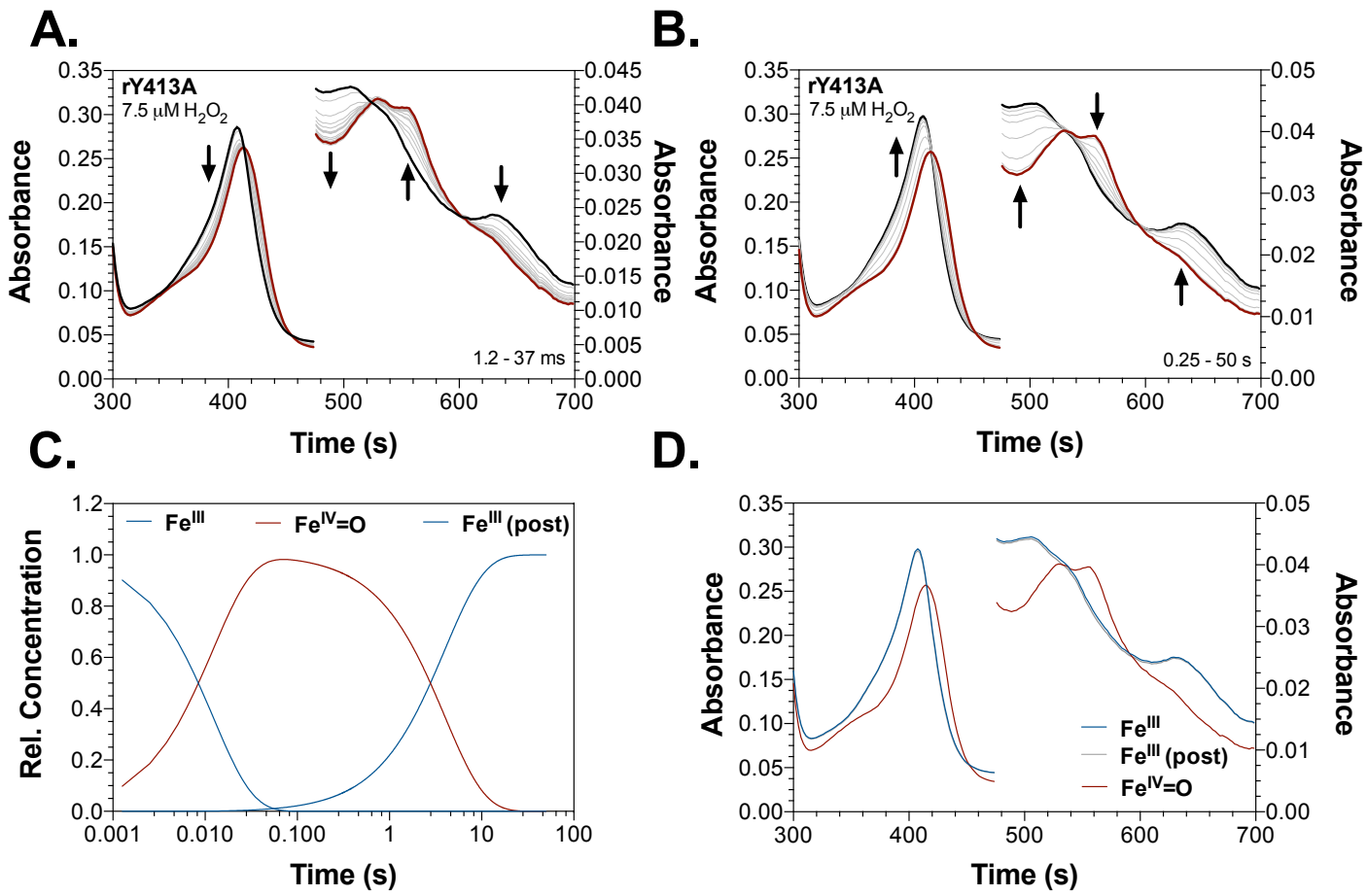

Figure 3.17. Stopped-Flow spectroscopy of *r*Y413F KatG reacted with low [H_2O_2]. 15 μM H_2O_2 *r*Y413F KatG advances from ferric enzyme to Compound II-like state (A), then a return to the ferric state (B). Concentration profile (C) predicted spectra (D) All reactions have been carried out using 3 μM KatG in 50 mM acetate, pH 5.0 at 4° C.

This was followed by a slow (i.e., 50 s) reversion of the compound II-like state back to the Fe^{III} enzyme (Figure 3.17B). Interestingly, the initial reaction of *r*Y413F KatG was appreciably faster than the analogous reactions observed for *r*W321F, *r*W412F, or *r*W91F KatG. As a result, a sufficient H_2O_2 concentration range could not be utilized to determine an accurate value for the second-order rate constant. Global analysis of this single reaction of *r*Y413F KatG with 7.5 mM H_2O_2 was best fit by two rate constants describing the sequential reactions of two species (Figure 3.17C and 3.17D). A value of 81 s^{-1} was obtained for the first and 0.27 s^{-1} for the second. The initial reaction rate was clearly H_2O_2 concentration-dependent, and we estimated that the second order rate constant is about 8×10^6 $M^{-1}s^{-1}$

When H_2O_2 concentrations were sufficient to support steady-state catalase activity (e.g., > 300 molar equivalents), the first *r*Y413F heme state detected was the Fe^{IV}=O enzyme (Figure 3.18A). In this respect, Y413F KatG displayed the same behavior as the W412F variant. Over several seconds, this Fe^{IV}=O state converted the KatG catalase steady-state Fe^{III}-$O_2^{\cdot -}$ form (Figure 3.18A). Once *r*Y413F KatG completed the *catalatic* consumption H_2O_2, the resting (Fe^{III}) state of the enzyme slowly returned (Figure 3.18B). Consistent with all of the other reconstituted variant preparations (*r*W321F, *r*W412F, and *r*W91F), the conversion of the *r*Y413F Fe^{IV}=O intermediate to its steady-state Fe^{III}-$O_2^{\cdot -}$ intermediate coincided with an irreversible increase in absorbance around 310 nm (Figures 3.18A and 3.19A) as would be expected for the formation of the MYW adduct and/or one of its covalent precursors.

As observed with rW412F and *r*W91F KatG the rate of establishment of the MYW covalent cofactor (as monitored at 315 nm) was H_2O_2 concentration independent

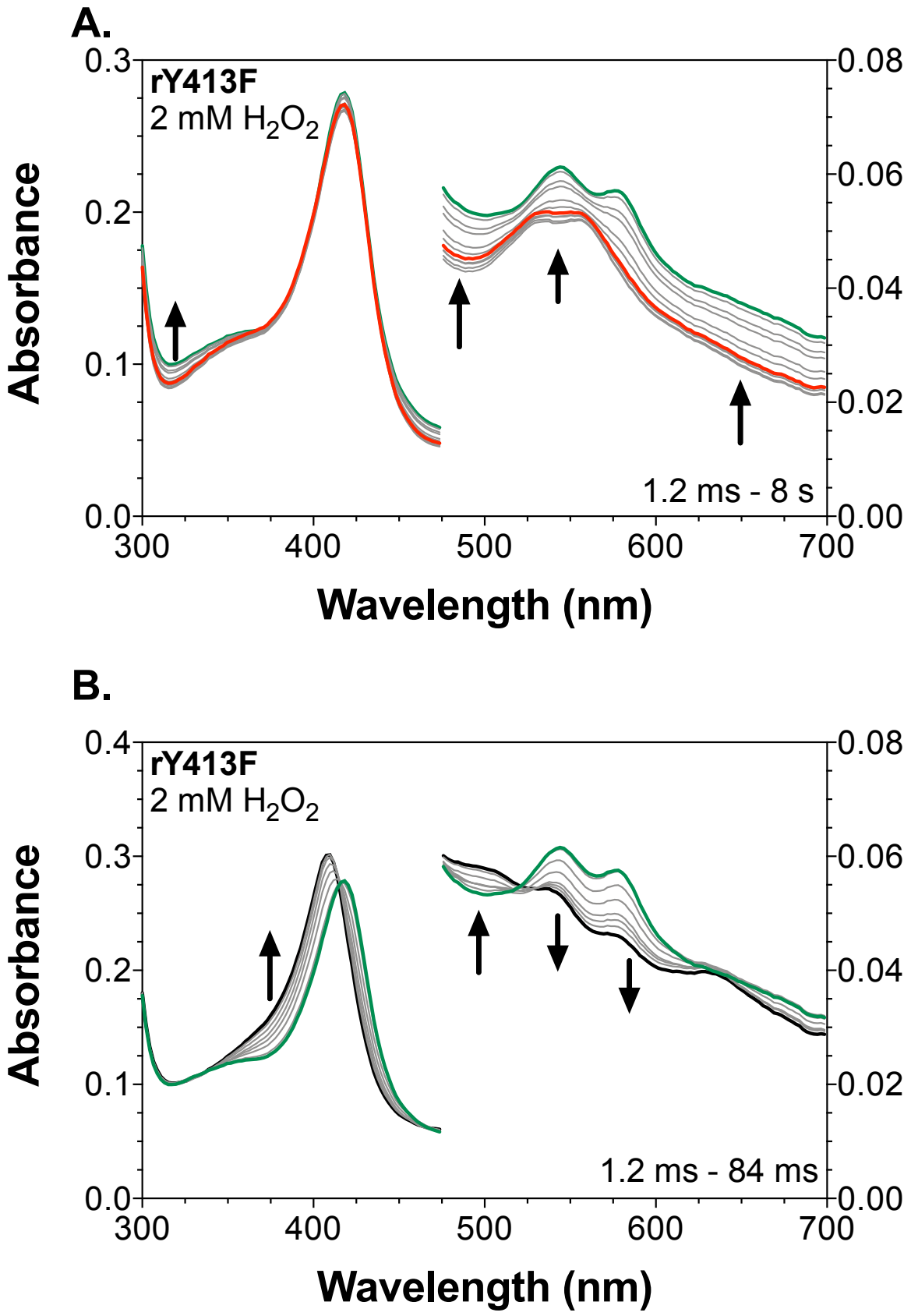

Figure 3.18. *r*Y413F KatG heme states observed upon reaction with an H_2O_2 concentration supportive of steady-state catalase turnover. Reaction with 667 molar equivalents H_2O_2 (i.e, 2 mM) produced a compound II-like intermediate first which transitioned to a compound III-like state (A) before returning to the ferric state (B). All reactions were carried out at 4° C in 50 mM acetate, pH 5.0, using 3 μM KatG. Arrows indicate the direction of absorption changes.

and was always complete before the conclusion of steady-state catalatic consumption of H_2O_2 (as monitored by the Fe^{III} state at 401 nm) (Figure 3.19A and B). Interestingly, despite multiple attempts with altered expression and/or purification protocols, we were never able to express and purify a stable *m*Y413F KatG enzyme. Accordingly, the comparisons between reconstituted and mature forms of enzyme that were carried out for W321F, W412F, and W91F KatG were not possible with the Y413F variant.

Protein-based radicals associated with MYW cofactor formation

Virtually all aspects of KatG's function involve protein-based radicals.[51, 80] The enzyme's peroxidase activity cannot operate without them, and if adequate/appropriate PxEDs are absent, protein-based radicals are among the oxidative protein modifications that inevitably lead to KatG's inactivation. The isoniazid pro-drug activation for which *M. tuberculosis* KatG is famous is proposed to depend on protein-based radical transfer reactions. The KatG-unique MYW cofactor, and therefore, KatG's novel catalase activity depends on the redox cycling of the cofactor between its fully covalent and radical states. Finally, as described earlier (see Figure 3.2), the mechanism proposed for conversion of the unmodified Met 252, Tyr 229, and Trp 107 side chains to produce the KatG unique MYW cofactor invokes transient protein-based radicals centered on Trp 107 and/or Tyr 229 as well as the proposed covalent precursor Tyr-Trp (YW).[34,43]

To date, substantial components of the mechanism of autocatalytic MYW formation and the intermediates involved remain unknown and uninvestigated. For example, although protein-based radicals are a critical part of this mechanism, no radical species associated with MYW cofactor formation have been observed or characterized. The KatG variants described in this dissertation provide an excellent opportunity to

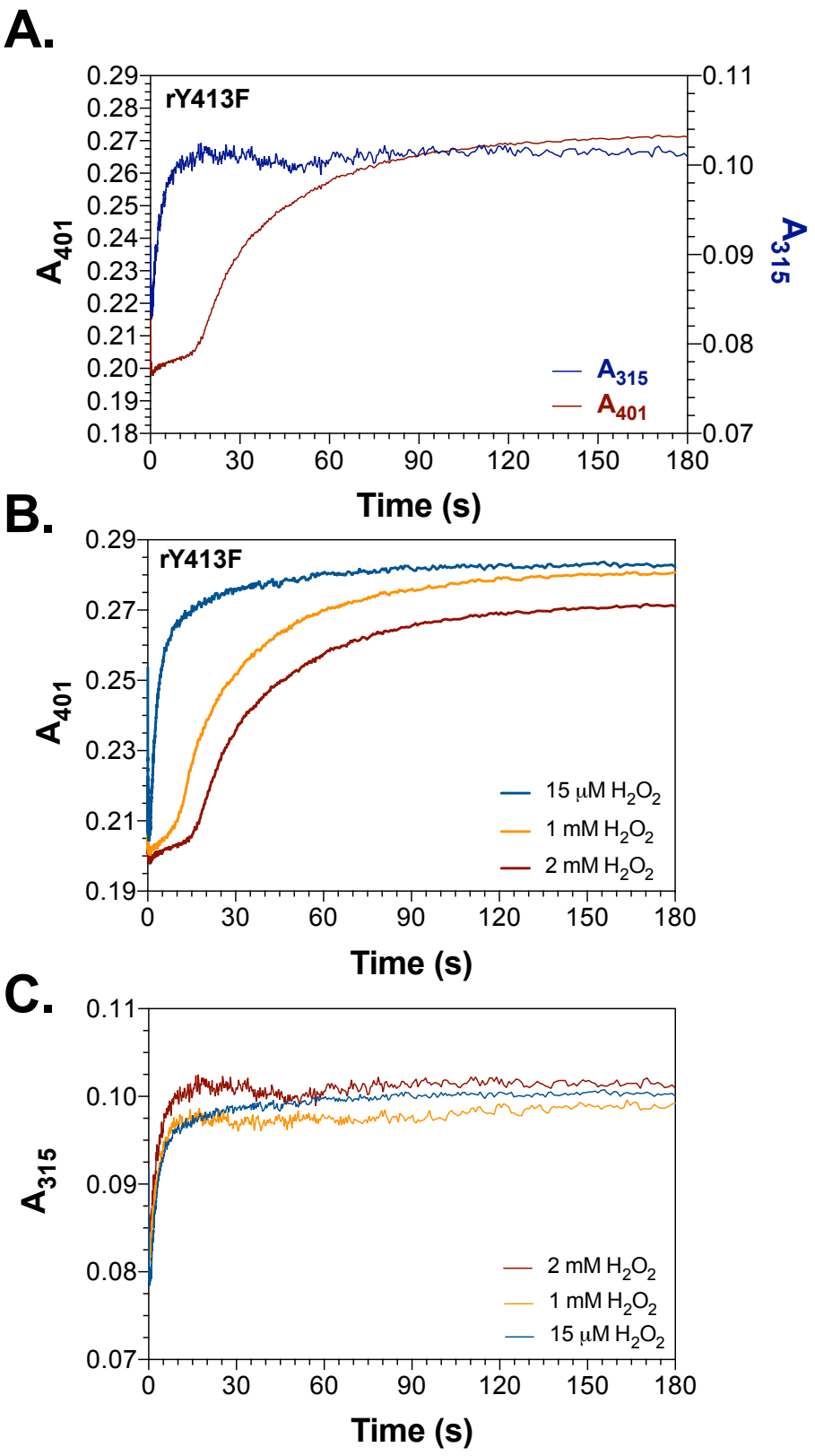

Figure 3.19 Stopped-Flow spectroscopy of *r*Y413F KatG reacted with varying H_2O_2. Change in absorbance at 401 nm and 315 nm (A) change in absorbance at 401 (B) change in absorbance at 315 nm. All reactions have been carried out using 3 μM KatG in 50 mM acetate, pH 5.0 at 4° C.

address two important questions: 1) what are the radical intermediates involved in MYW adduct formation, and 2) what part do other oxidizable amino acids around the KatG active site play in the establishment of this critical cofactor?

The reconstituted forms of the KatG variants described above clearly do not yet possess the mature MYW cofactor. The establishment of this cofactor has a clear impact on heme intermediates and the kinetics of transition from a catalase-inactive to catalase-active state. Finally, the targeting of different oxidizable side chains by these variants has produced novel properties in terms of the intermediates observed which we anticipate will be a strategic advantage in addressing these questions. For each of the Phe-substitution KatG variants, we used rapid freeze-quench (RFQ) electron paramagnetic resonance (EPR) spectroscopy to capture protein-based radicals produced early upon KatG variant reactions with H_2O_2. It is important to note that peroxide concentrations are noted in terms of molar equivalents because of the 50-fold higher concentrations of enzyme which are necessary to obtain detectable and clear EPR signals for protein-based radicals as compared to heme spectra observed in optical stopped-flow experiments. Accordingly, the RFQ-EPR experiments described here utilize one of two peroxidase concentrations 5 molar equivalents (i.e., limited-turnover conditions) or 667 molar equivalents (i.e., steady-state-supporting conditions).

rW321F KatG. When we reacted *r*W321F KatG with 5 molar equivalents of H_2O_2, protein-based radicals were observed at the earliest reaction times accessible by RFQ (i.e., 4.6 ms). A radical with doublet character was observed at this reaction time that persisted to later reaction times, though substantially muted, at 10 ms and 100 ms post-mixing (Figure 3.20) perhaps by the contribution of other radical species growing in

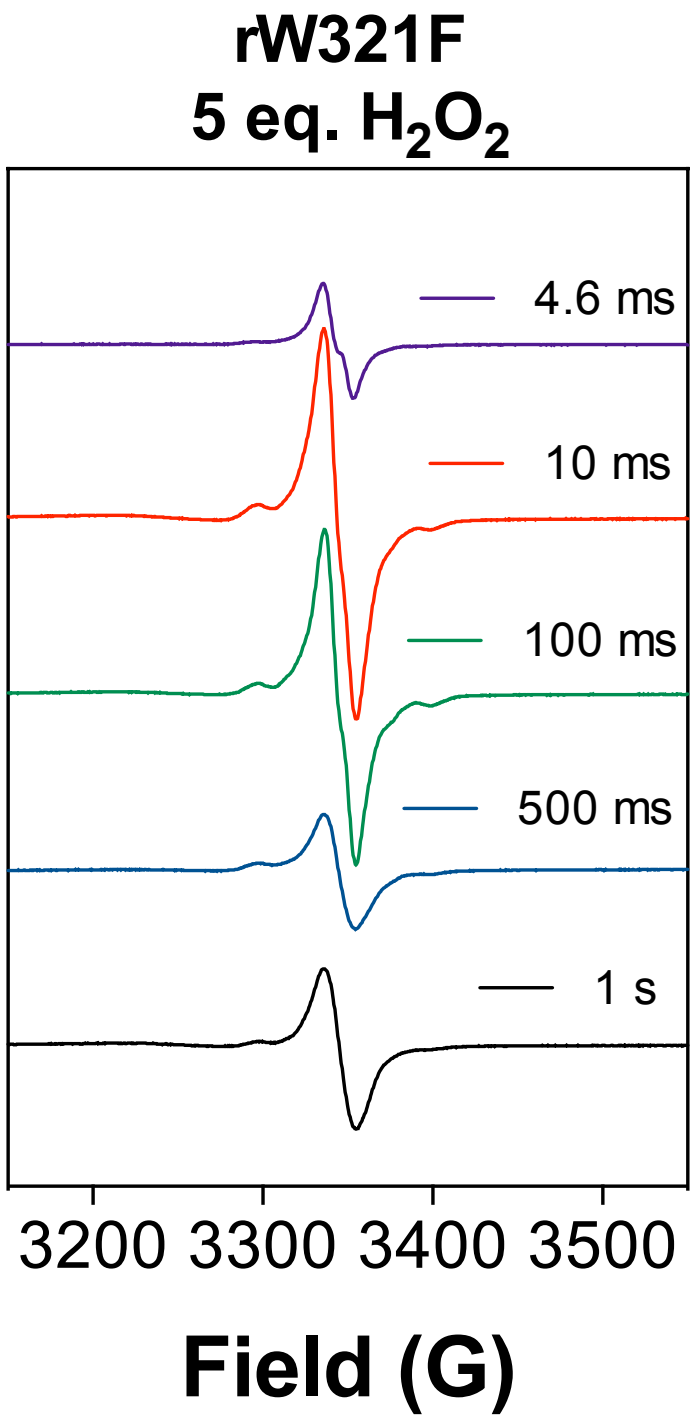

Figure 3.20. Protein-based radicals observed upon *r*W321F KatG with H_2O_2. The *r*W321F KatG variant (150 μM final concentration) was reacted with 5 molar equivalents of H_2O_2 in 50 mM acetate, pH 5, and reactions were quenched by rapid freezing in liquid ethane after the elapsed reaction time noted by each spectrum. Following transfer of the frozen material to an EPR tube, samples were kept frozen under liquid N_2 (77 K). All spectra were recorded at (4.5 K) using liquid He. All EPR spectrometer settings are reported in *Materials and Methods.*

intensity over time. For reactions quenched 0.5 and 1 s after mixing with H_2O_2, the doublet appeared to be absent or at least substantially diminished in intensity relative to more intense singlet species.

It is important to note what radicals are ***not*** evident in these spectra. There was no indication of the broad exchange-coupled signal, which has been associated with the KatG W321$^{\bullet+}$. This was anticipated given the fact that in this variant W321 had been replaced by a non-oxidizable phenylalanine residue. Though a doublet radical was detected over the first 100 ms of reaction time, this did not appear to be the narrow doublet, which has been assigned to the radical intermediate of the fully formed MYW cofactor (i.e., MYW$^{\bullet+}$).[40] Indeed, decreasing the microwave power to evaluate saturation effects revealed clear features of the doublet in the radical detected at 10 ms of reaction time (Figure 3.21). Finally, the signals detected were inconsistent with what has previously been assigned to the porphyrin$^{\bullet+}$ of a classical compound I-like (i.e., Fe^{IV}=O[porphyrin]$^{\bullet+}$.[88, 90] These have been shown to be exchange broadened in the extreme with signals spanning 2,000 Gauss. This last observation was perhaps the most surprising given the optical spectrum observed for *r*W321F KatG upon reaction with limited-turnover H_2O_2 (see Figure 3.4A); it has all the marks of a classical peroxidase compound I-like intermediate.

rW412F KatG. Reaction of *r*W412F KatG with 5 molar equivalents H_2O_2 produced two features which were in contrast to spectra observed with *r*W321F KatG (Figure 3.22). First, the contributions of a doublet radical were much more prominent across all reaction times from 4.6 ms – 1 s. However, we also detected contributions from a broad radical reminiscent of the exchange-broadened W321$^{\bullet+}$ which has been observed

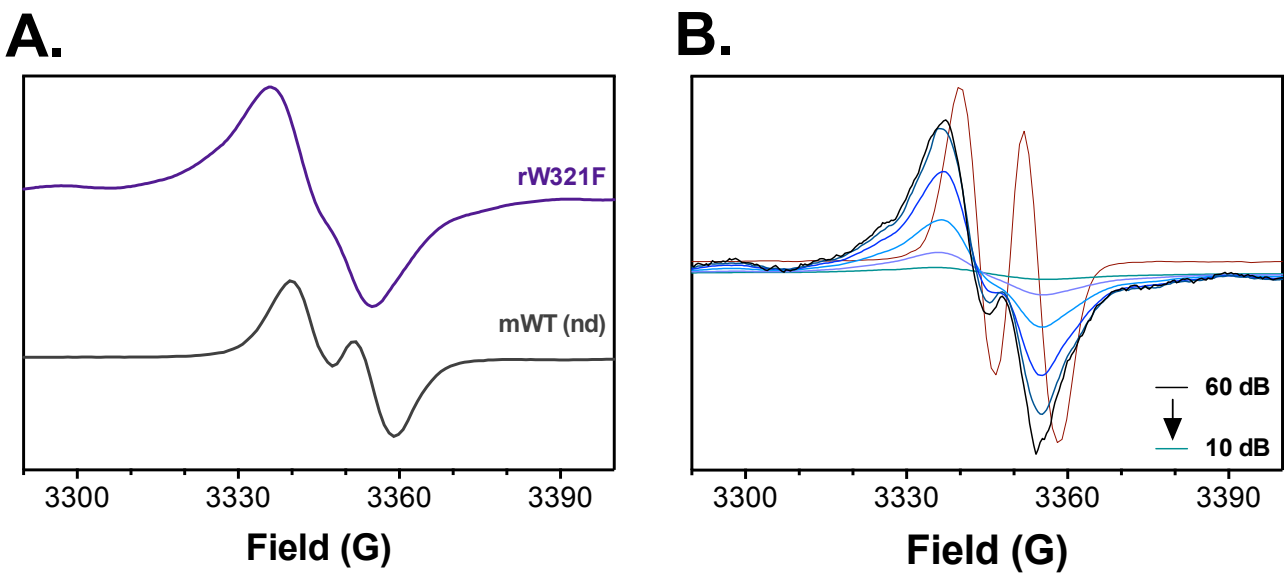

Figure 3.21. Comparison of rW321F protein-based radicals observed early in reactions with H_2O_2 against the *m*WT KatG narrow doublet. Reaction of rW321F KatG with 5 molar eq. H_2O_2 produces a protein-based radical spectrum (red) distinct from the mWT $MYW^{\bullet+}$ narrow doublet associated with KatG catalase turnover (blue) (A). The effect of microwave power attenuation on the rW321F KatG signal more clearly reveals its doublet character (B), but the signal is substantially broader than that of the $MYW^{\bullet+}$ narrow doublet observed at low microwave power. The *g*-value corresponding to the former is 2.00528; that of the latter is 2.00372. All reactions were carried out in 50 mM acetate, pH 5.0, at 4 ºC and were quenched 10 ms after mixing. All EPR spectra were recorded at 4.5 K.

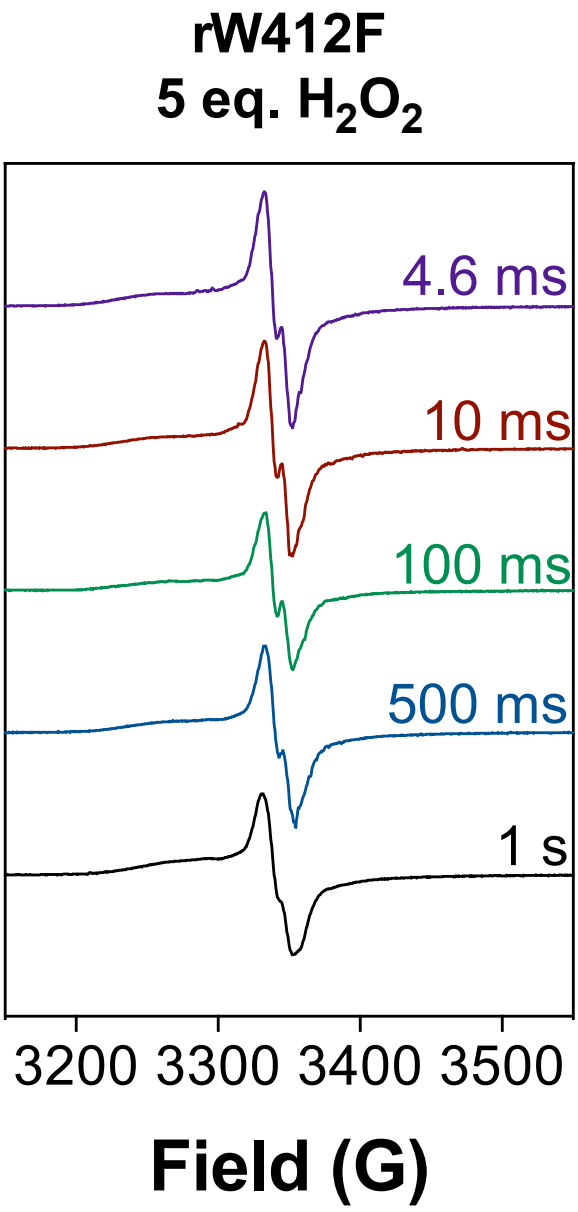

Figure 3.22. Protein-based radicals observed by EPR upon *r*W412F KatG with H_2O_2. All reactions contained 150 µM *r*W412F KatG in 50 mM acetate, pH 5. The enzyme was reacted with 5 molar equivalents H_2O_2, frozen, packed, stored, and evaluated in the same manner described for *r*W321F KatG (Fig. 3.20).

in wild-type KatG and connected with enzyme inactivation.[44] Since in contrast to *r*W321F KatG this variant still retains a proximal Trp (i.e., W321), the appearance of this feature is not unexpected. Reaction of *r*W412F KatG with 667 molar equivalents H_2O_2, produced a strong narrow doublet with relatively little contribution from the broadened species (shoulder at 3300 G) observed under limited-turnover conditions (Figure 3.23). Indeed, what broad signal contribution was evident at 3300 G was completely absent by 100 ms of reaction time. To further investigate these reactions and their narrow doublets we investigated power saturation of the radicals present at the earliest time points, 4.6 ms, for both H_2O_2 concentrations (Figure 3.24). We found that the radical present in the sample reacted with 5 eq. H_2O_2 became saturated easily (Figure 3.24 A, C). The broad shoulder feature (3300 G) of the radical(s) observed upon reaction of *r*W412F with 5 eq. H_2O_2 was very prominent and highly resistant to power saturation relative to the central signal in *r*W412F KatG EPR spectra (Figure 3.24C). For *r*W412F KatG reacted with 667 eq. H_2O_2 a radical that was not as easily saturated as the peak-to-trough signal was also observed (Figure 3.24 B, D). The power saturation profiles are poorly fit, indicating that there are multiple species present that need further experimentation to differentiate. Across the board, more reaction time points need to be collected to make any strong conclusions from this data.

rY413F KatG. Parallel experiments with *r*Y413F KatG achieved nearly identical results to *r*W412F KatG. At low concentrations of H_2O_2 we saw a narrow doublet with a broad peak in the 3300 range, both of which were still present at 1s (Figure 3.25). The similarities continued into the reactions at higher concentrations where only the narrow doublet was observed and a small peak at 3300 G that went away before 10 ms (Figure

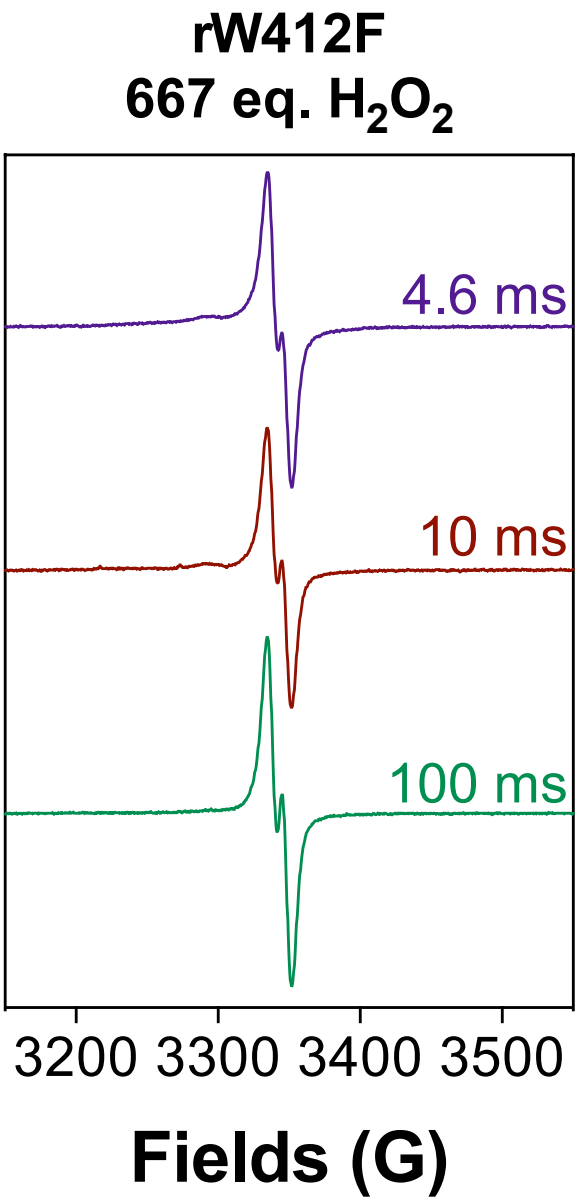

Figure 3.23. Protein-based radicals observed by EPR upon *r*W412F KatG reaction with steady-state concentrations of H_2O_2. All reactions were carried out using 150 μM *r*W412F KatG (final concentration) in 50 mM acetate, pH 5. The enzyme was reacted with 667 molar equivalents H_2O_2 and quenched by rapid freezing following the reaction times indicated. EPR samples were packed, stored, and evaluated in the same manner described for *r*W321F KatG (Fig. 3.20).

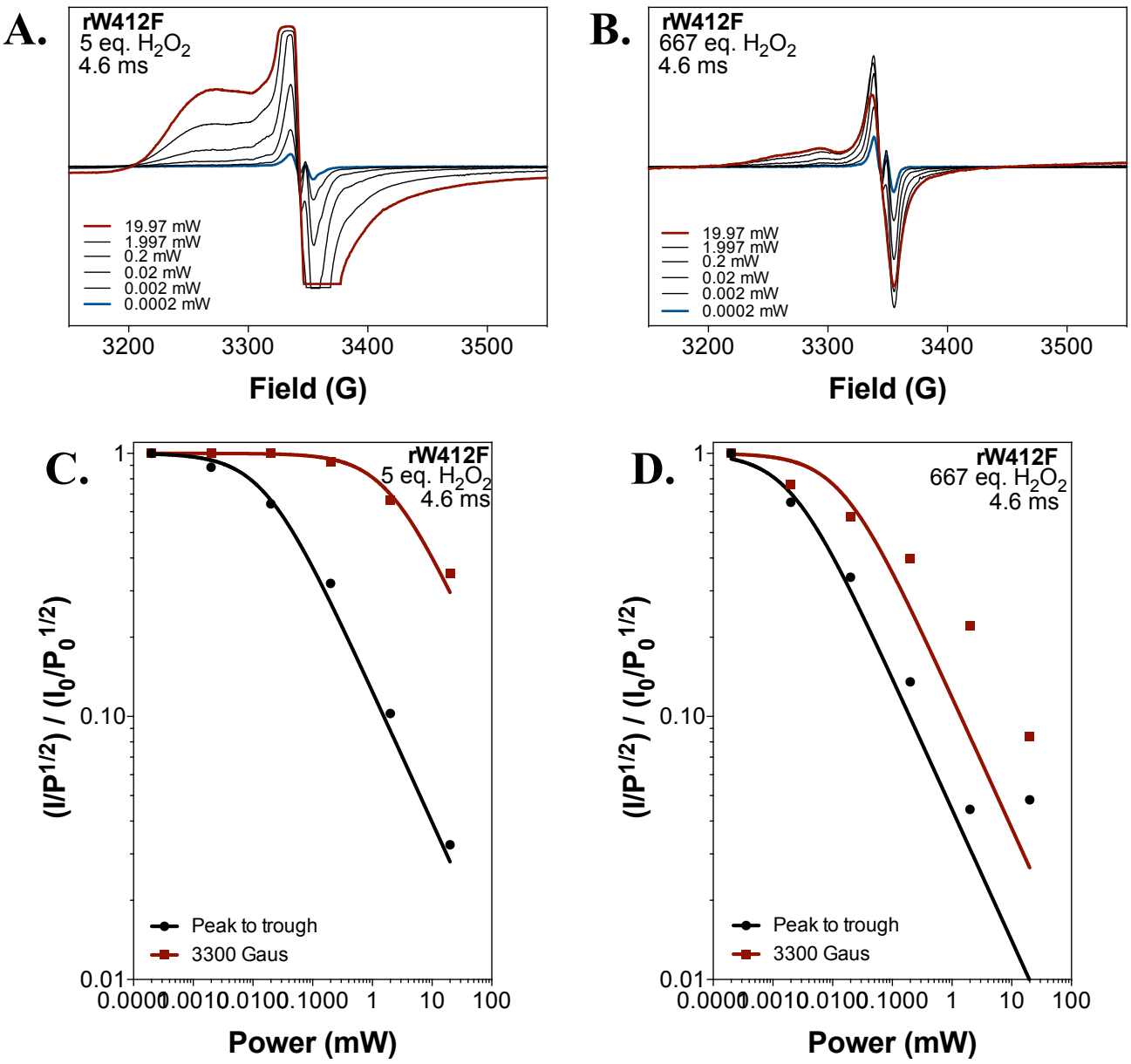

Figure 3.24. Power saturation protein-based radicals observed for *r*W412F KatG at early reaction times. Protein-base radicals observed for *r*W412F KatG when treated with 5 equivalents (A) and 667 equivalents (B) of H_2O_2 and frozen at 4.6 ms. The normalized signal intensity observed in the peak-to-trough of the central signal was evaluated as was the shoulder at 3300 Gauss for radicals observed after 4.6 ms of reaction time with 5 equivalents (C) or 667 equivalents (D).

3.26). Power saturation was also done on the earliest time points for *r*Y413F KatG and similar results were obtained (Figure 3.27). The 5 equivalents H_2O_2 was not as easily saturated as the lower concentration with *r*W412F KatG but the 3300 peak and the peak to trough were saturated at virtually the same rate (Figure 3.27. A, C). At the higher concentration we also saw that the 3300 G peak was not as easily saturated as the peak to trough signal (Figure 3.27. B, D). These data bearing such a strong resemblance to *r*W412F KatG is reasonable as these two variants target two amino acids that are not only immediately adjacent to one another in sequence, but also in the same path of oxidizable amino acids. Again, future studies monitoring a higher density of time points and a broader set of reaction conditions should be performed to more firmly establish the participation of these residues in KatG function.

Impact of Trp/Tyr Substitution on KatG Catalatic Turnover

When KatG variants were reacted with higher concentrations of H_2O_2, we were able to observe intermediates that were consistent with catalase active enzyme. In order to evaluate the impact of oxidizable amino acid substitution on catalatic turnover, we monitored the contribution of ferric state (407 nm) through initial reaction with H_2O_2, steady-state consumption of H_2O_2 to depletion, and the return of enzyme to its resting (i.e., ferric enzyme) thereafter. Of particular interest was the impact of each specific oxidizable residue on the return of the ferric enzyme after catalase activity (Figure 3.28). The *r*W321F KatG variant showed the most distinct behavior in this respect; three steps were apparent prior to the return of this enzyme's ferric state. The first phase concluded before 1 s of reaction time. The second component unfolded over a period of about 8 s. The final and slowest phase of the reaction was dominated by the return of the ferric

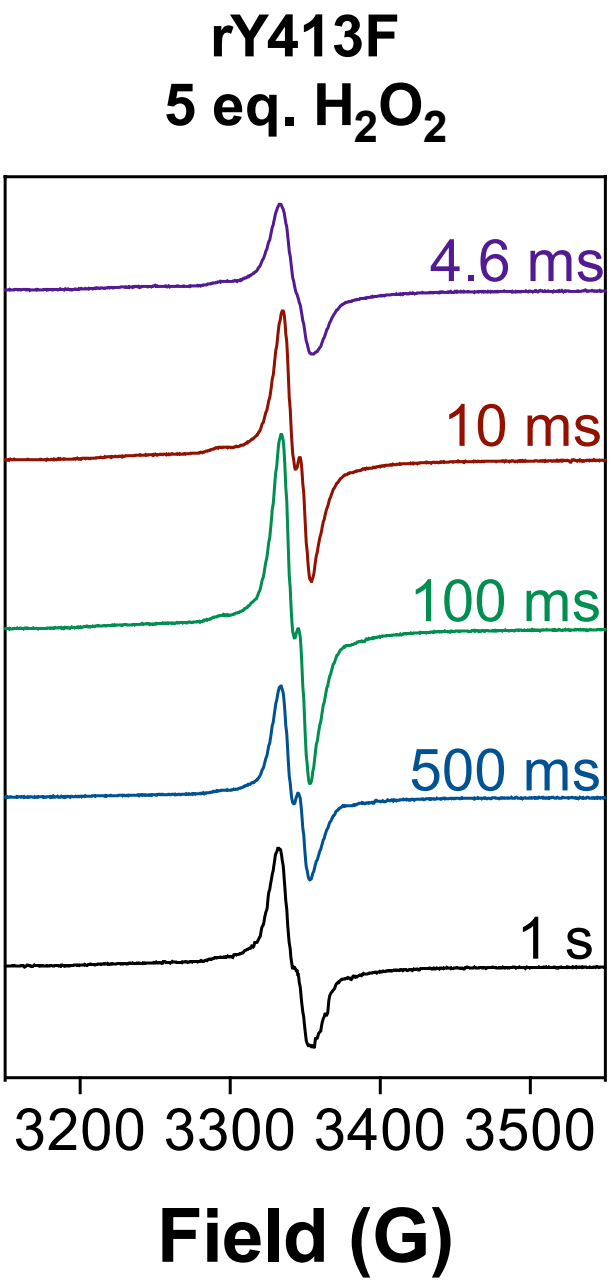

Figure 3.25. Protein-based radicals observed by EPR upon *r*Y413F KatG with H_2O_2. All reactions contained 150 µM *r*Y413F KatG in 50 mM acetate, pH 5. The enzyme was reacted with 5 molar equivalents H_2O_2, frozen, packed, stored, and evaluated in the same manner described for *r*W321F KatG (Fig. 3.20).

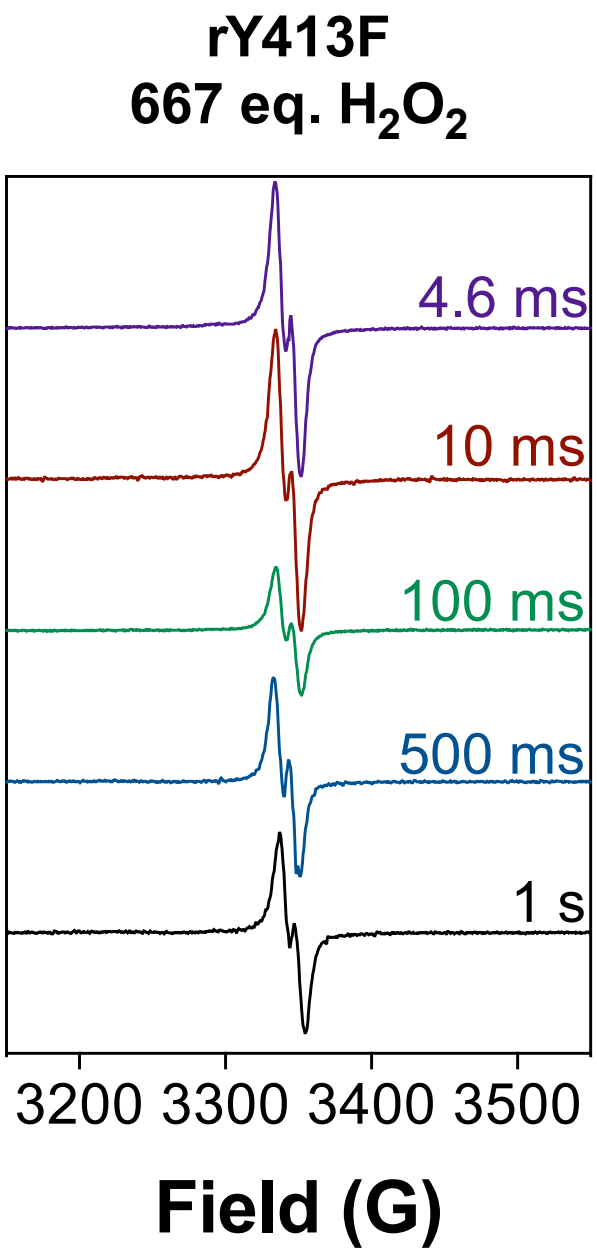

Figure 3.26. Protein-based radicals observed by EPR upon *r*Y413F KatG reaction with steady-state concentrations of H_2O_2. All reactions were carried out using 150 μM *r*Y413F KatG (final concentration) in 50 mM acetate, pH 5. The enzyme was reacted with 667 molar equivalents H_2O_2 and quenched by rapid freezing following the reaction times indicated. EPR samples were packed, stored, and evaluated in the same manner described for *r*W321F KatG (Fig. 3.20).

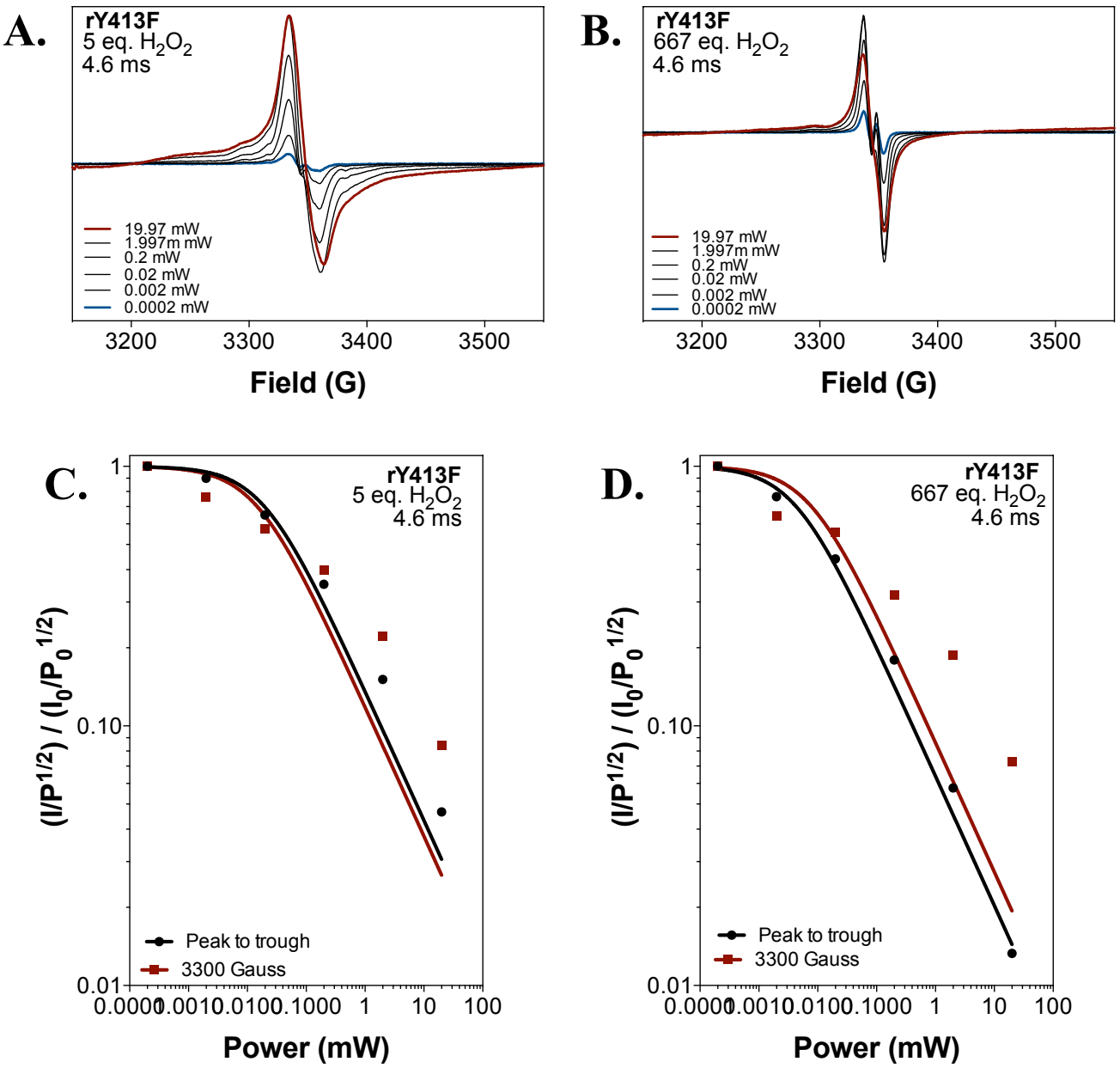

Figure 3.27. Power saturation *r*Y413F KatG protein-based radicals observed early in reactions with H_2O_2. Protein-based radicals from *r*Y413F KatG were observed following reaction with 5 molar equivalents of H_2O_2 (A) and 667 equivalents of H_2O_2 (B). Reactions were quenched by freezing at 4.6 ms of reaction time. Normalized intensities of the peak-to-trough of the central radical signal as well as the shoulder at 3300 Gauss were plotted as a function of microwave power. Data were evaluated for radicals observed following reaction with 5 molar equivalents (C) and 667 molar equivalents (D) of H_2O_2.

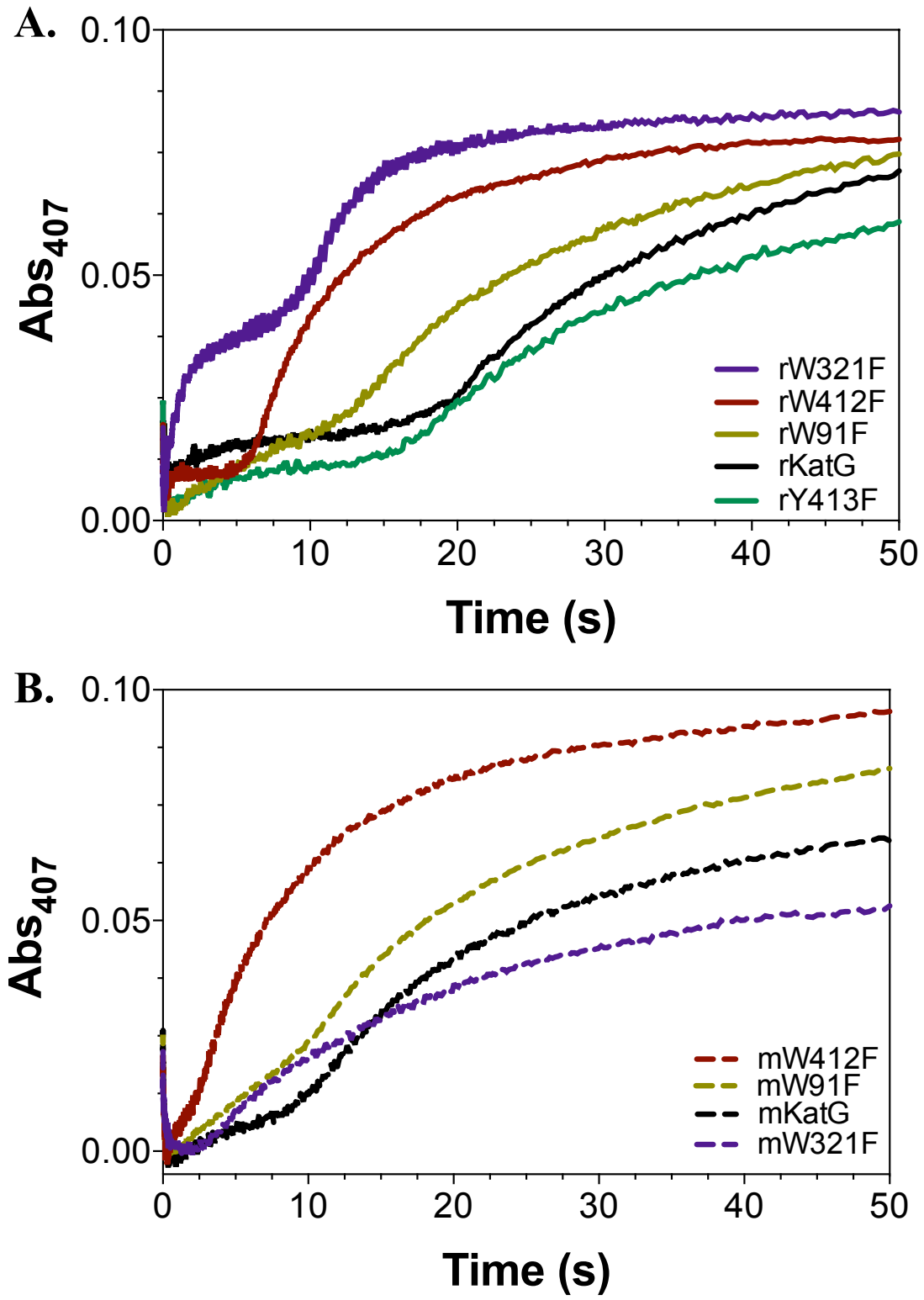

Figure 3.28. Reactivity of the ferric state of Trp/Tyr substitution variants of KatG. Variants (3 μM each) were reacted with 2 mM H_2O_2 and changes in the quantity of ferric enzyme present was monitored at 407 nm. Reconstituted forms *r*W321F (purple), *r*W412F (red), *r*W91F (orange), *r*Y413F (yellow), and *r*WT (black) KatG were evaluated (A), as were the mature forms *m*W321F (purple), *m*W412F (red), *m*W91F (orange), and *m*WT (black) (B). All reactions were carried out in 50 mM acetate, pH 5.0, at 4° C.

enzyme. These data are consistent with the formation of rW321F KatG compound I within the stopped-flow dead time and the relatively slow transition to a Fe^{IV}=O state within ~500 ms. The following stage included a transition from a Fe^{IV}=O state to a Fe^{III}-$O_2^{\cdot-}$ state, and included an apparent steady-state consumption of H_2O_2 until its depletion. Without H_2O_2 remaining in the system, the Fe^{III} form of the enzyme could then accumulate.

For all of the other *r*KatG variants and *r*WT KatG there are only two steps observed. However, these two steps were observed to occur at different rates for each variant. *r*W412F KatG is observed to deplete H_2O_2 first, enabling the earliest return of the ferric state. Starting with an initial reaction, which concluded in less than 1 s, *r*W412F KatG then entered what appeared to be a steady-state phase with a duration of about 6 s; this was followed by a relatively rapid return to the ferric enzyme. For *r*W91F KatG the initial transition also occurred over a 1 s interval. However, the subsequent apparent steady-state phase persisted for roughly twice as long, and the rate of return of the ferric state was clearly diminished relative to the *r*W412F variant. Interestingly, *r*Y413F and *r*WT KatG are the most similar in their reaction profiles. The initial progression to the apparent steady-state appears to complete after 1 s of reaction time. However, the subsequent steady-state phase endures for nearly 20 s before the return of the ferric state is evident. From these, W321 would seem to have the most impact on the return of the ferric enzyme when the MYW adduct is not present. Followed by W412 and W91. Whereas Y413 has little to no effect on the return of the ferric enzyme when the MYW adduct is not present (Figure 3.28A). We observed distinct reaction profiles with the *m*KatG preparations of the variants. However, it was clear that this was primarily due to

the presence of the MYW cofactor in these proteins at the start of the reaction as opposed to its absence in the *r*KatG proteins. Overall, the *m*KatG variants reacted with high concentrations of H_2O_2 exhibited fewer heme state transitions. Nevertheless, the trend in times elapsed prior to the return of the ferric enzyme held across the *m*W412F, *m*WT, and *m*W91F KatG's. The *m*W321F KatG enzyme was, again, distinct from the others. However, this is likely due to the fact that W321F KatG consistently shows the participation of heme states that are not observed with any of the other variants. Overall, these data may be viewed as a proxy for evaluating the level of influence of each tryptophan substitution on KatG performance. It appears that W321F has the most effect on the return of the ferric enzyme, followed by W412F, then W91F, and Y413F, which shows little to no effect.

Similarly, when *r*KatG variants were reacted with PAA *r*W321F KatG stood as distinct from the other variants. In the reactions of *r*W321F KatG with PAA an admixture of compound I/compound II-like intermediates was observed at early time points followed by light scattering and a full compound II-like intermediate (Figure 3.29A). This is different from the other *r*KatG variants as they indicated a compound II-like intermediate followed by light scattering, an increase in absorbance around 310 nm, and a formation of compound III-like intermediate (Figure 3.29 B, C, and D). The most striking observation from this experiment was the lack of increased absorbance around 310 nm for *r*W321F KatG. This increase in absorbance is thought to be contributed to the formation of the MYW adduct, indicating the adduct was formed for *r*W412F KatG, *r*W91F KatG, and *r*Y413F KatG but not for *r*W321F KatG. This further supports that the

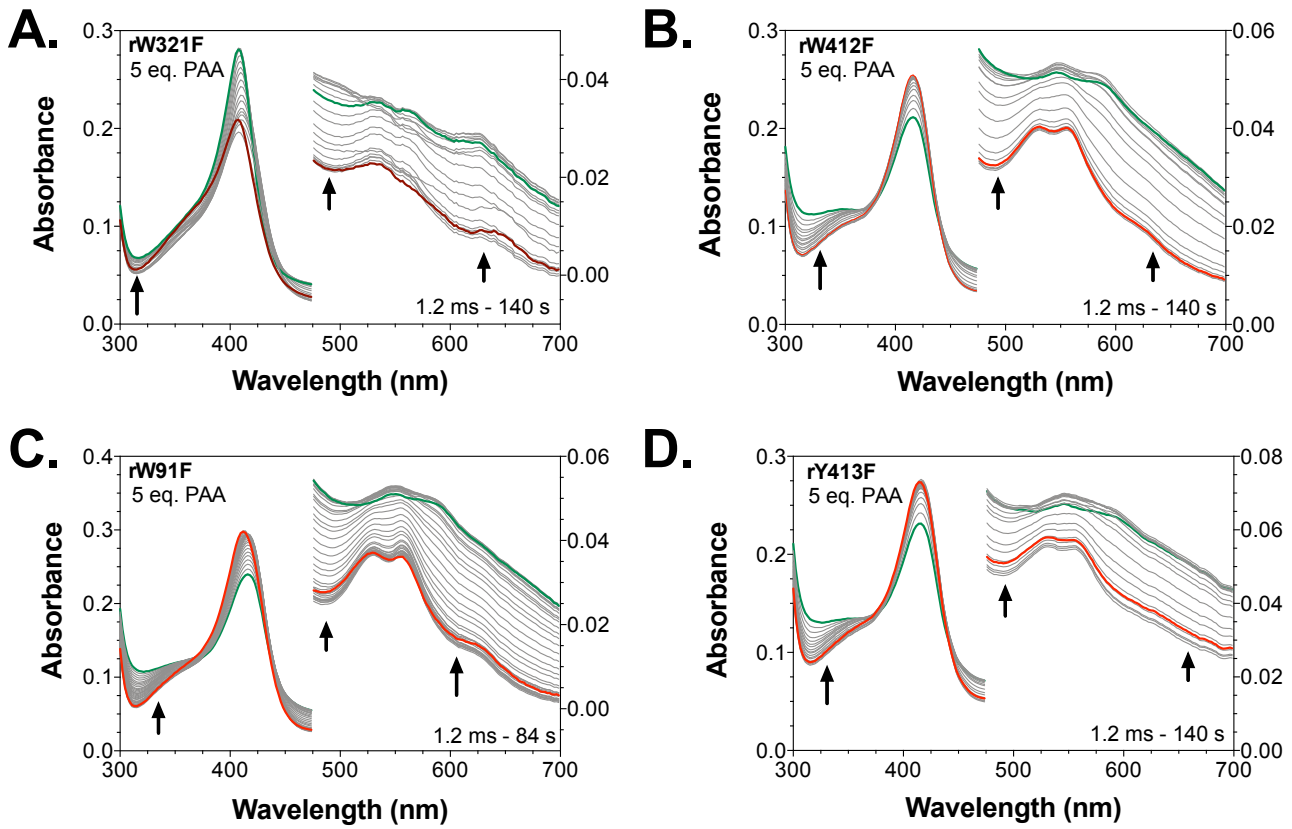

Figure 3.29. Reaction of *r*KatG variants with PAA monitored by optical stopped-flow methods. Each variant *r*W321F (A), *r*W412F (B), *r*W91F (C), and *r*Y413F (D) KatG was reacted with five molar equivalents of PAA. In each case, an initial compound II-like intermediate was observed (red traces) followed by transition to a compound III-like intermediate (green traces). There was no observation of a return of the ferric enzyme as PAA is a peroxide that does not support catalase turnover. All reactions were carried out using 3 μM KatG in 50 mM acetate, pH 5.0, at 4° C.

conclusion from Chapter 2 that W321F KatG is involved in the formation of the adduct and suggests that the other oxidizable residues may have a lesser role.

We also reacted these variants with H_2O_2 in the presence of ABTS to determine the rate and extent of $ABTS^{\bullet+}$ generated by each (Figure 3.30). The accumulation of $ABTS^{\bullet+}$ was monitored at 645 nm (ε = 12,000 $M^{-1}cm^{-1}$). Strikingly, across the board, *r*KatG variants produced significantly more $ABTS^{\bullet+}$ than the corresponding *m*KatG preparations of the same variants (Figure 3.30B). For the W412F variant, the *r*KatG form generated roughly twice as much $ABTS^{\bullet+}$ as the *m*KatG form. For the W321F variant, the *r*KatG form generated six-fold more $ABTS^{\bullet+}$. Comparing the *r*KatG forms of all the variants, the highest rates and extents of $ABTS^{\bullet+}$ were observed with the W91F variant, and the trend both in rate and extent had W321F followed by Y413F with the slowest rates lowest quantities of $ABTS^{\bullet+}$ generated by W412F KatG. The distinctions between the *m*KatG versions or proteins that we were able to investigate were much less. Rates of $ABTS^{\bullet+}$ production were identical, and there was little if any difference in the overall production of the radical between W321F and W412F KatG (Figure 3.30B).

The distinctions between rates on one hand and extents of $ABTS^{\bullet+}$production on the other were also noteworthy. For example, *r*W321F KatG showed substantially slower rates of $ABTS^{\bullet+}$ production than *r*W91F, but ultimately, the extent of radical generated by each protein was highly similar. On their own, the rates of $ABTS^{\bullet+}$ production are remarkable for the *r*W91F variant. Indeed, the peroxidase activity of this variant exceeds all others evaluated by at least a factor of five. This is a catalytic advantage that is diminished to a substantial degree (but not completely) by the establishment of the MYW

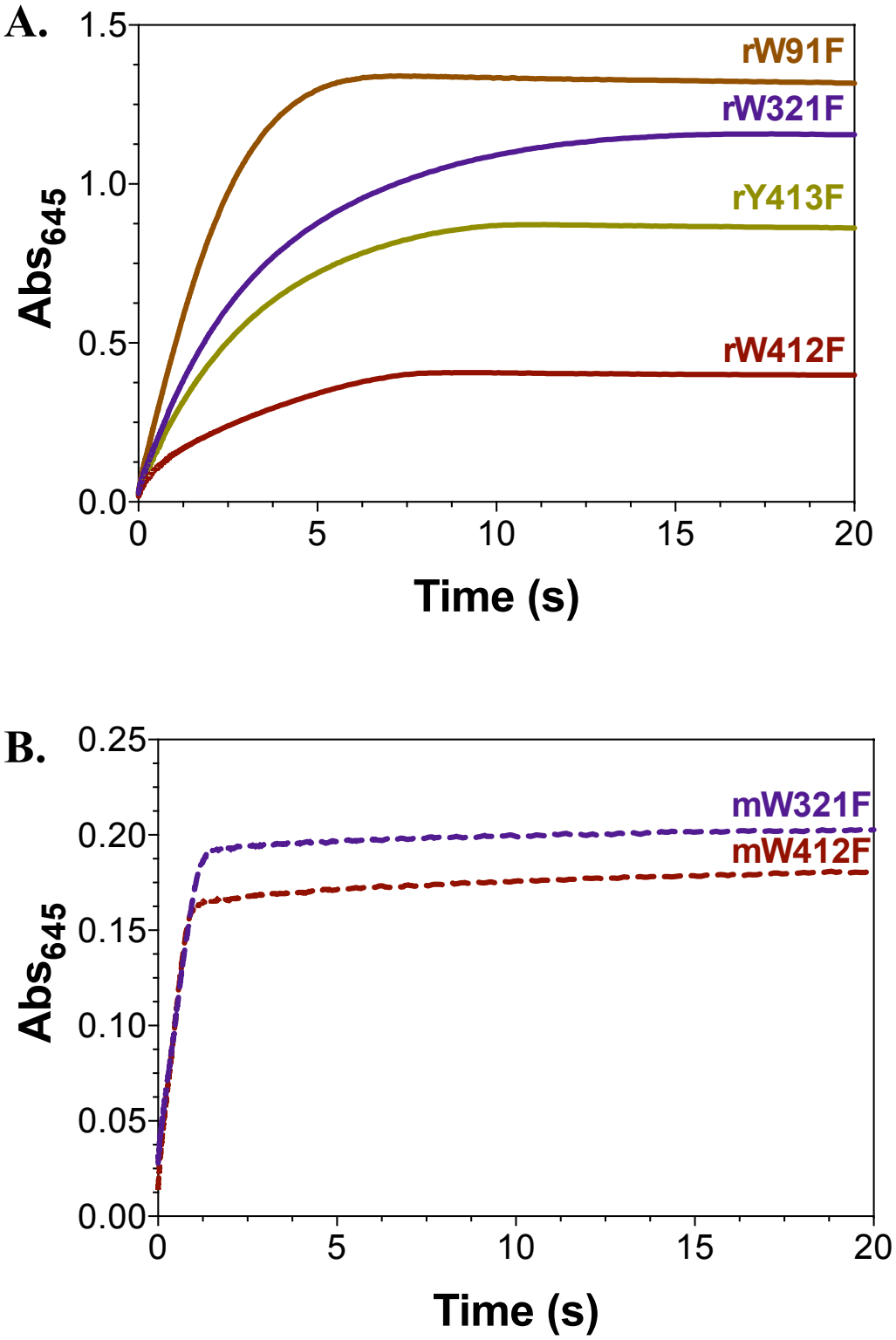

Figure 3.30. Peroxide-dependent formation of $ABTS^{\bullet+}$ by KatG Trp/Tyr substitution variants. Each variant was reacted with 2 mM H_2O_2 in the presence of 1 mM ABTS. The reconsistuted forms (A) of W321F (purple), W412F (red), W91F (orange), and Y413F (yellow) were evaluated. Similarly, the mature forms (B) of W321F (purple) and W412F (red) KatG were monitored at 645 nm to detect accumulation of $ABTS^{\bullet+}$. All reactions have been carried out using 3 μM KatG in 50 mM acetate, pH 5.0 at 4° C.

adduct. The connection between W91, the MYW adduct, and the through-protein peroxidase activity of KatG remains to be elucidated.

The rW91F and rW321F variants were followed by *r*Y413F KatG, which produced less $ABTS^{\bullet+}$ and *r*W412F KatG, which yielded the lowest quantities of the radical of all variants examined. The distinctions between *r*Y413F KatG and *r*W412F KatG are noteworthy in light of the fact that W412 and Y413 lie within the same grouping/electron-transfer pathway of KatG oxidizable amino acids. The W91F substitution is the furthest from the active site. It would appear that it not only produced minimal interruption of ABTS oxidation, but in fact, the absence of W91 appears likely to have stimulated this process. Compared to the *r*WT KatG enzyme, *r*W91F KatG displays ten-fold greater peroxidase activity. To date, the only KatG variants that produce such substantial increases in peroxidase activity are catalase-inactive (e.g., Y229F KatG and M255I KatG). [45, 46]

To better understand the peroxidase catalytic intermediates and properties of the variants, we reacted each enzyme with H_2O_2 and ABTS in the presence of ascorbate (Figure 3.31). By reducing the $ABTS^{\bullet+}$ at near diffusion-controlled rates, ascorbate prevents the accumulation of this intensely absorbing radical, enabling the direct observation of heme intermediates in optical stopped-flow experiments.[91] For *r*W321F KatG reacting with low H_2O_2 concentrations (i.e., 5 molar equivalents or 15 μM), we observed the initial transition to from a compound II-like intermediate within the first 40 ms (Figure 3.31A). It is highly likely that compound I formed first, but it did not appear to accumulate to any significant degree. This would be consistent with an increased rate of reduction of compound I in the presence of a PxED. The compound II-like

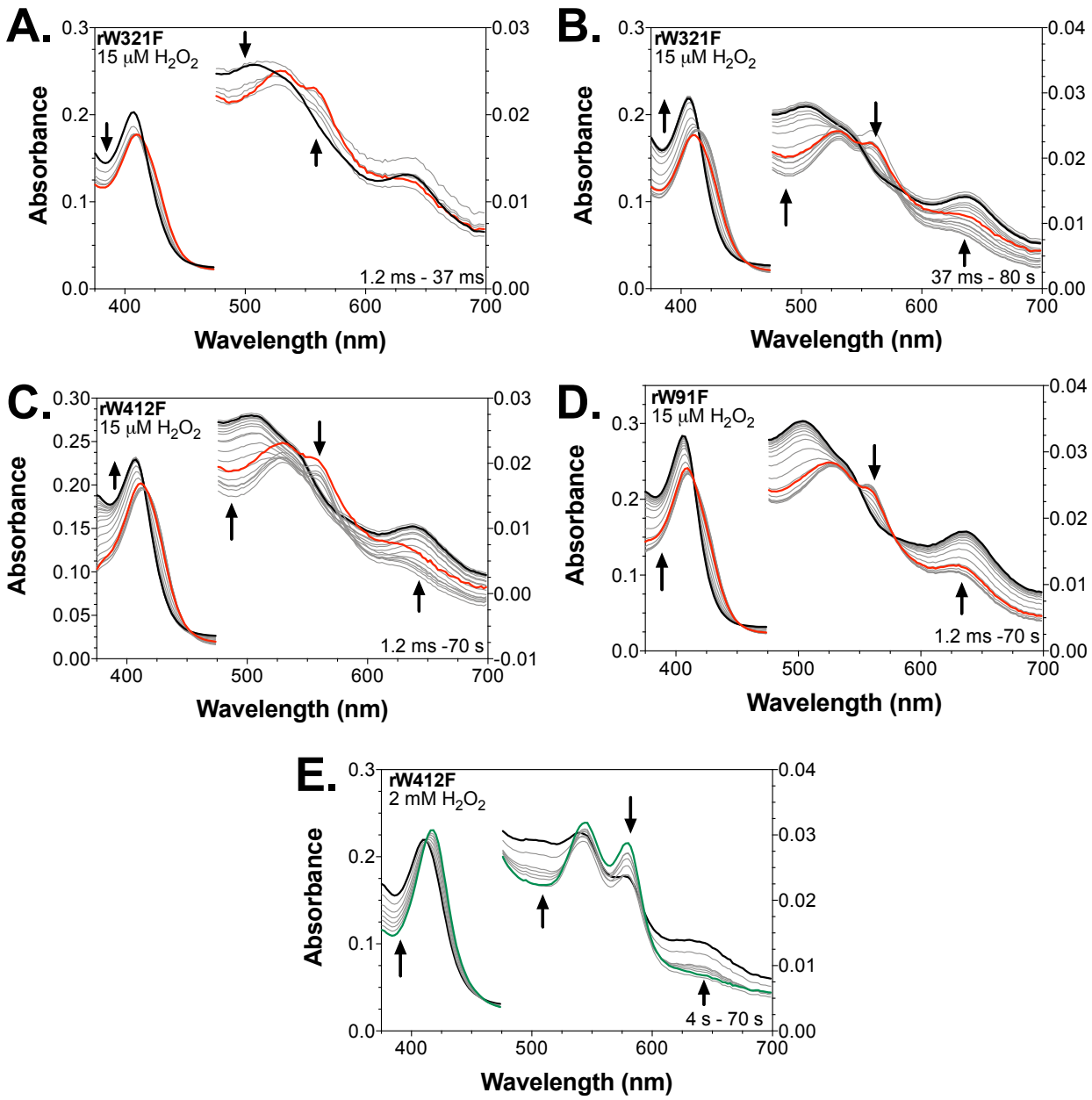

Figure 3.31. Effect of PxED on intermediates observed for *r*KatG Trp/Tyr-substitution variants upon their reaction with limited-turnover concentrations of H_2O_2. Reaction of *r*W321F KatG with 5 molar equivalents H_2O_2 was monitored for 1 – 37 ms (A) and 37 ms – 80 s (B) after mixing. The *r*W412F (C), *r*W91F (D), and *r*Y413F KatG (E) were each reacted with 5 molar equivalents of H_2O_2, and their reactions monitored from 1.2 ms – 70 s. All reactions were carried out with final concentration of KatG at 3 μM KatG. All reactions contained 1 mM ABTS, and 1mM ascorbate in 50 mM acetate, pH 5.0, at 4° C. Ascorbate was used for the diffusion-controlled reduction of $ABTS^{\bullet+}$ to prevent its interference with heme spectra.

intermediate then returned slowly to the ferric state over the next 80 s (Figure 3.31B). For the other variants the compound II-like state was formed within the deadtime of the stopped-flow instrument (~ 1 ms). Accordingly, only the slow return of this compound II state back the ferric enzyme was observed (Figure 3.31C, D, and E).

When the concentration of H_2O_2 was increased to support steady-state turnover of the enzyme in the presence of ABTS and ascorbate, similar results were obtained *r*KatG variants (Figure 3.31) as those observed in the absence of PxED (e.g., Figure 3.9). For *r*W321F KatG, spectra observed immediately after the deadtime had features consistent with a compound I state (Figure 3.31A). Here, the much higher concentration of H_2O_2 utilized apparently accelerated the initial reaction with ferric enzyme to accumulate compound I more rapidly than its reduction in the presence of ABTS/ascorbate. A subsequent transition to an intermediate with characteristics of compound III (i.e., λ_{max} at 540 and 578 nm) was observed, followed by a slow return of the ferric state (Figure 3.31B) Consistent with our previous observations (see Figure 3.5), the presence of the proximal Trp seems to facilitate a more rapid transition of compound I to the compound II-like state.

For the rW412F and rY413F variants, the compound-II like intermediate was the first heme state observed after the stopped-flow deadtime (Figure 3.32C and E, respectively). In both cases, this was followed by a transition to the compound III-like intermediate and a slow return of the ferric enzyme in latter time points (Figure 3.32B and D). Interestingly, *r*W91F KatG did not show an initial appearance of the compound II-like state; instead, the first species detected after the deadtime was the compound III-like state that slowly converted to the ferric enzyme over 70 s of reaction time. (Figure

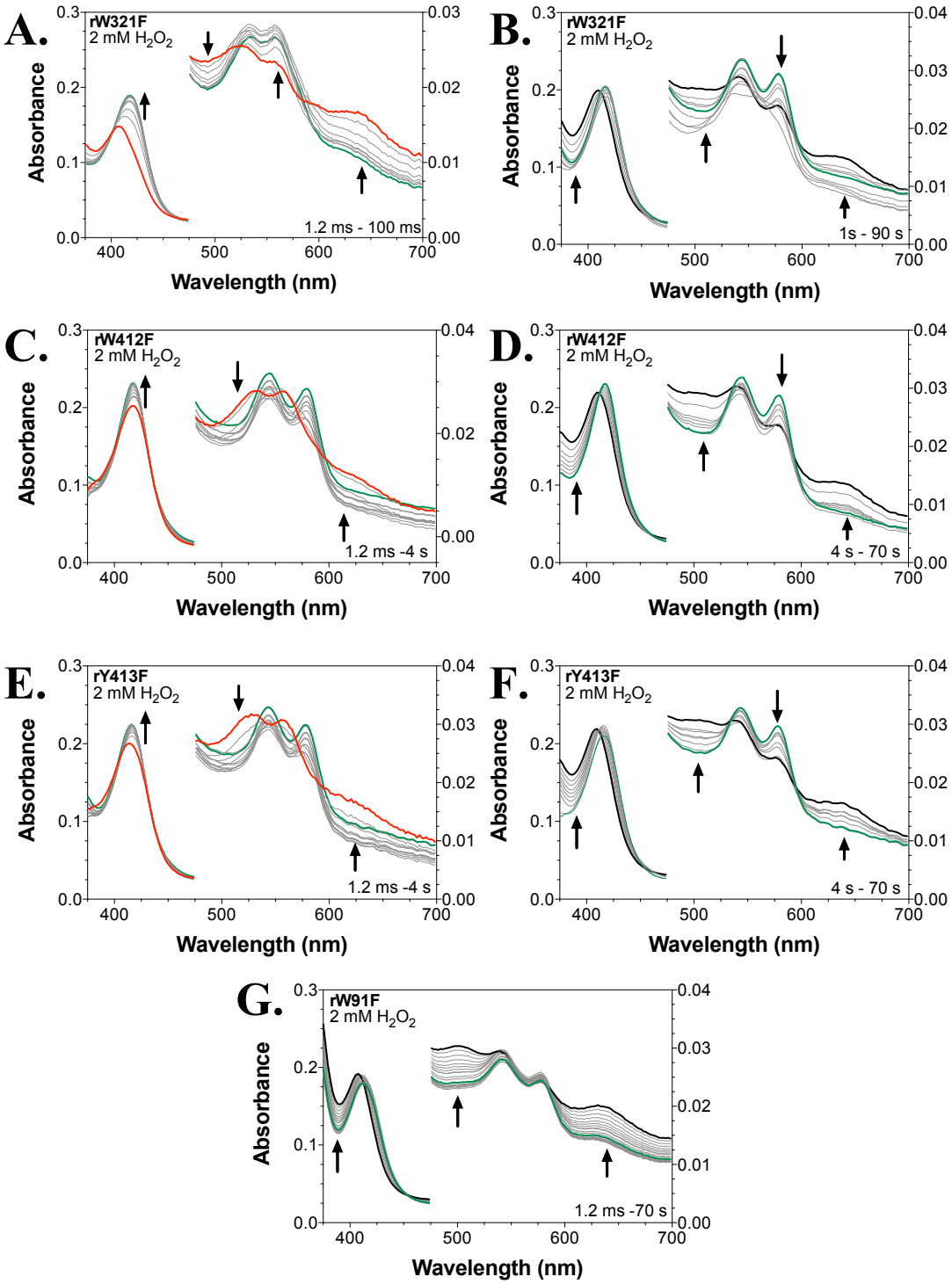

Figure 3.32. Effect of PxED on intermediates observed for *r*KatG Trp/Tyr-substitution variants upon their reaction with steady-state supporting concentrations of H_2O_2. Reactions of *r*W321F (A and B), rW412F (C and D), rY413F (E an F), and rW91F (G) KatG with 667 molar equivalents H_2O_2 were monitored. Panels A, C, and E focus on the earlier time points in the reaction where a compound II-like intermediate tranistioned to a compound III-like intermediate. Panels B, D, and F focus on late reaction events (i.e., up to 70 s) and are characterized by the transition of a compound III-like state back to the ferric enzyme. For *r*W91F evidence of protein aggregation was observed. In addition, a compound III-like intermediate was observed to transition to the ferric enzyme (G). All reactions were carried out using 3 μM KatG reacted with 2 mM H_2O_2, 1 mM ABTS, and 1mM ascorbate in 50 mM acetate, pH 5.0, at 4° C.

3.32G). The lack of accumulation of the compound II state would be consistent with the more rapid reduction of this species by the exogenous PxED present in the reaction. This is consistent with the substantially greater peroxidase activity of *r*W91F KatG and the ability of this variant to accumulate $ABTS^{\bullet+}$ at higher rates and to a greater extent than the other variants evaluated.

The data for the *m*KatG variants was not very conclusive given the substantial light scattering in the spectra as well as enzyme degradation (Figure 3.33). *m*KatG variants reacted with lower concentrations of H_2O_2 in the presence of ABTS and ascorbic acid did not produce any easily identifiable heme states (Figure 3.33A and B). This was expected, as it is not enough H_2O_2 for accumulation of intermediates to occur. However, when higher concentrations of H_2O_2 were introduced in this reaction, we observed a small amount of compound III-like intermediates form before light scattering due to protein aggregation/degradation overwhelmed the spectrum (Figure 3.33C and D).

Oxidizable Residues and the Sustained Catalase Activity of KatG: Extent of O_2 Production

With respect to KatG's catalase activity, there are two principal values which can be determined. Of course, the initial rate of H_2O_2-dependent O_2 production provides the clearest view of enzyme activity unobscured by substrate depletion, product inhibition (if applicable), or enzyme inactivation. From initial rate data, the standard kinetic parameters k_{on} (i.e., k_{cat}/K_M) and k_{cat} can be obtained and compared across variants, reaction conditions, etc. For W321F, W412F, W91F, and Y413F KatG, these values have all been reported in Chapter 2 (see Table 2.1). In contrast, the extent to which KatG catalase activity can be sustained is discerned from the quantity of O_2 produced over the course of

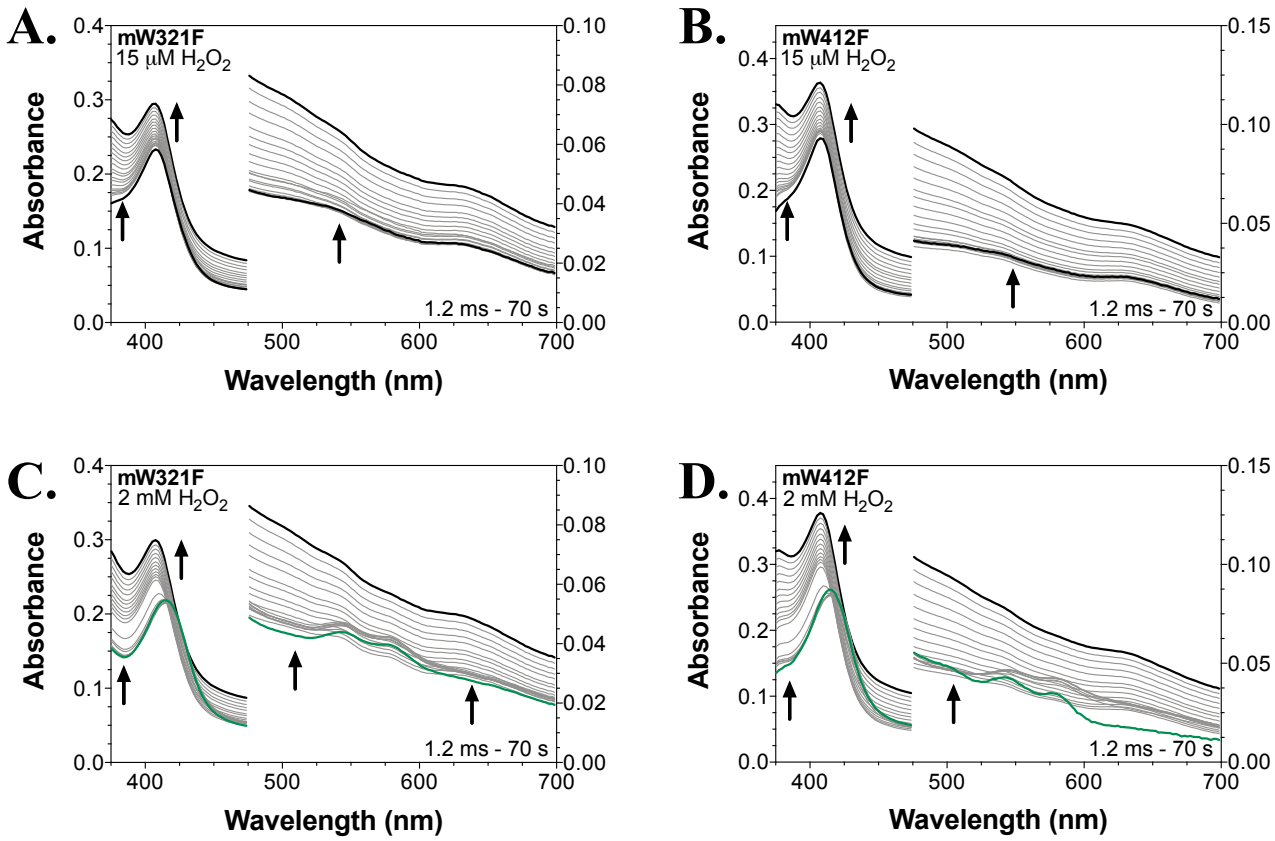

Figure 3.33. Effect of PxED on intermediates observed for *m*KatG Trp/Tyr-substitution variants upon their reaction with steady-state supporting concentrations of H_2O_2. Reaction of *m*W321F (A) and *m*W412F (B) KatG with limited-turnover concentrations of H_2O_2 produced light scattering and no clearly discernable intermediate. Reaction of *m*W321F (C) and mW412F (D) KatG with steady-state supporting concentrations of H_2O_2 reacted with high concentrations of H_2O_2 indicates a Compound III-like formation followed by light scattering and protein degradation (C). *m*W412F reacted with high concentrations of H_2O_2 indicates a Compound III-like formation followed by light scattering and protein degradation (D). All reactions were carried out using 3 μM KatG reacted with the indicated concentration of H2O2 in the presence of 1 mM ABTS and 1mM ascorbate in 50 mM acetate, pH 5.0, at 4° C.

the entire reaction (Figure 3.34). If the quantity of O_2 produced is less than the stoichiometrically expected amount based on the H_2O_2 used to initiate the reaction (2 H_2O_2 consumed to 1 O_2 generated), the enzyme has been inactivated over the course of the reaction. The lower the quantity of O_2 generated, the more rapidly inactivation has taken place. As a general practice, inactivation is confirmed (in parallel reactions) by a second addition of H_2O_2 or fresh KatG. If a second addition of H_2O_2 fails to induce additional O_2 generation and the addition of fresh KatG does produce a new burst of O_2 production, enzyme inactivation is confirmed.

In this study, the extent of O_2 production was evaluated for W321F, W412F, W91F, and Y413F KatG variants. We have previously observed that susceptibility of KatG to inactivation is highly pH dependent with greater sensitivity being observed at acidic (pH 5) as opposed to neutral pH. The capacity for PxEDs to intervene and prevent KatG inactivation is complementary with those conditions that produce greater H_2O_2 sensitivity in the first place.

Within error at pH 7, all of the Phe-replacement variants were able to sustain activity for the complete consumption of H_2O_2 as indicated by the stoichiometric production of O_2 relative to the 0.5 mM H_2O_2 used to initiate the reaction. That is, about 250 μM O_2 was generated in each case (Figure 3.35A). In each case, the addition of more H_2O_2 resulted in the production of additional O_2, indicating that active enzyme remained, not only for the wild-type enzyme, but also each of the Phe-substitution variants. As an alternative way to understand the data, one can consider the number of catalytic cycles the typical KatG active site undergoes prior to inactivation. This value is estimated simply by dividing the total concentration of O_2 generated (a once-per-cycle event) by the

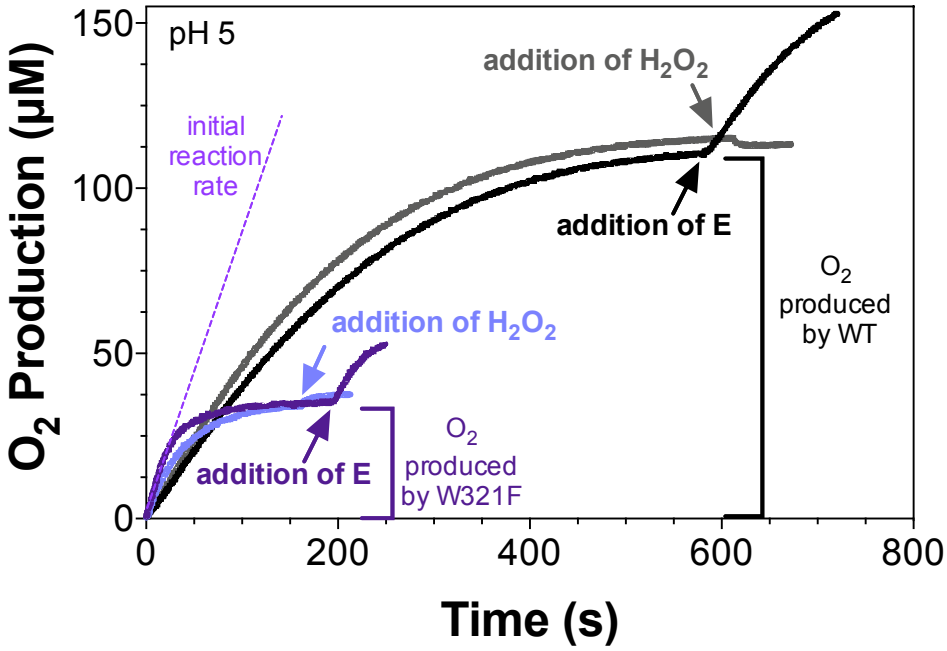

Figure 3.34 Kinetic and stoichiometric evaluation of KatG-based O_2 production. Catalatic O_2 production by W321F KatG is indicated in purple and lavender traces. Purple corresponds to an experiment where a second aliquot of enzyme (E) is introduced after the cessation of O_2 production from an initial introduction of H_2O_2. Lavender corresponds to an experiment where a second aliquot of H_2O_2 is introduced at the end of the initial reaction with H_2O_2. The calculated initial rate of O_2 production by W321F KatG is shown by the dashed tangent line. The calculated extent of O_2 production by W321F KatG is shown by the purple square bracket. In this experiment, roughly 30 μM O_2 is generated out of a possible 250 μM. That more O_2 production is observed only on adding more enzyme but not more H_2O_2 demonstrates that W321F KatG has been inactivated over the course of its reaction with H_2O_2. Traces for WT KatG O_2 production are shown in black and grey. Grey indicating the addition of more H_2O_2 and black indicating the addition of more enzyme (E) at the conclusion of the initial reaction with H_2O_2. The extent of O_2 production by WT KatG (black bracket) in this is experiment is ~100 μM out of an anticipated 250 μM. As with W321F KatG, the WT enzyme has been inactivated in this particular reaction. All reactions included 5 nM enzyme and were initiated by the addition of 0.5 mM H_2O_2. All reactions were carried out at ambient temperature in 50 mM acetate, pH 5.0.

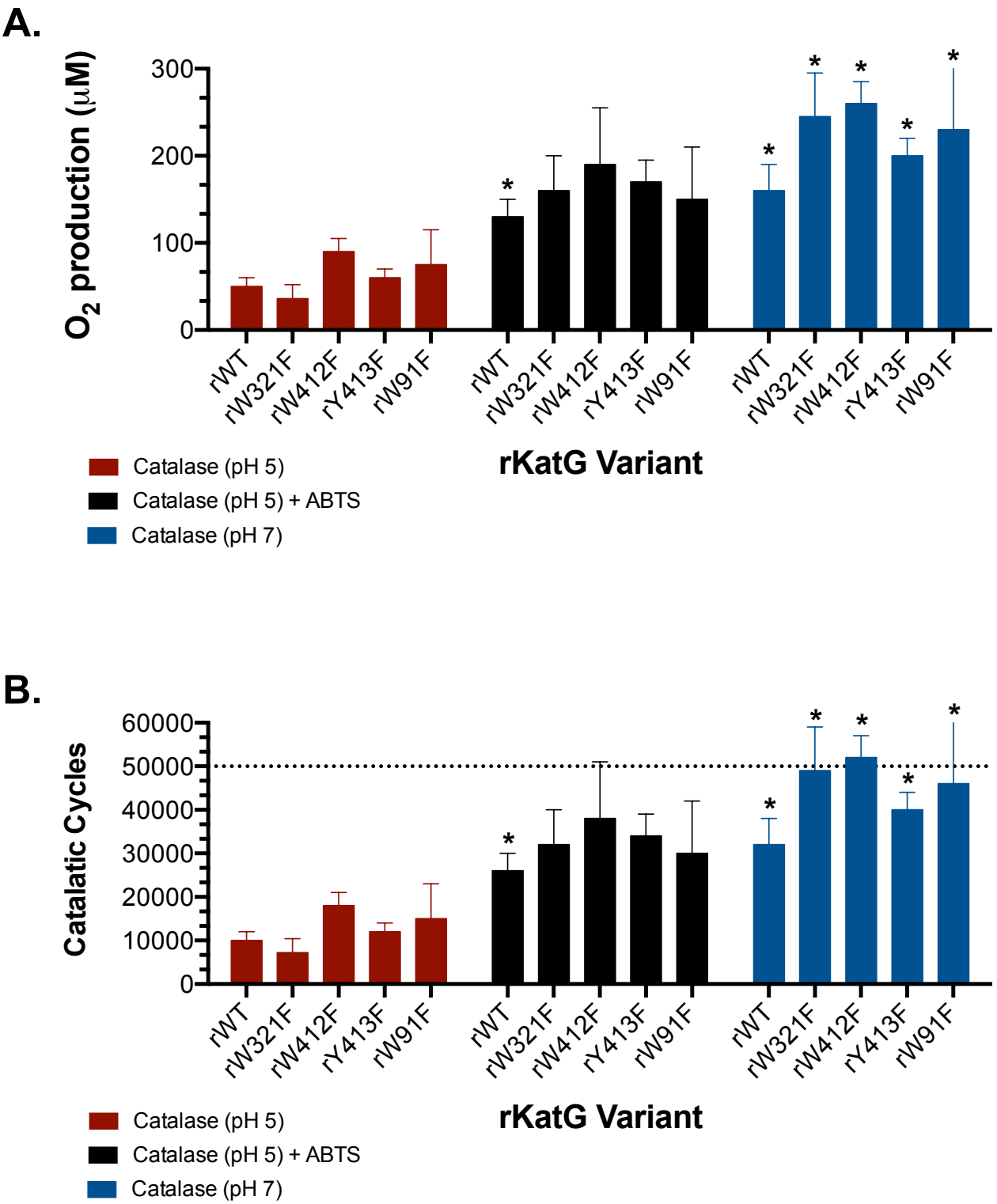

Figure 3.35. Extent of O_2 production by Trp/Tyr substitution variants of KatG. Catalatic O_2 production by the *r*KatG forms of each variant are plotted in terms of O_2 concentration produced (μM) (A) and in terms of catalatic cycles (B) (i.e., $[O_2]$ produced/$[E]_T$). Shown in red are results for reactions carried out at pH 5 in the absence of ABTS, in black are the reactions carried out at pH 5 in the presence of 0.01 mM ABTS, and in blue are the reactions carried out at pH 7 without ABTS. All reactions included 5 nM KatG and were initiated by the addition of 0.5 mM H_2O_2 at ambient temperature. Reactions were carried out in either 50 mM acetate, pH 5.0, or 100 mM phosphate, pH 7.0. Asterisks indicate variants/conditions where active enzyme remained at the conclusion of the assay.

concentration of active sites (determined from the quantity of heme present). By this calculation, one anticipates that the complete consumption of H_2O_2 in these experiments will require, on average, 50,000 catalytic cycles per active site.

In contrast to the sustained activity of KatG and its variants at pH 7, WT KatG and all of the variants were inactivated at pH 5 prior to the complete consumption of H_2O_2. This was confirmed by the complete lack of additional O_2 production upon the addition of more H_2O_2 to these reactions. Notably, this was observed for the *r*KatG *and* *m*KatG preparations of enzyme (Figure 3.36). With respect to the *m*KatG enzymes, there was a marked distinction between *m*WT KatG, which managed 21,000 ± 3,000 catalytic cycles before inactivation, and *m*W321F KatG which, was only able to achieve 7,000 ± 3,000 cycles with *m*W91F, *m*W412F, and *m*Y413F falling in between these two endpoints. As expected, when ABTS was included as a PxED in reactions carried out at pH 5, the WT KatG and all variants produced more O_2 than in the absence of ABTS. This was observed for the mKatG and rKatG preparations of all the variants. Surprisingly, only the *m*WT enzyme retained activity to the complete consumption of H_2O_2 (52,000 ± 5,000 cycles), and though *r*WT KatG did not produce the expected concentration of O_2, it was clear that the enzyme remained active for reaction with additional H_2O_2. For all the phenylalanine substitution variants no additional O_2 production was observed upon the addition of a second aliquot of H_2O_2 to each reaction (Figure 3.36). In general, reactions that occurred at pH 5, without ABTS, produced the least amount of oxygen across all variants. At pH 5 without ABTS *r*W321F KatG stands out from the other variants as it produced around 25 μM O_2 while the other variants produced around 50-75 μM O_2. Also, at pH 5 without ABTS the *m*KatG variants produced lower O_2 overall while producing

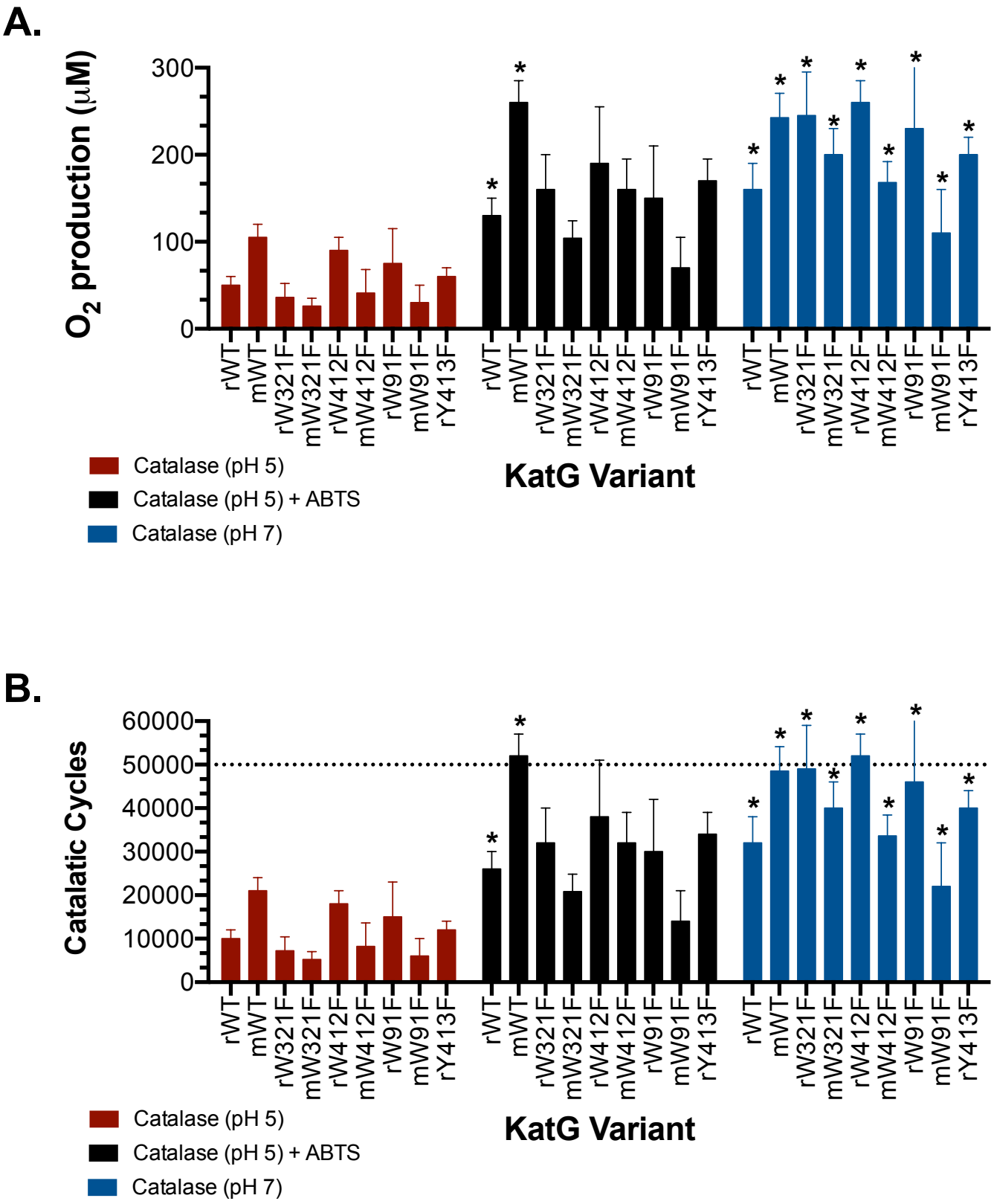

Figure 3.36. Extent of O_2 production by Trp/Tyr substitution variants of KatG. *r*KatG and *m*KatG preparations of the variants are compared in terms of [O_2] produced (μM) (A) and catalatic cycles (B). Shown in red are reactions carried out at pH 5 in the absence of ABTS, in black are the reactions carried out at pH 5 in the presence of 0.01 mM ABTS, and in blue are the reactions carried out at at pH 7 in the absence of ABTS. Reaction conditions were as described for Figure 3.35. Asterisks indicate variants/conditions where the enzyme retained catalase activity at the conclusion of an initial reaction with H_2O_2.

similar ratios across variants. When ABTS was introduced at pH 5, the overall production of O_2 increased significantly to around 200 μM for *r*KatG variants and 150 μM for *m*KatG variants. The interesting thing about pH 5 with ABTS and without ABTS is that with all variants enzyme inactivation was observed. This is unusual because with WT KatG, ABTS is able to prevent the enzyme from inactivation. The observed inactivation despite the presence of PxED indicates these oxidizable amino acids are necessary for electron transfer to the surface of the enzyme to prevent the enzyme from inactivation.

Oxidizable Residues and the Sustained Catalase Activity of KatG: Catalase Inactivation

We then investigated how much catalase activity these enzymes could preserve when pre-treated with varying amounts of H_2O_2 (Figure 3.37). Invariably, prereaction with H_2O_2 results in KatG inactivation. We have observed that pH, variant identity and other factors have a direct impact on the quantity of H_2O_2 that KatG can remove in pre-reaction before it is inactivated. Accordingly, in these "inactivation assays" we aim to quantitate each KatG protein's ability to resist H_2O_2-dependent inactivation. For the W321F variant, resistance to peroxide-based inactivation was markedly different between *r*W321F KatG and *m*W32F KatG. Specifically, *r*W321F KatG appeared to gain activity with the first 1,000 equivalents of H_2O_2, whereas *m*W321F retained about the same activity as untreated enzyme with these lower concentrations of H_2O_2 used in pre-treatment. As the equivalents of H_2O_2 used in pretreatment increased, *m*W321F KatG exhibited a lower resistance to H_2O_2-dependent inactivation than *r*W321F KatG (Figure 3.37A). With the other KatG variants, *r*W412F (Figure 3.37B), *r*W91F (Figure 3.37C), and *r*Y413F (Figure 3.37D), the lower equivalents were similar in that *r*KatG variants increased activity and *m*KatG variants remained the same. However, the other KatG

variants retained similar inactivation rates when treated with higher concentrations of H_2O_2.

We extended our study by determining relative sensitivity to H_2O_2-based inactivation by evaluating the quantity of peroxide necessary to produce complete inactivation of each variant. We found that among the *r*KatG variants, *r*W321F KatG was the most sensitive to inactivation, requiring the lowest number molar equivalents of H_2O_2 in pretreatment to produce complete inactivation of the enzyme. The rW321F variant followed by *r*W91F and *r*Y413F, which were inactivated by about the same concentration of H_2O_2 (Figure 3.38A). Surprisingly, *r*W412F KatG was not easily inactivated. Even upon prereaction with high concentrations of H_2O_2, *r*W412F KatG was able to retain activity. Evaluation of the *m*KatG variants showed that all became inactivated at about the same concentration of H_2O_2. The *m*W91F variant showed a slightly greater sensitivity to H_2O_2. However, this result may be due more to protein quality rather than the specific substitution itself (Figure 3.38B). Taken together, our data suggest that *r*W321F KatG displays the poorest resistance to inactivation by H_2O_2, indicating that W321 is more frequently involved in preventing inactivation via through-protein electron-hole transfer away from the active site. These data also suggest that W412 and Y413 have the least involvement in preventing the inactivation of KatG's catalase activity, Substitutions of these residues with nonoxidizable Phe were able resist inactivation the most effectively of all the Phe-substitution variants. The W91F variant showed a moderate resistance to inactivation, that the frequency for utilization of this residue for through-protein electron transfer may be less than the other residues evaluated in this study.

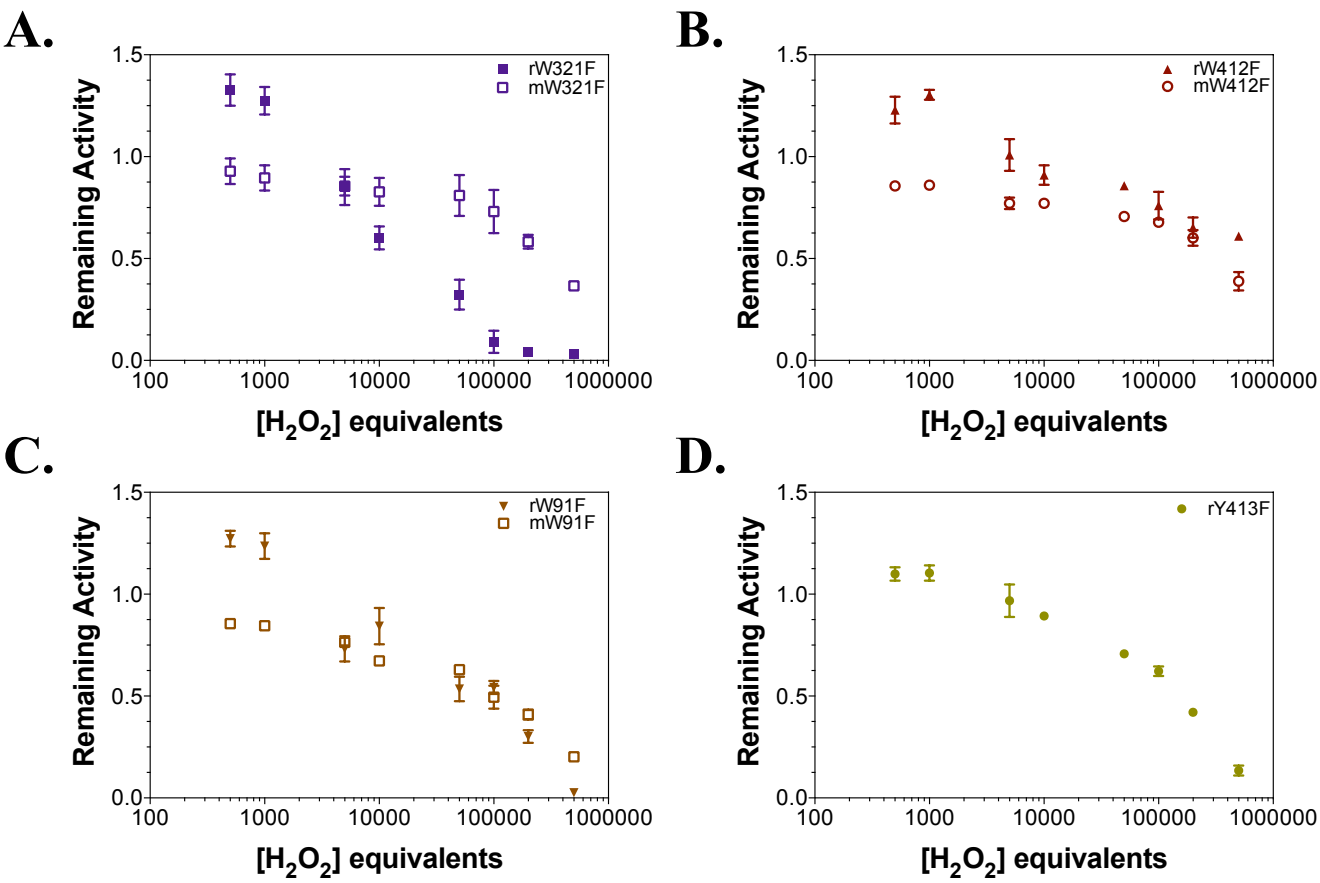

Figure 3.37. Sensitivity of KatG variants to peroxide-dependent inactivation. The *r*KatG and *m*KatG forms of W321F (A), W412F (B), and W91F (C) KatG were compared for sensitivity to peroxide-based inactivation by pre-reacting each enzyme with the indicated concentrations of H_2O_2 (in terms of molar equivalents) indicated. Because only the *r*KatG form of Y413F was available it is plotted alone (D). The concentration of the enzyme pre-reaction with H_2O_2 was so that the final concentration in the second reaction would be 200 nm. The second reaction was conducted in the cuvette of the UV-Vis with 50 mM acetate, pH 5.0. This reaction was monitored at 240 nm over 60 s.

Oxidizing equivalents required for the formation the MYW adduct

In this study, we sought to determine the number of molar equivalents of peroxide necessary to fully form the MYW adduct. To do this, we treated the enzyme with increasing equivalents of peroxide, followed by trypsinization of the enzyme and separation of the peptides by HPLC. From our LC-MS (see Chapter 2), it was determined that peak in the elution profile at 32 min corresponded to the MYW cofactor and its associated peptides. The area under this peak associated was averaged across three different trials and normalized. From these data, we estimated that *r*W321F KatG required 5 equivalents of peroxide to fully form the MYW cofactor (Figure 3.39), which is one more than that proposed in the mechanism mentioned above. There is also some error in this experiment as higher than 5 equivalents the error bars seem to increase dramatically. This experiment will be done with the other variants in the future to compare how many equivalents are needed based on how many active site oxidizable amino acids are present.

Conclusions

Impact of Oxidizable Residue Networks on MYW cofactor formation

After making KatG Trp/Tyr substitution variants, we were able to produce these proteins in their *r*KatG and *m*KatG forms, and we confirmed that only a small proportion of the former contained the MYW adduct. Accordingly, we used several methods to analyze the formation of the MYW adduct in the *r*KatG form of our Trp/Tyr substitution variants. Using these methods, we demonstrated character and reactivity of the *r*W321F KatG, *r*W412F KatG, *r*W91F KatG, and *r*Y413F KatG as well as their *m*KatG counterparts, where available.

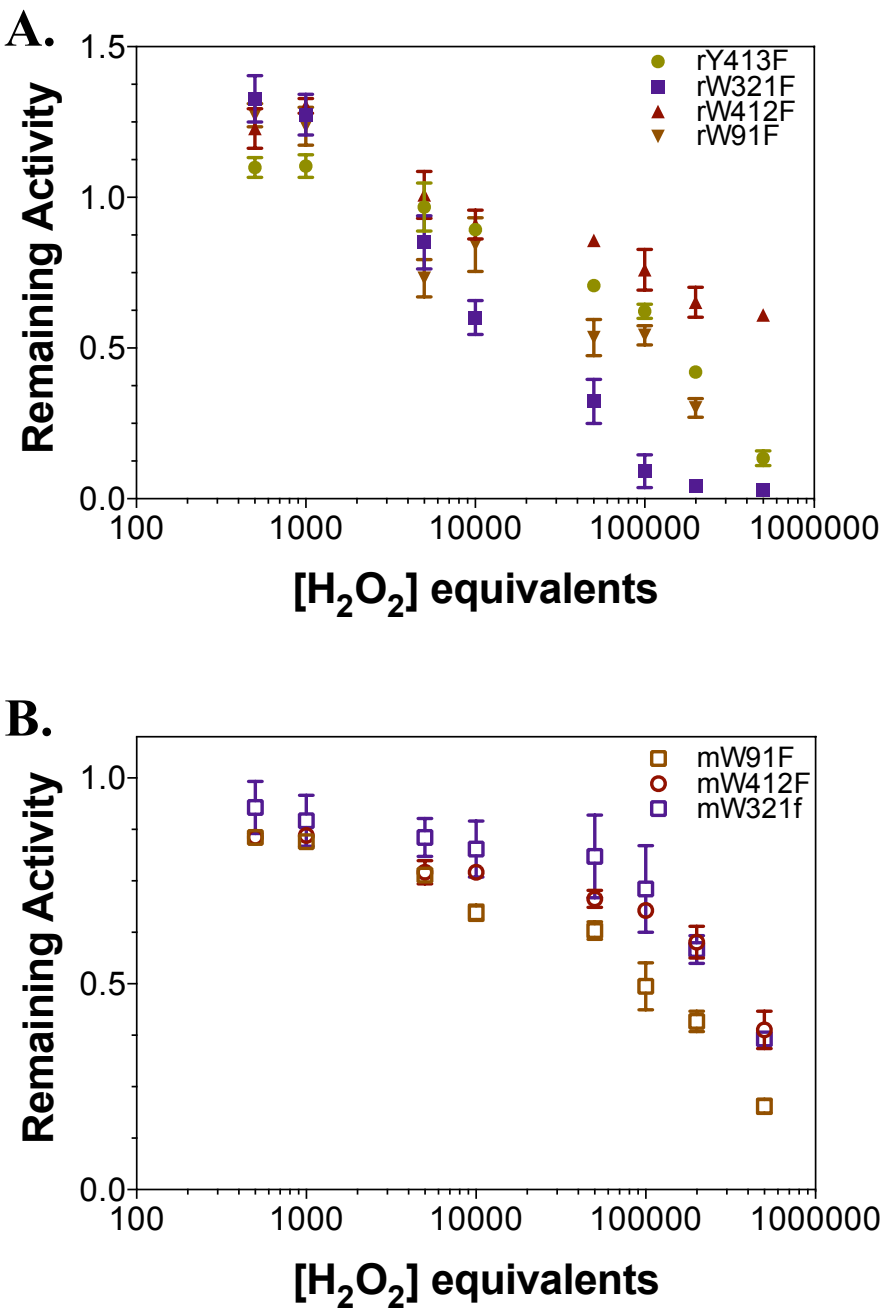

Figure 3.38. Comparison of rKatG variant preparations (A) and mKatG variant preparaations for their sensitivity to peroxide-dependent inactivation. Pre-reaction conditions and the conditions used to measure remaining activity are described in Figure 3.37.

With the *r*KatG preparations of all of the variants, intermediates were detected with limited-turnover concentrations of H_2O_2 that are not possible to detect with the *m*KatG preparations. Specifically, an intermediate with all the marks of a peroxidase Fe^{IV}=O (i.e., compound II) state was observed for all the variants. For all of the variants except *r*W321F KatG, the preceding formation of compound I (i.e., the Fe^{IV}=O[porphyrin]$^{\bullet+}$ state) could not be observed. It was anticipated that this was due to a very rapid intramolecular electron transfer to generate a protein-based radical at the expense of the porphyrin π cation radical. Remarkably, a compound I intermediate was readily detected with rW321F KatG. A much slower apparent intramolecular electron transfer ($k \sim 4\ s^{-1}$) enabled us to capture this species prior to its conversion to a compound II-like state. These data suggest that the proximal tryptophan (i.e., W321) is at least involved in very rapid reduction of the compound I porphyrin π cation radical. Importantly, the ability to capture these intermediates (Fe^{IV}=O[porphyrin]$^{\bullet+}$ and/or Fe^{IV}=O) was eliminated if the *r*KatG forms of these proteins were pretreated with a limited number of equivalents a peroxide unable to support catalase activity (e.g., peracetic acid). Under these circumstances, behavior analogous to the *m*KatG preparations of the variants was observed instead. These data confirmed that the lack of the MYW adduct and the catalase activity it supports accounted for the novel KatG kinetic behavior we observed with rKatG preparations of all of these Trp/Tyr substitution variants.

With the *r*KatG form of all the variants, the absence of the MYW adduct also had a clear impact on the early intermediates observed in reactions containing steady-state supporting concentrations of H_2O_2. Indeed, this behavior could best be characterized as a

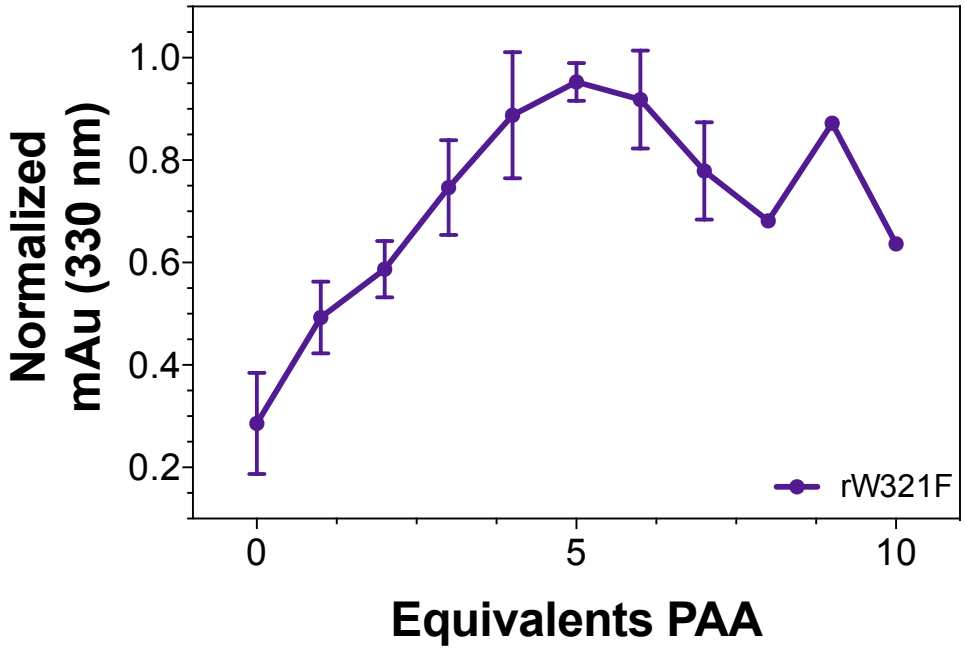

Figure 3.39. Equivalents of PAA needed to form the MYW adduct. *r*W321F KatG was first reacted with the number of molar equivalents of PAA indicated. The reacted enzyme was then trypsinized and the resulting peptides separated by LC, monitoring elution at 330 nm. The eluting MYW adduct and associated tryptic peptides (~32 min.) were quantitated using the area under the elution peak. These values were normalized against the maximum observed signal. Data points represent the average of four trials with standard deviations represented by the error bars. The maximum signal was detected following treatment with 5 equivalents of PAA, indicating the quantity needed to fully establish the adduct in KatG which lacks its proximal tryptophan (W321).

pre-steady-state condition. As above, intermediates that are never observed with the *m*KatG preparations of these variants were detected. Most prominently, a Fe^{IV}=O state was detected that gave way to a species with features of a Fe^{III}-$O_2^{\bullet-}$ state. With KatG, this type of intermediate is known to dominate during the steady-state removal of H_2O_2 by the enzyme's catalase activity. Together, these data suggested that an early Fe^{IV}=O state transitioned to a catalase-active form, giving rise to a steady-state phase dominated by a compound III-like intermediate. This was supported by the depletion of H_2O_2 in the reaction following the appearance of the Fe^{III}-$O_2^{\bullet-}$ state. Upon H_2O_2 depletion the return of the ferric (i.e., resting) state of each rKatG variant was observed. As with limited-turnover conditions, *r*W321F KatG was distinct in that a compound I form was observed in the pre-steady-state phase of the reaction. In addition, as with the limited-turnover experiments, prereaction of these rKatG proteins with PAA produced the kinetic behavior observed with the *m*KatG proteins. Specifically, the pre-steady-state formation of the Fe^{IV}=O state was not detected, rather, the Fe^{III}-$O_2^{\bullet-}$ was observed to contribute to the steady-state kinetic depletion of the H_2O_2 in the reaction followed by the slow return of the resting enzyme. Remarkably, this kinetic behavior enabled us to observe the irreversible single-exponential increase in absorbance at 315 nm which, occurred only in the pre-steady-state phase. This reaction always concluded before the appearance of the Fe^{III}-$O_2^{\bullet-}$ state and the steady-state catalase consumption of H_2O_2. Absorption at this wavelength range and at these intensities is consistent with the features of the MYW adduct and its covalent precursors (e.g., YW and YW quinoid).[34, 43] Together, these data indicate that we are monitoring, *in real time*, the establishment of the MYW adduct in the pre-steady-state phase of rKatG variants' reaction with H_2O_2.

This observation enabled us to compare the apparent kinetics of MYW formation observed at 315 nm. Remarkably, we observed that by this measure none of the Trp/Tyr substitutions had very large impact on the kinetics of pre-steady-state MYW formation (Figure 3.40). Indeed, the apparent rate constants obtained from single-exponential fits of the data for *r*W412F, *r*W91F, and *r*Y413F KatG were indistinguishable. Only the rW321F KatG variant showed an acceleration (~ two-fold) of MYW adduct formation, suggesting that the presence of the proximal tryptophan may slow the post-translational maturation of the KatG enzyme. Therefore, we conclude from these preliminary data that the proximal tryptophan plays an ancillary but not a crucial role in the formation of the MYW adduct. We also demonstrated that, W412F, W91F, and Y413F, most likely are not involved in the formation of the MYW adduct.

Future studies to determine the number of peroxide/oxidizing equivalents needed based on the residues available will need to be done by LC-UV and LC-MS/MS. This would be a direct way to observe if any of the residues have an impact on MYW cofactor formation. Other studies to confirm the electronic structure of heme intermediates involved in the MYW adduct formation and the kinetics of each step in the mechanism will also need to be completed. All of these things can be accomplished with a combination of optical stopped-flow, RFQ-EPR, and RFQ-Mössbauer spectroscopies along with LC-MS and LC-MS/MS analyses.

KatG Through-protein Radical Transfer and Preservation of Catalytic Activity

KatG is able to perform its peroxidase activity by utilizing its many oxidizable amino acids for through-protein electron transfer. In this chapter we investigated the impact of removing (i.e., rendered non-oxidizable) some of these active-site oxidizable

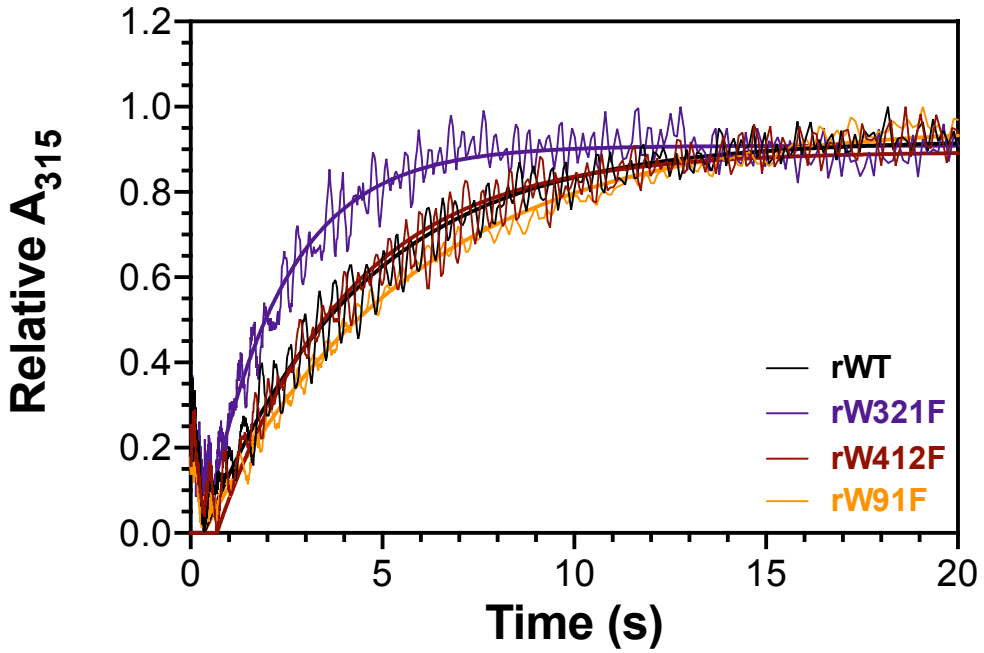

Figure 3.40. Change in absorbance at 315 nm when reacted with steady-state concentrations of H_2O_2. *r*WT indicated in black, *r*W321F indicated in purple, *r*W412F indicated in red, and *r*W91F indicated in orange.

residues on the enzyme's ability to produce O_2, prevent inactivation/sustain catalatic turnover. This included detection of changes in heme intermediates when reacted with H_2O_2, PAA, ABTS, and ascorbate, monitoring the ability to produce $ABTS^{\bullet+}$, and finally, the change in protein-based radical by RFQ-EPR at early reaction times. The ability to produce O_2 was retained for all variants across multiple conditions (i.e, pH 5, pH 5 with ABTS, and pH 7). Two phenomena of interest occurred when we evaluated O_2 production. First, *r*W321F KatG and *m*W321F KatG produced a significantly lower amount of O_2 than any other variant at pH 5. Second, when ABTS was present at pH 5 all variants (i.e., W321F, W412F, W91F, and Y413F) increased in the amount of O_2 produced accordingly. However, in contrast to WT KatG, all were inactivated at the end of the reaction. This was consistent regardless of the form of enzyme used, *r*KatG or *m*KatG. This was noteworthy because the consistent observation with WT KatG is that the presence of ABTS prevents the enzyme from inactivation.[44, 51]

The W321F variant also was of particular interest when we analyzed the return of the ferric state when reacted with H_2O_2 alone. This reaction required more steps than any of the other variants to return to the ferric enzyme. Following that, *r*W412F KatG also stood out in it showed the most rapid return of the ferric state, followed by *r*W91F KatG and *r*Y413F KatG; these were highly similar to *r*WT KatG. We observed the same trend in the ability of the variants to generate $ABTS^{\bullet+}$. With *r*W321F KatG standing out with its difference in rate of production, followed by *r*W412F KatG producing the least amount of $ABTS^{\bullet+}$, then *r*Y413F KatG, and *r*W91F KatG producing the most $ABTS^{\bullet+}$. This trend makes since as W412 and Y413 are so close together and are in the same path from the active site to the surface of the enzyme. It also makes sense that *r*W91F KatG

would have the least affect, as it is the furthest away from the active site, and therefore, the least likely to be utilized. The rate of inactivation was also analyzed and resulted in similar trends as seen before. *r*W321F KatG was inactivated at the faster rate with *r*W412F KatG being the most resistant to inactivation and *r*Y413F KatG following closely with *r*W412F KatG. Finally, *r*W91F KatG showed inactivation in the middle of all of these variants. RFQ-EPR also showed that *r*W321F was undergoing a different reaction than the other variants and *r*W412F KatG and *r*Y413F KatG showed almost identical spectrum. Overall, from the results presented in this chapter, we can conclude that W321 is used the most often as an offsite electron transfer followed by W412 and Y413 in tandem and W91 is used the least out of these pathways.

As observed throughout this research, the W321F KatG variant has continued to stand out in almost all aspects of its kinetic and functional behavior relative to the wild-type enzyme and other variants. Clearly, it is not essential for *catalase* activity, but it is also unmistakable that the proximal tryptophan has an impact on all aspects of KatG catalysis. Nevertheless, the mechanisms by which it participates in and modulates KatG function remain poorly defined.

Chapter 4: Kinetic evaluation of the S315T KatG variant

Introduction

KatG is found in numerous bacterial and fungal pathogens. Perhaps the most notorious of these is *Mycobacterium tuberculosis* (*Mtb*), which is the causative agent for the lung disease tuberculosis (TB). Isoniazid (INH), rifampin (RIF), ethambutol (EMB), and pyrazinamide (PZA) are the primary, front-line drugs for treatment of TB. KatG is thought to activate the antituberculosis durg isoniazid (INH).[92] Multi-drug resistant (MDR) TB strains occur due to resistance to the two most often administered antitubercular drugs, rifampin and INH. Isoniazid resistance arises most often due to mutations to the *katG* gene, and the single most common KatG modification observed in isoniazid-resistant *Mtb* is the S315T substitution. A recent study found a frequency of 48.33% with the S315T KatG mutation among MDR TB patients in South Sumatra.[72] The *Mtb* bearing the S315T KatG variant show a minimum concentration that inhibits 50% of bacterial growth (i.e., MIC_{50}) for INH treatment that is over 100-fold greater than that observed for WT KatG.[93] Interestingly, despite its near complete loss INH activation, the S315T KatG enzyme loses little, if any, of its catalase or peroxidase activities.[64, 65, 93] This negligible loss in catalase activity is consistent with the prominent selection for this mutation in *Mtb* as a result of INH treatment. Essentially, a strain with S315T KatG substitution can still effectively remediate oxidative stress while simultaneously preventing INH activation. The most notable alteration caused by the S315T substitution in KatG is the narrowing of its active-site channel (Figure 4.1A and C). This dramatic difference is caused by the addition of the methyl group in the change from Ser to Thr in S315T KatG (Figure 4.1B and D). This variant is known to cause

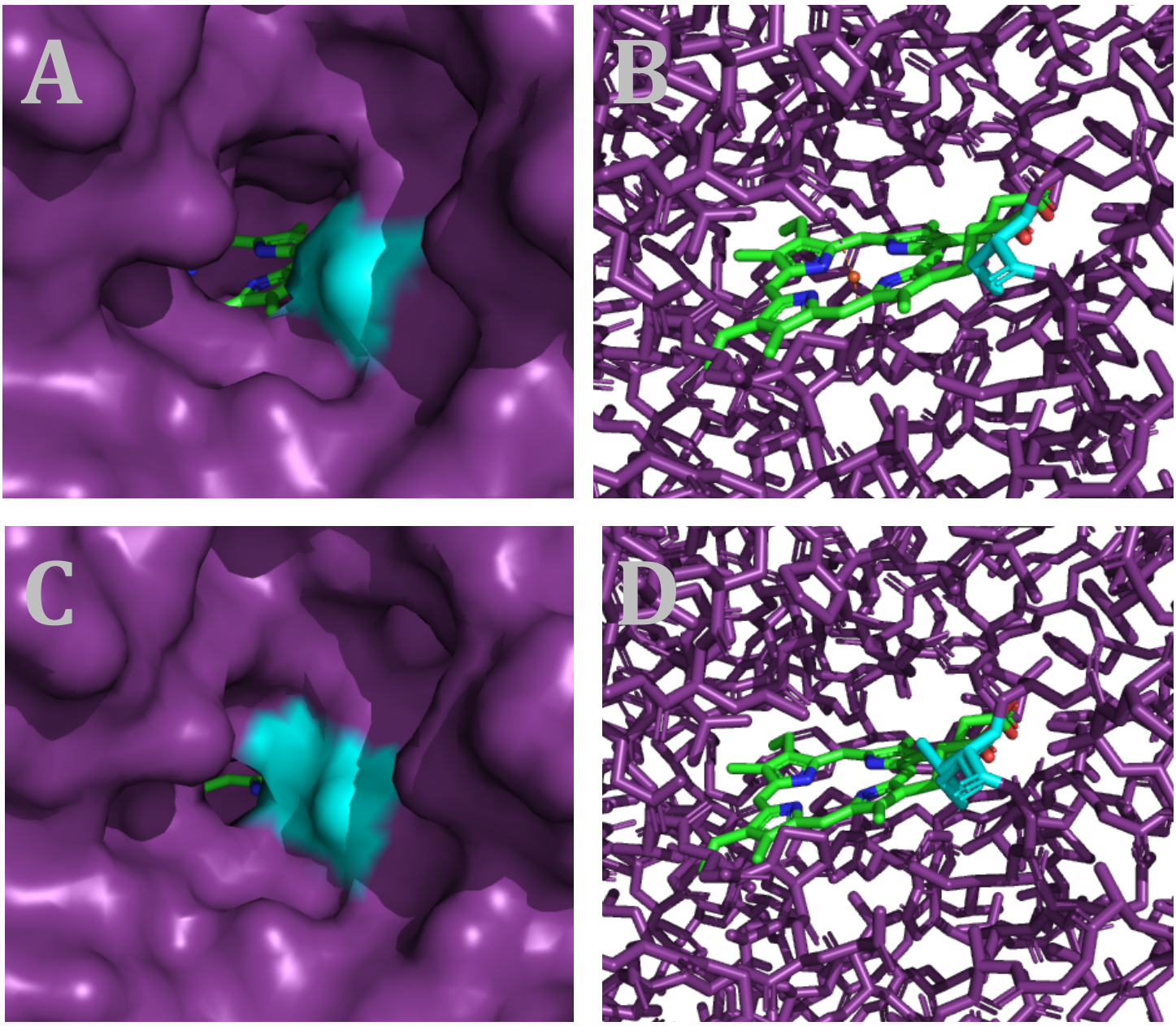

Figure 4.1. Effect of S315T substitution on the active-site access channel of KatG. The active-site channel of WT KatG is very narrow relative to other peroxidases (A), and it is made even more narrow with the S315T substitution (C). The WT KatG has a wider access channel than S315T KatG variant because there is no extra methyl group in the access channel (B) that is found in the access channel of S315T KatG variant (D). This image was constructed using PyMol, from coordinates deposited under the PDB accession entry 2CCA.[94]

modifications to the heme pocket as well as to generate have quantum mechanically mixed spin states for its resting state heme.[75] Despite its substantial distance from the heme iron, the S315T substitution does impact the heme environment and the network of H-bonded H_2O molecules that line the active site access channel. Because this variant is known to cause so much change in the heme states, which are closely related to the formation of the MYW adduct, it is possible that this variant will also have an effect on the formation of the MYW adduct.

Materials and Methods:

All materials and methods for this chapter have been discussed in previous chapters. For expression and purification, as well as spectral analysis and LCMS/MS see Chapter 2. For stopped-flow analysis, inactivation assay, and all other materials and methods see Chapter 3.

Results and Discussion

The S315T KatG variant was expressed and purified in two forms, as explained in Chapter 2. These two forms were then analyzed and it was concluded that the reconstituted S315T KatG variant (*r*S315T) did not have a fully formed covalent adduct and the mature S315T KatG variant (*m*S315T) did have a fully formed and functioning covalent adduct. In this chapter we will go more in depth on the effects S315T had on the formation of the adduct, as well as the effects this mutation had on the enzyme. These effects include the changes in heme intermediates, the rate of $ABTS^{\bullet+}$ observed, and the effects of pH on the extent of oxygen production.

Stopped-flow intermediates observed

Just as with other reconstituted proteins, heme state transitions were observable with *r*S315T KatG reacted with lower concentrations of H_2O_2. We also observed an additional heme state transition intermediate with *r*S315T KatG than we did with *m*S315T KatG, consistent with other KatG variants. When *r*S315T was reacted at low concentrations of H_2O_2, we observed a ferric enzyme transitioning to a Compound II-like intermediate followed by a return of the ferric state (Figure 4.2A). We were also able to observe a Compound II-like intermediate transition into a Compound III-like intermediate followed by a return of the ferric state when we reacted *r*S315T KatG with higher concentrations of H_2O_2 (Figure 4.2B). These observed intermediates are consistent with the intermediates observed for WT KatG at the corresponding H_2O_2 concentrations. Unfortunately, when we went to look at the intermediates for *m*S315T reacted with H_2O_2, we were not able to observe any clear intermediates (Figure 4.3). This could have been from poor protein quality or other unknown factors.

We investigated the intermediates we could be detected using alternative peroxides, specifically peracetic acid (PAA). PAA reacts with the enzyme's heme to form high-valent intermediates (e.g., Fe^{IV}=O[porphyrin]$^{\bullet+}$ or Fe^{IV}=O), but it does not allow the enzyme to turn over as a catalase in the way that H_2O_2 does. When *r*S315T was reacted with PAA, we observed a compound II-like intermediate followed by a compound III-like intermediate (Figure 4.4A). Because PAA cannot be a substrate to return the enzyme to its ferric state (*contra* H_2O_2), no further progression of intermediates was observed. The intermediates observed did not change with the increased concentration of PAA, only the rates of formation and decay of the observed intermediates changed. When we

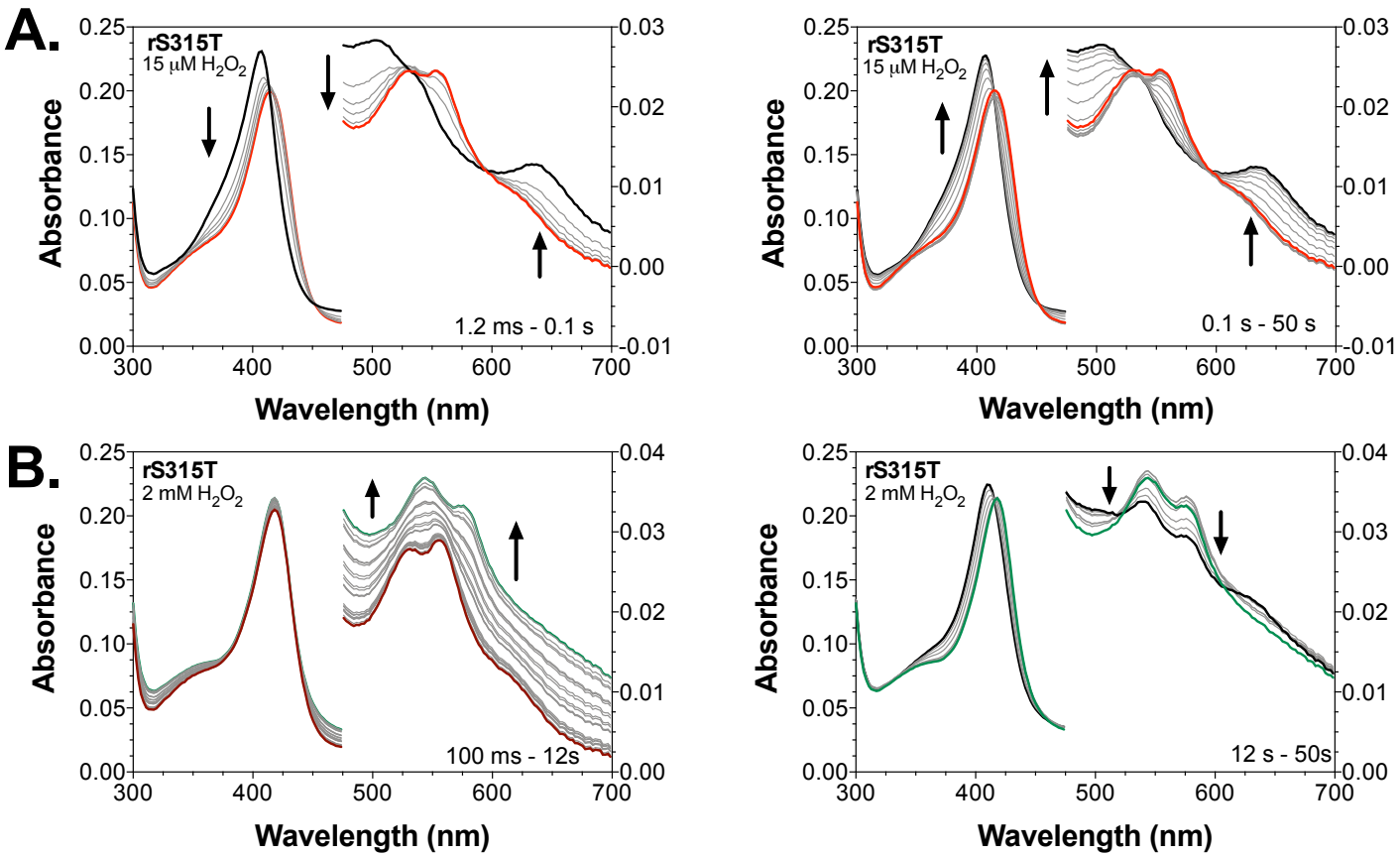

Figure 4.2. Heme states observed for *r*S315T KatG upon reaction with limited-turnover (A) and steady-state-supporting H_2O_2 concentrations (B). 15 μM H_2O_2 reaction with *r*S315T KatG was monitored to the formation of compound II at 0.1 s (A, left panel) and to the return of the ferric enzyme (A, right panel). 2 mM H_2O_2 reaction with *r*S315T KatG shows a conversion of compound II to a compound III-like state over 12 s (B, left panel) followed by a return to the ferric state (B, right panel). In all panels, the ferric state is represented by a heavy black spectra, compound II is represented by the red spectra, and the compound III-like state is represented by the green spectra. All reactions were carried out using 3 μM KatG in 50 mM acetate, pH 5.0, at 4° C.

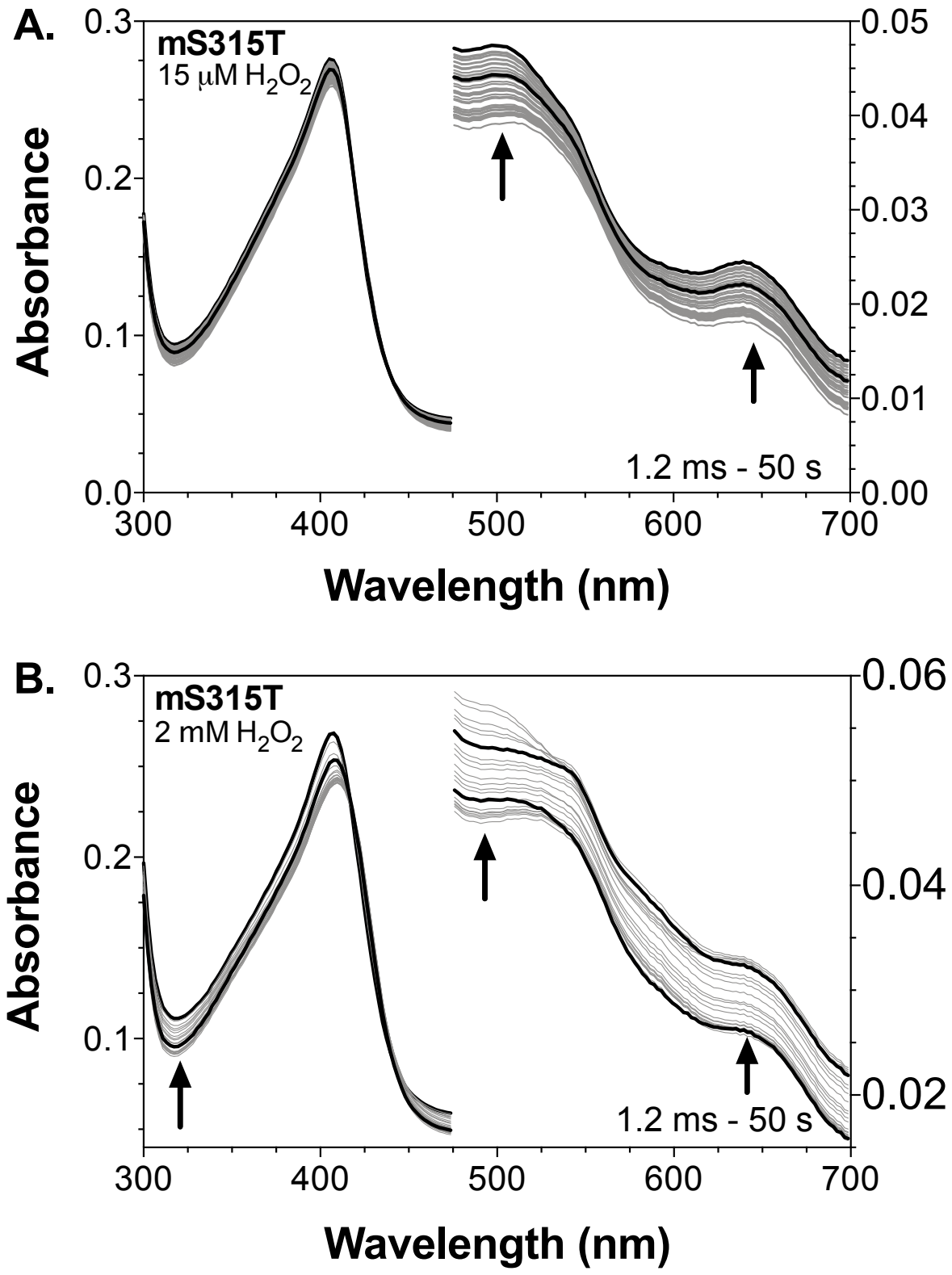

Figure 4.3. Optical spectra recorded for *m*S315T KatG reaction with limited-turnover (A) and steady-state-supporting concentrations of H_2O_2. The reaction of mS315T with 15 μM H_2O_2 was monitored over a period of 50 s without appreciable change in the ferric state. Reaction of mS315T with 2 mM H_2O_2 was also monitored over a period of 50 s. Here as well, changes to the ferric state appeard to be minimal (B). All reactions were carried out using 3 μM KatG in 50 mM acetate, pH 5.0, at 4° C.

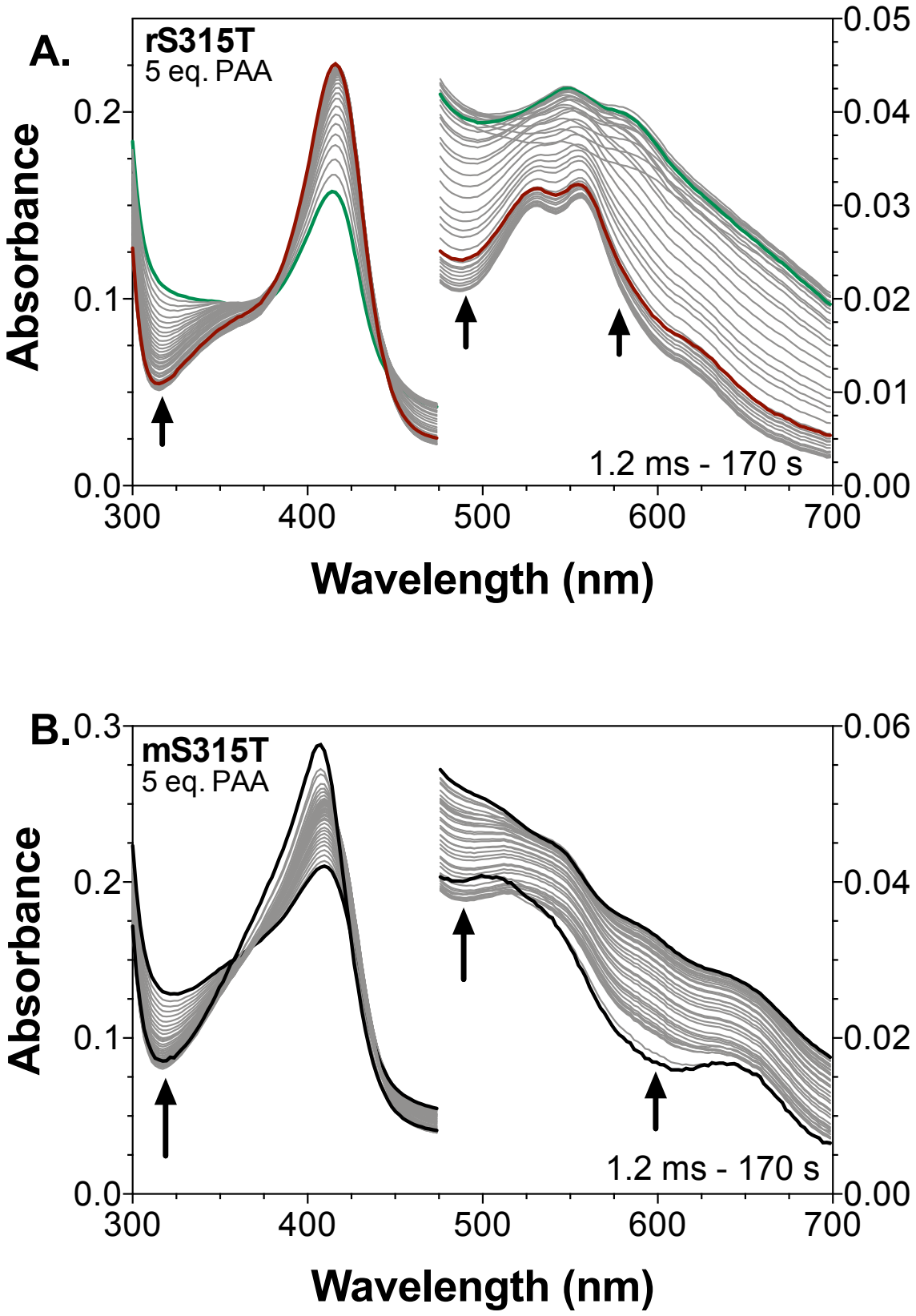

Figure 4.4. Effect of *r*- and *m*KatG preparations on the optical spectra observed for the S315T variant upon its reaction with PAA. Reactions of *r*S315T (A) and *m*S315T (B) were monitored over a period of 170 s. All reactions were carried out using 3 μM KatG in 50 mM acetate, pH 5.0, at 4° C.

reacted *m*S315T KatG with PAA we saw what looked like a ferric enzyme with light scattering effects (Figure 4.4B). The most striking difference here was the difference in absorption around 308 – 375 nm (Figure 4.4). This difference could be attributed to the formation of the MYW adduct, giving us a simple, spectral way, to watch the formation of the adduct. However, with the poor protein quality of *m*S315T KatG it is difficult to draw any firm conclusion. When a comparison of *r*S315T KatG and *m*S315T KatG was performed, monitoring changes in absorbance at 407 nm, the wavelength for maximum absorption of the ferric enzyme, we observed more steps involved in the reactions of *r*S315T KatG than those of *m*S315T KatG (Figure 4.5). Analogous to our findings with other variants, we surmised that the formation of the MYW adduct was accounting for these distinctions. However, because of the poor protein quality we are unable to conclude if the S315T variant has any effect on the formation of the MYW adduct. The data suggest that the S315T substitution does not impact rate or extent of MYW adduct formation; most of the kinetic responses of *r*S315T KatG were similar to those observed for *r*WT KatG. We have noted in Chapter 2, that novel features observed for mS315T KatG in terms of heme coordination state and the active site H-bonded network may arise from the cooperative contributions of the S315T substitution *and* the presence of the MYW adduct.

We also evaluated the impact of rKatG versus mKatG preparations of the S315T variant on ABTS oxidation. The *r*S315T form was able to produce $ABTS^{\bullet+}$ at higher rates and to greater extents than its *m*S315T KatG counterpart. This is shown by the change in absorption at 645 nm due to the $ABTS^{\bullet+}$ (Figure 4.6). The only heme intermediate observed during S315T KatG reactions with H_2O_2 in the presence of ABTS was a

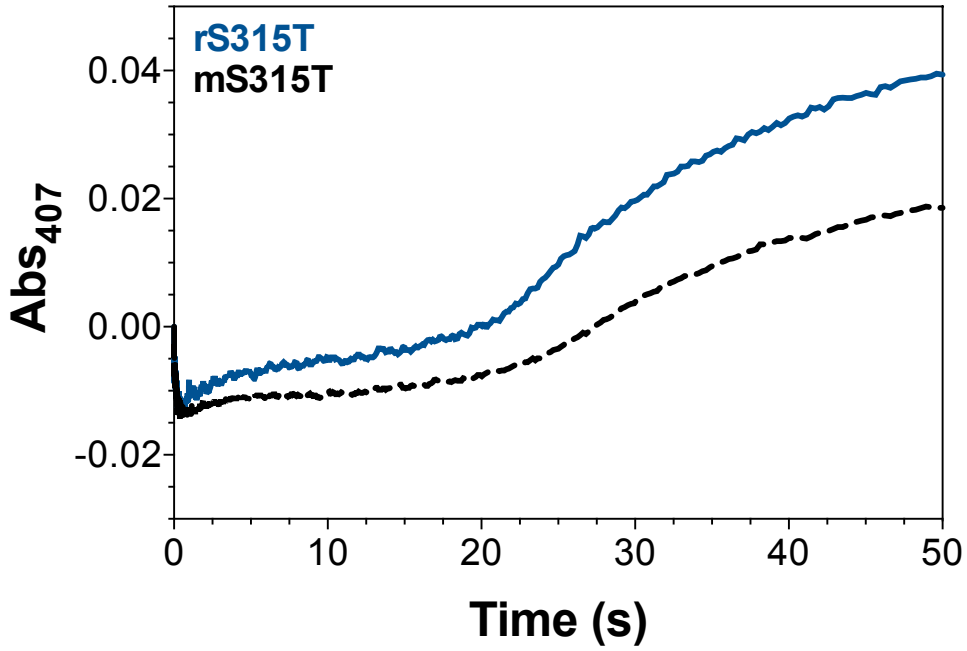

Figure 4.5. Reactivity of the S315T KatG ferric state upon reaction with H_2O_2. The ferric form of rS315T (blue) and mS315T (black) was monitored at 407 nm upon reaction with 2 mM H_2O_2. All reactions were carried out using 3 μM KatG in 50 mM acetate, pH 5.0, at 4° C.

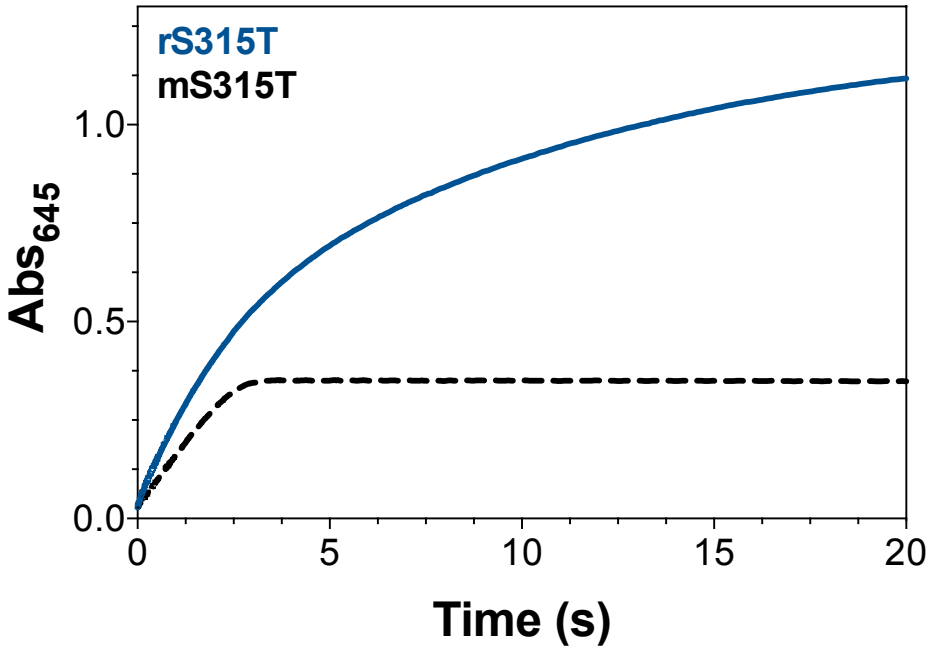

Figure 4.6. Comparison at ABTS oxidation by *r*S315T and *m*S315T KatG. The production of $ABTS^{\bullet+}$ was monitored at **645 nm upon reaction of** *r*S315T (blue) and *m*S315T (black) KatG with 2 mM H_2O_2 in the presence of 1 mM ABTS. All reactions were carried out using 3 μM KatG in 50 mM acetate, pH 5.0, at 4° C.

compound II-like intermediate followed by the accumulation of $ABTS^{\bullet+}$ that caused a large increase in absorption. In order to observe what intermediates are being produced, something that will break down the $ABTS^{\bullet+}$ as it is formed, which is the role of ascorbic acid. When *r*S315T KatG was reacted with ABTS, ascorbic acid, and low concentrations of H_2O_2 a Compound II-like intermediate was observed followed by a Compound III-like intermediate and the return of the ferric state (Figure 4.7A). When *r*S315T KatG was reacted with higher concentrations the same intermediates were observed (Figure 4.7B). The same phenomenon occurred for *m*S315T KatG, in that no intermediates were observed due to poor protein quality (Figure 4.8). These are the same intermediates observed as without ABTS and ascorbic acid, indicating these compounds do not have an effect on the intermediates observed for S315T KatG

Ability of S315T KatG to sustain catalatic O_2 production

The S315T KatG variant was analyzed using an oxygen electrode to determine the extent of oxygen production at different pH values in the presence and absence of ABTS (Figure 4.9). The results were similar to what is observed for WT KatG (not shown). For pH 5 without ABTS, O_2 production was around 50 μM for *r*S315T KatG, where *m*S315T KatG was a little lower around 25 μM. This trend of *m*S315T KatG being lower than *r*S315T KatG continued across pH values. At pH 5 in the presence of ABTS the O_2 production was increased dramatically to around 200 μM for *r*S315T KatG and 100 μM for *m*S315T KatG. This again, is consistent with WT KatG numbers. We also tested S315T KatG at pH 7 without ABTS and found *r*S315T produced around 250 μM O_2 and *m*S315T KatG produced around 200 μM O_2. This is consistent with the molar ratio of peroxide that should be produced based on the concentration of peroxide tested. Meaning,

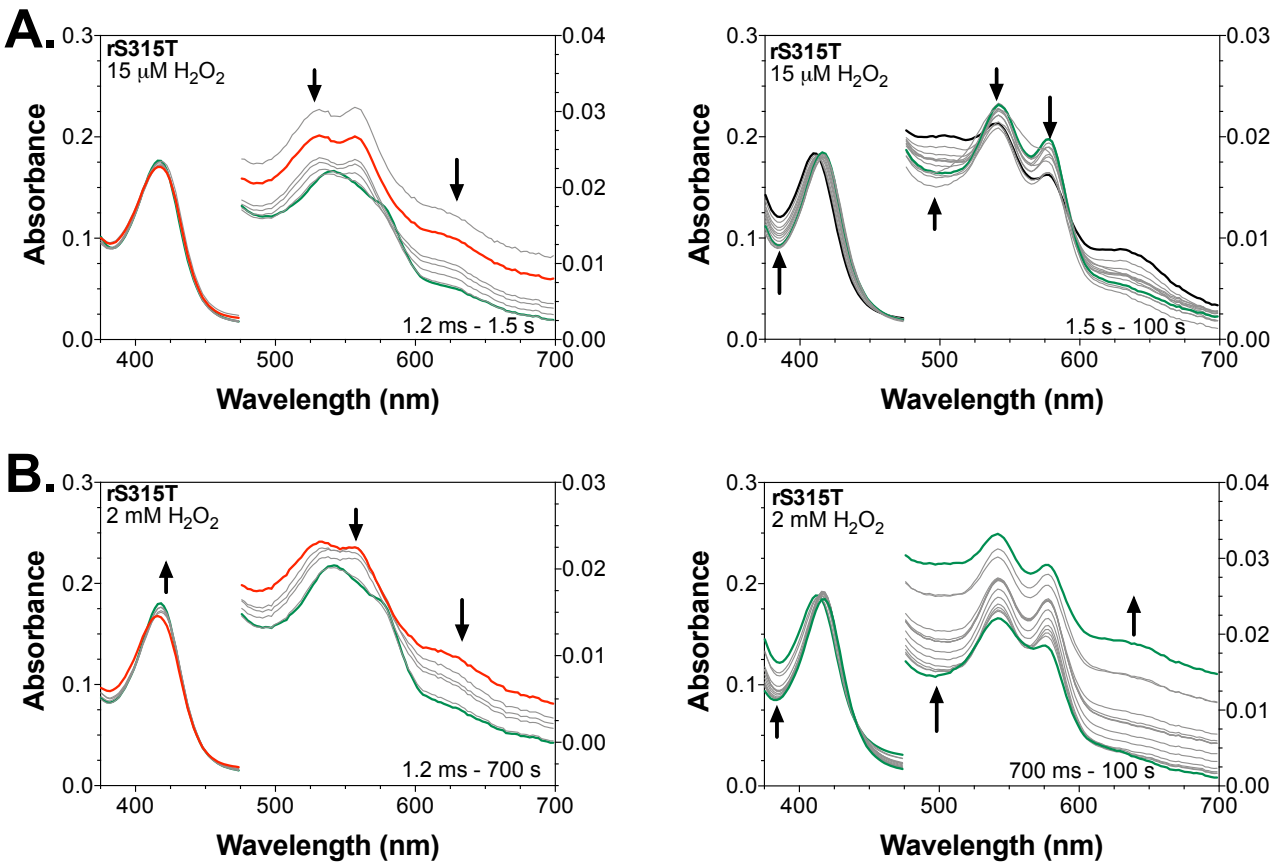

Figure 4.7. Effect of PxED on optical spectra observed for rS315T KatG reaction with limited-turnover (A) and steady-state-supporting concentrations (B) of H_2O_2. *r*S315T KatG reacted with 5 molar equivalents H_2O_2 was monitored up to 1.5 s (A, left panel) to observe accumulation of a compound II-like intermediate followed by a compound III-like intermediate. The return of the ferric enzyme (A, right panel) was observed over the next 100 s. Reaction of *r*S315T KatG with 667 molar equivalents H_2O_2 was monitored over 700 ms (B, left panel) to observe a compound II-like intermediate followed by a compound III-like intermediate. The return of the ferric enzyme was observed to occur to a minimal extent over the next 100 s of reaction time (B, right panel). reactions have been carried out using 3 μM KatG reacted with 15 μM H_2O_2, 1 mM ABTS, and 1mM ascorbic acid in 50 mM acetate, pH 5.0 at 4° C.

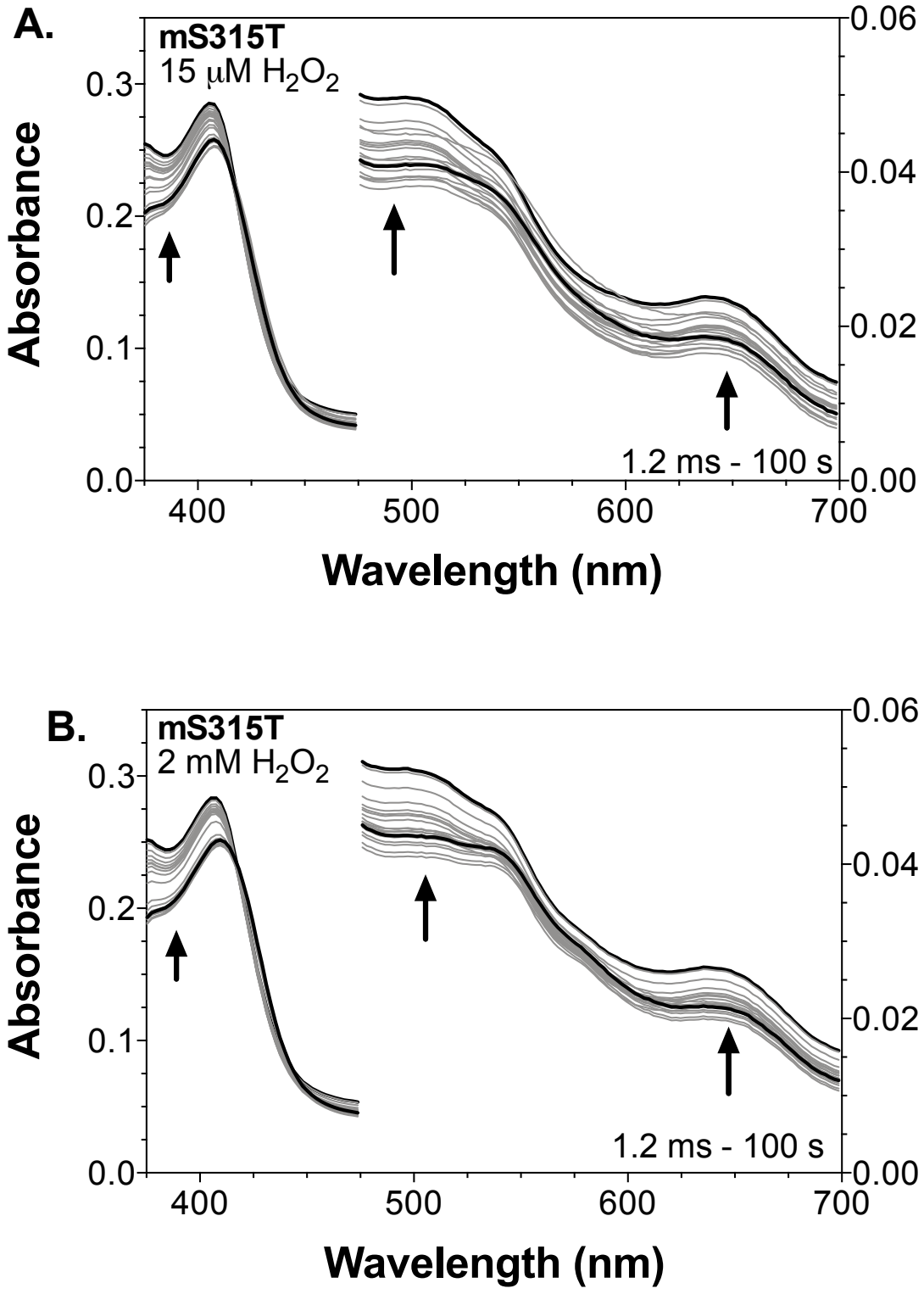

Figure 4.8. Optical spectra obtained for *m*S315T KatG upon reaction with H_2O_2 in the presence of PxED. *m*S315T KatG reaction with limited-turnover H_2O_2 concentration was monitored over 100 s (A) with minimal apparent change in spectra. mS315T KatG reaction with steady-state-supporting H_2O_2 concentrations (B) showed a minute blue-shift in the Soret band of 100 s of reaction time, but no clear progression of intermediates was observed. All reactions have been carried out using 3 μM KatG reacted with 15 μM H_2O_2, 1 mM ABTS, and 1mM ascorbate in 50 mM acetate, pH 5.0, at 4° C.

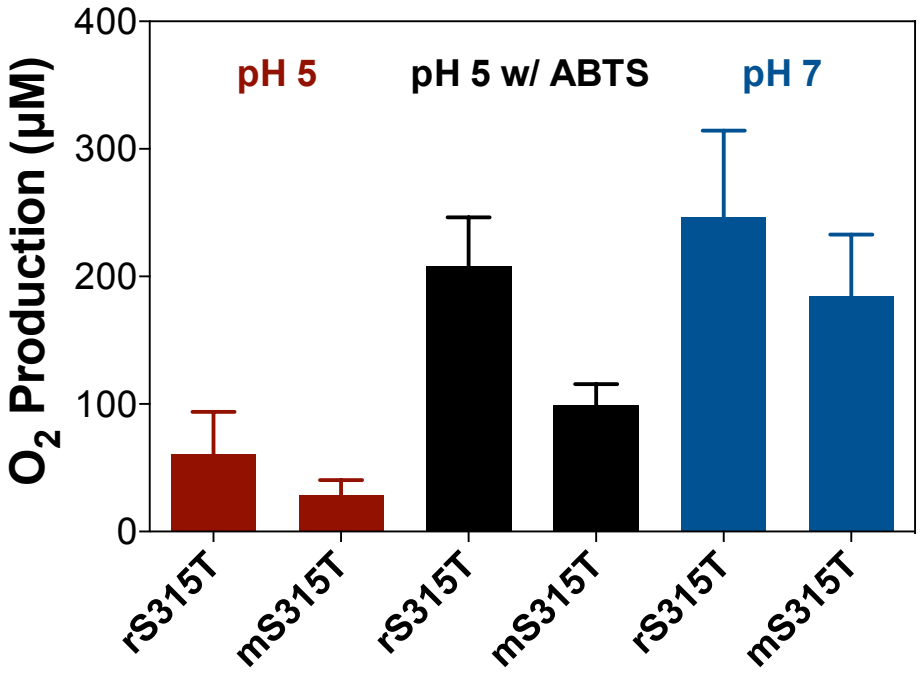

Figure 4.9. Extent of catalatic O_2 Production by S315T KatG. Shown in red are O_2 production concentrations obtained from *r* and *m*KatG preprations of S315T KatG. pH 5 without ABTS, pH 5 with ABTS included (black bars), and at pH 7 without ABTS included. All reactions were carried out with 5 nM KatG reacted with 0.5 mM H_2O_2 at ambient temperature. ABTS, when included, was present at 0.01 mM. Assays were either conducted in 50 mM acetate, pH 5.0, or in 100 mM phosphate, pH 7.0.

the S315T KatG variant is not hindering the production of O_2 in any way. At the end of each of these reactions, when O_2 production had stopped, we tested the S315T KatG variant by adding more enzyme or more peroxide to determine is the enzyme had become inactivated at the end of the reaction or consumed all of the peroxide available. In the case of pH 5 with no ABTS the enzyme was becoming inactivated, therefore when more enzyme was added more O_2 production was observed. When ABTS was added at pH 5 we observed the opposite, the enzyme was consuming all of the peroxide and to increase O_2 production more peroxide must be added. Finally, when we looked at pH 7 we observed that the enzyme was consuming all of the peroxide as well, meaning more peroxide was needed to increase O_2 production. All of these results are consistent with WT KatG, indicating S315T KatG, no matter the presence or absence of the MYW adduct, had no effect on the O_2 production of KatG.

Protein-based radical intermediates identified for S315T KatG

The next question to answer was, what are the protein-based radicals doing when we react the protein with vary equivalents of H_2O_2. When *r*S315T KatG was reacted with increasing equivalents of H_2O_2, let the reaction run to completion and then analyzed using EPR, we observed a slight change in the spin state of the heme. This change was not obvious when looking at the full field (Figure 4.10C) but was more evident when we focused in on G = 1250 (Figure 4.10B) and G = 3375 (Figure 4.10C). The same experiment was performed with PAA as the peroxide instead of H_2O_2, resulting in similar but different observations (Figure 4.11). From this, we learned that both H_2O_2 and PAA effect the spin state of the heme and the higher the concentration of peroxide the greater the effect.

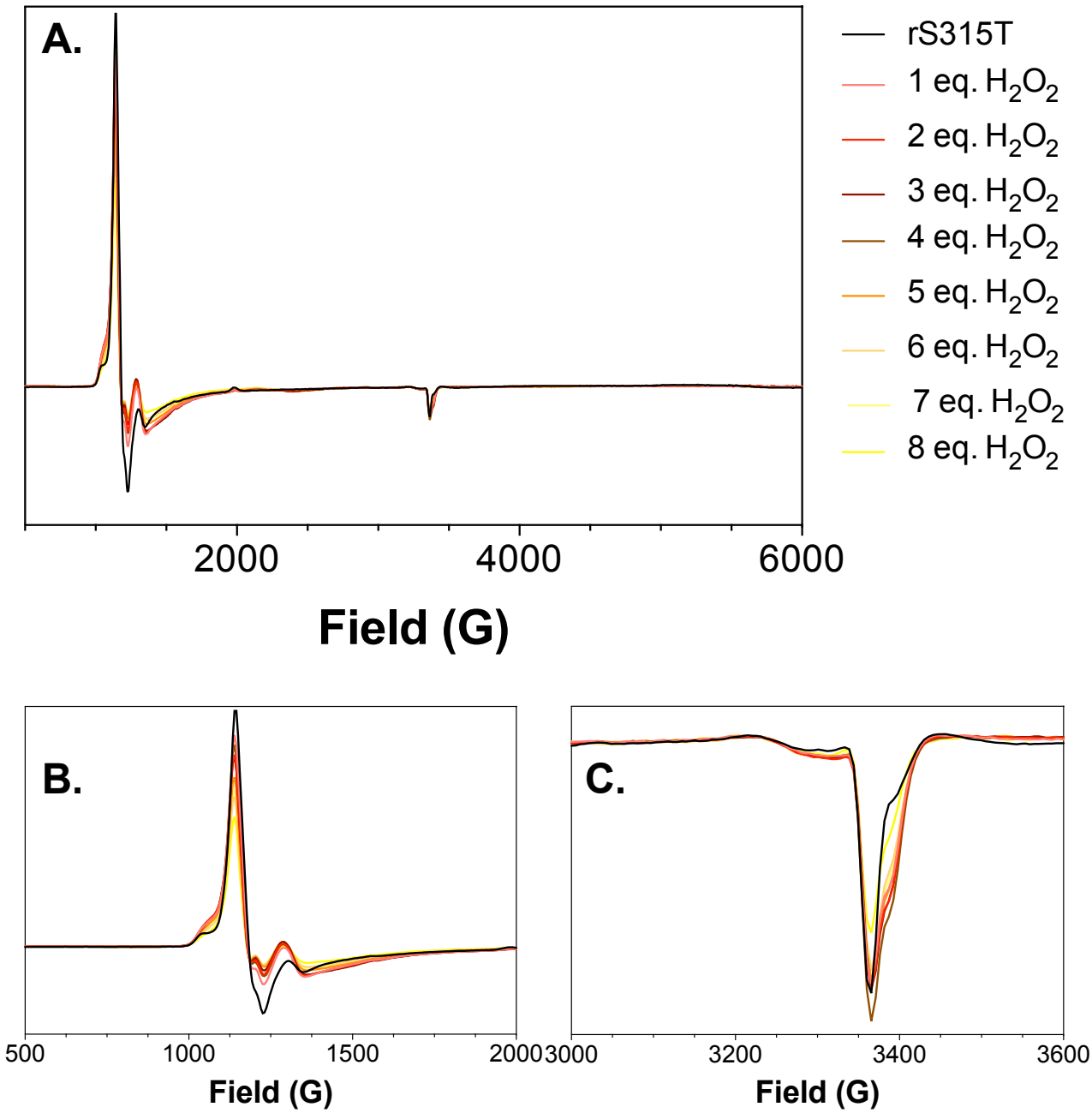

Figure 4.10. Changes in ferric EPR species observed for *r*S315T KatG upon reaction with increasing concentrations of H_2O_2. To simultaneously observe g_x, g_y, and g_z components of the anisotropic g tensor, the full field was swept (500 – 6000 Gauss) (A). To better focus on the g_x and g_y components of the mixed axial and rhombic signals the field from 500 to 2,000 Gauss was monitored (B), to observe the g_z component of ferric species present the field from 3000 – 3600 Gauss was covered (C)**.** All reactions contained 150 µM KatG in reacted in 50 mM acetate, pH 5. These samples were frozen using a manual quench method after reacting for 10 minutes and spectra were collected at 4.5 K.

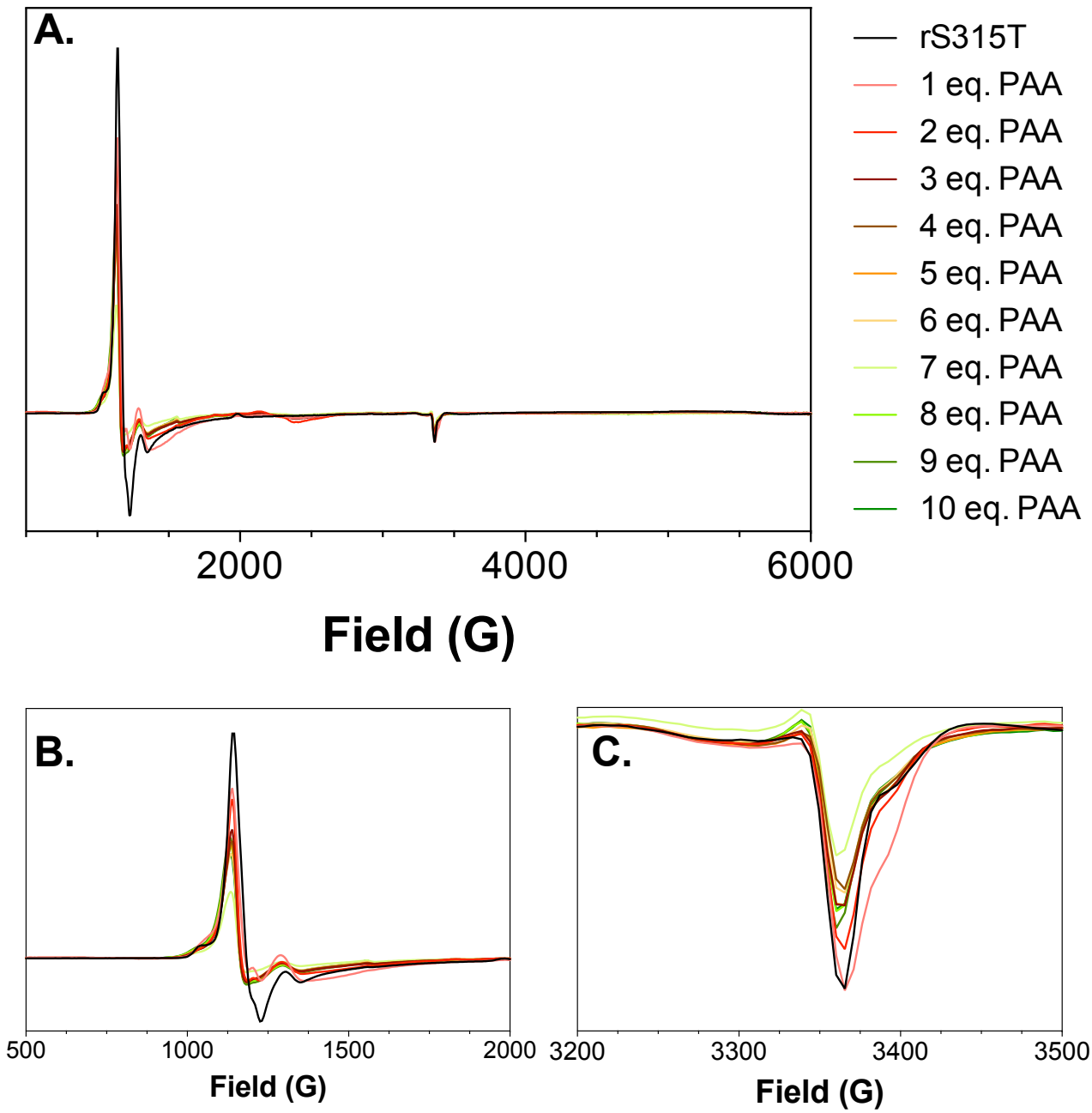

Figure 4.11. Changes in ferric EPR species observed for rS315T KatG upon its reaction with increasing equivalents PAA. To simultaneously observe g_x, g_y, and g_z components of the anisotropic g tensor, the full field was swept (500 – 6000 Gauss) (A). To better focus on the g_x and g_y components of the mixed axial and rhombic signals the field from 500 to 2,000 Gauss was monitored (B), to observe the g_z component of ferric species present the field from 3000 – 3600 Gauss was covered (C)**.** All reactions included 150 µM KatG in 50 mM acetate, pH 5. These samples were frozen using a manual quench method after reacting for 10 minutes and spectra were collected at 4.5 K.

Conclusion

The heme intermediates observed for *r*S315T KatG were interesting and agreed with findings from WT KatG and other KatG variants regarding the formation of the MYW adduct. Accordingly, these investigations did not reveal anything different or new about the S315T KatG variant itself, other than slight differences in rates of MYW formation. The *m*S315T preparation of enzyme showed a tendency toward instability, particularly in the presence of peroxides like PAA. As such, assignment of heme intermediates observed with *m*S315T KatG in optical stopped-flow experiments were not clear and inconclusive. Only the ferric state was observable without interference with *m*S315T KatG. Reactions with PAA produced substantial light scattering and protein aggregation effects when we reacted with PAA instead of H_2O_2, suggesting that this residue may have biological importance for protein stability.

O_2 production values were accessible for both *r*S315T KatG and *m*S315T KatG. *r*S315T KatG not only indicated more intermediates than *m*S315T KatG, it also produced more $ABTS^{\bullet+}$ and was able to produce intermediates at low concentrations of peroxide. For oxygen production, S315T KatG produced similar values as WT KatG for all pH values regardless of ABTS presence. It is also worth noting that *m*S315T KatG was able to produce O_2 even though intermediates were not observed with the stopped-flow. This could have been a result of the kinetics being to fast for the instrumentation and the intermediates occurring in the dead time of the instrument. Electron paramagnetic resonance (EPR) indicated a slight change in the heme state of the iron when reacted with increasing concentrations of H_2O_2 and PAA. While all of this information about S315T KatG seemed to only tell us it acts like WT KatG, we have then ruled out possible ways

that the enzyme could be preventing the inactivation of INH. We have also learned that S315T KatG does not seem to impact the formation of the MYW adduct, specifically, the active site channel access restriction did not effect this formation.

Chapter 5: Summary

Effect of oxidizable amino acids on formation of KatG's MYW cofactor

A new protocol developed for producing KatG protein with heme cofactor yet lacking its protein-derived cofactor was successfully applied across the full range of variants utilized in this research. These included W321F KatG, W412F KatG, W91F KatG, Y413F KatG, and S315T KatG. Across all of the variants, optical and EPR spectra, and ultimately, robust catalase and peroxidase activities demonstrated that the heme was bound and correctly oriented within the enzyme active site in each case. No adventitiously bound heme was evident in any of the reconstituted KatG Phe-substitution variants. Concomitantly, we utilized LC-MS/MS of trypsinized KatG variant preparations to confirm the presence of the fully formed MYW adduct in *m*KatG variants. Correspondingly, little if any MYW adduct-derived tryptic peptides were observed with KatG variants that were either apo- (i.e., *a*KatG) or reconstituted (i.e, *r*KatG) preparations. For the latter, this was provided that the *r*KatG variants had not been exposed to exogenously added peroxide (either H_2O_2 or peracetic acid). Upon treatment of the *r*KatG preparations of each variant with peroxides, tryptic peptides consistent with the presence of the MYW adduct were readily detected by LC-MS/MS. Spectra recorded by EPR for the ferric states of each of the variants confirmed that ferric high-spin states dominated with each purified enzyme. For nearly all of the variants, a hexacoordinate high-spin ferric state appeared to be the predominant species with lesser contributions from pentacoordinate high-spin species. This is typical for KatG. Successful preparation of the full set of *r*KatG variants enabled our investigation of the impact of key oxidizable Trp residues on KatG's ability to establish its unique MYW protein-based cofactor.

The single exception was the S315T KatG variant where the *m*S315T form showed a species with substantial rhombic *g*-tensor anisotropy as the dominant species present, consistent with a greater contribution from the pentacoordinate high-spin state with the Fe^{III} form of the enzyme. Remarkably, the *r*S315T KatG protein showed a much more typical distribution of axial and rhombic species. These data suggest that heme environment for the S315T variant which is characterized by an altered H_2O content and lacks an H_2O molecule in close association with the heme iron[94] arises due to a combination of effects from the S315T substitution as well as the presence of the MYW adduct. This is the first observation of a coordinated effect between the MYW cofactor and the critical substitution in isoniazid resistance.

The spectral features, transient kinetic behavior, and reactivity of *r*W321F KatG, *r*W412F KatG, *r*W91F KatG, and *r*Y413F KatG as well as their *m*KatG counterparts revealed important features of KatG catalysis. The fact that the MYW cofactor had not yet formed in *r*KatG preparations of each variant had a profound impact on the transient- and steady-state behavior of these enzymes upon their reaction with H_2O_2. High-valent heme states that have not been observable because of the robust catalase activity imparted by the MYW cofactor were detected and monitored. Direct observation of the oxidation of the KatG ferric state has only been accessible through reactions with alternative peroxides (e.g., peracetic acid), and these are almost always one to two orders of magnitude slower than reactions involving the physiological substrate, H_2O_2. For most of the variants (i.e., *r*W412F, *r*Y413F, *r*W91F, and *r*S315T), a classical Fe^{IV}=O intermediate (known in the heme enzyme community as "compound II") was the first observed species detected in optical stopped-flow experiments upon reaction of the Fe^{III}

enzymes with H_2O_2. Across the board, the rate constant for this transition was on the order of 10^6 $M^{-1}s^{-1}$. Conspicuously, absent in these reaction sequences was the appearance of a classical compound I-like state (i.e., Fe^{IV}=O[porphyrin]$^{\bullet+}$). This would be expected to come before the appearance and accumulation of a compound II-like state. The lack of an appearance from compound I is an indication that very rapid intramolecular electron transfer takes place reducing the porphyrin π cation radical and oxidizing a nearby redox active amino acid. This is what occurs in KatG's closest cousin, cytochrome *c* peroxidase where the proximal Trp (W191) is the electron source for porphyrin radical reduction. In this regard, it is noteworthy that our lone exception to the kinetics above came from *r*W321F KatG, which showed spectra indicative of a compound I-like form before the transition to a compound II-like species was detected. The rate constant for the initial reaction to form compound I was ~2 x 10^6 $M^{-1}s^{-1}$ in agreement with all the other variants. Given that the compound I-like species was only observed with *r*W321F KatG suggests that W321 (the so-called proximal tryptophan) is uniquely primed for rapid (>100 s^{-1}) intramolecular reduction of the porphyrin π cation radical of compound I. In its absence, it would appear that an alternative site of oxidation would be utilized according to a rate constant of ~4 s^{-1}.

Investigations of these *r*KatG variants with H_2O_2 concentrations enabling steady-state catalase activity also permitted the observation of intermediates not detected with the *m*KatG preparations of enzyme. Here, a transition from pre-steady state to steady-state turnover was marked the progression of a Fe^{IV}=O (compound II) to a compound III-like form (i.e., Fe^{III}-$O_2^{\bullet-}$). The latter is routinely detected during the steady-state catalase consumption of H_2O_2 by the *m*KatG preparations of WT KatG and all catalase-active

KatG variants. The detection of ferryl pre-steady states in KatG catalysis is remarkable in and of itself. However, most impactful was the fact that this permitted the monitoring formation of the MYW adduct in real time. This event was typified by an irreversible increase in absorbance at 315 nm, consistent with the expected spectral features of the MYW adduct as well as its YW and YW quinoid precursors. Applying these molecular tools to determining the impact of alternative sites of oxidation on the formation of the MYW adduct, we determined that the rate and extent of MYW cofactor formation is minimally influenced by the sites of oxidation presented by W321, W91, W412, and Y413 residues.

Oxidizable amino acids effect on electron transfer

The KatG variants W321F, W412F, W91F, and Y413F were used to investigate the effects of active site oxidizable amino acids on the enzymes ability to produce O_2, prevent inactivation, change in heme intermediates when reacted with an array of substrates, ability to produce ABTS radical, and finally the change in electron radicals observed with EPR. The ability to produce O_2 was retained for all variants across pH 5, pH 5 with ABTS, and pH 7. When we looked at O_2 production we found that *r*W321F KatG and *m*W321F KatG produced a significantly lower amount of O_2 than any of the other variants at pH 5, but was comparable at other pH values. We also found that when ABTS was present at pH 5 all variants had an increase in amount of O_2 accordingly but all became inactivated at the end of the first reaction. This was consistent across all *r*KatG variants and *m*KatG variants, this was unusual as the presence of ABTS is thought to prevent inactivation. W321F KatG stood out when we looked at the return of the ferric state when reacted with H_2O_2 alone. It required more steps than any of the other variants,

which we have attributed that extra step to the formation of the MYW adduct in previous discussion. Behind W321F was *r*W412F KatG, which stood out because its return to the ferric state was the quickest, followed by *r*W91F KatG and *r*Y413F KatG neither of which showed much difference than *r*WT KatG in terms of rate. This trend continued when looking at ABTS radical production, where *r*W321F KatG stood out with the largest difference followed by *r*W412F KatG producing the least amount of ABTS radical, then *r*Y413F KatG and *r*W91F KatG producing the most ABTS radical, similar to *r*WT KatG. These trends are consistent with the residues proximity within the active site. *r*W412F KatG and *r*Y413F KatG are in the same path from the active site to the surface of the enzyme, with *r*W412F KatG being the residue closer to the active site and therefore having more impact on the enzymes function. *r*W91F KatG is the furthest away from the active site, agreeing with its trend in being the least utilized. The rate of inactivation was also tested and followed these same trends. *r*W321F KatG was inactivated the quickest and *r*W412F KatG was the most resistant to inactivation, followed by *r*Y413F KatG. However, *r*W91F KatG was inactivated in the middle of these variants. EPR supported the conclusion that *r*W321F KatG underwent a different reaction than the other variants and *r*W412F KatG and *r*Y412F KatG showed almost identical spectrum. From all of these trends we can conclude that W321 is used the most often as an off-catalase electron transfer followed by W412 and Y413 in tandem, and W91 is used the least often out of the potential pathways.

S315T KatG

In investigating the *r*S315T KatG variant we observed heme intermediates that agreed with other findings about the formation of the MYW adduct, but did not indicate

that this variant had any definitive effect on the formation itself. The intermediates observed with *m*S315T KaG were not clear and ultimately inconclusive. We were only able to observed ferric enzyme and light scattering, no matter the substrate. This indicated a problem with protein quality. However, we were able to obtain O_2 production for both *r*S315T KatG and *m*S315T KatG and they resulted in values similar to WT KatG for both regardless of pH or presence or absence of ABTS. *r*S315T KatG not only produced more heme transitions than *m*S315T KatG but, it also produced more ABTS radical and was able to produce intermediates at a very low concentration of peroxide. EPR indicated a change in the heme state of the iron when reacted with peroxide. While all of our results for the S315T KatG variant indicated it functions similar to WT KatG, we have ruled out possible ways the enzyme could be preventing the inactivation of INH. Based on our data, we believe S315T KatG does not seem to be involved in the formation of the MYW adduct and the active site channel access does not effect that formation.

Knowing how this network of oxidizable amino acids interferes with, or contributes to, the formation of the MYW adduct can elucidate not only mechanistically how the formation occurs but also more specific roles for each of the amino acids investigated. Knowing the pathway of electron transfer throughout the enzyme can help to elucidate how KatG performs its catalase and peroxidase function more efficiently and how KatG prevents itself from becoming inactivated. This study will also revealed how often one of these pathways is used in relation to the other pathways and how that may be a function of distance from the active site. Further elucidating how electron transfer can occur within the active site. All of this knowledge, and more specifically the investigation of the S315T mutant can all contribute to the study on antibiotic resistance. Knowing

mechanistically how this mutant functions can help to develop future drugs to combat these specific INH resistance strains. This will provide for many future studies in drug development.

Future mechanistic studies could be done including more RFQ-EPR to further elucidate the protein radicals that are being observed. This would include possible deuterium labeling of the MYW tyrosine to elucidate its formation. Future HPLC studies could also be done to determine how many peroxides it would take, based on the oxidizable pathways available to form the MYW adduct. Other studies to confirm the electronic structure of heme intermediates involved in the MYW adduct formation and the kinetics of each step in the mechanism will also need to be completed. All of these things can be accomplished with a combination of optical stopped-flow, RFQ-EPR, and RFQ-Mössbauer spectroscopies along with LC-MS and LC-MS/MS analyses.

References

1. Messner, K.R., Imlay, J. A, *The identification of primary sites of superoxide and hydrogen peroxide formation in the aerobic respiratory chain and sulfite reductase complex of Escherichia coli.* J. Biol. Chem, 1999. **274**: p. 10119-10128.
2. Imlay, J.A., *Cellular defenses against superoxide and hydrogen peroxide.* Annu. Rev. Biochem 2008. **77**: p. 755-776.
3. Turrens, F.J., *Mitochondrial formation of reactive oxygen species.* J. Physiol, 2003. **552**: p. 335-344.
4. Cadenas., E., *Biochemistry of Oxygen Toxicity.* Annu. Rev. Biochem, 1989. **58**: p. 79-110.
5. Matthew M. Montemore, M.A.v.S., Robert J. Madix, and Cynthia M. Friend, *CO Oxidation on the Pd(111) Surface.* Chemical Reviews, 2018. **118**: p. 2816-2862.
6. Hess., Manson .L., *Molecular oxygen: friend and foe. The role of the oxygen free radical system in the calcium paradox, the oxygen paradox and ischemia/reperfusion injury.* J. Mol. Cell. Cardiol., 1984. **16**: p. 969-985.
7. Lindahl., S.G., *Oxygen and life on earth: an anesthesiologist's views on oxygen evolution, discovery, sensing, and utilization.* J. Anesthesiology 2008. **109**: p. 7-13.
8. Y. Zheng, A.R.Brash, *On the role of molecular oxygen in lipoxygenase activation: comparison and contrast of epidermal lipoxygenase-3 with soybean lipoxygenase-* J. Biol. Chem, 2010. **285**: p. 39876-39887.
9. Schmidt, C.Schmit.Reinhart., *Physical mechanisms of generation and deactivation of singlet oxygen.* Chem. Rev. , 2003. **103**: p. 1685-1757.
10. Pallavi Sharma, Ambuj Bhushan Jha, Rama Shanker Dubey, Mohammad Pessarakli, *Reactive oxygen species, oxidative damage, and antioxidative defense mechanism in plants under stressful conditions.* J. Botany, 2012.
11. E R Stadtman 1, R L Levine, *Protein oxidation.* Ann N Y Acad Sci, 2000. **899**: p. 191–208.
12. Gilbert O Fruhwirth, Albin Hermetter, *Mediation of apoptosis by oxidized phospholipids.* Subcell Biochem, 2008. **49**: p. 351–367.
13. Richard L Auten 1, Mary H Whorton, S Nicholas Mason, *Blocking neutrophil influx reduces DNA damage in hyperoxia-exposed newborn rat lung.* Am J Respir Cell Mol Biol, 2002. **26**: p. 391–397.
14. S M McKenna and K J Davies, *The inhibition of bacterial growth by hypochlorous acid. Possible role in the bactericidal activity of phagocytes.* Journal of Biochemistry, 1988. **254**: p. 685-692.
15. V.V. Barynin M.M. Whittaker, S.V.A., V.S. Lamzin, P.M. Harrison, P.J. Artymiuk, J.W. Whittaker, *Crystal structure of manganese catalase from Lactobacillus plantarum.* Structure 2001. **9**: p. 725-738.
16. M. Zamocky P.G. Furtmuller, C.O., *Evolution of catalases from bacteria to humans.* Antioxid. Redox Signal., 2008. **10**: p. 1527-1548.
17. Ma, Z., Strickland, K. T., Cherne, M. D., Sehanobish, E., Rohde, K. H., Self, W. T., and Davidson, V. L., *The Rv2633c protein of Mycobacterium tuberculosis is a non-heme di-iron catalase with a possible role in defenses against oxidative stress.* Journal of Biological Chemistry, 2018. **293**: p. 1590–1595.
18. Ma, Z., Abendroth, J., Buchko, G. W., Rohde, K. H., and Davidson, V. L., *Crystal structure of a hemerythrin-like protein from Mycobacterium kansasii and*

homology model of the orthologous Rv2633c protein of M. Tuberculosis. Biochemical Journal, 2020. **477**: p. 567–581.
19. Whittaker, J.W., *Non-heme manganese catalase - The "other" catalase.* Archives of Biochemistry and Biophysics, 2012. **525**: p. 111-120.
20. J Bai 1, A I Cederbaum, *Mitochondrial catalase and oxidative injury.* Cederbaum AI, 2001. **10**: p.
189-99.
21. Zámocký M Gasselhuber B, F.P., Obinger C, *Molecular evolution of hydrogen peroxide degrading enzymes.* Arch Biochem Biophys, 2012. **525**: p. 131-44.
22. P Chelikani 1, I Fita, P C Loewen., *Diversity of structures and properties among catalases.* Cell. Mol. Life Sci, 2004. **61**: p. 192-208.
23. Klotz MG Klassen GR, Loewen.P., *Phylogenetic relationships among prokaryotic and eukaryotic catalases.* Mol. Biol. Evol., 1997. **14**: p. 951-8.
24. Carpena X Soriano M, K.M., Duckworth HW, Donald LJ, Melik-Adamyan W, Fita I, Loewen PC., *Structure of the Clade 1 catalase, CatF of Pseudomonas syringae, at 1.8 A resolution.* Proteins, 2003. **50**: p. 423-36.
25. P. Chelikani X. Carpena, I.F., P.C. Loewen, *An electrical potential in the access channel of catalases enhances catalysis.* J. Biol. Chem., 2003. **278**: p. 31290-31296.
26. Visser, S.P.d., *What external perturbations influence the electronic properties of catalase compound I.* Inorg. Chem., 2006. **45**: p. 9551-9557.
27. Mercedes Alfonso-Prieto, Xevi Biarnés, Pietro Vidossich, and Carme Rovira, *The molecular mechanism of the catalase reaction.* J. Am. Chem. Soc., 2009. **131**: p. 11751-11761.
28. M. Zamocky, S.H., I. Schaffner, B. Gasselhuber, A. Nicolussi, M. Soudi, K.F. Pirker, P.G. Furtmuller, C. Obinger *Independent evolution of four heme peroxidase superfamilies.* Arch Biochem Biophys, 2015. **574**: p. 108-119.
29. D. Koua L. Cerutti, L.F., C.J. Sigrist, G. Theiler, N. Hulo, C. Dunand, *PeroxiBase: a database with new tools for peroxidase family classification.* Nucleic Acids Res, 2009. **37**: p. 261-266.
30. E. Torres, Marcela Ayala., *Biocatalysis based on heme peroxidases, Molecular Phylogeny of heme peroxidases.* Springer 2010. **2**.
31. K G Welinder 1, J M Mauro, L Nørskov-Lauritsen., *Superfamily of plant, fungal and bacterial peroxidases.* Curr. Opin. Struct. Biol., 1992. **2**: p. 388-393.
32. Rahul Singh, B.W., Taweewat Deemagarn, Vikash Jha, Jacek Switala, Peter C Loewen, *Comparative study of catalase-peroxidases (KatGs).* Arch Biochem Biophys, 2007. **471**: p. 207-14.
33. Zhao, X., *Specific function of the Met-Tyr-Trp adduct radical and residues Arg-418 and Asp-137 in the atypical catalase reaction of catalase-peroxidase KatG.* J. Bio. Chem, 2012. **44**: p. 37057-65.
34. Ghiladi, R.A.K., G. M., Medzihradszky, K. F., and Ortiz de Montellano, P. R. , *The Met-Tyr-Trp cross-link in Mycobacterium tuberculosis catalaseperoxidase (KatG): autocatalytic formation and effect on enzyme catalysis and spectroscopic properties.* J Biol Chem, 2005. **280**: p. 22651–22663.
35. D B Goodin 1, D E McRee, *The Asp-His-Fe triad of cytochrome c peroxidase controls the reduction potential, electronic structure, and coupling of the tryptophan free radical to the heme.* Biochemistry, 1993. **32**: p. 3313-3324.

36. Santoni, E.J., C., Obinger, C., and Smulevich, G., *Comparison between catalase-peroxidase and cytochrome c peroxidase. The role of the hydrogen-bond networks for protein stability and catalysis.* Biochemistry, 2004. **43**: p. 5792-5802.
37. Hillar, A., Peters, B., Pauls, R., Loboda, A., Zhang, H., Mauk, A. G., and Loewen, P. C., *Modulation of the activities of catalase-peroxidase HPI of Escherichia coli by site-directed mutagenesis.* Biochemistry, 2000. **39**: p. 5868-5875.
38. Regelsberger, G., Jakopitsch, C., Ruker, F., Krois, D., Peschek, G. A., and Obinger, C., *Effect of distal cavity mutations on the formation of compound I in catalase peroxidases.* J. Biol. Chem, 2000. **275**: p. 22854-22861.
39. Jakopitsch C Auer M, R.G., Jantschko W, Furtmüller PG, Rüker F, Obinger C, *The catalytic role of the distal site asparagine-histidine couple in catalase-peroxidases.* Eur J Biochem., 2003. **270**: p. 1006-13.
40. X. Zhao J. Suarez, A.K., S. Yu, L. Metlitsky, R.S. Magliozzo, *A radical on the Met-Tyr-Trp modification required for catalase activity in catalase-peroxidase is established by isotopic labeling and site-directed mutagenesis.* J. Am. Chem. Soc., 2010. **132**: p. 8268-8269.
41. Thomas Bertrand 1, Nigel A J Eady, Jamie N Jones, Jesmin, Judit M Nagy, Brigitte Jamart-Grégoire, Emma Lloyd Raven, Katherine A Brown, *Crystal structure of Mycobacterium tuberculosis catalase-peroxidase. Journal of Biological Chemistry.* 2004. **279**: p. 38991–38999.
42. Donald, L.J., K., O. v., Duckworth, H. W., Wiseman, B., Deemagarn, T., Singh, R., Switala, J., Carpena, X., Fita, I., and Loewen, P. C. , *Characterization of the catalase-peroxidase KatG from Burkholderia pseudomallei by mass spectrometry.* Journal of Biological Chemistry, 2003. **278**: p. 35687–35692.
43. Reza A Ghiladi, Giselle M Knudsen, Katalin F Medzihradszky, Paul R Ortiz de Montellano, *Role of the Met-Tyr-Trp cross-link in Mycobacterium tuberculosis catalase-peroxidase (KatG) as revealed by KatG(M255I).* Biochemistry., 2005. **44**: p. 15093–15105.
44. Olive J Njuma, Ian Davis, Elizabeth N Ndontsa, Jessica R Krewall, Aimin Liu, Douglas C Goodwin, *Mutual synergy between catalase and peroxidase activities of the bifunctional enzyme KatG is facilitated by electron hole-hopping within the enzyme.* J. Bio. Chem, 2017. **292**: p. 18408-18421.
45. C. Jakopitsch A. Ivancich, F.S., A. Wanasinghe, G. Poltl, P.G. Furtmuller, F. Ruker, C. Obinger, *Influence of the unusual covalent adduct on the kinetics and formation of radical intermediates in synechocystis catalase peroxidase: a stopped-flow and EPR characterization of the MET275, TYR249, and ARG439 variants.* J. Biol. Chem, 2004. **279**: p. 46082-46095.
46. C. Jakopitsch C. Obinger, S.U., A. Ivancich, *Identification of Trp106 as the tryptophanyl radical intermediate in Synechocystis PCC6803 catalase-peroxidase by multifrequency Electron Paramagnetic Resonance spectroscopy.* J. Inorg. Biochem, 2006. **100**: p. 1091-1099.
47. J. Suarez K. Ranguelova, A.A.J., J. Manzerova, V. Krymov, X. Zhao, S. Yu, L. Metlitsky, G.J. Gerfen, R.S. Magliozzo, *An oxyferrous heme/protein-based radical intermediate is catalytically competent in the catalase reaction of Mycobacterium tuberculosis catalase-peroxidase (KatG).* J. Biol. Chem., 2009. **284**: p. 7017-7029.

48. Ranguelova, K., Radical sites in *M. tuberculosis* KatG Identified using EPR spectroscopy, the 3-D Crystal Structure and Electron-transfer Couplings. J Biol Chem, 2007. **282**: p. 6255-6264.
49. Anabella Ivancich, Pierre Dorlet, David B. Goodin, and Sun Un, *Multifrequency high-field EPR study of the tryptophanyl and tyrosyl radical intermediates in wild-type and the W191G mutant of cytochrome c peroxidase.* J. Am. Chem. Soc., 2001. **123**: p. 5050–5058.
50. Sivaraja, M., *Identification by ENDOR of Trp191 as the free-radical site in cytochrome-c peroxidase compound ES.* Science, 1989. **245**: p. 738–740.
51. Njuma, O.J., Ndontsa, E.N., and Goodwin, D.C. *Catalase in peroxidase clothing: Interdependent cooperation of two cofactors in the catalytic versatility of KatG.* Arc. Biochem. and Biophys., 2014. **544**: p. 27-39.
52. Shin, D.V., *MauG, a diheme enzyme that catalyzes tryptophan tryptophylquinone biosynthesis by remote catalysis.* Arch Biochem Biophys, 2014. **544**: p. 112-8.
53. Wang Y Graichen ME, L.A., Pearson AR, Wilmot CM, Davidson VL., *MauG, a diheme enzyme that catalyzes tryptophan tryptophylquinone biosynthesis by remote catalysis.* Biochemistry, 2003. **42**: p. 7318–7325.
54. Erik T Yukl 1, Carrie M Wilmot, *Cofactor Biosynthesis through Protein Post-Translational Modification.* Curr Opin Chem Biol, 2009. **13**: p. 469–474.
55. Victor L. Davidson, *Generation of protein-derived redox cofactors by posttranslational modification.* Adv Protein Chem, 2001. **58**: p. 95–140.
56. Andres Andreo-Vidal, Kyle J. Mamounis, Esha Sehanobish, Dante Avalos, Jonatan Cristian Campillo-Brocal,1 Antonio Sanchez-Amat, Erik T. Yukl, Victor L. Davidson, *Structure and enzymatic properties of an unusual cysteine tryptophylquinone-dependent glycine oxidase from Pseudoalteromonas luteoviolacea.* Science, 1991. **252**: p. 817–824.
57. Pearson AR De La Mora-Rey T, G.M., Wang Y, Jones LH, Marimanikkupam S, Agger SA, Grimsrud PA, Davidson VL, Wilmot CM, Biochemistry, 2004. **43**: p. 5494–5502.
58. Yukl ET Liu F, K.J., Shin S, Jensen LM, Davidson VL, Wilmot CM, Liu A., Proc Natl Acad Sci U S A, 2013. **110**: p. 4569–4573.
59. Li X Fu R, L.S., Krebs C, Davidson VL, Liu A., Proc Natl Acad Sci USA, 2008. **105**: p. 8597–8600.
60. Abu Tarboush N, J.L., Feng M, Tachikawa H, Wilmot CM, Davidson VL., Biochemistry, 2010. **49**: p. 9783–9791.
61. Abu Tarboush N Jensen LMR, Y.E., Geng J, Liu A, Wilmot CM, Davidson VL., Proc Natl Acad Sci U S A., 2011. **108**: p. 16956–16961.
62. Choi M, S.S., Davidson VL., Biochemistry, 2012. **51**: p. 6942–6949.
63. Van der Palen CJ Slotboom DJ, J.L., Reijnders WN, Harms N, Duine JA, van Spanning RJ. Eur J, Biochemical Journal, 1995. **230**: p. 860–871.
64. D A Rouse 1, J A DeVito, Z Li, H Byer, S L Morris, *Site-directed mutagenesis of the katC gene of Mycobacterium tuberculosis: Effects on catalaseperoxidase activities and isoniazid resistance.* Molecular Microbiology, 1996. **22**: p. 583–592.
65. Thomas Scior 1, Iván Meneses Morales, Solón Javier Garcés Eisele, David Domeyer, Stefan Laufer, *Antitubercular isoniazid and drug resistance of Mycobacterium tuberculosis- A review.* Archiv der Pharmazie., 2002. **335**: p. 511–525.

66. Marttila, H.J.S., H., Huovinen, P., and Viljanen, M. K., *katG mutations in isoniazid-resistant Mycobacterium tuberculosis isolates recovered from Finnish patients.* Antimicrobial Agents and Chemotherapy., 1996. **40**: p. 2187–2189.
67. Lei, B.W., C. J., and Tu, S. C., *Action mechanism of antitubercular isoniazid: Activation by Mycobacterium tuberculosis KatG, isolation, and characterization of InhA inhibitor.* Journal of Biological Chemistry, 2000. **275**: p. 2520–2526.
68. Rawat, R.W., A., and Tonge, P. J., *The isoniazid-NAD adduct is a slow, tight-binding inhibitor of InhA, the Mycobacterium tuberculosis enoyl reductase: Adduct affinity and drug resistance.* Proceedings of the National Academy of Sciences of the United States of America. , 2003. **100**: p. 13881–13886.
69. Singh, R. Wiseman, B., D.T., Donald L.J., Duckworth H.W., Carpena, X., Fita, I., Loewen PC, *Catalase-peroxidases (KatG) exhibit NADH oxidase activity.* J Biol Chem, 2004. **279**: p. 43098–43106.
70. Wengenack, N.L. Hoard, H.M., Rusnak, F., *Isoniazid oxidation by Mycobacterium tuberculosis KatG: a role for superoxide which correlates fit isoniazid susceptibility.* J Am Chem Soc, 1999. **121**: p. 97480–97449.
71. Wiseman B, Carpena, X., Feliz, M., Donald L.J., Pons M, Fita I., Loewen P.C., *Isonicotinic acid hydrazide (INH) conversion to isonicotinyl-NAD by catalase-peroxidases.* J Biol Chem, 2010. **285**: p. 26662–26673.
72. A. Fathurrachman, R.L.A., Z. Ahmad, *Frequency of Mutation katG S315T Mycobacterium Tuberculosis in Multi Drug Resistance Tuberculosis Patients in South Sumatera,.* International Journal of Infectious Diseases, 2022. **116**: p. 1201-9712.
73. Gray, Harry B., and Jay R. Winkler., *Hole hopping through tyrosine/tryptophan chains protects proteins from oxidative damage.* Proc. Natl. Acad. Sci, 2015. **35**: p. 10920-10925.
74. Kelley, J.R. *OpenWetWare*. 2005.
75. Kapetanaki S Chouchane S, G.S., Yu S, Magliozzo RS, Schelvis JP, *Conformational differences in Mycobacterium tuberculosis catalase-peroxidase KatG and its S315T mutant revealed by resonance Raman spectroscopy.* Biochemistry, 2003. **42**: p. 3835-45.
76. Baker, R.D., Cook, C.O., Goodwin, D. C. *Catalase-peroxidase active site restructuring by a distant and "inactive" domain.* Biochemistry, 2006. **45**: p. 7113-21.
77. Wang, Y., Goodwin, D. C. *Integral role of the I'-helix in the function of the "inactive" C-terminal domain of catalase–peroxidase (KatG).* Biochimica et Biophysica Acta -Proteins and Proteomics 2013. **1834**: p. 362-371.
78. Baker, R.D., Cook, C.O., Goodwin, D.C. *Properties of catalase-peroxidase lacking its C-terminal domain.* Biophys Research communications 2004. **320**: p. 833-839.
79. Ndontsa EN, Moore RL, Goodwin DC, *Stimulation of KatG catalase activity by peroxidatic electron donors.* Arch Biochem Biophys, 2012. **525**: p. 215-22.
80. Jessica R. Krewall, L. E. Minton, and Douglas C. Goodwin, *KatG Structure and Mechanism: Using Protein-Based Oxidation to Confront the Threats of Reactive Oxygen.* Mechanistic Enzymology: Bridging Structure and Function 2020. **5**: p. 83-120.

81. Harry B. Gray, Jay R.Winkler *Functional and protective hole hopping in metalloenzymes, Royal Society of Chemistry (Perspective).* Chem Sci, 2021. **12**: p. 13988-14003.
82. Meena Kathiresan, Ann M. English, *LC-MS/MS suggests that hole hopping in cytochrome c peroxidase protects its heme from oxidative modification by excess H2O2.* Chem. Sci., 2017. **8**: p. 1152-1162.
83. Anabella Ivancich, Lynda J Donald, J.V., Ben Wiseman, Ignacio Fita, Peter C Loewen, *Spectroscopic and kinetic investigation of the reactions of peroxyacetic acid with Burkholderia pseudomallei catalase-peroxidase, KatG.* Biochemistry 2013. **52**: p. 7271-82.
84. Kudalkar, S.N., Campbell, R.A., Li, Y., Varnado, C.L., Prescott, C., and Goodwin D.C. 2012. *Enhancing the peroxidatic activity of KatG by deletion mutagenesis* J. Inorg. Biochem. **116**, 106 - 115.
85. Zhao X, Y.S., Ranguelova K, Suarez J, Metlitsky L, Schelvis JP, Magliozzo RS, *Role of the oxyferrous heme intermediate and distal side adduct radical in the catalase activity of Mycobacterium tuberculosis KatG revealed by the W107F mutant.* J Biol Chem, 2009. **284**.
86. J. Colin, B. Wiseman, J.S., P.C. Loewen, A. Ivancich, *Distinct Role of Specific Tryptophans in Facilitating Electron Transfer or as [Fe(IV)=O Trp•] Intermediates in the Peroxidase Reaction of Bulkholderia pseudomallei Catalase-Peroxidase: A Multifrequency EPR Spectroscopy Investigation.* J. Am. Chem. Soc., 2009. **131**: p. 8557–8563.
87. Ten-I T Kumasaka T, H.W., Tanaka S, Yoshimatsu K, Fujiwara T, Sato T., *Expression, purification, crystallization and preliminary X-ray analysis of the Met244Ala variant of catalase-peroxidase (KatG) from the haloarchaeon Haloarcula marismortui.* Acta Crystallogr Sect F Struct Biol Cryst Commun., 2007. **63**: p. 940-3.
88. H.B. Dunford, Hewson, W.D., and Steiner, H., *Horseradish peroxidase. Reactions in water and deuterium-oxide, cyanide binding, compound-I formation, and reactions of compound-I and compound-II with ferrocyanide.* Can. J. Chem., 1978. **56**: p. 2844-2852.
89. Wonwoo Nam, Hui Jung Han, So-Young Oh, Yoon Jung Lee, Mee-Hwa Choi, So-Yeop Han, Cheal Kim, Seung Kyun Woo, and Woonsup Shin, *A Homolytic Mechanism of O-O Bond Scission Prevails in theReactions of Alkyl Hydroperoxides with an OctacationicTetraphenylporphinato—Iron(III) Complex in Aqueous Solution.* J. Am. Chem. Soc., 1995. **117**: p. 4533-4544.
90. Anabella Ivancich, Christa Jakopitsch, M.A., Sun Un, and Christian Obinger, *Protein-Based Radicals in the Catalase-Peroxidase of Synechocystis PCC6803: A Multifrequency EPR Investigation of Wild-Type and Variants on the Environment of the Heme Active Site.* JACS 2003. **46**: p. 14093-14102.
91. D C Goodwin, I Yamazaki, S D Aust, T A Grover, *Determination of Rate Constants for Rapid Peroxidase Reactions.* Analytical Biochemistry 1995. **231** (333-338).
92. Kapetanaki SM Chouchane S, Y.S., Zhao X, Magliozzo RS, Schelvis JP, *Mycobacterium tuberculosis KatG(S315T) catalase-peroxidase retains all active site properties for proper catalytic function.* Biochemistry, 2005. **44**: p. 243-52.
93. Christine E Cade, Adrienne C Dlouhy, Katalin F Medzihradszky, Saida Patricia Salas-Castillo, Reza A Ghiladi, *Isoniazid-resistance conferring mutations in Mycobacterium tuberculosis*

KatG: catalase, peroxidase, and INH-NADH adduct formation activities. Protein Sci., 2010. **19**: p. 458–474.

94. Zhao X Yu H, Y.S., Wang F, Sacchettini JC, Magliozzo RS, *Hydrogen peroxide-mediated isoniazid activation catalyzed by Mycobacterium tuberculosis catalase-peroxidase (KatG) and its S315T mutant.* Biochemistry, 2006. **45**: p. 4131-40.
95. Bravo J, Verdaguer N, Tormo J, Betzel C, Switala J, Loewen PC, Fita I. *Crystal structure of catalase HPII from Escherichia coli*. Structure, 1995. **3:** p. 491-502.
96. Finzel BC, Poulos TL, Kraut J. *Crystal structure of yeast cytochrome c peroxidase refined at 1.7-A resolution*. J Biol Chem. 1984. **259**: p. 13027-36.